INSTITUT FÜR PHYSIK

LEIBNIZ INSTITUTE FOR BALTIC SEA RESEARCH WARNEMÜNDE

Observation of internal waves in the Baltic Sea: Motions near the inertial and buoyancy frequencies

PhD Thesis

Eefke Marijn van der Lee

Rostock, 2012

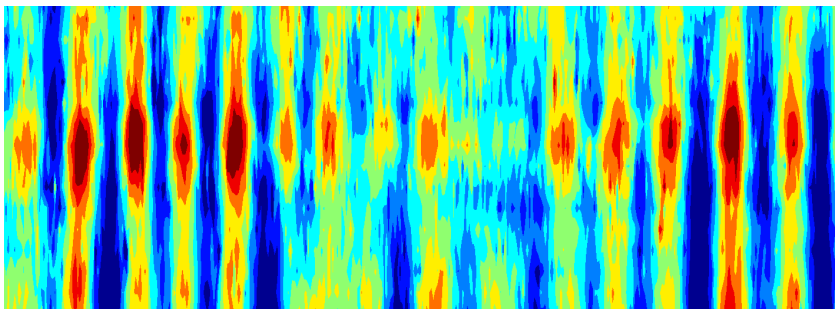

urn:nbn:de:gbv:28-diss2013-0091-0

Observation of internal waves in the Baltic Sea: Motions near the inertial and buoyancy frequencies

Dissertation
zur
Erlangung des akademischen Grades
doctor rerum naturalium (Dr. rer. nat.)
der Mathematisch-Naturwissenschaftlichen Fakultät
der Universität Rostock

vorgelegt von
Eefke Marijn van der Lee
aus Rostock

Rostock, Januar 2012

Gutachter/Reviewers:

Prof. Dr. Hans Burchard
Leibniz Institute for Baltic Sea Research Warnemünde, Germany

Prof. Dr. Ilker Fer
Geophysical Institute, University of Bergen, Norway

Dr. Lars Umlauf
Leibniz Institute for Baltic Sea Research Warnemünde, Germany

Datum der Einreichung/Submission date: 31.01.2012
Datum der Verteidigung/Defence date: 11.05.2012

Every wave, regardless of how high and forceful it crests,
must eventually collapse within itself.
Stefan Zweig (Austrian novelist (1881–1942))

Contents

Abstract

The dynamics of internal wave motions and their relation to mixing were investigated here with an extensive, high-resolution data set from two cruises in summer 2008 and winter 2010 in the Bornholm Basin of the Baltic Sea. In the absence of tides, it was shown that the basin-scale energetics were governed by wind-generated, low-mode, near-inertial wave motions. These motions were associated with persistent, narrow bands of high shear (S^2), high stratification (N^2) and enhanced dissipation rates of turbulent kinetic energy (ε). These bands of turbulent dissipation, being the major source of mixing inside the permanent halocline, scaled with both the density stratification and the velocity shear. This deviates from the canonical, Richardson-number dependent ($Ri = N^2/S^2$) ε-parameterisations for the open ocean of Garrett-Munk and Gregg-Henyey, but follows a continental shelf parameterisation by MacKinnon and Gregg. In winter a large storm increased the energy in the entire internal wave frequency range. In the wake of the storm a long-lasting energy maximum of strong internal waves with frequencies near the buoyancy frequency was observed. These high-frequency motions were highly coherent over depth for vertical velocity, but less so for isopycnal displacements. This thesis shows that internal waves were energetic at a wide range of frequencies and the main mixing mechanism in the interior of the basin.

Zusammenfassung

Die Dynamik der internen Wellenbewegungen und ihre Beziehung zur Mischung wurden hier mit einem umfangreichen, hochaufgelösten Datensatz der zwei Messfahrten im Sommer 2008 und im Winter 2010 ins Bornholm Becken der Ostsee untersucht. In Abwesenheit von Gezeiten wurde gezeigt, dass die beckenweite Energetik von Wind-generierten internen Wellen mit kleinen Modenzahlen und Frequenzen nahe der Inertialfrequenz bestimmt ist. Diese Bewegungen waren mit andauernden, schmalen Schichten von hoher Scherung (S^2), hoher Schichtung (N^2) und erhöhter Dissipation turbulenter kinetischer Energie (ε) verbunden. Diese Schichten der turbulenten Dissipation waren die Hauptquelle der Mischung innerhalb der permanenten Salz-Sprungschicht. Es wurde gezeigt, dass die Dissipationsrate der kinetischen Energie sowohl mit der Dichteschichtung der Wassersäule als auch mit der vertikalen Scherung der Geschwindigkeiten skaliert. Dieser Zusammenhang weicht von den kanonischen, Richardson-Zahl-abhängigen ($Ri = N^2/S^2$) ε-Parameterisierungen von Garrett-Munk und Gregg-Henyey ab und folgt stattdessen der Kontinentalplattenparameterisierung von MacKinnon und Gregg. Ein Sturm während der Winterfahrt erhöhte die Energie im internen Wellenspektrum. Im Nachlauf des Sturmes wurde ein langlebiges Energiemaximum von internen Wellen nahe der Brunt-Väisälä-Frequenz gemessen. Für diese Frequenzen wurde eine hohe Kohärenz der vertikalen Geschwindigkeiten über die Tiefe gefunden, jedoch keine hohe Kohärenz der Auslenkungen der Isopyknen. Diese Dissertation zeigt, dass interne Wellen über einen großen Frequenzbereich energetisch und der Haupt-mischungsmechanismus im Inneren des Bornholm Beckens sind.

1 Introduction

1.1 Internal waves

Fridtjof Nansen is said (by e.g.: *Munk*, 1981) to be the first person to explain the long-dreaded phenomenon known as "dead water". Where stratification is shallow and very strong, e.g. in fjords or, as Nansen found it, near Taimur Island in the Kara Sea, almost all of the energy a ship expends at going forwards can be lost to the generation of waves at the density interface. Nansen first named the ripples on the surface in the wake of the ship to be the cause of the slow progress. He thereby discovered (a surface signal of) internal waves, as he describes in his books (*Nansen*, 1897a,b) and his paper from 1902. Today this small surface signal (an elevation of 2 cm for internal waves with amplitudes of tens of metres) are tracked from space by satellite (*Ray and Mitchum*, 1996; *Zhao et al.*, 2011). Already many years before Nansen's discovery, theories on the movement of waves, interfacial waves (e.g. *Stokes*, 1847) and of waves in continuously stratified fluids (e.g. *Lord Rayleigh*, 1883) were being formed by, among many others, Isaac Newton, Pierre-Simon Laplace, Augustin-Louis Cauchy, George Airy and George Stokes (for histories see *Darrigol*, 2003; *Craik*, 2004, 2005). The first observations in natural waters, however, came with Nansen's Arctic voyage on the *Fram* at the end of the nineteenth century. A few years later *Watson* (1904) and *Wedderburn* (1907) deduced the existence of internal seiches from temperature fluctuations in Loch Ness, Scotland. Since then internal waves have been found in all water bodies and *Munk* (1981) states that internal waves are even more common then surface waves since "*no one has ever reported an interior calm*". Internal waves are a ubiquitous feature not only of the ocean and lakes, but of many types of fluids. They also exist, for example, in the atmosphere (e.g. *Francis*, 1975; *Taylor and Hapgood*, 1988; *Senf and Achatz*, 2011), in the Earth's core (e.g. *Olson*, 1977; *Aldridge and Lumb*, 1987) and in the sun and other stars (e.g. *Press*, 1981; *Charbonnel and Talon*, 2005).

Internal waves in the ocean can be excited by a variety of processes besides exploration vessels. Globally the most energetic are the internal waves generated by the tides flowing over rough topography generating internal tides (e.g. *Alford et al.*, 2006; *Beckenbach and Terrill*, 2008). These internal tides have the same frequency as the surface tide, but shorter wavelength and larger amplitudes (*Ray*, 2009). Any other mean current flowing over topography can radiate internal waves as well. Currents can also interact with other, not quite so solid, boundaries, for example layers of strong stratification or the outer boundaries of eddies. Multiple internal waves can even interact with each other, either constructively or destructively,

generating new wave components with different frequencies and wavenumbers (*Müller et al.*, 1986). If multiple waves are resonantly interacting they may exchange energy (*McComas and Bretherton*, 1977; *Thorpe*, 2005). Internal waves can, at least in theory and laboratory experiments, also be generated from turbulent patches (e.g. *Dohan and Sutherland*, 2003, 2005; *Kantha and Clayson*, 2007). Apart from the tides the other main driving force is the atmosphere; near the surface internal waves can be generated, e.g. from the impact of the atmosphere through changes in surface pressure or buoyancy and through the impact of the wind and surface waves. One of the main examples here are near-inertial waves, resonant waves set up by intermittent or sudden wind events such as storms (*Gustafson and Kullenberg*, 1933; *Garrett*, 2009, see Chap. 5).

The study of internal waves in the ocean, and in lakes, is interesting for many reasons. The waves advect and disperse sediment particles and can shape the sea bed, for example through resuspension of sediment due to the relatively strong near-bed flows (e.g. *Puig et al.*, 2004; *Butman et al.*, 2006). As strong internal waves are formed upon interaction with a near-critical slope (where wave angle equals slope angle), internal tides (with angles of 2–4°) are proposed to be the reason for the universal 3° slope of the continental shelf (*Cacchione et al.*, 2002; *Zhang et al.*, 2008). Internal waves can also move biological particles and nutrients. In a model by *Kahru* (1983) of the summer-time surface nutrient-depleted layer, internal wave mixing and wave pumping were found to be important processes that locally raised the nutrient concentration and increased the primary production creating a patchy field of phytoplankton blooms. *Lucas et al.* (2011) found from measurements on the continental shelf that internal waves transport nitrate shorewards at approx. the rate of phytoplankton nutrient uptake, thereby contributing significantly to the enhanced biological productivity over the continental shelf.

However, the main thing internal waves transport and disperse is momentum, causing stirring and mixing in the ocean. This transport is not only from one place to another, but also across scales; from low to high wavenumbers and from low to high frequencies (and possibly vice versa). Internal waves can occupy many scales and might therefore be an important link in the energy cascade, converting large 2-D motions to small scale 3-D turbulence (*Müller et al.*, 1986). In his canonical paper *Abyssal recipes* from 1966 Walter Munk computed that, in order to keep the global thermohaline circulation going, there should be a vertical velocity in the ocean of 1.2 cm per day ($w_M = 1.4 \times 10^{-7}$ m s^{-1}) and an eddy diffusivity of 1.3 cm^2 per second ($K_M = 1.3 \times 10^{-4}$ m^2 s^{-1}). His reasoning came from a simple budget for the central Pacific Ocean of the cold bottom waters produced in the Antarctic and a "what goes down must come up" principle in order to preserve the steady state. How these vertical velocities and diffusivities originate was, and still is, however, largely unknown. Munk considered 4 possibilities "*in the order of increasing strangeness*": (1) boundary mixing, (2)

thermodynamic mixing, (3) shear mixing and (4) biological mixing. In the first mixing along boundaries (continental shelfs, mid-ocean ridges, seamounts or islands) is due to current shear and internal wave breaking; also the third depends on internal waves as the shear suggested is provided by internal tides. Hence, many suggest internal waves play an important role in the overturning circulation; as the main mixing process in the ocean's interior and as one of the main mixing agents responsible for the enhanced mixing near boundaries. Measurements (e.g. *Toole et al.*, 1994; *Polzin et al.*, 1997; *Ledwell et al.*, 1998) reveal however that the diffusivity is generally an order of magnitude lower than K_M, except around rough or shallow topography (*Ledwell et al.*, 2000), so that the "missing diffusivity" is being sought.

The great deep ocean, away from bottom and surface boundaries, is assumed to be saturated with internal wave energy at all sorts of scales forming a frequency continuum. The total amount of energy might vary, but the spectral shape, i.e. the distribution of energy over wavenumbers/frequencies, is thought to be constant. A general spectrum for surface waves was published by Owen Phillips in 1958 and became hugely popular. Trying to find something similar, Christopher Garrett and Walter Munk published a paper in 1972 describing the proposed shape of the universal spectrum for internal waves. After some refinements (*Garrett and Munk*, 1975, 1979; *Munk*, 1981) it is still very widely and successfully used today as a reference spectrum, although Munk himself says that "*the spectrum was developed on the basis of rank empiricism, with no trace of underlying theory*" (*Munk*, 1981). In such an ocean saturated with internal wave energy the internal waves can also be described by means of vertical normal modes (*Kundu and Cohen*, 2008, and Sec. 3.4 and Chap. 5). Close to generation areas of e.g. the internal tide, a better way to describe the internal waves is in terms of beams along which the energy propagates (*Ray*, 2009). Away from the generation area energy gets dissipated, more quickly in the higher modes, so that, with distance from the generation area, beams widen and the structure disintegrates to just the few lowest modes found by normal mode analysis (*Ray*, 2009).

The life cycle of internal waves follows a general pattern. Internal waves are born mainly at the large and slow scales, by tides and by wind, their energy is then cascaded down to smaller/faster scales, through a frequency continuum following (or not following) the Garrett-Munk shape, before dying in dissipation. When waves break in mid-water, due to overturning or shear instabilities forming Kelvin-Helmholtz billows, turbulent eddies are formed (*Müller et al.*, 1986). Internal waves can also break on sloping boundaries; in processes similar to surface wave breaking on a beach (*Vlasenko and Hutter*, 2002) or through critical reflectance (*Thorpe*, 1997). The bathymetry is "critical" to an internal wave if the angle of the slope is the same as the angle θ the group velocity vectors of internal waves make with the horizontal (*Gayen and Sarkar*, 2011), see (1.16c) in Sec. 1.2.2. If an internal wave hits a (near-)critical slope its energy gets so concentrated that most of it dissipates (*Dauxois and Young*, 1999). At the

smallest scales of the power spectrum, at the Kolmogorov scale, the turbulent eddies produced in the breaking process are turned into heat by viscosity, as described by Lewis Richardson's ditty: "*Big whirls have little whirls that feed on their velocity, and little whirls have lesser whirls and so on to viscosity*" (*Thorpe*, 2005, p. 33). In addition to the scale, also the spectrum describing the energy cascade at these small scales was proposed by Andrey Kolmogorov. At small scales, within the inertial subrange, energy E is only transferred to smaller scales at the rate of dissipation, the rate at which energy is dissipated in the dissipating range (*Kundu and Cohen*, 2008). From dimensional analysis Kolmogorov found that the energy decay in the inertial subrange should have a slope of -5/3, i.e. $E(k) \propto k^{-5/3}$ (*Kolmogorov*, 1991a,b; *Phillips*, 1991). Within the dissipating range the slope is much steeper, see Sec. 3.2 & Chap. 6.

1.2 The mathematics of gravity waves

Waves are one of the most basic mechanisms of moving energy without moving mass (*Kundu and Cohen*, 2008). Gravity waves can occur at fluid interfaces, e.g. at the sea surface (see Sec. 1.2.1). Other fluid interfaces occur within the water column where there is a jump in density due to a sudden change in temperature and/or salinity (see Sec. 1.2.2). If the water is continuously stratified internal gravity waves are not bound to interfaces anymore and can propagate with a vertical component as well (see Sec. 1.2.2). Compressional waves, e.g. sound waves, and waves affected by surface tension ($\lambda > 7$ cm) are ignored here.

The basic terms related to (interfacial) gravity waves are depicted in Fig. 1.1. In space, the wavelength λ is the horizontal distance between subsequent wave crests or subsequent troughs. The amplitude a is the vertical distance between the undisturbed level and the top of the crest, so that the instantaneous surface elevation η is then maximal, $0 < \eta < a$. In time, the wave period Π is the distance in time between subsequent wave crests and the frequency is its inverse $f = 1/\Pi$, i.e. the number of waves passing a fixed point within a unit of time. Deduced from the wavelength and the frequency are the wavenumber and the angular frequency, respectively. The wavenumber along the direction of wave propagation k is the number of wavelengths per 2π units of distance, $k = 2\pi/\lambda$. The same can be done with the period, creating the angular frequency $\omega = 2\pi/\Pi = 2\pi f$.

Waves can be described according to their amplitude and phase, e.g. assuming a simple sinusoidal shape gives $\eta = a\cos(\phi)$, where ϕ is the phase given by $\phi = kx - \omega t$. If multiple sinusoidal waves, with different frequencies and wavelengths, are superposed, they form packets; at certain times/distances they will amplify each other while at others the surface elevation is suppressed as the waves cancel, see Fig. 1.1b. These points of minimum amplitude are called nodes and they form the envelope; the boundaries of a wave packet.

1.2.1 Surface waves

The dispersion relation

The speed of gravity waves at the water's surface can be described by a dispersion relation. There are two kinds of wave velocities; the phase velocity and the group velocity. The phase velocity c is the speed at which the phase of a wave, e.g. a crest, with a set frequency propagates: $c = \lambda/\Pi = \omega/k$. The group velocity is the speed at which an envelope of waves, e.g. a node, propagates and is given by $c_g = \mathrm{d}\omega/\mathrm{d}k$. An equation for the angular frequency ω can be derived from the Laplace equation, which is formed when velocity potentials are substituted into the continuity equation, by considering kinematic boundary conditions and assuming the sinusoidal waveform $\eta = a\cos(kx - \omega t)$ for the linearised case as shown by *Kundu and Cohen* (2008, p. 219–223). Also assumed is that the fluid is incompressible, the flow is irrotational and inviscid, i.e. the Bernoulli equation is used. This resulting equation for ω can then be used to derive expressions for the phase and group velocities:

$$\omega = \sqrt{gk\ \tanh(kH)} \tag{1.1a}$$

$$c = \frac{\omega}{k} = \sqrt{\frac{g}{k}\ \tanh(kH)} \tag{1.1b}$$

$$c_g = \frac{\mathrm{d}\omega}{\mathrm{d}k} = \frac{1}{2}c\left[1 + \frac{2kH}{\sinh(2kH)}\right] \tag{1.1c}$$

where g is the gravitational acceleration and H is the water depth.

The equation for ω (1.1a) is called the dispersion relation since it describes the dependency of the wave velocity on the wavenumber; longer waves are faster. This means that if a signal consists of multiple sinusoidal components they will separate, or disperse, with long waves at the leading edge and short waves trailing behind.

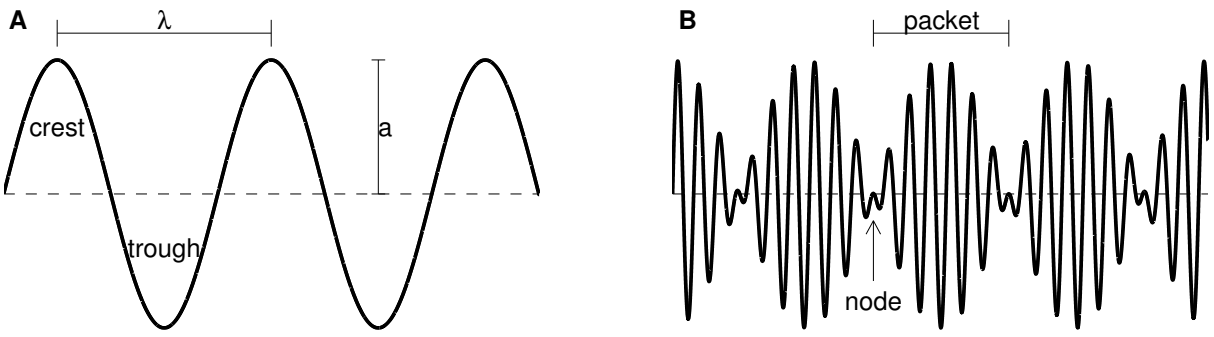

Figure 1.1: Wave terminology of (a) a single wave and (b) wave packets produced by the interaction of two waves with slightly different frequencies.

Deep- and shallow water waves

Approximations exist for the limits that waves travel over, relative to their wavelength, deep ($H/\lambda \gg 1$) or over shallow water ($H/\lambda \ll 1$). Over deep water $kH \to \infty$ so that $\tanh(kH) \to 1$ and (1.1) simplifies to:

$$\omega = \sqrt{gk} \tag{1.2a}$$

$$c = \sqrt{\frac{g}{k}} = \sqrt{\frac{g\lambda}{2\pi}} \tag{1.2b}$$

$$c_g = \frac{1}{2}c\,[1+0] = \frac{1}{2}c \quad . \tag{1.2c}$$

For this simplification to be a good approximation the water need not be very deep; $\tanh(kH) = 0.95$ for $kH = 1.83$, corresponding to $H > 0.29\lambda$. The wave phase velocity, independent of water depth, increases with wavelength hence deep water waves are dispersive. Particle orbits are circular at all depths and the pressure change due to these deep water waves decays exponentially with depth so that the radius of these particle orbits reduces with depth (*Kundu and Cohen*, 2008). For deep water the group velocity simplifies to $c_g = 1/2c$ since $\sinh(2kH) \to \infty$, therefore $2kH/\sinh(2kH) \to 0$ and in (1.1c) $[...] \to 1$.

Over shallow water $kH \to 0$ so that $\tanh(kH) \to kH$ and (1.1) simplifies to:

$$\omega = \sqrt{gk^2H} \tag{1.3a}$$

$$c = \sqrt{gH} \tag{1.3b}$$

$$c_g = \frac{1}{2}c\,[1+1] = c \quad . \tag{1.3c}$$

For this simplification to be a good approximation the water needs to be pretty shallow; less than 7% of the wavelength (*Kundu and Cohen*, 2008). The wave phase speed is now independent of the wavelength so that shallow water waves are non-dispersive. The wave phase speed only depends on, and increases with, the water depth. Therefore waves slow down as they approach the beach, steepen and break. Vertical particle orbits are ellipses becoming flatter with increasing depth and the pressure change due to these shallow water waves is hydrostatic, i.e. it does not change with depth (*Kundu and Cohen*, 2008). For shallow water $\sinh(2kH) \to 2kH$, therefore $2kH/\sinh(2kH) \to 1$ and in (1.1c) $[...] \to 2$ so that the group velocity is equal to the phase velocity $c_g = c$, which confirms that waves are non-dispersive.

Potential and kinetic energy and their flux

The energy of a wave consist of a kinetic energy, due to its movement, and a potential energy, due to the surface elevation displacing the centre of mass. The derivations of E_k and E_p show that they are equal in magnitude $E_k = E_p = 1/2\rho g\overline{\eta^2}$ (per unit horizontal area) so that the total energy equals:

$$E = E_k + E_p = \rho g\overline{\eta^2} = \frac{1}{2}\rho g a^2 \tag{1.4}$$

since, averaged over a wavelength, $\cos^2(\eta^2) = 1/2a^2$ (*Kundu and Cohen*, 2008).

Individual wave components of a wave packet propagate at the phase velocity, but the wave energy E moves at the group velocity since the packet moves with the group velocity and energy cannot cross a node (*Kundu and Cohen*, 2008). The energy flux F is therefore a multiplication of E and c_g:

$$F = Ec_g = \frac{1}{2}\rho g a^2 \left(\frac{1}{2}c\left[1 + \frac{2kH}{\sinh(2kH)}\right]\right) \quad . \tag{1.5}$$

1.2.2 Internal waves

Interfacial waves

Interfacial waves, waves on density interfaces *inside* the water column, are essentially the same as surface waves. However, due to the much reduced density difference across the interface, these waves require less energy to be generated, have larger amplitudes and have longer wavelengths and periods (i.e. they travel slower) than surface waves. This can be shown for e.g. two infinitly deep layers where an interfacial wave behaves as a deep water wave. A term is added to the dispersion and to the wave energy equations to take into account the density difference between the upper layer ρ_1 and the lower layer ρ_2 (*Kundu and Cohen*, 2008):

$$\omega = \sqrt{gk\,\frac{\rho_2 - \rho_1}{\rho_2 + \rho_1}} \tag{1.6a}$$

$$E = E_k + E_p = \frac{1}{2}(\rho_2 - \rho_1)\, g a^2 \quad . \tag{1.6b}$$

If, however, the upper layer of depth H_1 is assumed to be shallow in comparison to the wavelength of the interfacial wave the shallow water approximation comes into play again and the dispersion relation and phase velocity are given by:

$$\omega = g' k^2 H_1 \tag{1.7a}$$

$$c = \sqrt{g' H_1} \tag{1.7b}$$

where g' is the reduced gravity taking into account the density difference between the two layers:

$$g' = g\left(\frac{\rho_2 - \rho_1}{\rho_2}\right) \quad . \tag{1.8}$$

Waves in a rotating, continuously stratified fluid

The situation becomes a lot more complex for a more realistic water column. Here stratification is not limited to a discontinuity layer, but spread over the depth so that the water column is continuously stratified. Also the earth's rotation is taken into account, although the latitude ς is assumed to be constant so that the Coriolis parameter, $f_i = 2\Omega\sin(\varsigma)$ with Ω as the rotation rate of the earth ($2\pi/(24 \cdot 3600) = 7.29 \times 10^{-5}$ s^{-1}), is constant as well. Other assumptions are those inherent to the Boussinesq approximation, mainly that the density can be treated as constant except where it is multiplied with the gravitational acceleration in the vertical momentum equation (1.9d), but also that the dynamic viscosity, thermal conductivity and specific heat are constant and that sound/shock waves are ignored. Further it is assumed that the amplitudes are small, so that non-linear terms can be neglected, and that the flow is inviscid, so that the viscous term can be neglected. All these assumptions are used to reduce the Navier-Stokes equations, the fundamental equations describing fluid motion named after Claude-Louis Navier and Sir George Gabriel Stokes, to the equations of motion for a rotating fluid (for the derivation see *Kundu and Cohen* (2008)):

$$\frac{\partial u}{\partial x} + \frac{\partial v}{\partial y} + \frac{\partial w}{\partial z} = 0 \tag{1.9a}$$

$$\frac{\partial u}{\partial t} - f_i v = -\frac{1}{\rho_0}\frac{\partial p}{\partial x} \tag{1.9b}$$

$$\frac{\partial v}{\partial t} + f_i u = -\frac{1}{\rho_0}\frac{\partial p}{\partial y} \tag{1.9c}$$

$$\frac{\partial w}{\partial t} = -\frac{1}{\rho_0}\frac{\partial p}{\partial z} - \frac{\rho g}{\rho_0} \tag{1.9d}$$

$$\frac{\partial \rho}{\partial t} - \frac{\rho_0 N^2}{g} w = 0 \quad , \tag{1.9e}$$

where u, v, w are the velocities in the x, y, z (often east, north and vertical) directions respectively, while p stands for the pressure and t for time. N^2 is the squared buoyancy frequency $N^2(z) = -g/\rho_0 \, \mathrm{d}\rho/\mathrm{d}z$, with ρ_0 a constant reference density, see also Sec. 4.2.2. The continuity equation (1.9a) shows conservation of mass while (1.9e) is the density equation showing the incompressibility of the fluid. The momentum equations are given in three directions, two

horizontal (1.9b,c) and a vertical (1.9d) direction. It is not assumed in (1.9d) that the motion is hydrostatic.

After a derivation shown in App. A the set (1.9) can be reduced to an equation depending only on one velocity direction, the vertical velocity w:

$$\frac{\partial^2}{\partial t^2}\left(\nabla^2(w)\right) + N^2\nabla_H^2(w) + f^2\frac{\partial^2 w}{\partial z^2} = 0 \quad , \tag{1.10}$$

where ∇^2 is the three-dimensional Laplacian operator and ∇_H^2 is the horizontal Laplacian operator:

$$\nabla^2 \equiv \nabla_H^2 + \frac{\partial^2}{\partial z^2} \equiv \frac{\partial^2}{\partial x^2} + \frac{\partial^2}{\partial y^2} + \frac{\partial^2}{\partial z^2} \quad . \tag{1.11}$$

Since (1.10) is independent of u and v a solution of the form

$$[u, v, w] = [\check{u}(z), \check{v}(z), \check{w}(z)]\ \mathrm{e}^{i(kx+ly-\omega t)} \tag{1.12}$$

can be assumed, with complex amplitudes $[\check{u}(z), \check{v}(z), \check{w}(z)]$ and the horizontal wavenumber vectors k in the x-direction and l in the y-direction (*Kundu and Cohen*, 2008). If this solution is substituted in (1.10) it becomes:

$$\frac{\partial^2 \hat{w}}{\partial z^2} + m^2\hat{w} = 0 \tag{1.13}$$

where m is the vertical wavenumber vector in the z-direction:

$$m^2(z) = \frac{(k^2+l^2)(N^2-\omega^2)}{\omega^2 - f_i^2} \quad . \tag{1.14}$$

From the dispersion relation for internal waves in a stratified rotating fluid (1.14) it can be deduced that:

$$f_i < \omega < N \tag{1.15}$$

The dispersion relation thus shows that propagating internal waves are only possible within certain frequency limits; between the lowest possible wave frequency f_i and the highest possible frequency N. This will form a central theme in this thesis. The inertial frequency, or Coriolis parameter, that forms the long-period limit is given by the earth's rotation and varies with latitude, from a minimum at the equator to maxima at the poles (see Chap. 5). The highest possible wave frequency N is determined by the stratification, the change of density over depth (see Chap. 6).

Direction of waves in a continuously stratified fluid

If rotation is ignored for a moment , i.e. $f_i = 0$, and the axes are turned so that waves propagate in the directions of k and m, i.e. $l = 0$, and N is assumed constant with depth, then (1.14) simplifies to:

$$m^2 = \frac{k^2(N^2 - \omega^2)}{\omega^2} \tag{1.16a}$$

$$\omega^2 = \frac{k^2}{k^2 + m^2}\, N^2 \tag{1.16b}$$

$$\omega = \frac{k}{\sqrt{k^2 + m^2}}\, N = \frac{k}{K}\, N = N\cos(\theta) \quad . \tag{1.16c}$$

Here K is the magnitude of wavenumber vector $\mathbf{K} = (k, l, m)$ and θ is the angle between wavenumber vector and the horizontal. This shows that the frequency of an internal wave ω depends on the direction of the wavenumber vector and not its magnitude $\omega \propto \theta \not\propto K$ (*Kundu and Cohen*, 2008). Or, formulated differently, the direction θ of a wave with a certain frequency ω is given by the stratification N, as was first derived by *Görtler* (1943), but often attributed to *Mowbray and Rarity* (1967). Contrary to other forms of reflection (light or billard balls), it is the angle θ of the wave ray to the horizontal that stays constant, not the angle normal to the slope (*Thorpe*, 1987).

For the just (re-)introduced assumptions the velocities can be written and differentiated as follows:

$$u = u_0\, \mathrm{e}^{i(kx+ly+mz-\omega t)} \qquad \frac{\partial u}{\partial x} = iku_0\, \mathrm{e}^{i(kx+ly+mz-\omega t)} = iku \tag{1.17a}$$

$$v = v_0\, \mathrm{e}^{i(kx+ly+mz-\omega t)} \qquad \frac{\partial v}{\partial y} = ilv_0\, \mathrm{e}^{i(kx+ly+mz-\omega t)} = ily \tag{1.17b}$$

$$w = w_0\, \mathrm{e}^{i(kx+ly+mz-\omega t)} \qquad \frac{\partial w}{\partial z} = imw_0\, \mathrm{e}^{i(kx+ly+mz-\omega t)} = imw \tag{1.17c}$$

On account of the continuity equation (1.9a) $iku + ily + imw = 0$, i.e. $\mathbf{K} \cdot \mathbf{u} = 0$, meaning that particle motions are perpendicular to both the wavenumber vector $\mathbf{K}$ and the phase velocity c. Therefore, θ is also the angle between the partical motion and the vertical. If $\theta = 0$ then $\cos(\theta) = 1$ and $\omega = N$ so that the wave frequency is maximal if the motion is purely vertical and low if the motions are mainly horizontal. As shown in *Kundu and Cohen* (2008) also the phase and group velocities are perpendicular.

Since the energy flux is in the direction of the group velocity, see (1.5), this is also perpendicular to the phase velocity and the wavenumber vector. The kinetic energy E_k and the

potential energy E_p are redefined, now per unit volume, for a non-rotating stratified fluid as (*Kundu and Cohen*, 2008):

$$E_k = \frac{1}{2}\rho_0 \left\langle (u^2 + v^2 + w^2) \right\rangle \tag{1.18a}$$

$$E_p = \frac{g^2 \rho'^2}{2\rho_0 N^2} \tag{1.18b}$$

where ρ' is the perturbation density following the Reynolds decomposition into a mean and a perturbation part: $\rho = \langle\rho\rangle + \rho'$. It can be shown that $E_k = E_p$ is still valid (*Kundu and Cohen*, 2008, p. 270–272).

1.3 The Baltic Sea

1.3.1 Geological history and present-day hydrography

Geological history

Since the dawn of the Baltic Sea, a large landlocked sea in northwestern Europe, it has been a dynamic system. In its present form, with only one shallow connection to the ocean, the Baltic Sea is a very young sea (*HELCOM*, 1981). *Andersen and Borns* (1994) (see also: *Sauramo*, 1958; *Björck*, 1995; *Emeis et al.*, 2002) describe the formation history of the Baltic Sea after the Pleistocene glaciation as the area went through four main marine and limnological stages, switching from one to the other due to the delicate balance between local isostatic rebound (uplift of the land due to the removed weight of the icesheets) and global eustatic sealevel rise (due to the melting of the icesheets). The first "ancestor" of the present-day Baltic Sea was created after the last ice age, as the North Europe Ice Sheet, covering Scandinavia with up to 3 km of ice (*Grasshoff*, 1975), started melting, creating a freshwater lake known as the Baltic Ice Lake. It occupied approximately the southern half of the present-day Baltic Sea and was separated from the ocean by an ice dam. At the start of the Holocene (10,000 B.P.) temperatures increased, the Atlantic Ocean became ice-free and its sea level rose eustatically flooding the northern part of the present-day North Sea and estabilising a connection between the Baltic Ice Lake and the Atlantic Ocean. As salt entered the lake it was renamed the Yoldia Sea after one of the prominent genera; the saltwater mussel *Yoldia arctica* (*Schoning*, 2001). The sea existed for around 1,000 years until the isostatic land uplift balanced the sea level rise and closed the connection to the North Sea. Cut-off from the ocean the water slowly lost its salt content and the basin turned into the Ancylus Lake, which derived its name from the freshwater snail *Ancylus fluviatilis* (*Tikkanen and Oksanen*, 2002). This cycle was repeated around 8,000 B.P. when the lake renewed its connection to the ocean changing its

name to the Littorina Sea. The Littorina Sea was saltier, hence the naming after the saltwater snail: *Littorina littorea*, and bigger than the present-day Baltic Sea (*Emeis et al.*, 2002). As isostatic rebound continued the Littorina Sea area was raised, hence, relatively speaking, sea level sank decreasing the surface area of the sea, narrowing and shallowing the connection of the sea to the North Sea thus decreasing the exchange flow, causing the sea to slowly become fresher. At some points during this gradual transition the sea was was given new names to reflect ecosystem changes due to the drop in salinity; from Littorina Sea to Limnaea Sea (snail: *Lymnaea ovata*) and on to the Mya Sea (*Broszinski*, 2002). The sudden appearance of the clam species *Mya arenaria* has now been linked to the Vikings, who might have found it in American waters and introduced it in the Baltic, rather than to a change in salinity (*Björck*, 2008). Only since 1,500 B.P. has this area been known as the Baltic Sea (*HELCOM*, 1981). Its name could change again since a balance between isostatic land uplift and eustatic sea level rise has not yet been reached; the northern Baltic is still recovering from the glaciation whereas the southern Baltic is sinking slightly (*Winterhalter et al.*, 1981).

Present-day hydrography

Today, after shrinking in size since the Littorina Sea stage, the Baltic Sea extends ∼1300 km north to south from 54° to 66°N and ∼1100 km (10°–30°E) east to west (*Lass and Matthäus*, 2008) and has a volume about half that of the North Sea (*Pohlmann*, 1996). It is not a single basin, but, due to the differences in the base rock and the action of the ice during and after the glaciation (*Grasshoff*, 1975), a labyrinth of smaller and larger basins connected by channels and separated by sills, see Fig. 1.2. Following these from the southwest to the north starting in the North Sea, the Skagerrak is an over 400 m deep channel while the Kattegat is already much shallower with a mean depth of 25 m (*Grasshoff*, 1975). The real bottleneck for water exchange are the Danish Straits; the Øresund, Great Belt and Little Belt. The Drogden Sill at the end of the Øresund is 7 m deep, while water coming in via the Little or Great Belt has to flow through the Fehrmarn Belt and over the 18 m deep Darss Sill before entering the first main basin of the Baltic Sea: the 45 m deep Arkona Basin (*Reißmann et al.*, 2009). The area between the Kattegat and the Arkona Basin is known as the transition area from North to Baltic Sea. Continuing north, inflowing water (see Sec. 1.3.2) would travel, via the Bornholm Channel to the north of Bornholm, into the Bornholm Basin (max. depth 95 m), over the Stolpe Sill (60 m), via the Stolpe Channel into the Gulf of Gdansk and the Eastern Gotland Basin (*Reißmann et al.*, 2009). This is the largest deep basin (250 m), although the Landsort Deep in the Western Gotland Basin is, with its 460 m, by far the deepest point (*Lass and Matthäus*, 2008). This area of the Bornholm and Gotland Basins is also known as the Baltic Proper. North of the Gotland Basins the water could flow east into the Gulf of Finland or north through the Åland Sea, into the Gulf of Bothnia consisting of the Bothnian Sea and the

Bay of Bothnia, see Fig. 1.2 and *Lass and Matthäus* (2008).

Through the transition area of the narrow, shallow Danish Straits the Baltic Sea has a tenuous, but important, connection to the Atlantic Ocean. This connection hampers exchange between the sea and the open ocean, which has two main consequences. Firstly, tides are almost negligible as co-oscillation with the ocean is weakened (*Schmager et al.*, 2008). Secondly, the water in the Baltic Sea is brackish, i.e. between fresh and oceanic. Actually, after alternating between marine and freshwater regimes over the last 10,000 years, the Baltic Sea is now one of the largest brackish water areas in the world and is said to be a huge estuary (*Lass et al.*, 2003).

Meridionally throughout the sea there is a salinity gradient; from 25 g kg^{-1} in the southwestern Baltic, over 9 g kg^{-1} in the Arkona Basin and 7 g kg^{-1} in the Gotland Basin to nearly fresh in the Gulf of Bothnia (*Kullenberg*, 1981; *Reißmann et al.*, 2009). Not only is the Baltic Sea less saline than the ocean, also its composition of salts is different compared to "Standard Seawater" (*Millero et al.*, 2008), especially the calcium (Ca^{2+}) content is high due to the riverine input of $CaCO_3$, causing a salinity anomaly of 27–32 mg kg^{-1} (*Rohde*, 1966; *Feistel et al.*, 2010). These anomalies cause the conversion of conductivity to salinity and then to density to be off by up to $\sim$0.01% (*Feistel and Weinreben*, 2008), which has not been compensated for in the following. Due to this wide range, salinity is the main factor contributing to density, with temperature playing a minor role.

Also vertically there is a pronounced salinity gradient, with a strong and permanent halocline. The depth of this halocline depends on the depth of the basin, and especially on the depth of the sill, and deepens from southwest to northeast. In the transition area it's only 10–20 m deep, deepening to $\sim$50 m in the Bornholm Basin and 65–70 m in the East Gotland Basin (*Grasshoff*, 1975). Only in the Gulfs of Finland and Bothnia the halocline ($\sim$30 m deep) can be broken down by winter convection. A shallower thermocline is a temporary feature in all basins and forms in summertime, during March/April in the shallow southwestern area and approximately a month later in the deeper parts. The seasonal thermoclines are broken down in autumn (September/October) when general cooling and storms mix the water column (*Grasshoff*, 1975).

On a yearly basis there is a net input of freshwater from direct precipitation, that is not quite balanced by evaporation, and from river run-off (*Reißmann et al.*, 2009). The excess freshwater leaves the Baltic Sea via the Danish Belt Sea system, giving a net water outflow of 473 km^3 y^{-1} for a surface water outflow of 947 km^3 y^{-1}. Hence 474 km^3 of North Sea water flow into the Baltic Sea on average per year to compensate for the loss of water through outflow (*Mattsson*, 1996; *Reißmann et al.*, 2009). Since the North Sea water is saltier, it is denser and it flows along the sea bed. This often occurs in bursts known as inflow events.

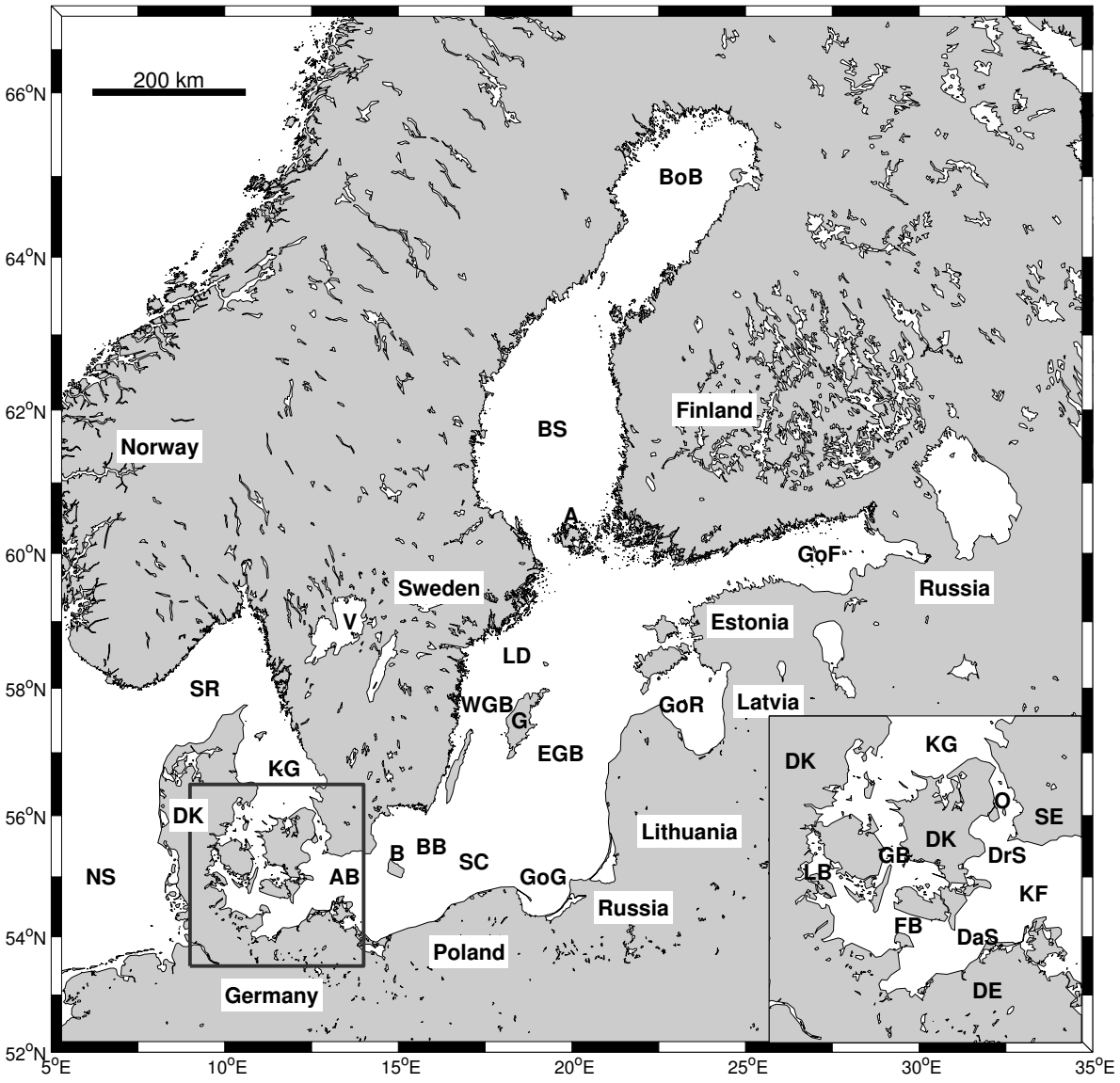

Figure 1.2: Map of the Baltic Sea. For abbreviations see Tab. 1.1 below.

Table 1.1: Abbreviations of basins, countries, islands and a lake (in alphabetical order).

Abbr.	Name	Abbr.	Name	Abbr.	Name
A	Åland	EGB	East Gotland Basin	LD	Landsort Deep
AB	Arkona Basin	FB	Fehmarn Belt	NS	North Sea
B	Bornholm	G	Gotland	O	Øresund
BB	Bornholm Basin	GB	Great Belt	SC	Stolpe Channel
BoB	Bay of Bothnia	GoF	Gulf of Finland	SE	Sweden
BS	Bothnian Sea	GoG	Gulf of Gdansk	SR	Skagerrak
DaS	Darss Sill	GoR	Gulf of Riga	V	Vänern
DE	Germany	KF	Kriegers Flak	WGB	West Gotland Basin
DK	Denmark	KG	Kattegat		
DrS	Drogden Sill	LB	Little Belt		

1.3.2 Inflow events

As explained above, water is moving backwards and forwards through the transition area all the time in response to pressure gradients that are either caused by atmospheric weather systems, sea level changes or by horizontal density gradients. Estuarine circulation caused by this latter pressure gradient transports water through the Belt Sea, although with a zero net input/output (*Knudsen*, 1900; *Lass and Matthäus*, 2008). However, averaged over at least multiple months, there is a net outflow of low-salinity water in the surface layer and a deeper return current of water with a higher salinity (*Knudsen*, 1900; *Lass and Matthäus*, 1996). For the salt water to reach the deeper basins this permanent, but weak exchange is insufficient; events of high-volume inflows of highly saline water are needed. The two ways in which this can be accomplished require nearly opposite meteorological conditions. During storms inflows are barotropic whereas the baroclinic type of inflow occurs only after long periods of calm weather.

Barotropic inflows

Barotropic inflows are forced by large-scale pressure gradients; sea level differences between e.g. the Kattegat and the Arkona Basin caused by weather systems, especially prolonged easterly storms, that push the water out of the Baltic Sea into the North Sea (*Lass and Matthäus*, 1996). If the wind direction then changes, or the wind speeds drop, water flows back into the Baltic Sea to regain the pressure equilibrium. The front of the salty, vertically well-mixed North Sea water is driven by the wind from the Kattegat through the Øresund and the Belts. When the front reaches the Drogden and Darss Sills high volumes of salt water can flow into the Arkona Basin. *Reißmann et al.* (2009) state that typically 200 km^3 of inflowing water imports 2×10^9 tonnes of salt and 1×10^6 tonnes of oxygen.

The new bottom water of the Arkona Basin flows as a deep gravity current through the Bornholm Channel into the Bornholm Basin. Once enough dense deep water has accumulated there to fill it from the bottom to the level of the Stolpe Sill it will overflow and the inflow will continue through the Stolpe Channel into the Gdańsk and Eastern Gotland Basins. Which basins are reached and ventilated depends on the volume and density of the inflowing water. The inflowing water only renews the old bottom water as long its density is higher, otherwise the water will interleave at its equilibrium depth. On its way it the inflowing water mixes with the ambient water so that its density steadily decreases with time and distance from the Belt Sea. This also causes the temporal variations to be much more pronounced in the "early" basins (i.e. the Arkona and Bornholm Basins) than in the "late" basins (i.e. Eastern and Western Gotland Basins). In all it takes a strong inflow about 3 months for the "renewal front" to move from the Belt Sea to the Eastern Gotland Basin (*Feistel et al.*, 2003a). These types

of inflows are infrequent because of the specific meteorological conditions that are required, but generally occur in winter as outlined above, although they can also occur in autumn and spring if the prerequisite persistent strong winds are available.

Baroclinic inflows

Baroclinic inflows, on the other hand, mainly occur in summer since they need prolonged periods of very calm weather and a strongly stratified Belt Sea. They are driven by baroclinic pressure gradients, i.e. the density differences across the Great Belt (*Knudsen*, 1900; *Reißmann et al.*, 2009). At some depth, between 10 and 20 m (*Lass and Matthäus*, 2008), the baroclinic pressure gradient matches the barotropic pressure gradient so that, below this depth, salt water flows into the Baltic Sea. The pathway through the Great Belt is therefore the only route taken by these inflows, the Drogden Sill at the end of the Øresund is too shallow.

This process was discovered only recently; *Feistel et al.* (2003a) were the first to describe baroclinic inflows, based on observations of a summer inflow in 2002. Inflowing water during a baroclinic inflow is salty, but also warm, especially when compared to the cold water flowing in during barotropic inflows in winter. In summer 2002 the deep-water temperature in the Gdańsk and Gotland Basins broke records (*Feistel et al.*, 2003a). However, due to this increase in temperature less oxygen can be dissolved since the oxygen saturation level drops with temperature (*Mohrholz et al.*, 2006). Also the stratification hinders gas exchange of the deep layers. Lastly, the oxygen consumption in the bottom layer of the Belt Sea is enhanced in summer (*Mohrholz et al.*, 2006) and the inflowing water contains more readily degradable biological material (*Matthäus*, 1986), so that more dissolved oxygen is taken from the water as it flows towards the Arkona Basin and deeper basins. Therefore these inflows generally fail to ventilate the Gotland Basins, although they can oxygenate the Arkona and Bornholm Basins.

Stagnation periods and residence times

Since inflows, especially MBIs, can be few and far between, the circulation within the Baltic Sea deep basins often stagnates and lateral exchange is diminished. Over the course of a stagnation period the density and salinity in the deep water slowly decrease due to vertical mixing so that isopycnals and isohalines are displaced to greater depth (*Matthäus*, 1986). Without an advective supply of oxygen-rich water the local oxygen concentration depends upon vertical exchange and the local budget of oxygen use and production. Generally more oxygen is used than produced so that the oxygen concentration decreases and can be depleted and replaced by hydrogen sulphide (*Matthäus et al.*, 2008) until the following inflow event provides "new" water and the area is oxygenated.

Inflows are not often single events, but generally occur in groups. Clusters, typically including 4–7 events, are often 2–3 years long (*Matthäus and Franck*, 1992). However, over the last 30 years there have been two 10-year periods without major Baltic Inflows (MBIs, see *Matthäus and Franck* (1992) for a classification) lasting from February 1983 to January 1993 and directly following that 1993 MBI to January 2003 *Matthäus et al.* (2008). This major inflow in January 2003, although it was only a weak one, was very important to the Eastern Gotland Basin due to the exceptionally long stagnation period preceding it (*Feistel et al.*, 2003b). Prior to 1983 MBIs were more regular and stagnation periods, while still lasting a few years, were significantly shorter than 10 years, as can be seen in the time-series, starting in 1880 but excluding the world wars, by *Matthäus et al.* (2008).

1.3.3 The ecological importance of inflows and mixing

The interaction between, and timing of, inflows and stagnation periods is very important to the organisms living in the Baltic Sea, especially to those living in the deeper basins or on/in the bottom sediment. Not only the hydrographic state, but also many geochemical settings, including the oxygen concentration already mentioned, depend upon the water renewal and/or its stagnation (*Matthäus et al.*, 2008).

Oxygen dynamics

Higher marine organisms need oxygen to survive, but during stagnation periods the concentration of dissolved oxygen decreases over time in the deep water. If the oxygen falls below the limit where organisms start to experience physiological stress, the water mass is termed hypoxic. Oxygen levels below 1 ml l^{-1} are "acutely toxic" (*Axe*, 2010) and no benthic species are expected to survive if the water above the sediment reaches this threshold. This does not only have a direct impact on the sedentary species, as during the mass mortality of benthic fauna from the Bornholm Basin in the 1950s (*Tulkki*, 1965), but affects species feeding on them such as demersal fish like cod. On a transect through the Bornholm Basin *Stepputtis et al.* (2011) found that, from the halocline onwards, the oxygen concentration decreased rapidly with depth. Near the bed the oxygen could be totally depleted and in some places the 1 ml l^{-1} isoline was just a few metres underneath the halocline. This isoline roughly corresponded to the lower boundary for sprat (*Sprattus sprattus balticus*), underneath which there was a "fish free zone" (*Stepputtis et al.*, 2011).

If oxygen is completely depleted the water is said to be anoxic. When oxygen is absent anaerobic bacteria thrive by metabolising organic material using sulphate, SO_4^{2-}, as the oxygen donor (*Matthäus et al.*, 2008). During this process they produce hydrogen sulphide H_2S, which is highly poisonous to most organisms (*Jahn et al.*, 1996). The concentration of H_2S is

therefore often given as a negative oxygen concentration, using a conversion method described by *Fonselius* (1969) or simple stoichiometry (*Gustafsson and Stigebrandt*, 2007). In autumn, when the remineralisation of dying phyto- and zooplankton by aerobic bacteria uses up the available oxygen, the oxygen concentration is lowest and areas of hypoxia and anoxia have a seasonal maximum (*Axe*, 2010).

One commercially important species affected is cod (*Gadus morhua*): their eggs have a specific density so that they are neutrally buoyant at 11 g kg^{-1}, i.e. in the Bornholm Basin at the halocline depth of 50–75 m (*Wieland and Zuzarte*, 1991; *Bagge et al.*, 1994; *Hinrichsen et al.*, 1997). Also the larvae, one developmental stage further, need this minimum salinity and oxygen concentrations above 2.1 ml l^{-1} (*Axe*, 2010). If the anoxic or hypoxic part of the water column includes the halocline depth many eggs die and the recruitement for the next season is serverely hampered (see e.g. *Hinrichsen et al.*, 1997; *Stepputtis et al.*, 2011).

One of the most abundant copepod species in the Baltic Sea is *Pseudoclanus elongatus* (*Hällfors et al.*, 1981). During its life cycle its dependency on salinity changes, but at least the nauplii and adult females need relatively high salinity levels for maturation and reproduction respectively (*Möllmann et al.*, 2003). Comparing data from the start (1983) and end (1993) stage of a stagnation period *Flinkman et al.* (1998) found that the weight of herring (*Clupea harengus*) at certain ages had halved, as had their stomach fullness and fat content. They propose this was due to the reduction in abundance of *Pseudoclanus elongatus*, one of the three favourite foods of herring, as a consequence of the reduction in salinity. This type of bottom-up control ensures that even species that can swim out of the hypoxic areas are affected.

Some Baltic Sea species, however, seem to have developed some ways to better deal with hypoxic conditions, either physiologically or behaviourally. The small benthic crustacean *Cyprideis torosa* can metabolise sulphide to non-toxic substances and it can switch to anaerobic metabolism (*Jahn et al.*, 1996). While herring needs at least 50% oxygen saturation, *Neuenfeldt* (2002) report that cod would tolerate oxygen saturation levels down to 16%. A later study (*Neuenfeldt et al.*, 2009) specified that cod would often "pop in" to the hypoxic area for a few hours to feed, but would then return to oxic waters to digest their catch.

Nutrient dynamics

Not only the changes in oxygen, and hydrogen sulphide, concentrations are important during stagnation periods. The inflowing water also carries nutrients and possibly contaminants into the Baltic Sea (*Matthäus and Franck*, 1992). Generally more important however are in situ reactions of nutrients to the changing salinity and oxygen levels. Just as anaerobic bacteria use SO_4^{2-} under anoxic conditions, nitrate (NO_3^-) can be used as an oxygen donor at low oxygen concentrations (*Matthäus et al.*, 2008). When H_2S is present both nitrate and nitrite (NO_2^-)

become unstable and ammonium (NH_4^+) is the only nitrogen compound that stays (*Matthäus et al.*, 2008).

Both nitrate and phosphate (PO_4^{3-}) are released from (the pore waters of) the sediment under anoxic conditions; especially phosphate concentrations can increase significantly if iron(III)phosphate ($FePO_4$) is reduced to iron(II)phosphate ($Fe_3(PO_4)_2$) and dissolved from the sediment (*Graca et al.*, 2006; *Gustafsson and Stigebrandt*, 2007; *Matthäus et al.*, 2008). At the end of a stagnation period the reverse happens: iron(III)phosphate is precipitated and diluted by lateral mixing *Matthäus et al.* (1999). Also iron and silicate are enriched in the deep waters under anoxic conditions (*Matthäus et al.*, 2008).

In summer, when phytoplankton are nitrogen-limited, this excess phosphate of the stagnating deep waters can bring on a cyanobacteria bloom if it reaches the surface layers. Cyanobacteria, e.g. *Nodularia spumigena*, can metabolise nitrogen from the atmosphere that is unavailable to phytoplankton and thus bloom without much competition (*Wasmund et al.*, 2011). In this way nitrogen is added to the ecosystem and, when the bloom ends and the bacteria die and sink down, remineralised at depth so that the oxygen deficiency is enhanced. Due to this positive feedback loop of fertilisation and the toxicity of the blooms themselves cyanobacteria blooms are a big concern in the Baltic Sea (*Kahru et al.*, 2000).

1.3.4 Mixing processes in the Baltic Sea

As seen above; circulation, horizontal and vertical exchange, stirring and mixing are of great importance for the ecosystem of the Baltic Sea and many other oceanic and limnic systems. However, circulation in the Baltic Sea is limited, because it is restricted in the horizontal by the bottom topography and in the vertical by the permanent halocline (*Matthäus and Franck*, 1992). Still, there are a myriad of processes that mix the water of the Baltic Sea, as summarised by Fig. 1.3 from *Reißmann et al.* (2009). An ongoing debate in limnology and oceanography discusses the relative importance of surface layer mixing, bottom layer mixing and of mixing in the basin's interior for basin scale mixing (e.g. *Goudsmit et al.*, 1997; *Cyr et al.*, 2011). It will be touched upon in Chap. 5. Many of the processes involved are interrelated and therefore difficult to separate. In the following they are introduced in groups.

Mixing processes related to inflows

The inflows discussed above, depicted in Fig. 1.3 as dark-coloured overflows, are the cause of some mixing processes. On its way over the sill and down the sloping side of the basin the volume of the gravity current grows due to entrainment. In the shallow parts close to the sills wind mixing can mix surface waters into the propagating deep water plume, thereby adding to the plume's volume (*Kõuts and Omstedt*, 1993; *Lass and Mohrholz*, 2003). In deeper

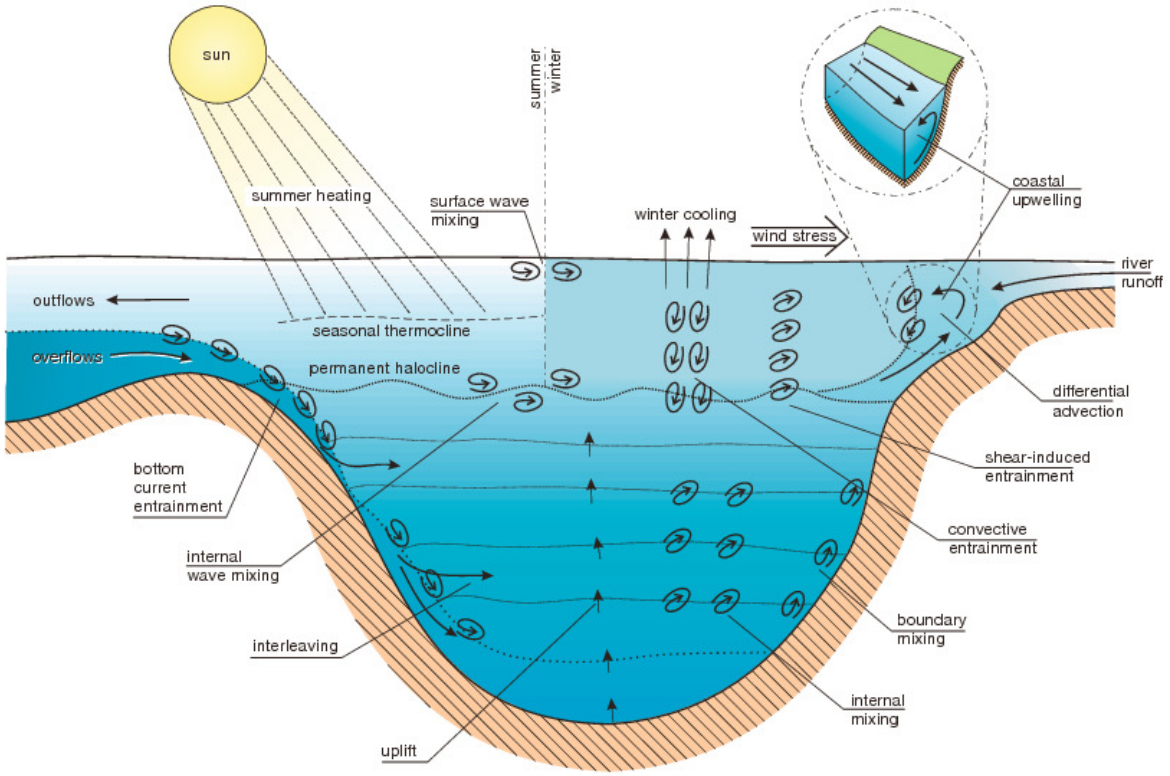

Figure 1.3: Scheme of vertical mixing and transport processes in the Baltic Sea. Reprinted from *Reißmann et al.* (2009) with permission from Elsevier.

water entrainment also happens at the top of the bottom current due to shear instabilities generated by the propagation of the plume (*Reißmann et al.*, 2009). Especially in summer this entrainment of ambient water can increase the oxygen content of the inflowing water.

Another mixing mechanisms associated with inflows is the differential advection at its front (*Lass and Mohrholz*, 2003). As the front of the inflowing plume flows downslope the plume water higher above the bed is faster than the water at the bed due to friction. This dense water than shears over the lighter, older water in front of the front, causing unstable stratification and mixing. *Lass and Mohrholz* (2003) claim this is the main mixing mechanism of inflows.

If the inflowing water reaches its equilibrium depth, i.e. the depth at which its density equals the density of the surrounding water, it will interleave. This mixes waters with equal density, but potentially different temperature and salinities, thus "setting the scene" for processes driven by the different molecular diffusivities of temperature and salinity like salt fingering or double diffusion, although *Wieczorek et al.* (2008) claim these are of minor importance. Interleaving also increases the volume of water within this specific isopycnal range and if the inflowing water is very dense it will replace the bottom water. Interleaving and "underleaving" therefore lift the old (bottom) water vertically upwards, eventually to the surface layer.

Surface layer mixing processes

Many processes are limited to the upper water column, especially ones interacting with the atmosphere, and only cause mixing in the surface layer. One of the most obvious effects is that of solar radiation; during summer there is a net heat input that strengthens the stratification (*Reißmann et al.*, 2009). In winter the atmosphere is colder than the water so that the near-surface water cools down and becomes denser than the water underneath; convection homogenises the water column. To a lesser extend the exact same process also happens at night (*Reißmann et al.*, 2009).

The other way the atmosphere changes the surface density field is through precipitation and evaporation as well as through freezing and melting. Precipitation and ice melting introduce freshwater into the surface layer, thereby stabilising the water column, whereas evaporation and sea ice formation (through brine rejection) have the opposite effect (*HELCOM*, 2007).

Most other atmosphere-related mixing processes are a result of the stress exerted by the wind on the sea surface. The wind causes waves to form and to break supplying momentum to the upper layer and entraining air bubbles into the water and sea spray into the air, which has a large inpact on the air-sea gas exchange (*Gemmrich*, 2010). Wind mixes the surface layer and can break down the thermocline, thereby increasing the depth to which wind can mix the water directly. Wind action also sets up Langmuir circulation, rows of counter-rotating cells aligned in the wind direction named after *Langmuir* (1938), that homogenises the surface layer (*Craik and Leibovich*, 1976; *Brown et al.*, 2001).

Bottom layer mixing processes

Basin scale currents, e.g. due to seiches or inertial oscillations, experience drag from the sea bed. This bottom friction leads to turbulence and mixing close to the sea bed and the generation of a bottom boundary layer (*Soulsby*, 1983; *Gloor et al.*, 2000). Also the breaking of internal waves or the collapse of Beddies (see below) on the topography will increase the turbulent dissipation close to the sea bed.

At sloping sea beds this combination of currents and bottom friction causes an additional mixing mechanism called shear-induced convection. In the center of the basin isopycnals are generally horizontal plains, aligned with the sea surface and -bed, but close to the sea bed at the sloping boundaries isopycnals are normal to the slope, i.e. bend down from the horizontal, to preserve the no-flux condition through the sea bed (*Lorke et al.*, 2005). Periodic up- and downslope flow (*Moum et al.*, 2004; *Lorke et al.*, 2005, created by near-inertial oscillations, tides or seiches:), in combination with a logarithmic increase of velocity with distance from the bed (this is known as the law-of-the-wall), can cause asymmetrical patterns (*Lorke et al.*, 2005; *Becherer and Umlauf* , 2011). During upslope flow differential advection can push denser

water over less dense water, destabilising the water column and leading to convection. During downslope flow the opposite happens with stratification, and thus stability, being enhanced by light water being advected over heavier water.

Mixing within the bottom boundary layer can affect the interior waters too. Water that is mixed at the slope creates a horizontal density gradient with the stratified water inside the basin. This water therefore "collapses" into a thin layer that travels as an intrusion into the basin along the isopycnal of the mixed water's density (*Gloor et al.*, 2000; *Wain and Rehmann*, 2010). This process is very similar to the interleaving of inflowing water. This process has been found to be the main mixing mechanism in lakes (*Becherer and Umlauf*, 2011; *Wüest et al.*, 2000) and medium-sized oceanic basins (*Ledwell et al.*, 2000; *Holtermann and Umlauf*, 2012).

Coastal mixing processes

Freshwater input from rivers flowing into the Baltic Sea sets up lateral salinity gradients and causes estuarine circulation and other local mixing processes near the river mouths, similar to processes in the Belt Sea.

The coast of the Baltic Sea is highly convoluted, see Fig. 1.2, so that, for every wind direction, there is a strech of coastline affected by upwelling (*Lass and Matthäus*, 2008; *Reißmann et al.*, 2009). Winds blowing along the coast (with the coastline to the wind's left) cause the surface water to be moved away from the coast due to Ekman transport; the Coriolis force deflects currents to the right on the northern hemisphere because of the Earth's rotation (*Ekman*, 1905; *Lehmann and Myrberg*, 2008). As the surface waters are advected away from the coast they are replaced by waters coming from below. This results in a vertical transport of deeper water masses and a mixing in the surface layer if the depth of the compensation flow is below the halocline (*Reißmann et al.*, 2009).

Gravity waves can interact with upwelling, e.g. *Avicola et al.* (2007) found that internal waves enhance turbulence within an upwelling coastal jet. Irregularities in the alongshore wind or in the coastline can generate Kelvin waves (*Lehmann and Myrberg*, 2008) that in turn can modify the upwelling signal and even produce downwelling under upwelling-favourable conditions according to *Fennel and Seifert* (1995).

Biogenic mixing processes

Although not included in Fig. 1.3, recently a resurgence of interest in biogenic mixing led to some controversial papers. Some supporters of the significance of biogenic mixing compare schools of fish to storms in terms of energy dissipation (*Huntley and Zhou*, 2004) or calculate that if only 1% of oceanic net primary production is dissipated in the deep ocean this constitutes

the same order of energy input as by the wind (*Dewar et al.*, 2006). A study on mixing by jellyfish claims drift mixing, mixing of water that is transported by an animal due to their body's pressure field and the water's viscosity, is more important that wake mixing and the turbulent dissipation also of the order of the winds and tides (*Katija and Dabiri*, 2009). Others conclude that drift mixing is negligible for vertically migrating copepods (*Leshansky and Pismen*, 2010) and other small active swimmers (*Subramanian*, 2010) since only 1% of swimming energy goes into mixing (*Visser*, 2007). *Visser* (2007) and *Dewar* (2009) claim the mixing efficiency is too small since the length scales involved (e.g. zooplankton length $\sim$1 mm) are smaller than the Ozmidov scale (Sec. 4.2.4). Mechanical energy is therefore dissipated to heat before it mixes (*Katija and Dabiri*, 2009). Larger organisms might be more efficient than e.g. krill, but are also much less abundant. Although jellyfish, zooplankton and fish are plentyful biogenic mixing will be disregarded in the following since so far no agreement has been reached and no studies have been done in the Baltic Sea.

Beddies

A common feature in the ocean, and also the Baltic Sea are mesoscale eddies; circulating lenses of water. This water contained in an eddy might have very different water properties from the surrounding water. In the core of rotating eddies the water and isopycnals are either moved up or down depending on their temperature: warm-core eddies rotate anti-cyclonically and isotherms are displaced downward (*Brown et al.*, 2001). In the Baltic Sea mesoscale eddies have been given a nickname; they are known as Beddies (*Reißmann et al.*, 2009), have radii of 4–30 km and temperature anomalies of e.g. 4°C (*Aitsam et al.*, 1984; *Sturm et al.*, 1988). Up to 15 Beddies were found to be "cohabiting" in the Bornholm Basin at any one time, taking up 12%, or 2 km^3, of the basin's volume (*Reißmann*, 2005). In the oceans mesoscale eddies, e.g. those shed by the Gulfstream, can survive for months, even a year (*Katsman et al.*, 2003; *Cheney and Richardson*, 1976). Beddies will probably not live so long since they would encounter the basin sides and collapse there before they would "die of natural causes", i.e. fade away due to dissipation *Reißmann et al.* (2009).

Internal wave mixing

The two main generation mechanisms of internal waves are flow over topography and action of the wind, see also Sec. 1.1. In the Baltic Sea (internal) tides are absent so that the wind is the main internal wave generator. Additionally, internal waves can be generated by Beddies upon their collapse at a sloping boundary; as the Beddies' kinetic and potential energies are released much is used for mixing, but some is radiated away as internal waves (*Reißmann et al.*, 2009). Before collapse the interaction between Beddies and internal waves is largely

unknown; *Talipova et al.* (1998) suggest Beddies have no large impact on long waves, but they might enhance mixing by creating scattering bodies or critical layers, as for coastal upwelling jets (*Avicola et al.*, 2007).

On the slopes internal waves are one of the mechanisms generating turbulence. Increased turbulent dissipation has been measured on the sloping boundaries of, for example, the Gotland Basin (*Ozmidov*, 1995; *Stigebrandt et al.*, 2002; *Holtermann and Umlauf*, 2012). However, it is not clear how much of the boundary mixing is induced by breaking internal waves, although *Holtermann and Umlauf* (2012) suggest the main energy sources are topographic waves and a deep rim current. Within the relatively quiet interior internal waves are generally assumed to be the main mixing agent, especially on short time scales and during stagnation periods (e.g. *Reißmann et al.*, 2009). This mixing has thus far only been assessed by calculating turbulent diffusivities (*Matthäus*, 1990; *Axell*, 1998; *Lass et al.*, 2003; *Holtermann and Umlauf*, 2012).

1.4 The Bornholm Basin

With a lateral scale of 100 km, and a depth of approximately 95 m at the deepest point, the Bornholm Basin forms one of the large, deep basins of the Baltic Sea. It is located in the southern Baltic Sea (Fig. 1.2), at the start of the chain of deep basins. It covers a surface area of $\sim$ 39000 km^2 of which $\sim$ 16000 km^2 have depths greater than 50 m (*Christoffersen et al.*, 2007). The latitude is approximately 55.25°N, corresponding to a local inertial period of $\Pi_i = 14.56$ h, and a Coriolis parameter of $f_i = 2\pi/\Pi_i = 1.20 \times 10^{-4}$ s^{-1}.

Like the rest of the Baltic Sea the Bornholm Basin was formed after the Last Glacial Maximum (LGM), see Sec. 1.3.1. Sediment deposition over the 20,000 years since the LGM has given the deep part of the basin a sea bed that consists mainly of mud, whereas higher up the sloping boundaries the sediment is coarser and consists of silts and sand. The thickness of the Holocene sediment varies strongly (0–12 m) and locally (*Christoffersen et al.*, 2007) and grows around 1 mm per year (*Winterhalter et al.*, 1981). Along the path of strongest currents (northwest–southeast), i.e. along the path of inflows, sediments are considerably less thick than in the northeastern part of the basin, in some areas even absent (*Christoffersen et al.*, 2007).

During the warm season, vertical stratification is dominated by a permanent thermocline at 10–30 m depth, and a deeper halocline located at 50–60 m depth. In winter, the thermocline is gradually eroded, and convection and wind-driven mixing occasionally penetrate down to the halocline depth. The entrainment associated with these processes may deepen the surface mixed layer substantially, and sharpen the halocline; however, it is generally not strong enough to completely erode the halocline even under extreme atmospheric forcing, see Chap. 4 for

more on (the effect of a large storm on) stratification. The halocline forms the upper edge of a weakly stratified salt-water pool that is intermittently replenished by the dense, saline water masses intruding as dense gravity currents from the North Sea, as explained in Sec. 1.3.2. These near-bottom currents propagate from the Arkona Basin through the Bornholm Channel, which lies between the island of Bornholm and the Swedish mainland, into the Bornholm Basin (*Umlauf and Arneborg*, 2009). If the volume of the inflow is large enough to fill the basin it will spill over the Stolpe Sill and flow through the Stolpe Channel towards the next deep basin (Fig. 1.2). This way the Bornholm Basin acts as a buffer and regulates the effectivity of the inflow in the following basins (*Matthäus et al.*, 2008).

The effects of inflows and stagnation periods are also captured in the age of the water. The age of a water particle is the time (in years) that has elapsed since the last time that particle was in contact with the atmosphere at the sea surface. *Meier* (2005) calculated the water's age for 5 basins of the Baltic Sea. In the deep Bornholm Basin, at HELCOM station BMPK02 (see Sec. 2.4), the median (maximum) age of water at 93 m depth between 1903 and 1998 was 1.2 (2.8) years. This is short compared to the 4.5 (9.9) years at the bottom of the Gotland Basin and 7.1 (10.7) years at 231 m in the Landsort Deep. The surface layers were well ventilated, but there was another local age maximum at the top of the halocline of 0.5 (5.8) years. The Baltic Sea as a whole has a residence time of 26–29 years (*Döös et al.*, 2004).

Inflows can either be barotropic inflows primarily occuring in autumn and winter or warm summertime baroclinic inflows. The latter occur more frequently but possess generally less oxygen, which, together with their much smaller volume, makes them less able to ventilate the deep basins (Sec. 1.3.3). On the Bornholm basin though, these small but warm inflows can have a large effect; from oxygen records *Mohrholz et al.* (2006) showed that, contrary to popular thought, these small inflows could ventilate the Bornholm Basin, although probably not the deeper basins further east. The percentage of the Bornholm Basin that is anoxic is, with the exception of "inflow years", relatively constant at 3–5% while another 30–40% is hypoxic (*Axe*, 2010, Fig. 3). *Mohrholz et al.* (2006) speculate the baroclinic inflow "*may be the reason that the* [Bornholm Basin] *remains one of the most important spawning grounds for Baltic cod, especially during stagnation periods*". The spring recruitement of the copepods *Acartia longiremis* and *Acartia bifilosa* was shown to be very dependent on the temperature of the deeper sediments of the Bornhom Basin where the nauplii hatch (*Dutz et al.*, 2004).

The Bornholm Basin was used by the Soviet military administration in Germany 2–3 years after the end of the second World War as a chemical munition dumpsite (*Missiaen and Noppe*, 2010; *Missiaen et al.*, 2010). The primary dumpsite, with a diameter of 11 km, is located in the northeastern part of the deep basin, although the chemical weapons, including mustard gas, Clark I and II, and Adamsite (*HELCOM*, 2010), are probably spread over a larger area, in

70–95 m water depth. On their seismic survey *Missiaen and Noppe* (2010) found a large variety of war material (mines, bombs, grenades, etc.) to be buried less than 1 m in the sediment. *Missiaen et al.* (2010) also found out that arsenic containing compounds are widespread in the sediment in and around the dumpsite suggesting that the shells, drums and and other containers have been leaking. Since four ship wrecks and over half a million dumped objects (*Missiaen and Noppe*, 2010) clutter the area "*anchoring and fishing* [is] *not recommended*", as stated on nautical charts, this area has been avoided for mooring and profiling work (Sec. 2.1).

1.5 Aims

The aims of the ILWAO (International Leibniz Graduate School for Gravity Waves and Turbulence in the Atmosphere and Ocean) project are to study the effects of internal gravity waves on turbulence and mixing in the atmosphere and ocean. This thesis looks at the effect of internal waves in the ocean (the Baltic Sea), in particular in the "quiet interior" where turbulence is generally low and internal waves are assumed to be the main mixing agent. Hardly any observational data of internal waves exist in the Baltic Sea, hence the first aim was to collect an extensive multi-parameter set of high-resolution measurements at many frequency scales and under a variety of circumstances. Further aims consisted of characterising the internal wave field in terms of energy levels and dominant frequencies, narrowing down generation and dissipation processes and estimating the relevance of internal waves mixing to the basin-wide mixing.

1.6 Document structure

In the next two chapters the methods used throughout the rest of the thesis, both for measurements (Chap. 2) and for subsequent data analysis (Chap. 3), will be explained. Chapter 4 will detail the background stratification, and thus the water column's stability, that will "set the scene" for Chaps. 5 & 6. These are the main chapters on internal waves, looking first at the low-frequency limit of internal waves; near-inertial waves in Chap. 5. Afterwards, in Chap. 6, high-frequency waves near the buoyancy frequency and the transition to instability and turbulence are looked at. A general summary with outlook (Chap. 7) then completes the thesis. For background information App. B gives explains the microstructure profiler and the steps involved in calculating the turbulent dissipation rate from microstructure shear.

Chap. 5 has been published in *Journal of Geophysical Research – Oceans* (*van der Lee and Umlauf*, 2011), while Chap. 6 will be submitted to *Continental Shelf Research* shortly (*van der Lee and Umlauf*, 2012). Both chapters have therefore been written with the help of the co-author Dr. Lars Umlauf. It is hoped that Dr. Hans van Haren will also contribute to

van der Lee and Umlauf (2012), in which case he would become a co-author. Parts of the method and stratification chapters are expanded from sections of the papers.

2 Methods: Measurements

2.1 Research cruises

Hydrographic and turbulence data were obtained in the Bornholm Basin (Fig. 2.1a) during a cruise with R/V *Poseidon* in late summer 2008 (18–29 September) and with R/V *Alkor* in winter 2010 (27 February–10 March). On these 12-day cruises the available time was divided between various stations and transects. The two main ones, the ones visited on both cruises, were the central station (S1) and the boundary transect (T1), see Fig. 2.1b. Station S1 was located in the relatively flat, deeper part of the basin, local depth ~ 86 m, near the centre of the basin (just outside the extended chemical dumpsite area (*Missiaen et al.*, 2010)). Transect T1, meanwhile, covered a 40 m depth range over 17 km up the southeastern flank of the basin, with this slope of 1:425 it is one of the steepest slopes of the basin.

An overview of the time schedule during the cruises is given in Fig. 2.2, with station/transect numbers indicated together with the MSS (see Sec. 2.2.1) measurement periods. The convention is that time is measured in decimal days, defined here as days and fraction of days since the midnight starting that year, i.e. day 0.75 is 18:00 UTC (Coordinated Universal Time) on 01 January. Local time is UTC + 1 hour in winter and UTC + 2 hours in summer. Both cruises started at the central station S1, where the ship stayed until approximately two days worth of microstructure measurements had been gathered. In 2010 measurements were interrupted for 1.5 days because of a storm (see Sec. 4.3). After station S1 the ship continued to transect

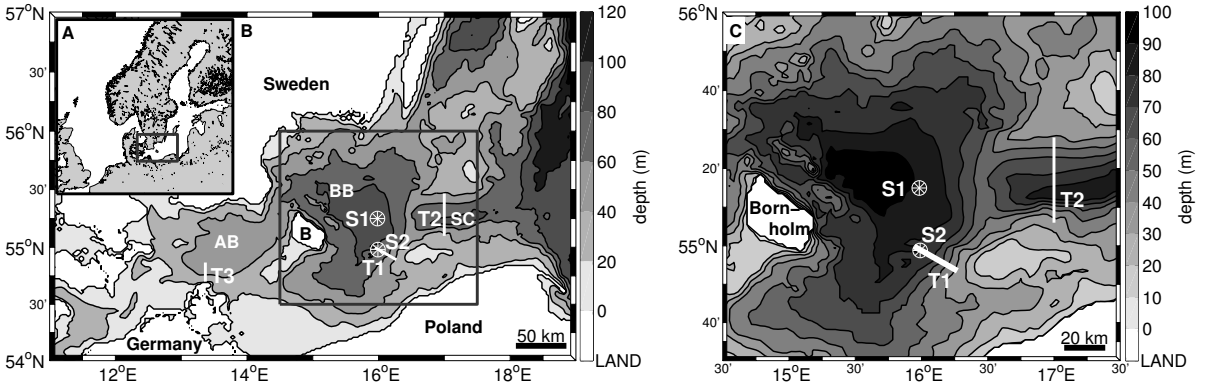

Figure 2.1: Maps of the southern Baltic Sea and study area: (a) overview map with the Western Baltic marked by a rectangle, (b) Western Baltic Sea with study area marked by rectangle, and (c) study area with central station S1 and transect T1 on the southern slope. For abbreviations see Tab. 1.1.

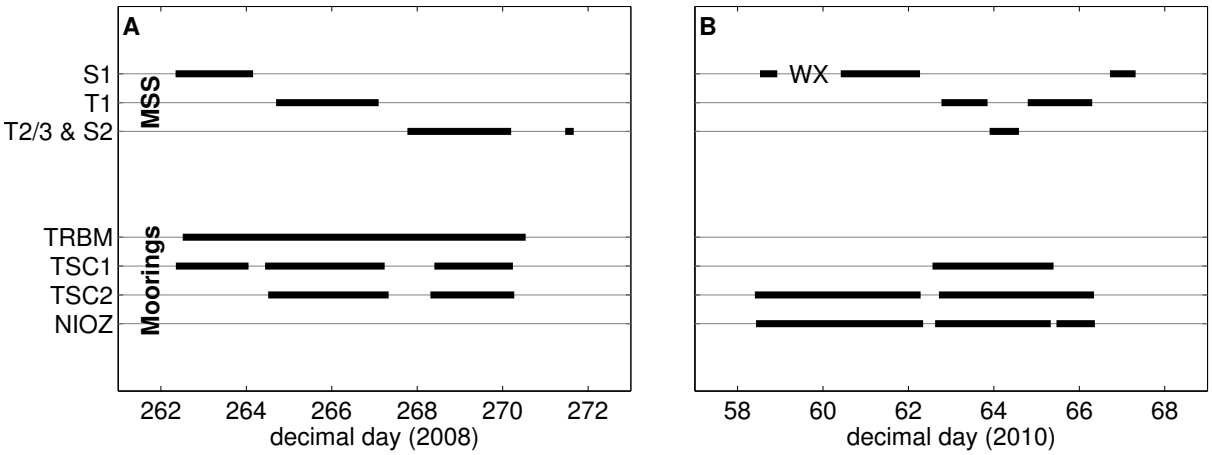

Figure 2.2: Timelines of (a) POS373 and (b) AL351, with indication of time spent at each station and the duration of MSS/mooring/ADCP deployments. WX in (b) stands for Winterstorm Xynthia. For station positions see Fig. 2.1 and for mooring "content" see Sec. 2.3.

T1, where also ~ 2 days per cruise were spent. Some other transects and station were visited as well, but not necessarily the same ones on different cruises; in summer 2008 some transects (T2) across the Stolpe Channel were sailed (Fig. 2.1b), while in winter 2010 an additional station (S2) was located on the deeper half of transect T1. In 2010 the ship returned shortly to station S1 at the end of the cruise for microstructure measurements only.

During these cruises instruments were either deployed directly from the ship (see Sec. 2.2) or mounted on moorings and deployed on the sea bed for multiple days (see Sec. 2.3). Together these instrument types provided high-resolution measurements both in time and in space. A very schematic view of this experimental set-up can be seen in Fig. 2.3, while more details follow below. In Fig. 2.3 two moorings are shown, on the left a Temperature-Salinity Chain (TSC) and on the right a bottom-mounted acoustic Doppler current profiler (ADCP), as well as the microstructure sonde (MSS) deployed from the ship's back deck.

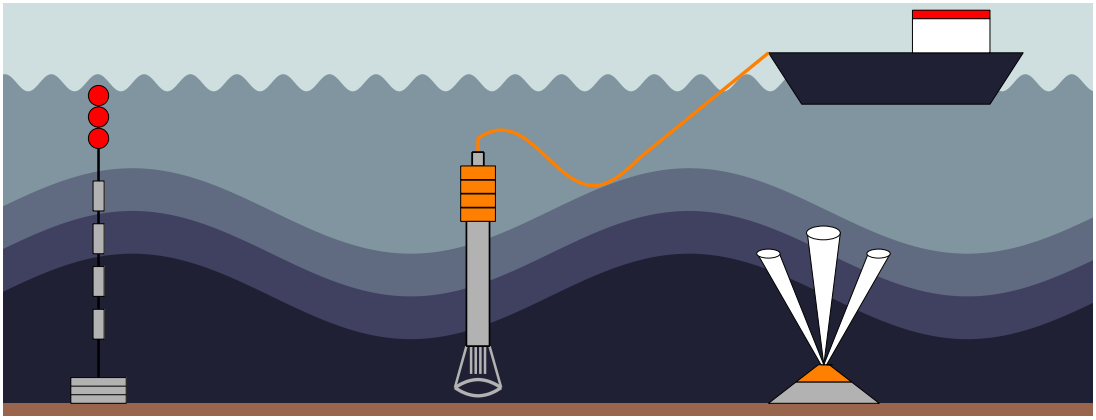

Figure 2.3: Scheme of instrumentation deployed. Note: figure is (absolutely) not to scale!

2.2 Ship-based measurements

2.2.1 Microstructure measurements

During the cruises in September 2008 and February/March 2010, full-depth stratification and shear-microstructure profiles were obtained on the stations and transects using a MSS90L microstructure profiler from In-Situ Wassermesstechnik (ISW). The MSS90L was equipped with precision CTD (Conductivity/Temperature/Depth) sensors from Sea & Sun Technology (SST), a fast-response temperature sensor (FP07), as well as 2 airfoil shear probes (PNS06 from ISW) for the analysis of microscale vertical shear. For a more detailed overview of the (theory behind) microstructure shear measurements see App. B. All sensors were sampled at 1024 Hz with 16-bit resolution, while the profiler was free-falling on a loosely-tethered cable with a speed of 0.6–0.7 m s^{-1}. Using a sensor protection cage, it was possible to obtain nearly full-depth CTD and microstructure data until less than 0.1 m above the bottom. Before further use, all data were despiked and averaged to 256-Hz resolution for noise reduction. CTD data were then averaged into 0.1-m bins after correcting for differences in sensor response times to obtain spike-free salinity and density profiles. Dissipation rates estimated from the microstructure shear probes were averaged into non-overlapping bins of 0.5-m thickness for further analysis.

Continuous microstructure profiling was conducted from the stern of the ship 24 hours per day at an average rate of 5.6 (2008) and 7.2 (2010) minutes per profile. On each cruise we started at station S1. During these measurements the ship was slowly moving against the wind and waves on short transects inside a circle (radius: $\sim$ 2 km) around the station, see Fig. 2.4, to prevent the profiler from coming under the ship. At the end of each mini-transect,

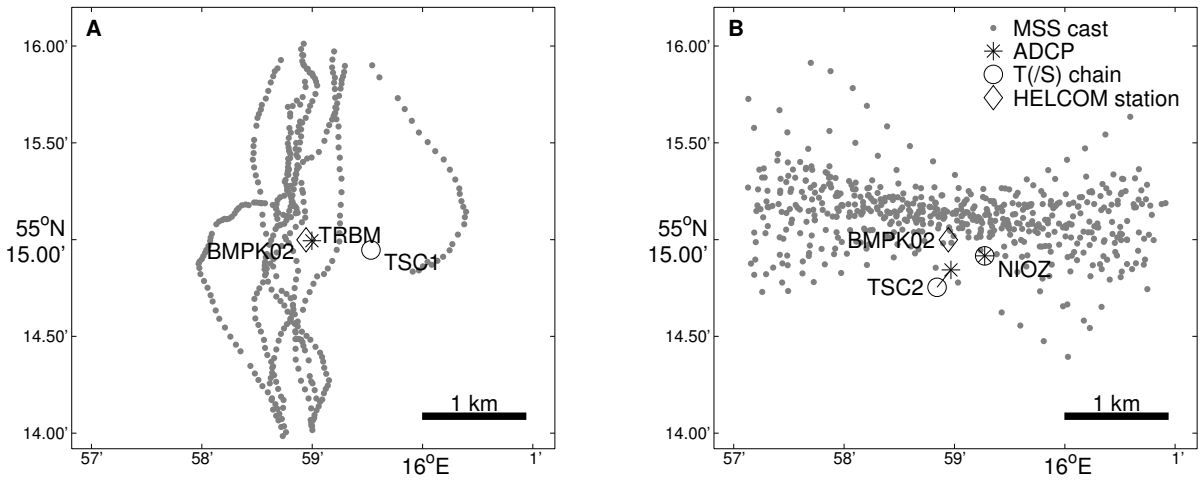

Figure 2.4: Maps of mooring positions and MSS cast locations at central station S1: (a) summer 2008, (b) winter 2010.

measurements were shortly interrupted to reposition the ship at the downwind end of the transect. The duration of individual transects was a few hours, depending on the sea state and the local weather conditions. With this method we were able to obtain 400 microstructure profiles at S1 on 7 transects in summer 2008 (see Fig. 2.4a). In winter 2010 we collected 431 microstructure profiles on 31 transects on our first stop at S1. After the first 6 transects (less than half a day), the passage of winterstorm Xynthia prohibited microstructure measurements for a period of 36 h due to high wind speeds (> 15 m s^{-1}, 8 Bf) and high sea state. As the wind abated the remaining 25 transects were sailed between days 60.4 and 62.3. After spending time at transect T1/station S2 we returned to S1 (see Fig. 2.2b) and collected another 119 profiles on 8 transects. Fig. 2.4b includes all MSS casts at S1 in winter 2010. Since no moorings were deployed, i.e. no velocity measurements taken, this second time around, data collected was used for the stratification information discussed in Chap. 4, but was largely ignored for other analysis (Chaps. 5 & 6).

In 2008 we sailed the transect T1 (Fig. 2.5a), from the deepest (71 m) to the shallowest (31 m) point, 7 times and collected between 88 and 108 profiles per transect. Each 17-km transect took approx. 6.7 hours, which corresponds to almost half an inertial period ($0.46\,T_i$), such that the measurements are not truly synoptic and each transect includes changes in time as well as in space. In 2010 we were a bit faster; on average, over the 9 transects sailed, we needed 5.4 hours ($0.37\,T_i$) for ~ 77 profiles along the 17-km track. Because the halocline was deeper than 71 m, which was the deepest end of the transect on the previous cruise, T1 was displaced towards the centre, on a line extending the summer transect, see Fig. 2.5b. T1 was also turned around from shallow (42 m) to deep (74 m) because of the strong (6 Bf) northerly winds. Due to the shallower depths compared to the basin centre, cast durations were shorter so that we managed a profile interval of 4 min on average on T1. In this thesis the focus is on processes in the interior of the basin, so that data shown are almost exclusively from station S1.

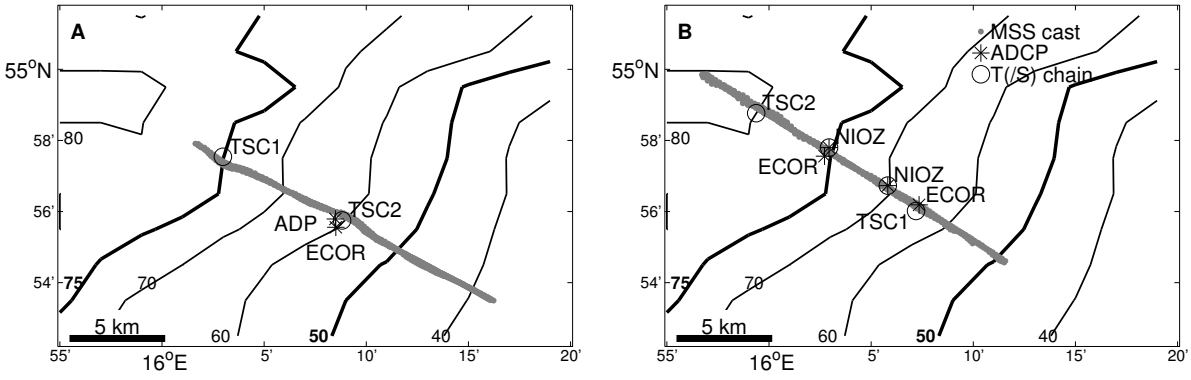

Figure 2.5: Maps of mooring positions and MSS cast locations at slope transect T1: (a) summer 2008, (b) winter 2010.

2.2.2 Meteorological data

Meteorological data, including wind speed and direction, air temperature and relative humidity, were obtained from the meteorological stations on board the research vessels with an interval of 1 s (POS373) or 1 minute (AL351). As quality control the European Local Model (Lokal-Modell Europa, LME, renamed to COSMO-EU in 2007) from the German Weather Service (Deutscher Wetterdienst, DWD) was also used. Three-hourly model data for the grid box ($\Delta x \sim 7$ km) closest to our station S1 and averaged over the Bornholm Basin area ($15-17^\circ$E, $54.5-57^\circ$N) was extracted for the periods covering the cruises. After a careful comparison, very good agreement with the data from the shipboard instruments was found, hence all weather data shown in figures and used for analysis is shipboard data.

2.3 Moored measurements

Parallel to the ship-based measurements various moorings were deployed at the station or along the transect, see Figs. 2.4 & 2.5, for durations of a few days, see Fig. 2.2. These moorings mostly combined a thermistor string with an Acoustic Doppler Current Profiler (ADCP) as detailed below. Other specialised moorings (ECOR-frame, ADP-frame and MPI-lander) were also deployed on transects, but are not discussed here.

2.3.1 Current profilers

In September 2008 (POS373), an upward-looking 300-kHz ADCP (Workhorse from RDI, Rowe Deines Instruments) was deployed at S1 for 8 days, covering almost the entire measuring period at S1 (MSS transects 2–7) and 6 more days. The instrument was located in a bottom-mounted gimballed suspension system to level it and to protect it from bottom-trawling fishers, hence its official name is the Trawl-Resistant Bottom Mount (TRBM), but is affectionately known as the turtle. Apart from the blanking regions near the surface (8 m) and bottom (5 m), this instrument sampled the full water column at 2-s intervals using 2-m bins with the centre of the lowest bin located 5.2 m above the ground.

In February/March 2010 (AL351), a 600-kHz upward-looking ADCP (RDI Broad-Band) was deployed on the bottom at S1 for 3.9 days as a part of the second Temperature/Salinity Chain (TSC2). The ADCP was operated in RDI "mode 12", providing high-precision velocity estimates at a rate of slightly less than 2 s from the average of 10 sub-pings at 120-ms intervals. Velocity estimates were obtained in 1-m bins with the centre of the lowest bin located 3 m above the ground. Signal attenuation limited the total range that could be sampled with this instrument to approximately 30 m. Velocities outside this range, higher up in the water column, were obtained from a 300-kHz ADCP (RDI Workhorse), with transducers located on top of the

mooring from the Royal Netherlands Institute for Sea Research (Koninklijk Nederlands Instituut voor Onderzoek der Zee, NIOZ), 1.5 m above the bottom, at approximately horizontal 350 m distance from the 600-kHz ADCP. This instrument sampled velocities every 2 s (based on 6 pings per ensemble 250 ms apart) from 5.4 mab up to a level of 22 m depth, also with a 1-m vertical interval.

All three ADCPs had 4 beams with a beam angle of 20° from the vertical. For some applications, mainly for long time series where the focus is on "background conditions" and low-frequency near-inertial motions (Chap. 5), the velocity estimates were averaged over 300 s in time to further reduce the measurement uncertainty to below 0.01 m s^{-1}. For the high-frequency chapter (Chap. 6), data from the TSC2 ADCP (winter cruise 2010) was averaged over 10 s to resolve the motions near the buoyancy frequency.

2.3.2 Thermistor strings

Both of the moorings at S1 in 2010 carried thermistor chains in addition to the ADCPs mentioned above. The first mooring (TSC2) held a chain with 11 Seabird Microcats (SBE 37-SM) and 13 thermistors (NIOZ3 and NIOZ5) from 0.8 to 45.8 mab. These microcats sampled temperature and salinity every 15 s. The chain was connected by a groundline and approximately 213 m southwest from the 600 kHz ADCP, see Fig. 2.4b, to avoid interference of the microcats with the acoustic signal of the ADCP.

The NIOZ mooring mentioned above also held a high-resolution temperature chain with 151 thermistors (NIOZ3 and NIOZ4) located 20 cm apart from 0.1 to 30 mab. These thermistors, especially designed at NIOZ, have an accuracy of less than 0.001°C and a sensor response time of 0.25 s (for more details see *van Haren and Gostiaux*, 2009; *van Haren et al.*, 2009). The sensors were calibrated *in-situ* by attaching them to the CTD rosette (Seabird 911plus). Due to a programming error all thermistors were set to sample at 1-s intervals. Not all could keep up this pace, resulting in erroneous and missing values. Dr. Hans van Haren was able to repair some time series by filtering and subsampling. However, thermistors with too many bad values, including all on TSC2, had to be removed from the data set to ensure its accuracy.

2.4 HELCOM station BMPK02

In order to put our measurements of stratification in a wider context and to compare them with the Bornholm Basin climatology a 41-year long time series from HELCOM (Helsinki Commission) Baltic Monitoring Programme station BMPK02 were used. This station, at 15.9824°E, 55.2500°N, was less than 60 m away from our station S1 (Fig. 2.4). Since January 1970 monitoring cruises from the project COMBINE (Cooperative Monitoring in the Baltic

Marine Environment) stopped here 2 or 3 times per month, resulting in 1236 CTD casts until December 2010, the end of the record used here.

3 Methods: Analysis

In this chapter the methods used in the following chapters will be introduced. Temporal filtering (Sec. 3.1) and spectral analysis (Sec. 3.2) will be used for ADCP velocity data as well as for thermistor temperature and microcat density data. Spectral analysis shows the partitioning of energy between frequencies while certain frequencies can be separated out with a temporal filter. In Chap. 5 this will be used to isolate the internal wave band frequencies, while in Chap. 6 the energy cascade from low- to high-frequency motions is followed by comparing spectra at different times. Since these motions are directly or indirectly generated by the wind, the wind stress on the sea surface is quantified with the method in Sec. 3.3 and compared to the frictional stress on the sea bed. Decomposing the velocity signal into vertical profiles with time-varying amplitudes can be done based on stratification profiles, see vertical normal modes (Sec. 3.4). Chap. 5 will show how they can help show whether or not the internal wave field is in steady-state.

3.1 Temporal filtering

For many of the stationary time series low-pass, high-pass and band-pass filters have been used that leave, respectively, the low frequencies, high frequencies or the frequencies in a central passband unaltered (gain = 1). For a low-pass filter, frequencies well above the cut-off frequency are totally attenuated (gain = 0). A perfect filter would be a step function, but in practise filters have a cut-off band with a gain of $1/\sqrt{2} = 0.707$ at the given cut-off frequency (*Emery and Thomson*, 2001). Fig. 3.1 shows two filter types, a Chebyshev type `I` and a Butterworth filter, in comparison with the step function. Real-life filters also often suffer from "ringing" or "Gibbs's phenomenon", that is that the gain is not a flat function of frequency away from the cut-off frequency, but oscillates in the pass- and/or stopbands as exemplified by the Chebyshev filter in Fig. 3.1. This distorts the frequency signal in the passband and/or leaks energy from the stopband, which can be somewhat counteracted by using windows as smoothing functions (*Emery and Thomson*, 2001).

Various filter types were tested, but here a Butterworth filter, named after the physicist Stephen Butterworth who invented it in 1930, has been used. It is defined as:

$$|\text{gain}(f)|^2 = \frac{1}{1 + (f/f_c)^{2q}} \tag{3.1}$$

where f_c is the cut-off frequency and q the filter order (*Emery and Thomson*, 2001).

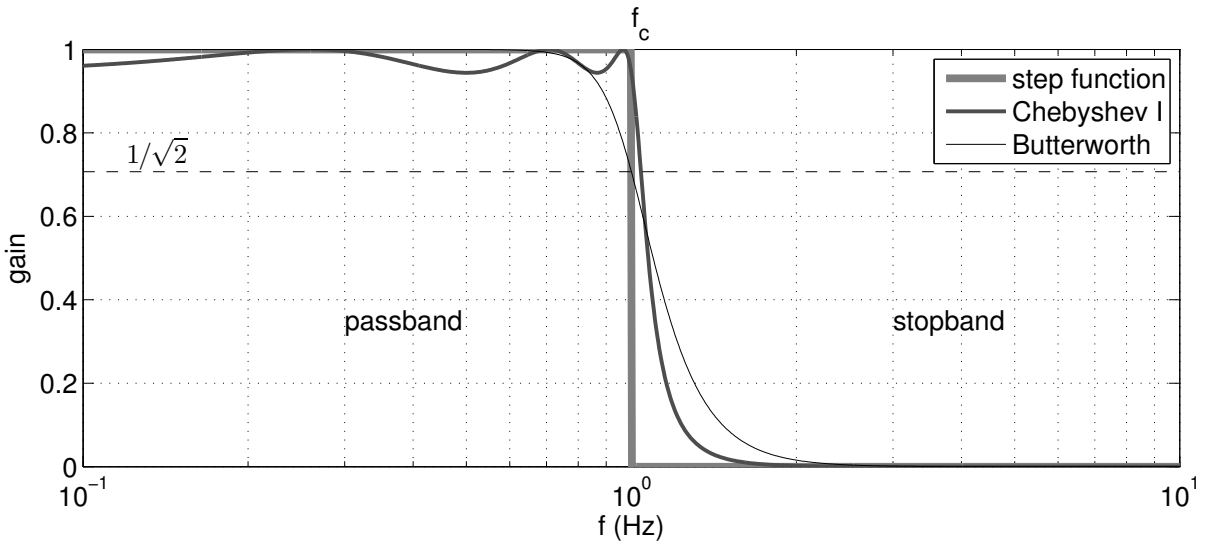

Figure 3.1: Diagram of filter types: gain over frequency comparison of the step function (thick, light grey) with a Chebyshev type I (dark grey) and a Butterworth filter (thin, black). Both filters are 6^{th}-order low-pass.

The Butterworth filter is one of the most commonly used filters in oceanography and is characterised by a smooth roll-off, a monotonic frequency response, maximally flat pass- and stopbands (i.e. no ripple problems for $q = 1$), and a fast computation time (*Roberts and Roberts*, 1978). However, it does not have a very sharp cut-off (see also Fig.3.1) and ringing problems can occur near the end of the filtered time series (*Emery and Thomson*, 2001). Increasing the filter order has the effect of steepening the roll-off, i.e. narrowing the cut-off band, but also increases the chance of ringing effects.

Since the filter is recursive, meaning that input and past output values are used to generate the output, a phase shift is generated (*Roberts and Roberts*, 1978). In all cases here the data were filtered twice, once forwards and once backwards, ensuring no phase distortion could occur. This double filtering also doubles the filter order; the (doubled) filter order and the cut-off frequency used are mentioned in the text for the filtered quantities.

3.2 Spectral analysis

3.2.1 Covariance

To determine the degree to which two time series ($x1$ and $x2$), e.g. from different depth levels, resemble each other their cross-covariance can be computed (*Garrett and Munk*, 1972). This gives the added information of the time lag Υ between the time series. The cross-covariance, which equals the cross-correlation if the means of $x1$ and $x2$ (μ_{x1} and μ_{x2}) are removed, is

given by:

$$R_{12}(\Upsilon) = \langle (x1(t) - \mu_{x1})\,(x2(t+\Upsilon) - \mu_{x2}) \rangle \tag{3.2}$$

where the pointy brackets indicate a time average (*Emery and Thomson*, 2001). For more details and a derivation see *Umlauf and van der Lee* (2010). These covariances were normalised so that, at zero lag, the auto-covariances R_{11} and R_{22} are 1.0. R_{12} ranges from -1 to 1. $R_{12} = 1$ is a perfect correlation and -1 is a perfect anti-correlation, i.e. maxima in $x1$ coincide with minima in $x2$ and vice versa.

3.2.2 Spectra

Spectra are used to show the amount of power in certain frequency bands, i.e. the power spectral density. Here power P has the squared units, per frequency, of the variable being spectrally analysed, e.g. $(\mathrm{m}^2\ \mathrm{s}^{-2})\ \mathrm{Hz}^{-1}$ for velocities. The spectrum for a time series of variable $x1$ is a Fourier transform of the autocovariance and is given by (*Kundu and Cohen*, 2008; *Umlauf and van der Lee*, 2010):

$$P_{12}(\omega) = \frac{1}{2\pi} \int_{-\infty}^{\infty} R_{12}\, \mathrm{e}^{-i\omega\Upsilon}\, \mathrm{d}\Upsilon \quad . \tag{3.3}$$

Borrowed from optics, oceanographic spectra can partly be described by the colours blue, red and white. A white spectrum has nearly equal power for all frequency bands, this is often the case for instrumental noise. A red (blue) spectrum is a spectrum where the power spectral density decreases (increases) with increasing (decreasing) frequency, since red (blue) has the longest (shortest) wavelengths of visible light (*Emery and Thomson*, 2001). Red spectra are very common for the frequency range of internal waves (Sec. 1.2.2), whereas blue spectra are rare.

If the variable $x1$ is complex, usually the horizontal velocities $u+iv$, P is a rotary spectrum. They show the rotation direction, i.e. clockwise or anticlockwise, and, via the ratio of clockwise to anticlockwise velocities, the degree of ellipticity of the current (see *Umlauf and van der Lee*, 2010). These were also calculated but are not shown, it is just mentioned that the near-inertial oscillations in Chap. 5 are near-circular and rotate in the clockwise sense. High-frequency motions (Chap. 6) move rectilinearly, i.e. with equal clockwise and anticlockwise components, while sub-inertial motions rotate circularly in the anticlockwise direction in the Gotland Basin (*Holtermann and Umlauf*, 2012).

3.2.3 Coherency

The coherence spectrum, or squared coherency, γ_{12}^2 is defined as (*Emery and Thomson*, 2001):

$$\gamma_{12}^2(\omega) = \frac{|P_{12}|^2(\omega)}{P_{11}(\omega)\ P_{22}(\omega)} \tag{3.4}$$

where, since P_{12} is the cross-spectrum, P_{11} and P_{22} are the auto-spectra of time series $x1$ and $x2$ respectively as defined above. The squared coherency has a value range of $0 \leq \gamma_{12}^2 \leq 1$ and gives the portion of variance in $x1$ attributed to $x2$ or vice versa via a linear relationship (*Emery and Thomson*, 2001). The squared coherency gives the added information of the frequencies at which the covariances between the two time series are high or low.

In Chap. 6 the subscripts 12 of P, R and γ^2 have been replaced by the variables used to compute the spectrum or coherency squared value.

3.3 Stresses and drags

3.3.1 Wind-induced surface stress

The stress on the sea surface created by the wind was computed from the ship's meteorological data. First the air density ρ_{air} was calculated from the air temperature and the relative humidity at the default air pressure of 1020 mb (1.020×10^5 Pa). Then the neutral drag coefficient was calculated according to the method by *Smith* (1988); $C_d^{air} = [\kappa / \ln(z/z_0^s)]^2$, where $\kappa = 0.4$ is the von Kármán constant, z is the height above the sea surface where the meteorological properties were measured and z_0^s is the sea surface roughness length: $z_0^s = \alpha_{Ch}(0.036|\mathbf{u}_w|)^2/g + \alpha_R \nu_{air}/(0.036|\mathbf{u}_w|)$. Here α_{Ch} is the Charnock constant (after: *Charnock*, 1955, 1958) for which the default value of 0.0110 was used (*Smith*, 1980, 1988), although this constant is not so constant and should be renamed to Charnock parameter according to *Bye et al.* (2010). The gravitational acceleration (9.8 m s^{-2}) is given by g, α_R is a roughness constant also set to the default (0.11, *Smith*, 1988) and ν_{air} is the kinematic viscosity of air (*Andreas*, 1989). This method assumes a logarithmic profile for the wind speed $|\mathbf{u}_w| = (u_*/\kappa)\ \ln(z/z_0^s)$, where u_* is the friction velocity and $|\mathbf{u}_w|$ is the magnitude of the total wind speed from the east u_w and north v_w wind speeds. The surface wind stress is then given by $\tau_u^s = \rho_{air} C_d^{air} |\mathbf{u}_w| u_w$ in the east and by $\tau_v^s = \rho_{air} C_d^{air} |\mathbf{u}_w| v_w$ in the north direction to combine in a total surface stress:

$$|\boldsymbol{\tau}^s| = \sqrt{\tau_u^{s2} + \tau_v^{s2}} = \sqrt{(\rho_{air} C_d^{air} |\mathbf{u}_w| u_w)^2 + (\rho_{air} C_d^{air} |\mathbf{u}_w| v_w)^2} \quad . \tag{3.5}$$

3.3.2 Law-of-the-wall: Bottom stress and drag

The bottom stress $\boldsymbol{\tau}^b$ was computed using the law-of-the-wall relationship:

$$\boldsymbol{\tau}^b = \rho_0(\varepsilon\kappa d)^{2/3} \quad , \tag{3.6}$$

where ρ_0 is a constant reference density (1000 g kg^{-1}), ε the dissipation rate per unit mass (see App. B) and d the distance from the bottom (*Dewey and Crawford*, 1988). In direct comparison with the surface stress the same logarithmic velocity profile is assumed here as well and the friction velocity is defined as $u_* \equiv (\boldsymbol{\tau}^b/\rho)^{1/2}$, which equals $(\varepsilon\kappa d)^{1/3}$ when using (3.6) (*Lozovatsky et al.*, 2012).

For this analysis, microstructure dissipation rates were averaged into 0.5-m bottom-fitted bins before computing the bin-average over each of the 25 transects of periods `II+III` in winter 2010 (see Sec. 5.3.3). From these averaged dissipation rates, estimates of $\boldsymbol{\tau}^b$ were computed for the lowest three bins according to the above formula. The lowest bin was excluded from further analysis because the strong increase of ε very close to the bottom (law-of-the-wall) is incompatible with the assumption of homogeneous turbulence involved in the spectral analysis of shear microstructure; the final value of $\boldsymbol{\tau}^b$ was therefore obtained from the average of bins 2 and 3. From the bottom stress, and the magnitude of the near-bed current velocity $|\mathbf{u}|$ taken from the lowest ADCP bin, a bottom drag coefficient can be calculated: $C_d = \boldsymbol{\tau}^b/(\rho_0|\mathbf{u}|^2)$. *Dewey and Crawford* (1988) state that estimating $\boldsymbol{\tau}^b$ from ε is more reliable than estimations using the more direct, but also more difficult, way of directly measuring velocity fluctuations in the near-bed layer to calculate Reynolds stresses: $\boldsymbol{\tau}^b = -\rho\langle u'w'\rangle$.

3.4 Vertical normal modes

A good way of describing the internal wave field away from generation sites is via vertical normal modes, as briefly mentioned in Sec. 1.1. The velocity signal is decomposed into a series of modes with time-dependent amplitudes and depth-dependent shape (the modal structure). Although infinite modes can be calculated, the first few already describe most of the internal wave field (see Chap. 5). The method of normal modes is similar to Empirical Orthogonal Functions (EOF), which also separates a signal in space and time variation and sorts them by importance (*Björnsson and Venegas*, 1997). EOF is based purely on statistics, whereas vertical modes are calculated from measured stratification profiles.

3.4.1 Separable functions and the Sturm-Liouville problem

The calculation of the vertical structures of normal modes starts with the shallow water equations for continuously stratified water column (*Kundu and Cohen*, 2008):

$$\frac{\partial u}{\partial x} + \frac{\partial v}{\partial y} + \frac{\partial w}{\partial z} = 0 \tag{3.7a}$$

$$\frac{\partial u}{\partial t} - f_i v = -\frac{1}{\rho_0}\,\frac{\partial p'}{\partial x} \tag{3.7b}$$

$$\frac{\partial v}{\partial t} + f_i u = -\frac{1}{\rho_0}\,\frac{\partial p'}{\partial y} \tag{3.7c}$$

$$0 = -\frac{\partial p'}{\partial z} - \rho' g \tag{3.7d}$$

$$\frac{\partial \rho'}{\partial t} - \frac{\rho_0 N^2}{g}\, w = 0 \tag{3.7e}$$

where p' and ρ' are the perturbation pressure and density respectively. This set is equal to set (1.9) introduced in Sec. 1.2.2, except that now it is assumed that the vertical scale of motion is much smaller than the horizontal scale so that the hydrostatic assumption can been applied to (3.7d), i.e. the term $\partial w/\partial t$ is ignored.

Normal modes are formed by assuming "separable functions" of the forms:

$$[u, v, p/\rho_0] = \sum_{m=0}^{\infty} [\hat{u}_m, \hat{v}_m, \hat{p}_m]\ \Psi_m \tag{3.8a}$$

$$w = \sum_{m=0}^{\infty} \hat{w}_m \int_{-H}^{0} \Psi_m \,\mathrm{d}z \tag{3.8b}$$

$$\rho = \sum_{m=0}^{\infty} \hat{\rho}_m\, \frac{\mathrm{d}\Psi_m}{\mathrm{d}z} \tag{3.8c}$$

where the vertical modal structure, Ψ_m, is a function of z only and $\hat{u}_m$, $\hat{v}_m$, $\hat{p}_m$, $\hat{w}_m$ and $\hat{\rho}_m$ are the amplitudes in x, y and/or t. The forms of (3.8) are chosen to be consistent with (3.7). Now the standard eigenvalue problem, called a Sturm-Liouville problem after the two mathematicians Jacques Charles François Sturm and Joseph Liouville,

$$\frac{\mathrm{d}}{\mathrm{d}z}\left(\frac{1}{N^2}\,\frac{\mathrm{d}\Psi_m}{\mathrm{d}z}\right) + \frac{1}{c_m^2}\Psi_m = 0 \tag{3.9}$$

can be solved for a profile of the squared buoyancy frequency N^2 (see Sec. 4.2.2) with boundary

conditions $\mathrm{d}\Psi/\mathrm{d}z = 0$ at the bottom ($z = -H$) and at the surface ($z = 0$). Here m is the mode number and c_m the corresponding "mode speed", which is different from the phase speed if rotation plays a role. $-1/c_m^2$ is the assumed form of the separation constant which is the result of substituting (3.8b) and (3.8c) into (3.7e), noticing a) that the quantity within the summation must vanish (as the modes are linearly independent) and b) that the functions of z equal the functions of x, y and t (*Kundu and Cohen*, 2008), i.e.

$$\frac{\mathrm{d}\Psi_m/\,\mathrm{d}z}{N^2 \int_{-H}^{0} \Psi_m \mathrm{d}z} = \frac{\rho_0}{g}\,\frac{w_m}{\partial\rho_m/\partial t} = -\frac{1}{c_m^2} \quad . \tag{3.10}$$

It is also assumed that the modes travel in a flow without a background mean shear since, as Walter Munk stated in 1981 "*A variable* $\mathbf{u}(z)$ *can have a more traumatic effect on internal waves than a variable* $N(z)$". In the absence of mean shear the solutions of (3.9) are orthogonal to each (*Bell*, 1974), hence the name normal modes, meaning:

$$\int_{-H}^{0} \Psi_n\, \Psi_m\, \mathrm{d}z \begin{cases} = 0 & \text{if } n \neq m \\ > 0 & \text{if } n = m \end{cases} . \tag{3.11}$$

In order for later calculations of the kinetic energy to show the depth-intergrated energy, i.e. energy per unit mass rather than per unit area, the profiles of Ψ_m are normalised (*Levine*, 2002; *MacKinnon and Gregg*, 2003a) such that:

$$\int_{-H}^{0} \Psi_m^2\, \mathrm{d}z = H \quad . \tag{3.12}$$

3.4.2 Projecting velocities onto modes

From (3.8a) an equation for $\hat{u}_m$ can be derived by multiplying by Ψ_n, integrating over z and dividing by the water depth:

$$\tilde{u}(t,z) = \sum_{n=0}^{\infty} \hat{u}_n(t)\, \Psi_n(z) \tag{3.13a}$$

$$\frac{1}{H}\int_{-H}^{0} \Psi_m\, \tilde{u}\, \mathrm{d}z = \frac{1}{H}\int_{-H}^{0} \Psi_m \sum_{n=0}^{\infty} \hat{u}_n\, \Psi_n\, \mathrm{d}z \tag{3.13b}$$

$$= \frac{1}{H}\sum_{n=0}^{\infty} \hat{u}_n \int_{-H}^{0} \Psi_n\, \Psi_m\, \mathrm{d}z \tag{3.13c}$$

$$= \frac{1}{H}\hat{u}_m\, H = \hat{u}_m \tag{3.13d}$$

where $\tilde{u}$ is the baroclinic east velocity; the east velocity u minus the depth mean velocity $\overline{u}$. The step from (3.13b) to (3.13c) is allowed as mixed terms disappear due to orthogonality (3.11). For the same reason the summation sign disappears; all terms are zero except for $n = m$. The east velocity of mode m at depth z is then simply $\tilde{u}_m(t, z) = \Psi_m(z)\ \hat{u}_m(t)$. Adding the east velocities of all modes gives us the original velocity signal. The same goes for $\hat{v}_m$ with $\tilde{v}$ giving v_m.

3.4.3 Energy in modes

The kinetic energy is given by E^{kin}, which can be integrated over depth and, if (3.8a) is applied, the depth-integrated kinetic energy for a particular mode E_m^{kin} can be calculated:

$$E^{kin} = \frac{1}{2}\ \left(\tilde{u}^2 + \tilde{v}^2\right) \tag{3.14a}$$

$$= \frac{1}{2}\ \left(\left(\sum_{m=0}^{\infty} \hat{u}_m\ \Psi_m\right)^2 + \left(\sum_{m=0}^{\infty} \hat{v}_m\ \Psi_m\right)^2\right) \tag{3.14b}$$

$$\frac{1}{H}\int_{-H}^{0} E^{kin}\,\mathrm{d}z = \frac{1}{2H}\ \int_{-H}^{0} \left(\left(\sum_{m=0}^{\infty} \hat{u}_m\ \Psi_m\right)^2 + \left(\sum_{m=0}^{\infty} \hat{v}_m\ \Psi_m\right)^2\right) \mathrm{d}z \tag{3.14c}$$

$$= \frac{1}{2H}\ \int_{-H}^{0} \left(\hat{u}_1^2\ \Psi_1^2 + \hat{u}_2^2\ \Psi_2^2 + ... + \hat{u}_m^2\ \Psi_m^2 + \hat{u}_1\ \hat{u}_2\ \Psi_1\ \Psi_2 + ...\right) \mathrm{d}z + \frac{1}{2H}\ \int_{-H}^{0} \left(\hat{v}_1^2\ \Psi_1^2 + \hat{v}_2^2\ \Psi_2^2 + ... + \hat{v}_m^2\ \Psi_m^2 + \hat{v}_1\ \hat{v}_2\ \Psi_1\ \Psi_2 + ...\right) \mathrm{d}z \tag{3.14d}$$

$$= \frac{1}{2H}\ \left(\hat{u}_1^2\ H + \hat{u}_2^2\ H + ... + \hat{u}_m^2\ H + \hat{u}_1\ \hat{u}_2\ 0 + ...\right) + \frac{1}{2H}\ \left(\hat{v}_1^2\ H + \hat{v}_2^2\ H + ... + \hat{v}_m^2\ H + \hat{v}_1\ \hat{v}_2\ 0 + ...\right) \tag{3.14e}$$

$$= \frac{1}{2H}\ \sum_{m=0}^{\infty} \left(\hat{u}_m^2\right) H + \frac{1}{2H}\ \sum_{m=0}^{\infty} \left(\hat{v}_m^2\right) H \tag{3.14f}$$

$$= \frac{1}{2}\ \sum_{m=0}^{\infty} \left(\hat{u}_m^2 + \hat{v}_m^2\right) \quad . \tag{3.14g}$$

The mixed terms disappear between steps (3.14d) and (3.14e) because of the modal normality and the integrals disappear because of the normalisation introduced in (3.12). Equation (3.14) gives us the vertical integral of the total kinetic energy. To split the kinetic energy between the

vertical modes, i.e. to get the depth-integrated kinetic energy per mode E_m^{kin}, we can simply remove the modal summation in (3.14g):

$$\frac{1}{H}\int_{-H}^{0} E_m^{kin}\,\mathrm{d}z = \frac{1}{2}\left(\hat{u}_m^2+\hat{v}_m^2\right) \quad . \tag{3.15}$$

3.4.4 Shear variance in modes

In addition to the modal kinetic energy the modal shear variance var(S_m) can be calculated. In agreement with (3.14) the shear squared S^2 is integrated over depth and (3.8a) is applied:

$$S^2 = \left(\frac{\partial u}{\partial z}\right)^2+\left(\frac{\partial v}{\partial z}\right)^2 \tag{3.16a}$$

$$= \left(\frac{\partial}{\partial z}\left(\sum_{m=0}^{\infty}\hat{u}_m\,\Psi_m\right)\right)^2+\left(\frac{\partial}{\partial z}\left(\sum_{m=0}^{\infty}\hat{v}_m\,\Psi_m\right)\right)^2 \tag{3.16b}$$

$$\frac{1}{H}\int_{-H}^{0} S^2\,\mathrm{d}z = \frac{1}{H}\int_{-H}^{0}\left(\left(\frac{\partial}{\partial z}\left(\sum_{m=0}^{\infty}\hat{u}_m\,\Psi_m\right)\right)^2+\left(\frac{\partial}{\partial z}\left(\sum_{m=0}^{\infty}\hat{v}_m\,\Psi_m\right)\right)^2\right)\mathrm{d}z \tag{3.16c}$$

$$= \frac{1}{H}\int_{-H}^{0}\left(\left(\sum_{m=0}^{\infty}\hat{u}_m\,\frac{\partial\Psi_m}{\partial z}\right)^2+\left(\sum_{m=0}^{\infty}\hat{v}_m\,\frac{\partial\Psi_m}{\partial z}\right)^2\right)\mathrm{d}z \quad . \tag{3.16d}$$

This gives us the total shear variance. To calculate the shear variance per mode the summation sign cannot simply be taken out (as was done for the energy in Sec. 3.4.3) since the mixed terms do not disappear, i.e. unlike

$$\int_{-H}^{0}\Psi_1\,\Psi_2\,\mathrm{d}z = 0 \quad , \tag{3.17a}$$

$$\int_{-H}^{0}\frac{\partial\Psi_1}{\partial z}\,\frac{\partial\Psi_2}{\partial z}\,\mathrm{d}z \neq 0 \quad . \tag{3.17b}$$

In this case adding all var(S_m):

$$\mathrm{var}(S_m) = \frac{1}{H}\int_{-H}^{0}\left(\left(\frac{\partial u_m}{\partial z}\right)^2+\left(\frac{\partial v_m}{\partial z}\right)^2\right)\mathrm{d}z \tag{3.18a}$$

$$= \frac{1}{H}\left(\hat{u}_m^2+\hat{v}_m^2\right)\int_{-H}^{0}\left(\frac{\partial\Psi_m}{\partial z}\right)^2\mathrm{d}z \quad . \tag{3.18b}$$

will not give the total S^2, but will still give an indication of the shear variance in one mode, so that comparison of modes is possible through this reference value.

4 Stratification and stability

4.1 The seasonal cycle

The average seasonal cycles of temperature T and salinity S are depicted over depth in Fig. 4.1a and 4.1b respectively. Both are based on the 41-year (1970–2010) HELCOM time series at station BMPK02, see Sec. 2.4 and Fig. 2.4. The temperature signal shows a strong seasonal response, especially in the surface layer where T ranges over 15.4°C, from 2.5°C at the end of winter (March) to 17.9°C in August. The thermocline starts forming in April/May, is 25 m deep in July and is broken down in autumn (October/November). At greater depths the temperature is more constant over the seasons, e.g. at 90 m depth the T-range is 2°C. Typical for deep stratified waters (*Simpson and Bowers*, 1984) is the shift of the seasonal cycle in comparison to the surface with minimum temperatures in May and maxima in December when the deeper water is heated by the surface water mixed down during autumn storms. In contrast, the salinity varies little over the year, but is strongly depth-dependent and ranges from 7.5 g kg^{-1} at the surface to 17 g kg^{-1} at the bottom with a halocline at 55–70 m.

In order to compare the two measurement years 2008 and 2010 to these mean values the monthly mean temperatures have been plotted on top of the climatological mean for a depth near the surface (10 m, Fig. 4.1c) and at the halocline, which is represented by T at the 14 g kg^{-1} isohaline (Fig. 4.1e). As is also apparent in Fig. 4.1a the temperature shows the largest seasonal difference in the surface layer. For the first 7 months of the year the years 2008 and 2010 lay on opposite sides of the mean, both at a distance of ~ 1 standard deviation (std) which corresponds to a temperature difference of ~ 3.3°C. Then for 3 months in late summer temperatures are nearly the same as the mean before separating again with 2008 being warmer than the mean in November and December, and 2010 being colder. At the halocline 2008 follows, by and large, the average seasonal cycle, though at the upper std. The year 2010, on the other hand, shows a nearly opposite sinusoidal temperature curve. In 2010 the halocline is warm between February and April (i.e. the temperature is higher than 1 std above the mean) and cold in September and October ($T <$ mean $-$ std). For a depth close to the sea bed the picture is very similar.

Comparing the 2008 and 2010 salinity signals at 10 and 80 m depth with the climatological mean, see Figs. 4.1d,f respectively, shows they are close to the mean. At 10 m in 2008 the values jump around the mean which varies only slightly over the year with a pattern opposite to the surface temperature (min. $S = 7.36$ g kg^{-1} in July, max. $S = 7.75$ g kg^{-1} in January). In

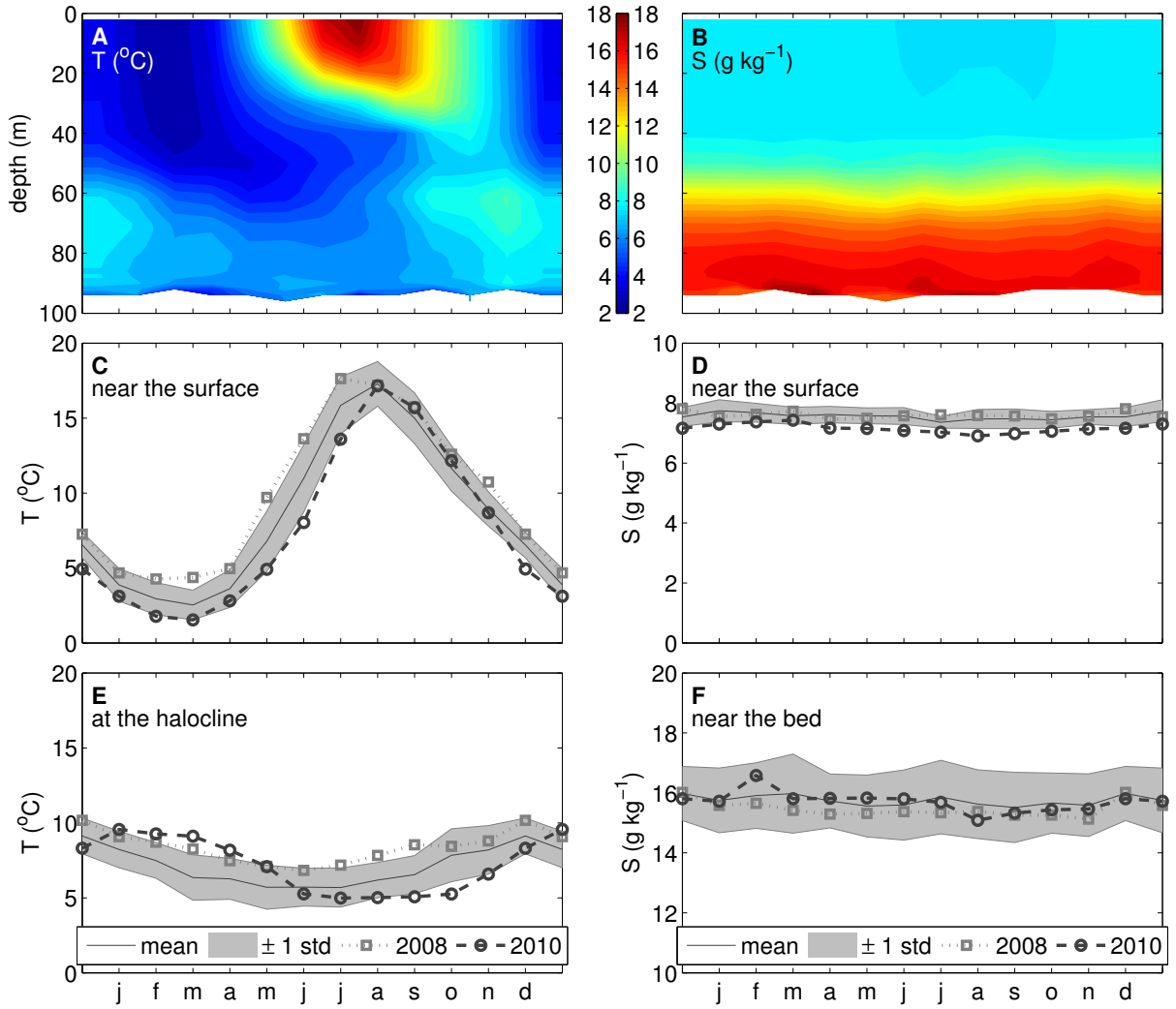

Figure 4.1: Top row: 41-year mean seasonal cycle of (a) temperature and (b) salinity at station BMPK02. Left column: mean T at (c) 10 m depth and (e) at the halocline ($S = 14$ g kg^{-1}). Right column: mean S at (d) 10 m and (f) 80 m depth, note the different scale for (d) and (f). To better show the turn of the year the months January and December have been copied to the very end and the very beginning of the curve, respectively.

2010 surface salinities are low, lower than 1 std below the mean, with a minimum of 6.9 g kg^{-1} in August. At 80 m depth the salinity is twice as high with a std twice as large. Both in 2008 and 2010 salinities are close to the climatological mean value, which shows no seasonal pattern.

At the time of the measurements the surface water had average temperatures in September 2008 and was at the lower std for March 2010. The halocline water was warm in both years, with 2.0°C and 2.8°C above the long-term mean and 0.7°C and 1.2°C above the upper std, respectively. In late 2008 the surface salinity was low at 1.5 std from the mean, but the other salinities (surface 2010 and near bed 2008, 2010) were close to the mean value. All monthly values for 2008 and 2010 fall within 2 std, or within the 95% confidence interval, of the climatological mean.

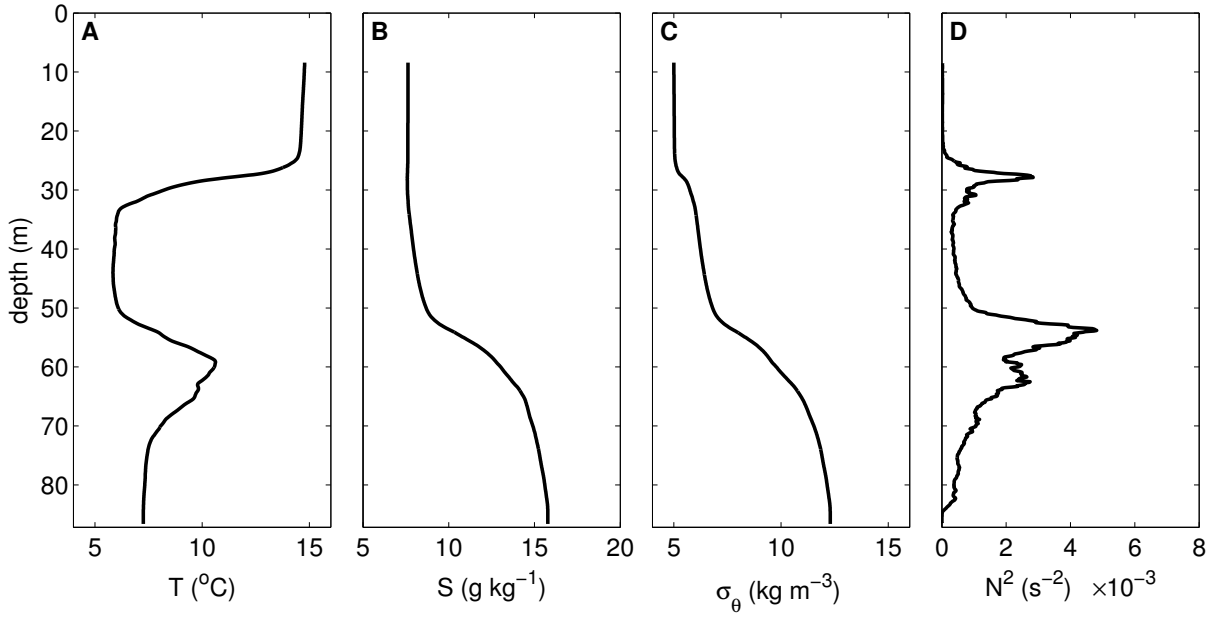

Figure 4.2: Summer microstructure profiles at S1 of (a) temperature T, (b) salinity S, (c) potential density σ_θ and (d) buoyancy frequency squared N^2. Profiles are averaged over all 400 casts.

4.2 The summer three-layer system

4.2.1 Temperature and salinity

Stratification parameters for late summer 2008 are summarised in Fig. 4.2, which is based on the average of 400 microstructure profiles, measured during 7 transects on days 262.3–264.2 within a radius of 2 km around station S1. These data reveal a three-layer structure with two pronounced interfaces that are typical for the Baltic Sea during late summer conditions: a sharp thermocline centered slightly above 30 m depth (Fig. 4.2a) and a thicker halocline between 50 and 65 m (Fig. 4.2b). The two interfaces isolate an intermediate layer of approximately 15 m thickness with cold, fresh water that is a remnant of the previous winter cooling (Fig. 4.2a). The region of enhanced temperatures inside and just below the halocline (Fig. 4.2a) is a manifestation of interleaving of warm and salty water that has flowed in from the North Sea. Above 23 m the surface mixed layer (SML) is, as the name says, well-mixed. Near the bed the bottom 2 m are well-mixed and form the bottom boundary layer (BBL).

Fig. 4.3 shows the temperature and salinity profiles averaged over the 7 mini-transects. Over time, from blue to red, the profiles did not change much; hardly at all in shape and only little in depth. Over time the halocline sank 2.5–3 m, whereas the thermocline seems to have dropped by 3.5 m on the last transect. For a highly resolved time series of T see Fig. 5.4 in Chap. 5. To compare these temperature/salinity combinations with the 41-year time series a TS-diagram has been plotted in Fig. 4.3c. The light dots represent TS-pairs

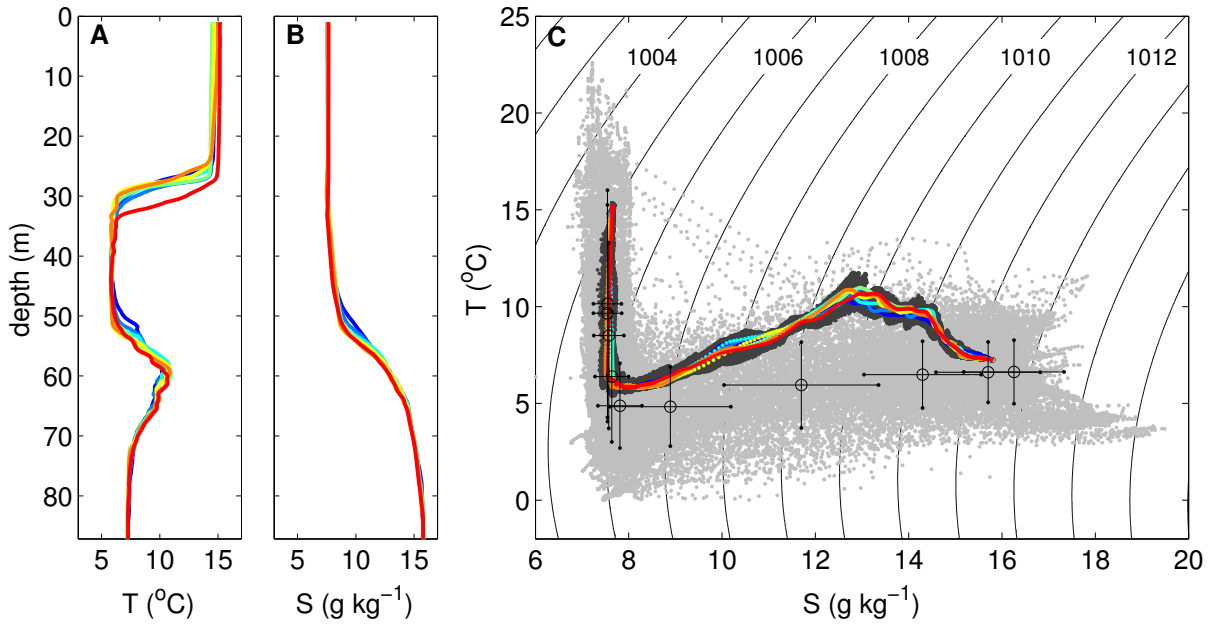

Figure 4.3: Summer microstructure profiles at S1 of (a) temperature T and (b) salinity S over time (transect 1–7, blue–red). (c) TS-diagram with 41-year BMPK02 data (light grey), POS373 MSS data (dark grey) and mean transect profiles (colour). Black open circles show mean values at 2 m and 10–90 m in steps of 10 m and crosses standard deviations of T and S at these levels. Contour lines in the background are of equal density.

measured at BMPK02 and, overlain as dark dots, are all values from all profiles at S1 for summer 2008. The large crosses are mean values, and their standard deviations, of T and S at the standard depth horizons spaced 10 m apart from 10 to 90 m and at 2 m depth. In the surface mixed layer, top left (low S, high T), the TS-pairs fall within 1 std from the 41-year mean, although, for e.g. 10 m, at the very limit of upper T-std. At 40 m depth, within the cold intermediate layer, and at 80 m, near the sea bed, the TS-pairs are clustered within the 1-std envelop, whereas at 50 and 70 m depth the temperature is above the upper T-std. The warm, salty inflowing water is most pronounced at 60 m where both the temperature and the salinity std-limits are exceeded.

4.2.2 Potential density, its anomaly and the buoyancy frequency

Dynamically relevant for the internal wave field are variations in potential density σ_θ, caused by the observed distribution of temperature and salinity. The potential density is the density a water parcel, with *in situ* density ρ, would have if moved adiabatically to a reference level, thereby removing compressional effects. Here the reference level is the sea surface and, for the shallow Baltic Sea, these effects are very small so that, when also subtracting 1000 by looking at the density anomaly, here $\sigma_\theta \approx \rho - 1000$. Fig. 4.2c illustrates that both the thermocline and the halocline are mirrored in two density interfaces, of which the lower is more pronounced.

Although the temperature stratification (Fig. 4.2a) is unstable in the halocline, the overall mean density stratification is stable, as σ_θ is constant over, or increases with, depth everywhere.

Overall the strength of the stratification can be calculated from the potential energy anomaly (PEA), a quantity first coined by *Simpson* (1981), although it had already been used, namelessly, in earlier work (e.g. *Simpson et al.*, 1978). PEA represents the work needed (per volume) to fully mix the water column and is defined as:

$$\mathrm{PEA} = \frac{1}{H}\int_{-H}^{0} (\hat{\sigma_\theta} - \sigma_\theta)\, gz \, \mathrm{d}z \tag{4.1}$$

where H is the water depth, z the vertical coordinate upwards from the sea surface and $\hat{\sigma_\theta}$ is the depth-averaged potential density. For the averaged σ_θ-profile of Fig. 4.2c PEA $=$ 635 J m^{-3}, considering the 87 m depth this gives 7.3 J m^{-3} m^{-1}. Calculating PEA for all 400 microstructure profiles gives a minimum of 546 J m^{-3}, a maximum of 658 J m^{-3} and a std of 14 J m^{-3}. These values are high compared to e.g. 55 J m^{-3} for the 100 m deep (0.55 J m^{-3} m^{-1}) western Irish Sea in mid-June (*Xing and Davies*, 2001), up to 20 J m^{-3} for the 20 m deep (1.0 J m^{-3} m^{-1}) Llyn Tegid in summer (*Simpson et al.*, 2011), or up to 60 J m^{-3} for a 13 m deep (4.6 J m^{-3} m^{-1}) modelled idealised estuary (*Burchard and Hofmeister*, 2008), and therefore show that the central Bornholm Basin is strongly stratified in summer.

The square of the buoyancy frequency,

$$N^2 = -\frac{g}{\rho_0}\,\frac{\partial \sigma_\theta}{\partial z} \quad , \tag{4.2}$$

where g is the acceleration of gravity and ρ_0 a constant reference density, quantifies the stratification in a depth-dependent way. This quantity is also known as the intrinsic, stability or Brunt-Väisälä frequency after the two meteorologists David Brunt and Vilho Väisälä (*Brunt*, 1927; *Väisälä*, 1926). It reaches values up to $N^2 = 5\times10^{-3}$ s^{-2} at 54 m (Fig. 4.2d), which sets a threshold of approximately 90 s for high-frequency internal wave motions (see Sec. 1.2.2). Note the presence of weak stratification ($N^2 > 0$) inside the layers between the two pycnoclines, and below the halocline. This buoyancy frequency can be divided into contributions made by temperature and by salinity,

$$N^2 = N_T^2 + N_S^2 = g\alpha\,\frac{\partial T}{\partial z} - g\beta\,\frac{\partial S}{\partial z} \quad , \tag{4.3}$$

where α is the thermal expansion and β the saline contraction coefficient. How N_T^2 and N_S^2 contribute to the total N^2 is shown in Fig. 4.4a. As expected N_T^2 is solely responsible for the peak in N^2 at 28 m, but plays a relatively minor role in the deeper water column as N_T^2 accounts for maximally 40% (at 68 m), but generally less than 20%, below 30 m.

4.2.3 Density ratios and Turner angles

The ratio of N_T^2 and N_S^2 (Fig. 4.4a) conveys some information about the stability of the water column. The nature of possible instabilities depends on which of the two is unstable and on how much the other compensates. The density ratio R_ρ can be calculated from the vertical derivatives of a temperature profile ($\partial_z T = \partial T/\partial z$) and a salinity profile ($\partial_z S$) in the following way (*Turner*, 1965):

$$R_\rho = \frac{\beta \partial_z S}{\alpha \partial_z T} = \frac{N_S^2}{N_T^2} \tag{4.4}$$

although now the inverse definition is generally used (e.g. *Ruddick*, 1983; *Zhurbas and Paka*, 1997, 1999; *Merryfield*, 2005; *Wieczorek et al.*, 2008).

In his paper from 1983 Barry Ruddick proposed defining an angle that, in principle, contains the same information as R_ρ, but is independent of the sign used for z or α and enables a simple subdivision of stratification/stability regimes. He named it the Turner angle Tu after the inventor of R_ρ and defined it as:

$$Tu = \tan^{-1}\left(\frac{\alpha \partial_z T - \beta \partial_z S}{\alpha \partial_z T + \beta \partial_z S}\right) = \tan^{-1}\left(\frac{N_T^2 - N_S^2}{N_T^2 + N_S^2}\right) \quad . \tag{4.5}$$

His definition can also be used inversely as e.g. in *Wieczorek et al.* (2008). The stratification regimes are then as follows:

(i)	$-135^\circ < Tu < -90^\circ$		gravitationally unstable
(ii)	$-90^\circ < Tu < -45^\circ$	$0 < R_\rho < 1$	diffusive convection
(iii)	$-45^\circ < Tu < +45^\circ$	$-\infty < R_\rho < 0$	stable
(iv)	$+45^\circ < Tu < +90^\circ$	$1 < R_\rho < \infty$	salt fingering
(v)	$+90^\circ < Tu < +225^\circ$		gravitationally unstable

These regimes form slices of the pie formed by the circle with N_T^2 on the y-axis and N_S^2 on the x-axis. Here isolines of R_ρ are lines radiating from the origin with a constant Turner angle (*Ruddick*, 1983). Although *Kuzmina et al.* (2005) showed that for intrusions in the Baltic Sea the stable regime is a bit wider ($-48.5^\circ < Tu < +45^\circ$, i.e. $R_\rho > 1/15$ see *Huppert* (1971)) than in the original definition, not the whole depth profile has a stable Tu, see Fig. 4.4b. A large part of the profile is close to, but on the stable side of, the diffusive convection boundary of -45°, as was also found by *Zhurbas and Paka* (1999) in the Gotland Basin. However, parts of the mean Tu profile fall within the salt fingering (0–30 m) or diffusive convective (50–60 m) regimes. Since the focus in Chaps. 5 & 6 is on interior and near-bed mixing, instabilities in the surface mixed layer will be ignored. At the top of the halocline, the depth where the warm, salty inflow interleaved, double diffusive effects could be important. Here the minimal Tu value of -59.8° is at 58 m, the depth of maximal halocline temperature, see Fig. 4.2a. *Kuzmina et al.*

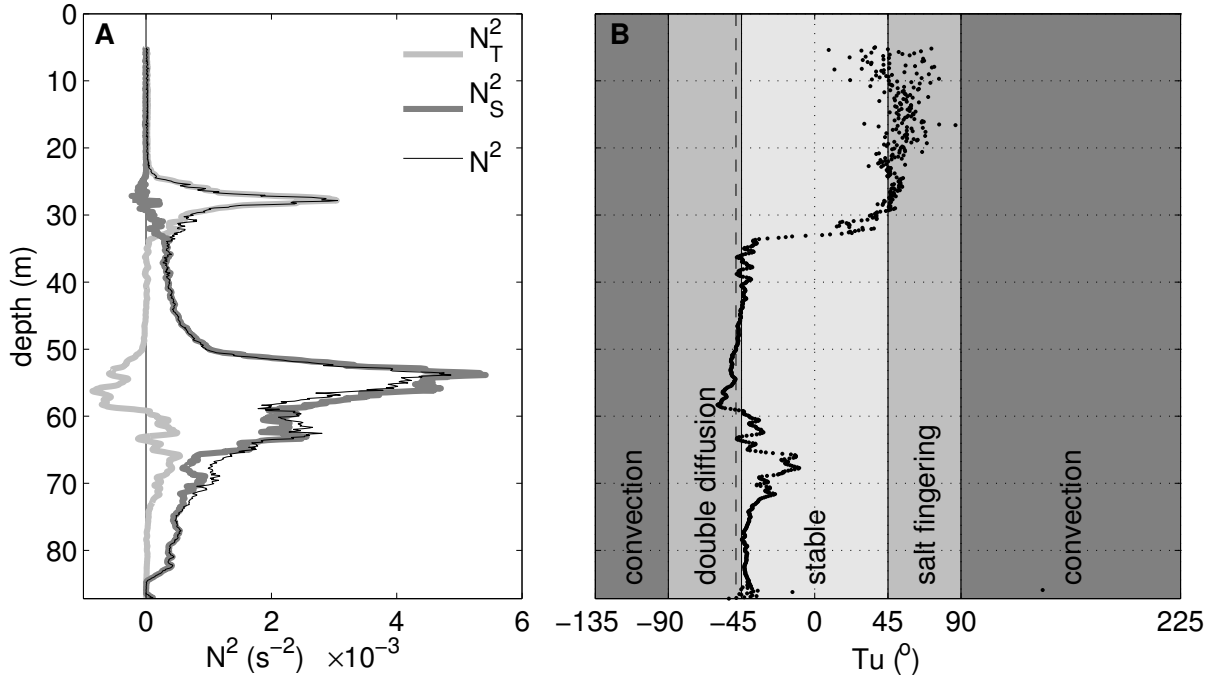

Figure 4.4: Summer microstructure profiles at S1 of (a) temperature stratification N_T^2 (thick, light grey), salinity stratification N_S^2 (thick, dark grey) and density stratification N^2 (thin, black, cf. Fig. 4.2) and (b) Turner angle Tu. Stability regimes are indicted by grey-shading and the *Kuzmina et al.* (2005) extention of the stable regime by a dashed line.

(2005) argue that the dynamics of thick tongue-shaped intrusions "*differs fundamentally from double-diffusive interleaving*". Also, as later Chapters will show, shear ($S = \partial u/\partial z$, where u is the current velocity) plays a large role at these depth. Although *Mueller et al.* (2007) say that shear and convective mixing are equally important in interleaving dynamics, *Smyth and Kimura* (2007) state that "*double diffusive stratification has little effect on shear instability except when the density ratio R_ρ is close to unity*" where $R_\rho = 1$ gives $Tu = -90°$, the border to the gravitationally unstable regime. In late stages of turbulence, when shear-driven turbulence is damped, double diffusion can take over, changing the sign of the buoyancy flux (*Smyth and Kimura*, 2010), which does not happen here (see Fig. 5.3). Hence the possibility of diffusive convection is to be held in mind, but since it might not play such a big role the focus will be on mixing by other phenomenon.

4.2.4 Length scales of turbulence

The sizes of instabilities, eddies and turbulence can be estimated using a variety of length scales. For example the Thorpe scale is a length scale that describes the vertical size of patches that are unstably stratified. It was first introduced in 1977 by the person whose name it now bears: Stephen Thorpe. In his method a vertical profile of potential density σ_θ is rearranged

adiabatically so that instabilities are ironed out and the density increases monotonically with depth (*Dillon*, 1982). The difference in depth of a certain σ_θ value between the original and sorted profiles is the Thorpe displacement d_T. The Thorpe scale is then the root mean square (rms) of these displacements,

$$L_T = \sqrt{\langle d_T^2 \rangle} \quad . \tag{4.6}$$

Fig. 4.5a shows d_T calculated from the average σ_θ profile shown in Fig. 4.2c. Within the surface mixed layer d_T is largest, quickly becoming positive away from the sea surface, with a maximum of 0.90 m at 2 m, changing to negative d_T at $\sim$ 10 m and to zero at 27.5 m. Beneath the thermocline d_T is very small, only reaching -0.02 m at the halocline, until the start of the bottom boundary layer where maximum Thorpe displacements are -0.13 m. It reinforces the view that strong stirring is happening in the SML and that there is stirring within the bottom 6 m. Most of the water column is stably stratified with only small d_Ts which is reflected in the overall Thorpe scale: $L_T = 1.6$ mm.

The influence of both buoyancy, $b = -g\left(\left(\sigma_\theta - \rho_0\right)/\rho_0\right)$, and shear S on eddies is proportional to the size of the eddy, such that when eddies get very small the effects of b and S become vanishingly small. The smallest scale that is still influenced by buoyancy, i.e. by stratification, is given by the Ozmidov scale L_O whereas the smallest scale where shear still plays a role is defined by the Corrsin scale L_C (*Smyth and Moum*, 2000a; *Simpson et al.*, 2011):

$$L_O = \sqrt{\frac{\varepsilon}{N^3}} \tag{4.7a}$$

$$L_C = \sqrt{\frac{\varepsilon}{S^3}} \tag{4.7b}$$

where ε is the dissipation rate of turbulent kinetic energy, a parameter which will be discussed at length in Chaps. 5 & 6 and App. B. Stratification and shear have opposite effects at scales larger than L_O and L_C, respectively. Buoyancy works to damp turbulence while shear provides a source of kinetic energy and thus increases turbulence and ε (*Smyth and Moum*, 2000a). A dimensionless number that compares the strength of these effects is the (gradient) Richardson number, $Ri = N^2/S^2$, which is said to have a critical level at $1/4$ (*Kundu and Cohen*, 2008). Below this value turbulence is said to be self-sustained, whereas above it turbulence decays (*Turner*, 1979). L_O (Figs. 4.5b,c) becomes unrealistically large in the unstratified SML (max. $L_O = 88.2$ m) and BBL (max. $L_O = 1.3$ m), but is much smaller in the stratified interior; between 30 and 80 m its maximum is 17 mm and its minimum is 3.4 mm, still just over twice as large as the depth-averaged L_T. This is consistent with (*Dillon*, 1982) who found that $L_O >> L_T$ in the wind-mixed surface layer, but of the same order of magnitude far from the surface. *Smyth and Moum* (2000a) found that $L_O << L_T$ in active turbulence, showing that

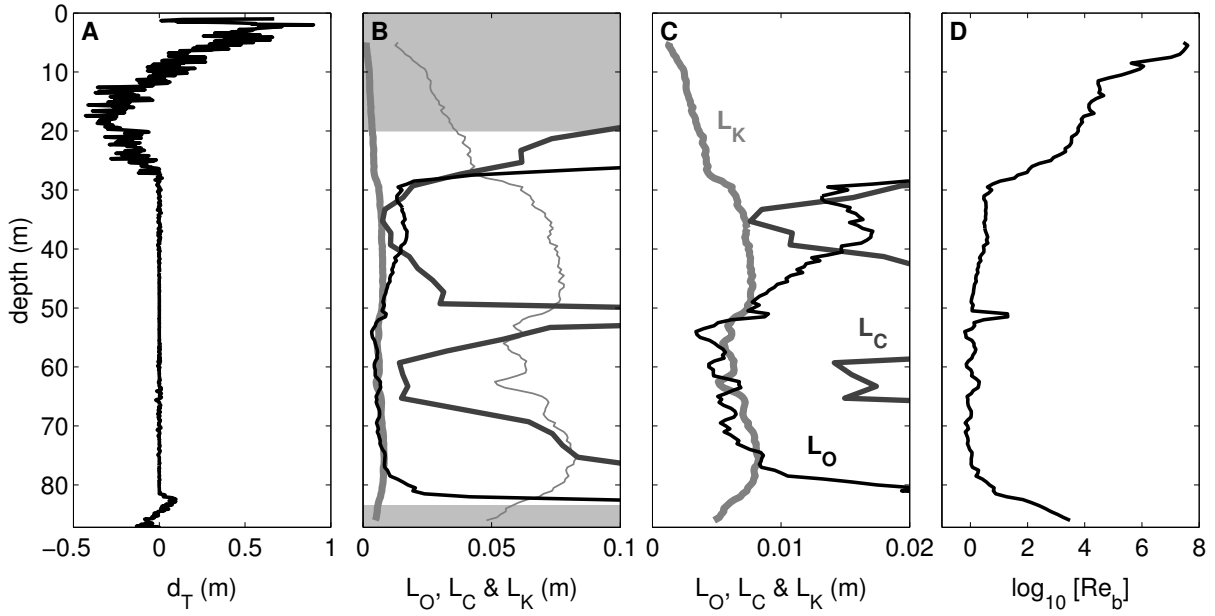

Figure 4.5: Summer profiles at S1 of (a) Thorpe displacements, (b) Ozmidov (thin, black), Corrsin (thicker, dark grey) and Kolmogorov (thick, light grey) scales, (c) zoom in on small L_O, L_C and L_K and (d) buoyancy Reynolds number. The thin light grey line in (b) shows $10L_K$ while the grey-shaded area corresponds to regions where $L_O < 0.4d$ (see text).

here turbulence has already decayed or that using profiles averaged over 400 profiles smears out too much of the turbulent activity, although profiles have been averaged in non-overlapping blocks of 5 first to preserve the signal of turbulent activity. The Corrsin scale has its minimum in the stratified region as well (7.6 mm at 35 m), but also has a large maximum at the top of the halocline; 263 mm at 51 m.

In papers from 1941 (translated into English as: *Kolmogorov*, 1991a,b) the Kolmogorov scale (L_K) was introduced as the scale of the smallest eddies at the end of the energy cascade. Turbulent motions are produced at the "large" scales and their energy is handed on to smaller and smaller scales through inviscid processes (*Pope*, 2000). At the Kolmogorov scale the kinetic energy of the smallest eddies is dissipated into heat, it therefore depends on the kinematic viscosity ν ($\nu \equiv \mu/\rho$ where μ is the dynamic viscosity) that smears out velocity gradients and the dissipation rate ε (*Kundu and Cohen*, 2008):

$$L_K = \left(\frac{\nu^3}{\varepsilon}\right)^{1/4} \quad . \tag{4.8}$$

The profile of L_K in Figs. 4.5b,c shows that is generally less than 10 mm. L_K does not vary as strongly as L_O & L_C and is minimal rather than maximal in the well-mixed regions ($L_K < 5$ mm) due to ε being in the denominator rather than the numerator. In the stratified regions $L_K > 7$ mm, with maximum value of 8 mm is at 76 m, except for the strongly stratified

halocline where there is a local minimum ($L_K = 5$ mm at 63 m depth). At $10L_K$, indicated by a thin grey line in Fig. 4.5b, the BIV (buoyant-inertial-viscous) transition indicates the largest size of eddies in the dissipative subrange that still feel the effects of buoyancy (*Smyth and Moum*, 2000a). This is the case in the range where $L_O < 10L_K$, i.e. from 27 to 82 m depth.

Some of these scales can be combined to give additional information. The Richardson number as ratio of stratification and shear forces has already been mentioned. *Smyth and Moum* (2000a) also show how the ratio of the Ozmidov scale to the Thorpe scale can be used as an "*indicator of the age [or activity] of a turbulent event*" if this event is due to a Kelvin-Helmholtz instability in a localised layer of high stratification and shear.

A dimensionless number that combines the Ozmidov and Kolmogorov length scales is the buoyancy Reynolds number Re_b:

$$Re_b = \left(\frac{L_O}{L_K}\right)^{4/3} = \frac{\varepsilon}{\nu N^2} \quad . \tag{4.9}$$

It is a measure for the length scales that are smaller than the ones affected by buoyancy, but larger than the ones affected by viscous dissipation *Smyth and Moum* (2000a), thus giving the separation distance between the small and large scales (*Lueck et al.*, 2002). It has also been suggested as a measure for the activity of turbulence, with a critical value of 20 below which active turbulence is not present.

As will be explained in more detail in Sec. 5.2.3 *Shih et al.* (2005) introduce a parameterisation for the mixing efficiency γ. Some assumptions used for this calculation do not hold in the weakly stratified layers in the immediate vicinity of the upper and lower boundaries. In such cases a cut-off has been introduced balancing the Ozmidov scale and the length scale for wall-bounded shear flows, so that only regions where $L_O > 0.4d$ (d is distance from the nearest, surface or bottom, boundary) are analysed. Regions where $L_O < 0.4d$ have been shaded grey in Fig. 4.5b. This parameterisation for γ is based on the buoyancy Reynolds number Re_b, a profile of which is shown in Fig. 4.5d. Re_b is negatively correlated to stratification and therefore largest in the SML, above 8 m depth Re_b is greater than 1 million, and BBL, at 86 m $Re_b = 3000$. Within the stratified interior however, values are generally smaller than 10, even down to 0.6. At the top of the halocline, at 51.5 m, there is a local maximum of 20, the minimum value for active turbulence (*Smyth and Moum*, 2000b).

Smyth and Moum (2000b) also state that the buoyancy Reynolds number can be used to estimate whether or not the flow is isotropic, which is important for the calculation of the turbulent dissipation rate (see App. B). If $Re_b > \mathcal{O}(10^5)$ the dissipation and inertial ranges can be considered isotropic, although at $\mathcal{O}(10^2)$ and above the assumption is accurate for the calculation of the dissipation rate from geophysical data (*Smyth and Moum*, 2000b). This gives us a depth range of 26–83 m where the assumption of isotropy would not hold. Many

others (e.g. *Holtermann*, 2011; *Fischer*, 2011) have faced the same problem, but, due to lack of an alternative, have still assumed isotropy as was done here as well, see also App. B.

In a completely equivalent way a shear Reynolds number can be defined as the four-thirds power of the ratio of the Corrsin and Kolmogorov scales:

$$Re_s = \left(\frac{L_C}{L_K}\right)^{4/3} = \frac{\varepsilon}{\nu S^2} \quad . \tag{4.10}$$

defining the length scales that are not affected by shear nor by viscous dissipation. The ratio of Re_s to Re_b is equal to N^2/S^2, i.e. the gradient Richardson number.

4.2.5 Vertical profiles of normal modes

To investigate the vertical structure of internal-wave modes supported by the stratification shown in Fig. 4.2d, the Sturm-Liouville was solved for the first 5 vertical normal modes (Ψ_{1-5}), see Sec. 3.4 for the computational details. c_m is the "mode speed", which is different from the phase speed if rotation plays a role (*Kundu et al.*, 1983), corresponding to mode m with

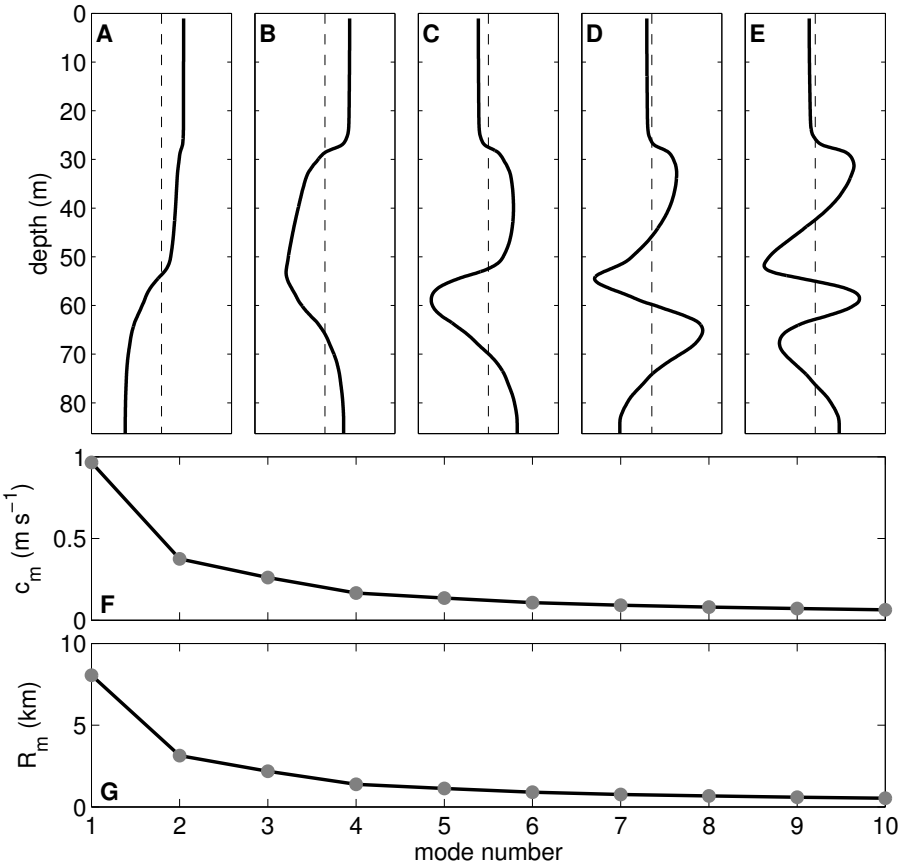

Figure 4.6: Vertical structure of the first 5 normal modes (a–e) at S1 calculated using (3.9) from the N^2 profile in Fig. 4.2d. Modal speeds (f) and Rossby radii (g).

the vertical structure for u, v and p given by $\Psi_m(z)$.

Fig. 4.6a illustrates that the fundamental first mode has a zero-crossing at the top of the halocline at 54 m and therefore represents halocline interface waves. With a zero-crossing at the bottom of the halocline and an additional crossing at 28 m the vertical structure of the second mode suggests a dynamic coupling of interfacial waves in the thermocline and halocline (Fig. 4.6b). Higher modes (Figs. 4.6c–e) are seen to contribute to the total shear also *inside* the weakly stratified layers, except for the surface and bottom-boundary layers, which are well-mixed and do not support baroclinic shear. It should be kept in mind that the assumption of a flat bottom involved in the derivation of (3.9) is usually satisfied only in an approximate sense when comparing internal-wave modes with observations in real oceanic basins.

The mode speeds c_m in Fig. 4.6f give the maximum speeds at which energy in the wave front moves (*Kundu et al.*, 1983), whereas Fig. 4.6g shows, through the Rossby radii $R_m = c_m/f_i$, the width of the border along the coast that feels the effects of coastal waves. See Sec. 5.1.1 for a discussion.

4.3 The winter two-layer system

4.3.1 Stratification structure and the effect of a storm

In autumn the decreasing air temperature and increasing wind speeds cause the thermocline to be eroded. By about November nothing is left of the summer structure, see Fig. 4.1. The second cruise was timed at the end of winter (February/March 2010) so that near-surface stratification would be at a minimum and indeed the vertical structure (Fig. 4.8) is typical for this time of year. As noted in Sec. 2.1 a storm interrupted our measurements at station S1.

Winterstorm Xynthia was born on 26 February 2010 south of the Azores (*Deutscher Wetterdienst*, 2010), from where it moved northeastward to nip the northwestern corner of the Iberian Peninsula. Due to interaction with a strong southern-European jet wind, velocities were strongly intensified over the Bay of Biscay (*Liberato et al.*, 2011) and reached hurricane-force (12 Bf, $>$118 km h^{-1}) before a renewed landfall on the French coast (*Grumm*, 2010). Passing Brittany and Paris Xynthia continued to move northeastward along the Belgian and Dutch coasts before crossing Denmark and reaching the Baltic Sea by 1 March 2010, day 59 (*Grumm*, 2010). Its eye passed north of the Bornholm Basin over the southern coast of Sweden (*Deutscher Wetterdienst*, 2010). As the storm reached the Bornholm Basin its velocity had decreased substantially to only 8 Bf (maximum measured wind velocity onboard: 20 m s^{-1} = 73 km h^{-1}, see Fig. 4.7). The storm caused widespread damage in western Europe, including floods and power outages, most severely in France where the extreme winds and a spring high tide combined with a storm surge to breach the sea wall near L'Aiguillon-sur-Mer

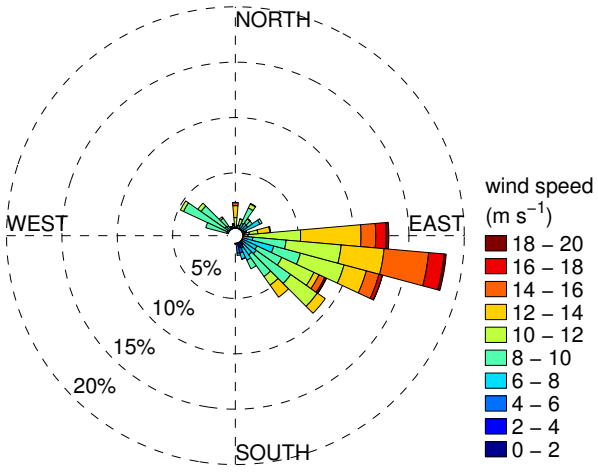

Figure 4.7: Wind rose indicating the wind speed, wind direction and their relative frequency over the winter cruise period.

(*Grumm*, 2010). The 62 fatalities caused *Knox et al.* (2011) to list winterstorm Xynthia as the 5th deadliest in Europe during the last 60 years in their table on "notable non-convective high wind events".

Winterstorm Xynthia also had a strong effect on the stratification, hence our microstructure measurements have been divided into four periods. Period `I` are our 6 transects before the storm, while, for easy comparison, period `II` covers the first 6 transects after the storm. Period `III` then consists of the remaining 19 transect before we left S1 for transect T1. The 8 transects we sailed at the end of the cruise form period `IV`, see also Sec. 2.1 & Fig. 2.2.

Focussing on the "starting position", the thick light grey lines of period `I` in Fig. 4.8, it can be seen that the thermocline has been nearly completely eroded (Fig. 4.8a). A bit of stratification persist so that, with a N^2-threshold of 5×10^{-5} s^{-2}, the bottom of the SML is at 17 m depth. Below the SML the 10–15 m thick halocline (Fig. 4.8b), which survives throughout the year, gradually merges into the stratified water column underneath. Near the bed the BBL reaches up to 84 m. As in summer, the thermal stratification in, and now also below, the halocline is dominated by a pool of warm summer-water which contains inversions and is clearly unstable. The density in Fig. 4.8c is, however, mainly determined by the salinity which has a monotonically increasing profile. Not shown are the profiles of N_T^2 and N_S^2 which show that temperature's portion of N^2 (Fig. 4.8d) is less than 20% and often less than 10%. The only exception is a sharp maximum of 32% between 58 and 60 m. The Turner angles also indicate almost all of the water column is stable, although in and below the halocline some Tu-values lie in the double diffusive regime. As said above double-diffusive effects are unlikely to have a significant effect on mixing. This is corroborated by the clear correlation between shear and dissipation rates discussed in Chap. 5. Within the surface layer gravitational convection might occur.

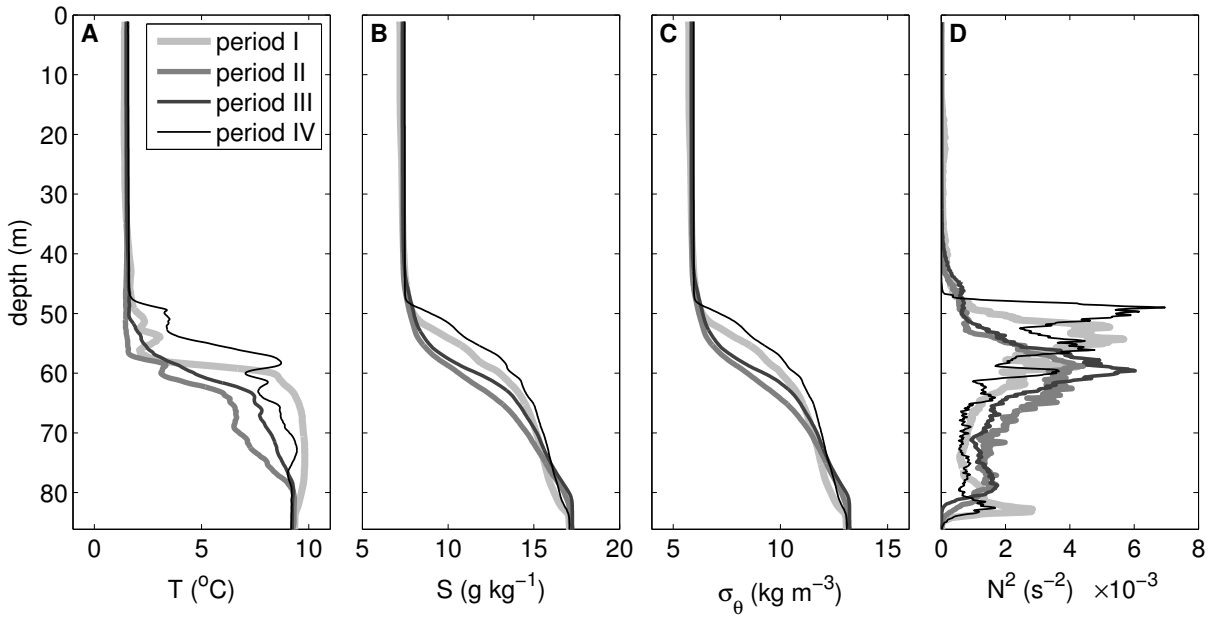

Figure 4.8: Winter microstructure profiles at S1 of (a) temperature T, (b) salinity S, (c) potential density σ_θ and (d) buoyancy frequency squared N^2 for the four microstructure periods (see text).

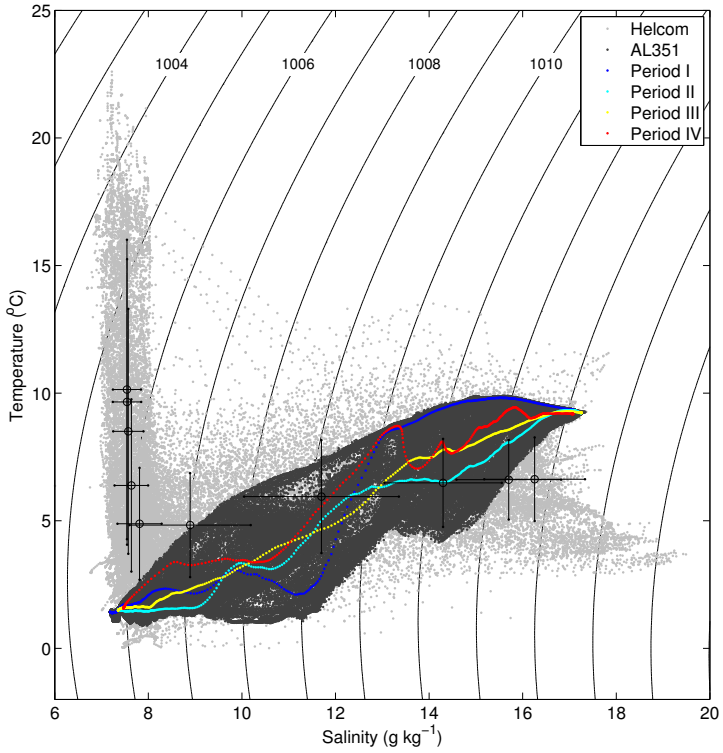

Figure 4.9: Winter *TS*-diagram with 41-year BMPK02 data (light grey), AL351 MSS data (dark grey) and mean period profiles (colour). Black open circles show mean values at 2 m and 10–90 m in steps of 10 m and crosses standard deviations of T and S at these levels. Contour lines in the background are of equal density.

Comparing period I to the situation after the storm, the thinner and darker lines, suggests that increased mixing during the windy period has resulted in a significant modification of the vertical structure of the water column. The water column down to $\sim$ 45 m is homogenised in terms of T (1.5°C) and S (7.5 g kg^{-1}) so that the depth of the well-mixed surface layer has increased by more than 20 m and extends down to 41, 37 and 46 m respectively for periods II–IV. At the same time the halocline, and therefore peaks in σ_θ and N^2, descended by more than 5 m from period I to II and approximately doubled its width. The latter points at the influence of internal wave mixing inside the halocline. Note that these estimates are based on averages over more than 10 hours, such that random displacements due to internal waves are likely to be removed by the averaging. During period III the halocline is already on the rebound. The BBL, in addition to the SML, also grows after the storm from 2.2 m in period I and 2.4 m in period II to 4.5 m in period III.

Compared to summer the band of dark dots in Fig. 4.9 is wide and high, showing the high variability of T on isolines of S and vice versa. The waters of the SML can now be found in the bottom left-hand corner, near the 41-year temperature and salinity minima. Also the BBL forms one small cluster outside the 1-std range of T for this depth. The halocline region occupies most of the graph, e.g. along the 1009-isopycnal the temperature varies by 6°C and salinity by 0.3 g kg^{-1}.

Due to the halocline and the stratified waters underneath the potential energy anomaly has only gone down to 561 J m^{-3} (6.5 J m^{-3} m^{-1}) giving a winter stratification strength that is 88% of that in summer. Due to the storm and its effects on the halocline the PEA ranges has widened to 413–621 J m^{-3} and the std has gone up to 31 J m^{-3}. During period I the average PEA is 557 J m^{-3}, while just 36 hours later winterstorm Xynthia has weakened it to 529 J m^{-3} (period II). From transect 6 to 7 the PEA even weakens by 57 J m^{-3}. After the storm the stratification increases linearly during period III from 532–601 J m^{-3} and is stable around 586 J m^{-3}, higher than before the storm, during period IV, 6 days after the storm.

4.3.2 Length scales of turbulence

The general structure of the Thorpe displacement profile before the storm (Fig. 4.10a) is very similar to the summer one (Fig. 4.5a); a shallow positive peak (80 cm at 4 m) and a broader region with mainly negative displacements below. Between 25 and 84 m $|d_T| < 3$ cm and in the BBL it peaks at 9 cm. Overall the Thorpe scale is almost 4 times larger than in summer at 6.1 mm, indicating that more, and larger, patches of unstable stratification are observed. Directly after the storm (Fig. 4.10e) large displacements, $|d_T| > 5$ cm and up to 52 cm, are found down to 44 m. Below this depth $|d_T| < 3$ cm, including in the BBL, but not in a patch below the halocline at 70–75 m. The overall Thorpe scale has gone down a little to 5.7 mm.

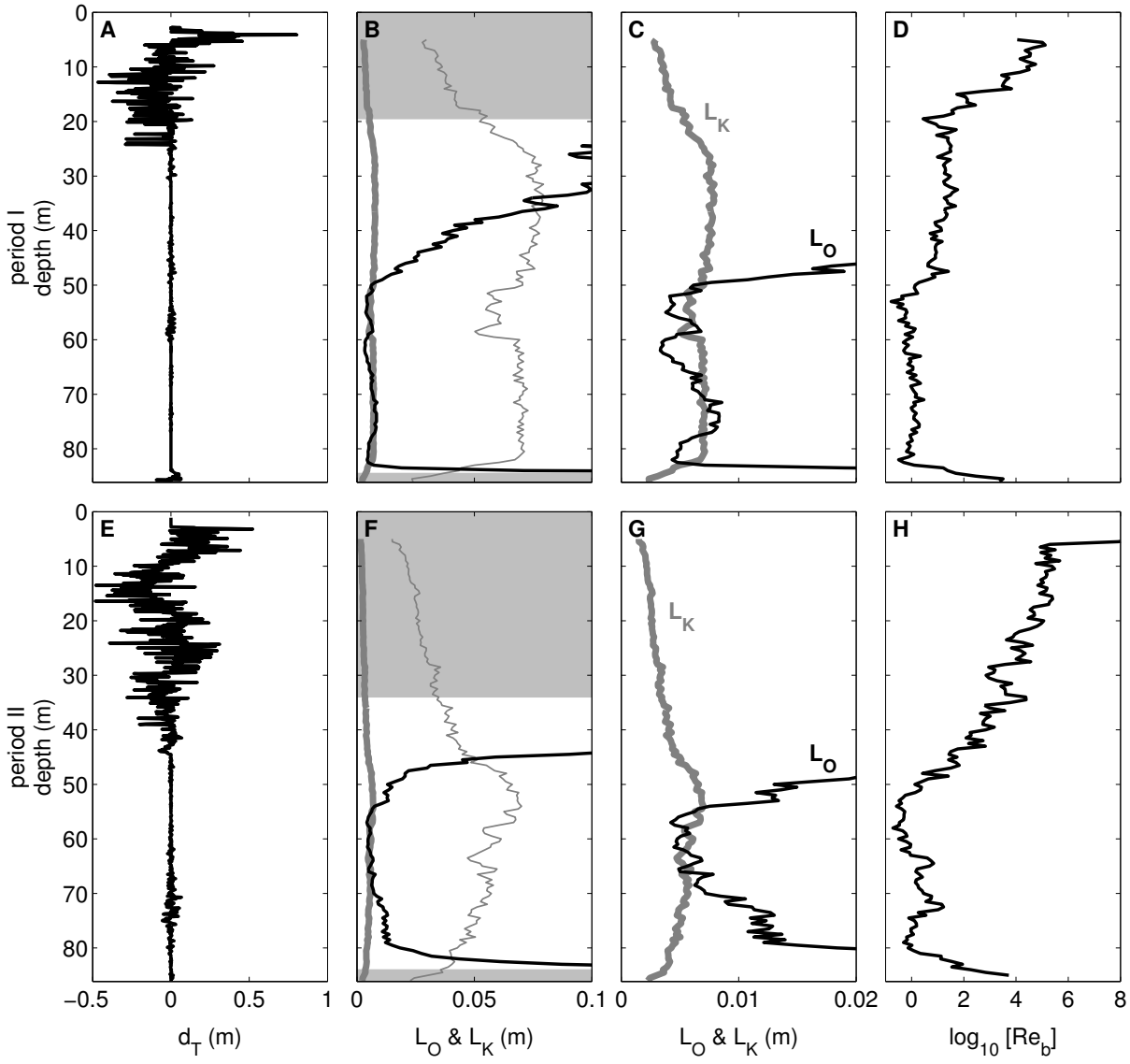

Figure 4.10: Winter microstructure profiles at S1 of (a,e) Thorpe displacements, (b,f) Ozmidov (thin, black), and Kolmogorov (thick, grey) scales, (c,g) zoom in on small Ozmidov and Kolmogorov scales and (d,h) buoyancy Reynolds number. The thin light grey line in (b,f) shows $10L_K$ while the grey-shaded area corresponds to regions where $L_O < 0.4d$ (see text). Profiles are averaged over all casts of a period; top row (a–d) period I, bottom row (e–h) period II.

During period III L_T increases a little again to 6.5 mm, but is more than twice as large (14.67 mm) over period IV (not shown). This jump in L_T is possibly linked to the increased occurrence of Tu-values around 135°, indicating gravitational convection, in the SML of period IV. Here d_T ranges from 136 cm at 3 m to -81 cm at 34 m. Displacements are also enhanced, up to 10 cm, in the halocline, leaving only the depth ranges 48–60 and 74 m to the sea bed where $|d_T| < 3$ cm.

The Ozmidov and Kolmogorov scales (Figs 4.10b,c,f,g) have not changed much in the deep layers compared to summer. Closer to the surface the deepening of the SML is apparent

in the larger values for L_O, and smaller values for L_K, in the depth range 25–50 m, especially after the storm in period II. The depth region that has to be ignored for the calculation of γ (see Sec. 4.2.4) increased from the surface 20 m to 34 m from period I to II. In the BBL the region where $L_O < 0.4d$ has a constant height of 2 m. The depth range where dissipating eddies are influenced by buoyancy, i.e. where $L_O < 10L_K$, shrank from 35–84 m to 45–82 m due to the decrease in stratification.

The story is also similar for the buoyancy Reynold number Re_b, which is large ($> 10^2$) in the surface and bottom mixed layers and minimal in the halocline. During period I (Fig. 4.10) $Re_b > 10^2$ above 18 m and below 85 m, around 20 in the range 19–38 m and around 1 from 52 to 83 m. The storm increases Re_b, especially in the SML, so that regions of anisotropy ($Re_b < 10^2$) and inactive turbulence ($Re_b < 20$) are reduced to 43.5–83.5 m and 48–82 m respectively.

4.3.3 Vertical profiles of normal modes

The disappearance of the thermocline and the near-doubling of the surface mixed layer preclude shear within the surface 40 m from period II onwards. Before the storm the slight stratification between 23 and 40 m enables zero-crossing in this depth-region for higher modes, see Fig. 4.11. The vertical structure of mode 1 (Fig. 4.11a) is very similar to that in summer (Fig. 4.6a), whereas mode 2 now shows shear at the top and bottom of the halocline (Fig. 4.11b) rather than being a coupling between the halo- and thermocline (Fig. 4.6b). Also for higher modes (Figs. 4.11c–e) all shear is "squashed" within the lower part of the water column, more so after the storm than before.

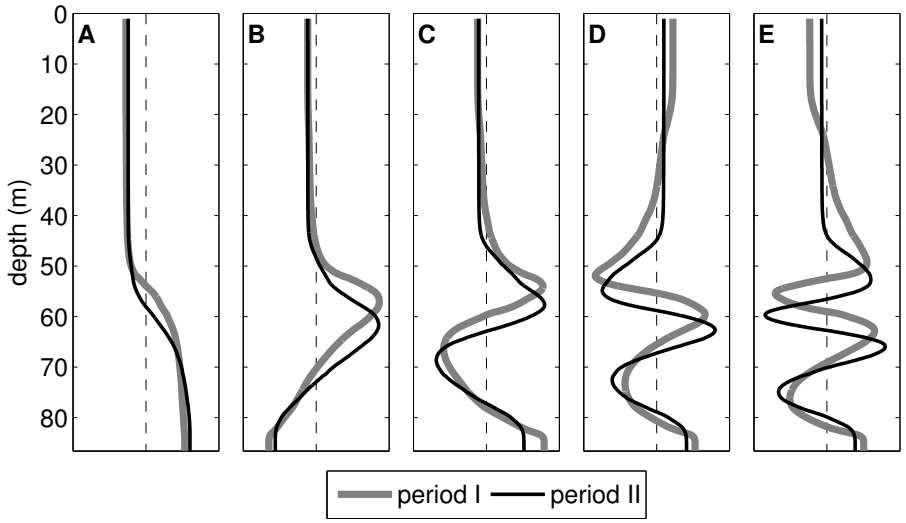

Figure 4.11: Vertical structure of the first 5 normal modes (a–e) at S1 calculated using (3.9) from the N^2 profiles of periods I & II in Fig. 4.8d.

The mode speeds and Rossby radii are extremely similar for all four periods; e.g. for periods I & II and modes 1–4, c_m and R_m are within 3% of each other (7% for mode 5). Also compared to the summer, values are nearly equal and therefore not shown again. The only significant difference between the summer and winter lies in the mode speeds and Rossby radii of modes 2 & 3 that are 15–20% lower/smaller in winter than in summer. This can be related to the "missing" thermocline, so that all shear needs to be packed into a smaller depth-range.

4.4 Conclusions

Overall the stratification in the Bornholm Basin is strong, as was shown by the potential energy anomaly, mainly due to the permanent halocline and in summer strengthened by the seasonal thermocline. In terms of temperature and salinity neither 2008 nor 2010 differed significantly from the climatological mean, although the warm ex-inflow water underneath the halocline raised the temperature of the 14 g kg^{-1} isohaline to above mean + 1std. Despite this temperature increase in the halocline, the density, which is mainly dependent upon salinity, increased monotonically with depth so that the water column was stable in both years/seasons.

The summer stratification was invariant over the measurement period; a thermocline at 30 m and a halocline at 50–65 m depth divided the water column into a three-layer system. The Turner angles at the top of the warm halocline suggest the possibility of double diffusive effects, although Thorpe scales are small here. The buoyancy Reynolds number indicates a depth range of 26–83 m where the assumption of isotropy is not satisfied. The main vertical modes show halocline interfacial waves and a coupling between the two pycnoclines.

In winter the stratification was all but invariant; winterstorm Xynthia caused significant changes over the four days of measurements. The last remainder of the thermocline was eroded so that the surface mixed layer doubled in size from 17 to 45 m and also the halocline deepend a few metres. Due to the increase in energy and turbulence the Thorpe displacements, Ozmidov scale and the buoyancy Reynolds number increased, whereas the Kolmogorov scale decreased in size. Because of their dependence on stratification the vertical normal modes only showed shear in the halocline and the deep layer above the bottom boundary layer.

5 Waves near the inertial frequency

5.1 Introduction

The natural frequency limit of internal waves at the low-frequency end of the spectrum was found (Sec. 1.2) to be the inertial frequency f_i, also known as the Coriolis parameter, which depends on the latitude. A sudden onset of strong winds or a rapid change in air pressure creates horizontal inertial oscillations in the surface layer. Although the wind is known to be the main generation mechanism of inertial oscillations and near-inertial waves (for a distinction between these see the next section) in the surface layer (e.g. *Krauß*, 1981; *D'Asaro*, 1985), also flow over topography can generate near-inertial waves (*Fennel and Schmidt*, 1993). Near-inertial waves have long been known to exist in the Baltic Sea; scientific papers reach back to the 1930s (*Gustafson and Kullenberg*, 1933). They are indeed hard to overlook, especially in the tideless Baltic Sea, as they often form a dominant peak in the power spectrum of current velocities (*Garrett*, 2001). These near-inertial waves generate high shear and have the ability to erode the thermocline (*Krauß*, 1981), as probably happened in winter 2010. Due to their dependence on the wind, a seasonal cycle of near-inertial kinetic energy has previously been observed with energy maxima in winter (*Alford and Whitmont*, 2007; *Silverthorne and Toole*, 2009).

5.1.1 Near-f wave motions

For the interpretation of the measurements at S1 it is helpful to briefly review the available theory for geostrophic adjustment in the presence of lateral boundaries. Considering a stratified, semi-infinite ocean with a flat bottom and a straight coast, *Kundu et al.* (1983) derived analytical solutions for the linear problem. For a suddenly imposed wind stress along the coast, these authors found that instantaneously generated inertial oscillations in the mixed layer with frequency $\omega = f_i$ can only exist for a short period before the arrival of the barotropic and baroclinic Poincaré modes generated at the coast.

The first disturbance results from the fast barotropic mode that arrives almost immediately for the small spatial scales investigated here. For this case, *Kundu et al.* (1983) showed that, after the barotropic front has passed, inertial oscillations in the mixed layer are replaced by slab-like motions with frequency $\omega = f_i$ affecting the whole water column with a current reversal across the base of the mixed layer. While this motion is purely barotropic, it does provide shear across the thermocline that can easily be misinterpreted as that from near-

inertial interfacial waves. *Kundu et al.* (1983) demonstrated that the subsequent arrival of higher-mode baroclinic wave fronts generated at the coast results in a small shift towards higher frequencies ($\omega > f_i$), and in the appearance of motions with upward phase propagation indicative of the downward transport of energy. These propagating motions with $\omega > f_i$ are near-inertial waves.

Fennel (1989) pointed out that in a closed basin Poincaré waves may be reflected from adjacent coasts, which considerably complicates the problem. Extending the theory of *Kundu et al.* (1983) for an infinitely long, straight channel, *Fennel* (1989) finds that multiple reflections of dispersive Poincaré waves at the channel walls lead to a complex superposition of modes that has random appearance. Nevertheless, many of the features of the solution found by *Kundu et al.* (1983) (e.g. the spectral blue shift and tilt of phase lines after the arrival of higher baroclinic modes) are retained.

The mode speeds c_m shown in Fig. 4.6f correspond to the maximum speeds at which energy in the Poincaré wave fronts generated at the coasts can travel towards the centre of the basin (*Kundu et al.*, 1983). Taking 50 km as a typical distance between S1 and the lateral slopes of the basin (Fig. 2.1), mode-1 waves are expected to arrive at S1 after approximately half a day, whereas signals from higher modes generally propagate for more than a day before they can be identified at S1. The corresponding Rossby radii are small compared to the lateral scale of the basin (Fig. 4.6g), suggesting that baroclinic Kelvin-type waves and coastal jets have no effect at station S1 in the centre.

5.2 Summertime near-inertial waves

The stratification parameters for late summer 2008 were discussed in the previous chapter; two pycnoclines divided the nearly 90 m deep water column in 3 near-equal layers. The summertime thermocline separated the warm, fresh surface mixed layer from the cold, fresh intermediate layer, which in turn was separated from the deep warm, salty layer by the halocline. The overall density stratification was stable and strong in the pycnoclines and the deep layer so that vertical normal modes had turning points in these regions. Mode-1 shear was centered on the halocline and mode-2 combined a shear layer in the thermocline with one in the halocline (Sec. 4.2.5).

5.2.1 Observations

For the analysis of the vertical structure of the observed velocities, the horizontal velocity vector was decomposed according to $\mathbf{u} = \bar{\mathbf{u}} + \tilde{\mathbf{u}}$, where $\bar{\mathbf{u}}$ and $\tilde{\mathbf{u}}$ correspond to the vertically averaged and residual parts, respectively. We use the convention that the components of $\mathbf{u}$

are denoted by u (to the east) and v (to the north). It should be recalled from the discussion above that $\tilde{\mathbf{u}}$ includes the baroclinic shear from internal waves and mesoscale motions, as well as the purely barotropic shear across the thermocline due to inertial oscillations. To separate motions with frequencies inside ($\omega > f_i$) and outside ($\omega < f_i$) the internal wave range, $\tilde{\mathbf{u}}$ was further split into an internal wave band contribution denoted by $\tilde{\mathbf{u}}_>$, and a sub-inertial part defined as $\tilde{\mathbf{u}}_< = \tilde{\mathbf{u}} - \tilde{\mathbf{u}}_>$. Technically, $\tilde{\mathbf{u}}_>$ was computed by high-pass filtering $\tilde{\mathbf{u}}$, using a 6^{th}-order phase-preserving Butterworth filter with a cut-off period of 20 h, following *Lass et al.* (2003). Note that $\tilde{\mathbf{u}}_>$ includes both internal wave motions and internal oscillations, which cannot be separated from each other by time filtering.

The variability of the velocities observed over a period of approximately 8 days in September 2008 (days 262.5–270.5) at station S1 is shown in Fig. 5.1. Velocities in the internal wave band (Figs. 5.1b,c) are dominated by clockwise rotating near-inertial motions, which clearly mirror the density interfaces shown in Fig. 4.2d. During the passage of several wind events (Fig. 5.1a), strong variations in the near-inertial motions are observed. The decay of these motions in the surface layer after the wind stress has decreased (days 268–270.5) is contrasted by stationary, or even weakly increasing, near-inertial energy levels in the intermediate and, subsequently, in the lower layers. The latter observation cannot be explained by any local generation mechanism; however, it is consistent with the idea that near-inertial waves in the deeper layers drain energy from the inertial motions in the surface layer near the lateral boundaries, and transport it towards the centre of the basin as suggested by *Kundu et al.* (1983). Further support for this is provided by the observation that phase lines in the intermediate layer show an increasing tilt, indicating upward phase propagation during and after the wind events as qualitatively predicted by *Kundu et al.* (1983) and *Fennel* (1989) as a result of the subsequent arrival of higher vertical modes.

The strongest tilt of phase lines (shortest vertical wave length) is observed in the deepest layer below the halocline, with a particularly clear signal during the period of the microstructure measurements on days 262.3–264.2 (Figs. 5.1b,c). Since wind speeds are low during this period (Fig. 5.1a), these motions likely indicate the delayed arrival of higher modes generated at the lateral boundaries during the wind event observed a few days before the start of our measurements (not shown). Observed periods in the upper layer are indiscernible from the inertial period $T_i = 14.56$ hours, whereas in the layer below the halocline $\omega \approx 1.08 f_i$, supporting the theoretical finding that the spectral blue shift is more pronounced in the deeper layers (*Kundu et al.*, 1983; *Fennel*, 1989).

Our observations do not show any indication of the existence of random patterns generated by the super-position of Poincaré modes reflected at the coasts, as suggested by *Fennel* (1989). In view of the complex structure of the bathymetry and coastline, possible reasons for this may be related to the attenuation of reflected signals by wave scattering and dissipation, or

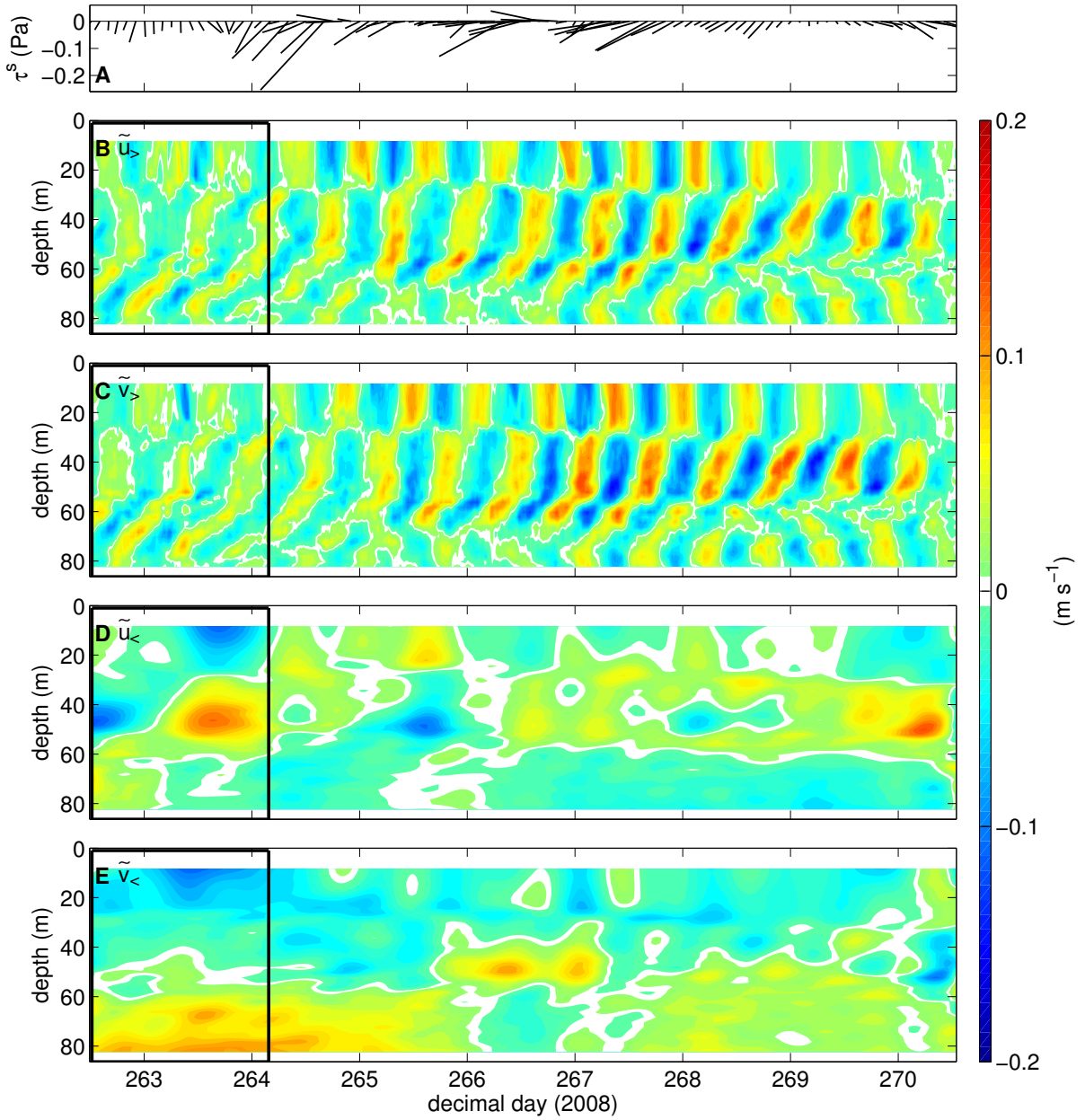

Figure 5.1: (a) Time series of wind stress during the measurements in September 2008. Contour plots show east (b) and north (c) components of the super-inertial velocity $\tilde{\mathbf{u}}_>$, and east (d) and north (e) components of sub-inertial velocity $\tilde{\mathbf{u}}_<$. Black rectangles mark the period of microstructure measurements.

by the different generation mechanisms for internal waves on sloping bathymetry compared to the vertical channel walls assumed by *Fennel* (1989).

It is worth pointing out that Figs. 5.1d,e suggest that additional baroclinic shear is associated with the sub-inertial motions $\tilde{\mathbf{u}}_<$ with possible implications for mixing that will be evaluated in more detail below.

5.2.2 Energetics

To study the contribution of the eigenmodes shown in Fig. 4.6 to the super-inertial velocities displayed in Figs. 5.1b,c, the standard decomposition of internal wave motions into vertical and time-varying contributions (*Kundu and Cohen*, 2008) was used:

$$\tilde{\mathbf{u}}_{>}(z,t) = \sum_{m=1}^{\infty} \hat{\mathbf{u}}_m(t)\Psi_m(z) \quad , \tag{5.1a}$$

$$\hat{\mathbf{u}}_m(t) = \frac{1}{H}\int_{-H}^{0} \tilde{\mathbf{u}}_{>}(z,t)\Psi_m(z)\mathrm{d}z \quad , \tag{5.1b}$$

where $\hat{\mathbf{u}}_m$ describes the projection of $\tilde{\mathbf{u}}_{>}$ onto mode m, see Sec. 3.4. From (5.1), it can be shown that the vertically averaged kinetic energy, E^{kin}, in the internal wave band can be expressed as

$$E^{\mathrm{kin}} = \frac{1}{H}\int_{-H}^{0} \frac{\tilde{\mathbf{u}}_{>}\cdot\tilde{\mathbf{u}}_{>}}{2}\mathrm{d}z = \frac{1}{2}\sum_{m=1}^{\infty}(\hat{u}_m^2 + \hat{v}_m^2) \quad , \tag{5.2}$$

from which $E_m^{\mathrm{kin}} = (\hat{u}_m^2 + \hat{v}_m^2)/2$ is identified as the vertically averaged kinetic energy in mode m. Note that this definition of energy includes contributions from both baroclinic wave modes and barotropic inertial oscillations (there is no objective method for separating these two components in a single-point data set).

The vertical energy flux $\boldsymbol{\tau}\cdot\mathbf{u}$ varies with depth across the mixed layer as both the local stress $\boldsymbol{\tau}(z,t)$ and the horizontal velocity $\mathbf{u}(z,t)$ are variable. Assuming a linear decrease of the stress from $\boldsymbol{\tau} = \boldsymbol{\tau}^s$ at the surface to zero at the surface mixed-layer base ($z = -H_{SML}$), this energy flux can be expressed as

$$F(z) = \frac{\boldsymbol{\tau}\cdot\mathbf{u}}{\rho_0 H} = \frac{(z+H_{SML})}{H_{SML}}\frac{\boldsymbol{\tau}^s\cdot\mathbf{u}}{\rho_0 H} \quad , \tag{5.3}$$

where F has been normalised by ρ_0 and the local water depth H to make the cumulative (i.e. time-integrated) flux directly comparable to E^{kin}. It is assumed that $H_{SML} = 26$ m (Fig. 4.2), and $\mathbf{u}$ is evaluated at the upper end of the ADCP range $z \approx -H_{SML}/2$. This definition excludes the strongly sheared near-surface region, where most of the surface-layer dissipation is thought to occur. Due to the clockwise rotating velocity vector in the surface layer, the strongest signals in F are fluctuations with near-inertial frequency (Fig. 5.2a). Most of the cumulative energy flux (Fig. 5.2b) occurs during the first two days, where it should be observed that the direct energy input into internal wave band motions ($\tilde{\mathbf{u}}_{>}$) is comparatively small (Fig. 5.2b).

Fig. 5.2c illustrates that the velocity field synthesised from only 5 modes, according to (5.1), yields a rather detailed description of the observed structure. The strong phase shift across

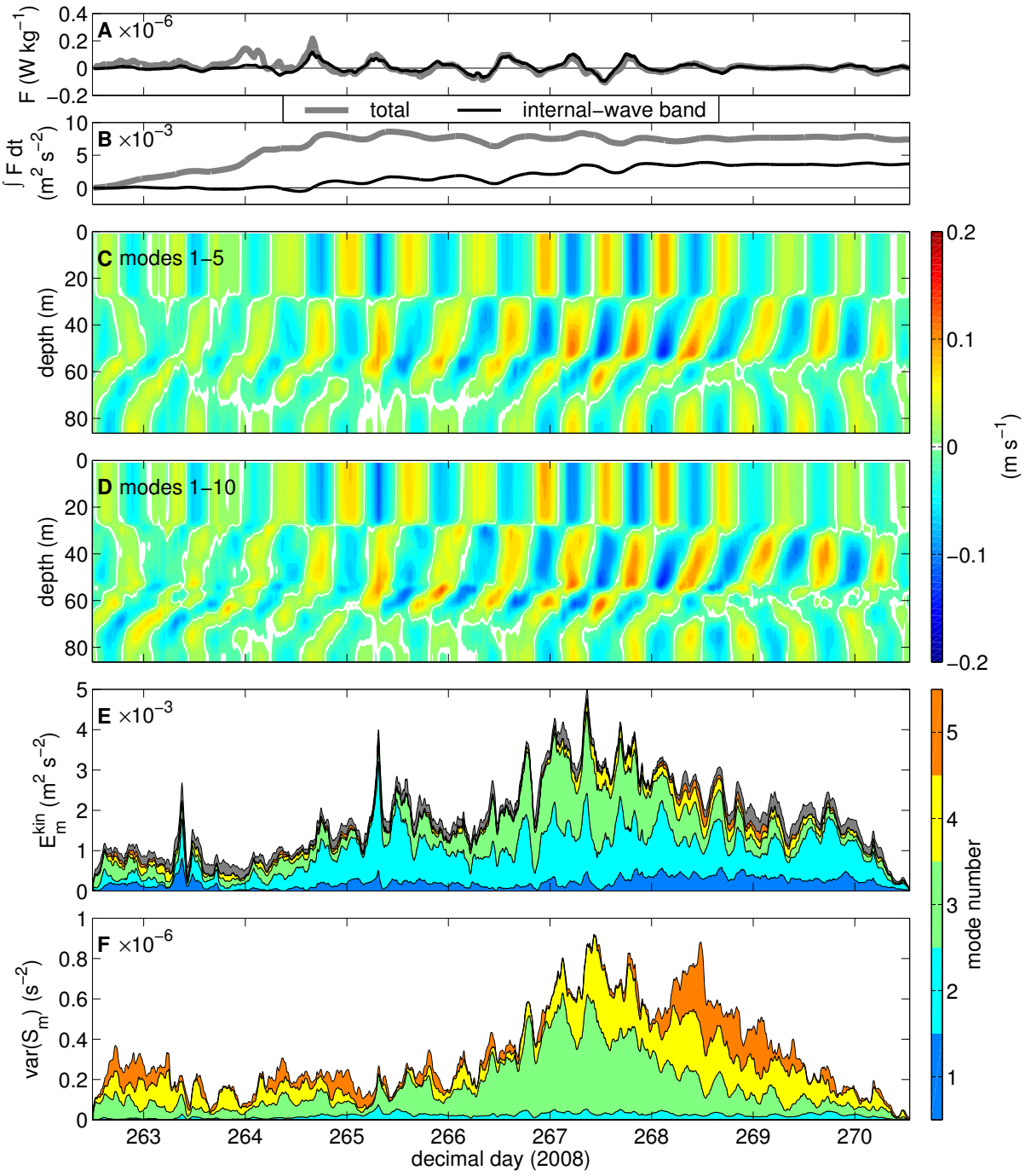

Figure 5.2: Instantaneous (a) and cumulative (b) energy input due to wind. East component of internal wave band velocity $\tilde{\mathbf{u}}_>$ projected on the first 5 modes (c) and the first 10 modes (d). Lower panels show kinetic energy (e) and shear variance (f) per mode. The grey area in panel (e) represents the total kinetic energy in the internal wave band.

the density interfaces, as well as the vertical phase propagation inside the weakly stratified intermediate layer are well described. A closer examination reveals, however, that the vertical phase propagation in the region below the halocline during the first days, coinciding with the period of microstructure measurements discussed below, is significantly underestimated. Inclusion of higher modes (Fig. 5.2d) resolves this problem, suggesting that a substantial fraction of the shear in this region originates from modes 6–10 that have travelled with low speeds (see Fig. 4.6f) from their generation areas on the lateral slopes towards S1. This is also consistent with the presence of a strong wind event observed before the start of our measurements as mentioned above.

The partitioning of E^{kin} between modes (Fig. 5.2e) is dominated by the contribution from the lowest 3 modes, which contain approximately 81 percent of the total kinetic energy in the internal wave band. Mode 2 contains substantially more energy than mode 1, which is different from the dominance of mode-1 motions found by *MacKinnon and Gregg* (2003a) on the shelf. This can be understood from the fact that, here, mode 2 provides shear across the mixed-layer base, i.e. just below the layer directly accelerated by the wind stress (Fig. 4.6b). Note that the kinetic energy in the water column is of the same order as the cumulative energy input from the wind (see Fig. 5.2b), consistent with the above-mentioned fact that the energy loss in the upper half of the surface layer (e.g. due to near-surface dissipation) is not included in the analysis. The relatively large energy input into sub-inertial motions (Fig. 5.2b) suggest a conversion from sub-inertial to near-inertial energy during the geostrophic adjustment process near the lateral slopes, in agreement with the theory outlined in Sec. 5.1.1.

The superposition of different internal wave modes also results in variations in vertical shear squared, $S_>^2 = (\partial\tilde{u}_>/\partial z)^2 + (\partial\tilde{v}_>/\partial z)^2$, which may be quantified in terms of the vertical shear variance $\int_{-H}^{0} S_>^2 \mathrm{d}z/H$ as suggested by *MacKinnon and Gregg* (2003a) and explained in Sec. 3.4. The contributions of individual modes is shown in Fig. 5.2f, revealing that, although low modes dominate the energy budget, higher modes contain most of the shear variance. Increased shear variance in modes 4 and 5 after day 267 reflects the delayed arrival of higher modes much more clearly than the energy budget displayed in Fig. 5.2e. When interpreting Fig. 5.2f it should be kept in mind that, contrary to the mode energies, the shear variances in individual modes do *not* sum up to yield the total shear variance, as can be shown from (5.1) and the fact that derivatives of Ψ_m are not normal. Further, as discussed in detail below, more relevant for mixing than the bulk shear variance is the fact that the quasi-random superposition of internal wave modes may generate localised shear bands that are directly related to enhanced dissipation levels.

Thus, as one of the main conclusions from this section, it was found that the partitioning of energy and shear variance between low-wavenumber near-inertial waves is not constant, which is at variance with the Garrett-Munk spectral model (*Munk*, 1981), and the finescale

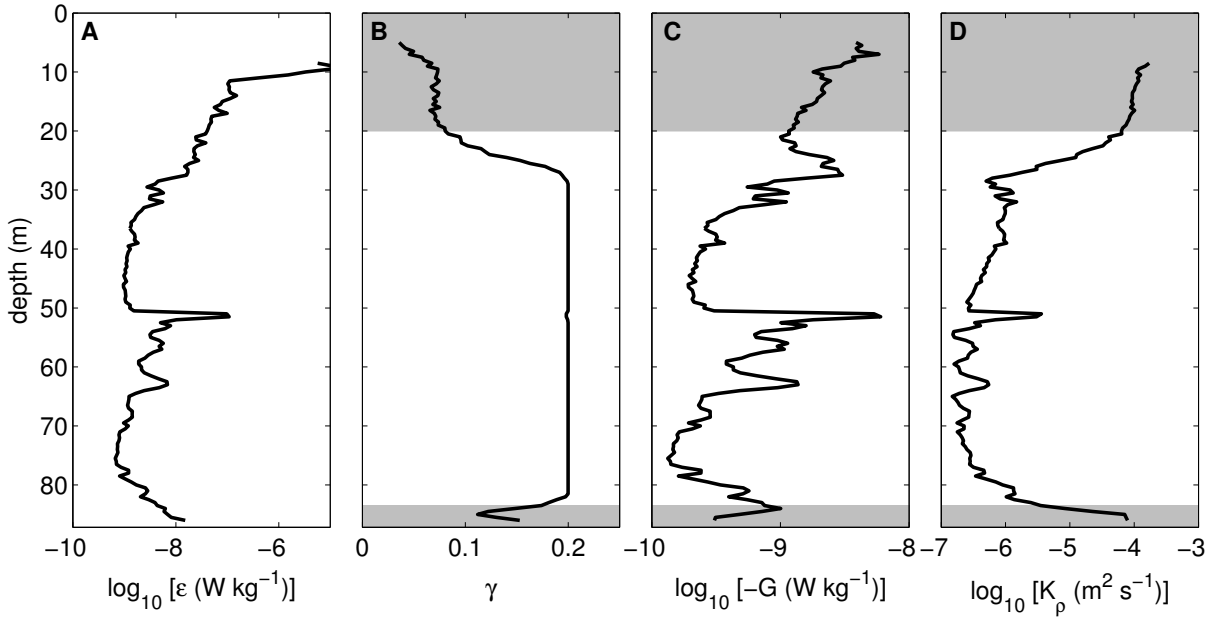

Figure 5.3: As in Fig. 4.2 but now for (a) dissipation rate, (b) mixing efficiency, (c) buoyancy flux, and (d) turbulent diffusivity. In (b)–(d), only data with $L_0 < 0.4d$ (d distance from bottom and surface, respectively) have been included in the averaging. The near-boundary regions affected by this correspond to grey-shaded areas.

parameterisations of internal wave mixing that rely on it (e.g. *Polzin et al.*, 1995; *Gregg et al.*, 2003). Even in the absence of tides, this makes the situation in the Baltic Sea energetically more similar to that on the shelf than to the deep ocean (*MacKinnon and Gregg*, 2003a, 2005a).

5.2.3 Mixing parameters

Our analysis of mixing in the centre of the basin is based on 400 microstructure profiles, obtained near station S1 during a period of slightly less than 2 days at the beginning of the velocity observations shown in Fig. 5.1. The vertical structure of the most important mixing parameters averaged over this period is summarised in Fig. 5.3. The dissipation rate (Fig. 5.3a) reveals 3 layers of enhanced turbulence: the two boundary layers near the surface and the bottom, and a 15 m thick interior layer located inside and just below the halocline. The latter is of particular interest for the following discussion because mixing inside this layer is likely to be energised by shear-instabilities due to internal wave motions. Turbulence directly above and below this energetic layer is seen to be weak, with dissipation rates generally close to or below the noise level ($\varepsilon \approx 10^{-9}$ W kg^{-1}) of our instrument.

The vertical turbulent buoyancy flux G can be inferred from these dissipation rate estimates using the relationship $G = -\gamma\langle\varepsilon\rangle$, where γ is the mixing efficiency, and $\langle\cdots\rangle$ denotes a suitably

defined average (see below). The canonical value $\gamma = 0.2$ is likely to overestimate the buoyancy flux in the surface and bottom boundary layers, and possibly also in the halocline mixing layer, where mixing is energetic, and reduced mixing efficiencies may be expected. Here, *Shih et al.* (2005) were followed, who analysed Direct Numerical Simulations of stratified shear layers, suggesting a relationship of the form:

$$\gamma = \begin{cases} 2Re_b^{-\frac{1}{2}} & \text{for } Re_b > 100 \\ 0.2 & \text{otherwise,} \end{cases} \tag{5.4}$$

where $Re_b = \langle\varepsilon\rangle/(\nu\langle N^2\rangle)$ is the buoyancy Reynolds number, and ν the molecular viscosity. Direct evidence for the applicability of (5.4) in the ocean has been reported by *Fer and Widell* (2007). This model for γ has previously been used to describe the reduction of the mixing efficiency also in other types of stratified shear layers in the ocean (e.g. *Sundfjord et al.*, 2007; *Umlauf and Arneborg*, 2009). Since it cannot be expected that (5.4) also holds in the weakly stratified layers in the immediate vicinity of the upper and lower boundaries, regions where the Ozmidov scale $L_O = (\varepsilon/N^3)^{1/2}$ becomes larger than the length scale $0.4d$ for wall-bounded shear flows (d is the distance from the boundary) were excluded from the analysis.

Once the buoyancy flux G is known, the turbulent diffusivity can be computed from $K_\rho = -G/\langle N^2\rangle$. To increase the statistical signifcance of our estimates for γ, G, and K_ρ, their computation is based on averaged dissipation rates $\langle\varepsilon\rangle$ and stratification $\langle N^2\rangle$. Practically, the filtering symbol $\langle\cdots\rangle$ denotes a non-overlapping average over 5 neighbouring profiles that has been chosen as a compromise between statistical significance and resolution in time.

The average mixing efficiency for the whole period (Fig. 5.3b) shows strongly reduced mixing efficiencies only in the surface and bottom boundary layers, whereas mixing in the interior occurs at or close to the maximum efficiency ($\gamma = 0.2$). The high mixing efficiency in this layer is also reflected in the large buoyancy flux shown in Fig. 5.3c, which is comparable to the fluxes in the surface layer, where mixing is more energetic but less efficient. Fig. 5.3d shows that the turbulent diffusivity is largest in the boundary layers but generally does not exceed the threshold of $K_\rho = 10^{-6}$ m^2 s^{-1} in the interior. These averaged mixing rates result from strongly turbulent but rather localised mixing bands as discussed in the following.

The temporal evolution of mixing for the period marked in Fig. 5.1 is illustrated in Fig. 5.4. These data were obtained during 7 transects near S1 as described in Sec. 2.2.1. In spite of the fact that winds were comparatively weak during the microstructure measurements (Fig. 5.1a), it is clear from Fig. 5.4b that the highest dissipation rates are directly related to wind mixing in the surface layer. Wind-generated turbulence closely follows the variability of the wind energy input that is proportional to the wind speed cubed (Figs. 5.4a,b). However, the permanent tendency for surface-layer restratification (Fig. 5.4c) generally limits the penetration of surface-

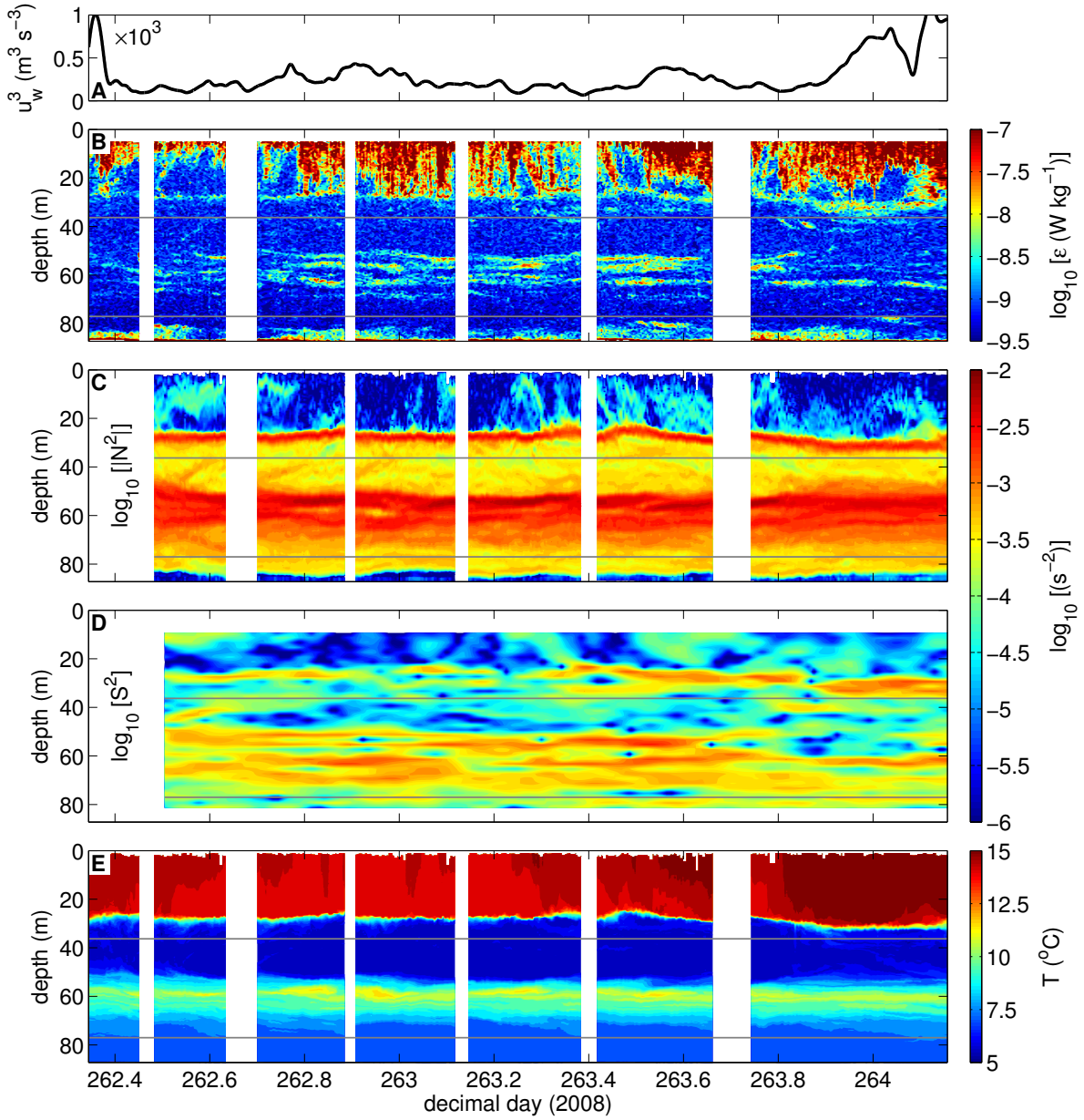

Figure 5.4: Time series of (a) wind speed cubed, (b) dissipation rate, (c) buoyancy frequency squared (based on vertically filtered quantities, see text), (d) shear squared, and (e) temperature, all for station S1 (summer). Horizontal grey lines define the upper and lower edges of the "interior" region.

layer turbulence to depths shallower than the thermocline level. This suggest that the thin band of enhanced dissipation rates inside the thermocline (Fig. 5.4b) results from the shear across the thermocline (Fig. 5.4d), rather than being directly related to near-surface turbulence. A similar phenomenon has recently been reported by *Burchard and Rippeth* (2009) for the thermocline of the North Sea.

Turbulence in the bottom boundary layer is substantially weaker than in the surface layer but strong enough to create a nearly well-mixed layer of a few meters thickness (Figs. 5.4b,c).

Significant energy dissipation in the interior is confined to the strongly stratified halocline layer between 50 and 70 m depth (Fig. 5.4b), where mixing is seen to occur in narrow bands with a surprisingly large correlation in time (and in space, since the ship is moving on the transects). Fig. 5.4d illustrates that these mixing bands are highly correlated with the occurrence of narrow shear bands observed by the high-resolution ADCP at station S1. Even rather fine structures like the two shear bands at approximately 50–53 m depth on days 262.8–263, or the extended shear band at 60 m depth after day 263.9 are directly reflected in the dissipation rates. The temperature distribution shown in Fig. 5.4e illustrates the intrusion of warm North Sea waters (see Sec. 4.2) at the level of the halocline mixing bands. Since these intruding water masses have different biogeochemical properties (e.g. oxygen and nutrient concentrations, redox potential, etc.) than the ambient water (*Mohrholz et al.*, 2006), it is likely that mixing enhances biochemical transformations. The ecological relevance of this process has also been emphasised by *Konovalov et al.* (2003), who studied a similar situation in the Black Sea, where intrusions consist of oxygenated Bosporus waters.

To investigate whether the observed correlation between shear and dissipation (and possibly stratification) follows a systematic pattern, observed dissipation rates have been averaged into logarithmically spaced bins of S^2 and N^2 as suggested by *MacKinnon and Gregg* (2003b). Only data outside the regions affected by the surface and bottom boundary layers have been used for this analysis as indicated in Fig. 5.4. To reduce the bias introduced by the different vertical resolutions of shear and stratification data, the latter were vertically filtered in order to match the triangular response characteristics of the 300-kHz ADCP with 2-m bins. To this end, temperature and conductivity data from the microstructure CTD sensors, available at 0.1-m resolution, were vertically filtered with a 4-m Bartlett window before computing density. Density was then interpolated onto the ADCP grid, and N^2 was computed from finite differencing (the result is shown in Fig. 5.4c). Accordingly, dissipation rates were vertically averaged over the 2-m ADCP bins. Since the focus is not on high-frequency internal wave shear, ADCP data were 1-h low-pass filtered in time before computing the shear. Following *MacKinnon and Gregg* (2003b), no attempt was made to compensate for lost shear variance due to limited vertical resolution and filtering response of the ADCP.

Fig. 5.5a illustrates that our data are located in the strongly stratified regime with typical values of the Richardson number $Ri = N^2/S^2$ larger than $Ri = 1$, and no clear dependency of the dissipation rates on this parameter. However, dissipation rates do show a clear correlation with N^2 and S^2, with a trend for increased mixing in both strongly stratified and sheared regions. The observed pattern is qualitatively similar to the parameterisation developed for internal wave mixing on the shelf by *MacKinnon and Gregg* (2003b):

$$\varepsilon_{MG} = \varepsilon_0 \frac{N}{N_0} \frac{S}{S_0} \quad , \tag{5.5}$$

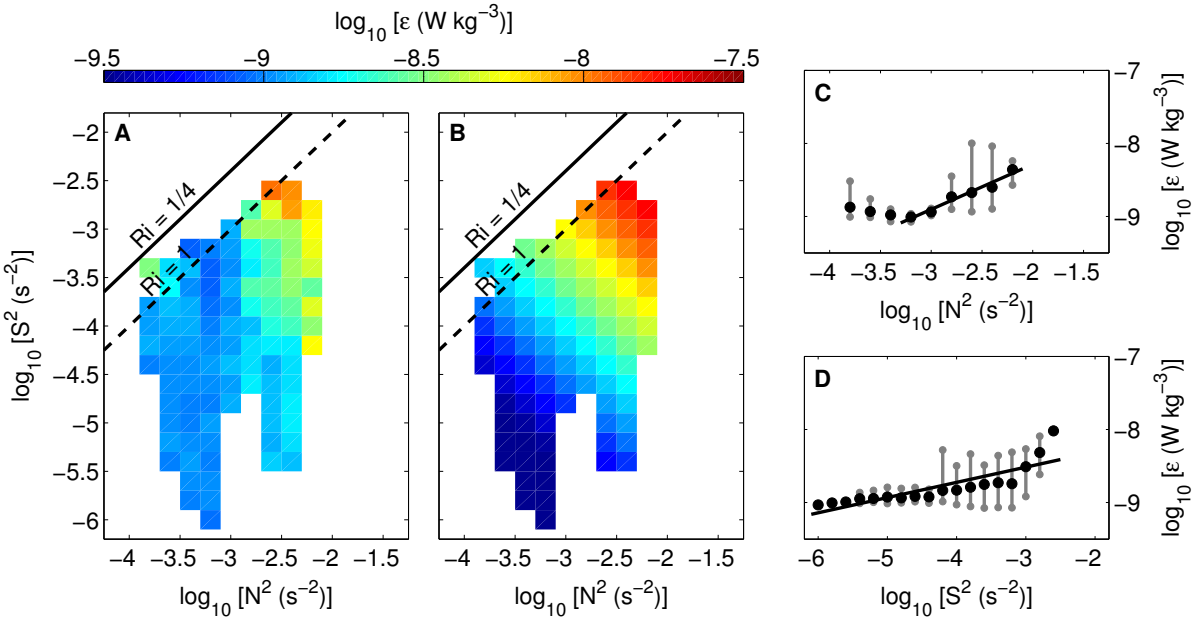

Figure 5.5: Bin-sorted dissipation rates from (a) observations and (b) the parameterisation in (5.5) with $\varepsilon_0 = 1.5 \times 10^{-10}$ W kg^{-1}. Panels (c) and (d) show the data from (a), now sorted in bins of constant N^2 and S^2, respectively. Black dots show the average, grey dots/lines indicate the maximum and minimum values for each bin. Black lines correspond to the best straight-line fit, respectively. All data are based on the interior region marked in Fig. 5.4.

where $N_0 = S_0 = 3$ cph (5.24×10^{-3} s^{-1}), and ε_0 is an unknown model constant. If the latter is adjusted to $\varepsilon_0 = 1.5 \times 10^{-10}$ W kg^{-1}, such that ε_{MG} matches the observed mean dissipation rate, this model exhibits a reasonable agreement with the data (Fig. 5.5b). Similar to *MacKinnon and Gregg* (2003a), it was found that finescale parameterisations developed for the open ocean (*Gregg*, 1989; *Polzin et al.*, 1995; *Gregg et al.*, 2003) predict a qualitatively different functional dependency on N^2 and S^2.

Averaging the bin-sorted dissipation rates $\varepsilon(N^2, S^2)$ shown in Fig. 5.5a over S^2 and N^2, respectively, reveals clear trends in these parameters, however, with a large scatter around the average (Fig. 5.5c,d). Only for the smallest values of N^2 and S^2, significant trends cannot be established anymore, which is likely a result of the fact that the observed dissipation rates in these regions are in the vicinity of 10^{-9} W kg^{-1}, i.e. close to the noise level of the profiler.

5.3 Wintertime near-inertial waves

The observations during winter conditions in February/March 2010 cover a period of slightly less than 4 days (days 58.5–62.3) for which high-resolution continuous velocity measurements are available (Fig. 5.6) from a combination of data from two moored ADCPs (see Sec. 2.3.1). This period is characterised by a strong wind event, as discussed in Sec. 4.3.1, with highest

hourly wind speeds around 15–20 m s^{-1} (8 Beaufort, $\tau^s = 0.43$–0.89 Pa) during days 59.5–60, complicating the measurements but on the other hand also allowing a study of the generation of near-inertial wave motions, and corresponding variations in mixing (Fig. 5.6a). Microstructure measurements were performed on 39 transects in the vicinity of S1 as described in Sec. 2.2.1 with an interruption of approximately 36 h due to high sea state. Measurements are therefore grouped into 4 periods: period `I` with 6 transects taken just before the wind event, period `II` with 6 transects directly after the wind event, and period `III` with 19 transects measured during the decay period (Fig. 5.6b). Period `IV` hardly mentioned in the following due to the lack of velocity measurements here.

5.3.1 Mixing parameters

The stratification at the end of winter exhibits the two layer vertical structure typical for this time of the year (Sec. 4.3). The nearly well-mixed surface layer of about 50 m thickness was bounded from below by a 10–15 m thick halocline that gradually merged into the stratified lower part of the water column. Comparing the situation over the four periods before and after the wind event suggests that increased mixing during the windy period resulted in a significant modification of the vertical structure of the water column. The depth of the well-mixed surface layer increased by more than 20 m, and the halocline has both descended by more than 5 m and approximately doubled its width (Fig. 4.8). The latter points at the influence of internal wave mixing inside the halocline. Note that these estimates are based on averages over more than 10 hours, such that random displacements due to internal waves are likely to be removed by the averaging.

The effect of the wind event can also be directly identified in the mixing parameters. Dissipation rates (Fig. 5.7a) and turbulent diffusivities (Fig. 5.7d) in the surface mixing layer have increased by 1–2 orders of magnitude during the storm, and the active "mixing layer", defined as the near-surface region with $\varepsilon > 5 \times 10^{-9}$ W kg^{-1}, has penetrated down from initially 24 m to 50 m. In the stratified layer below the halocline not directly affected by wind mixing, dissipation rates have increased by approximately one order of magnitude, which mirrors the effect of internal wave mixing as shown below. Turbulent diffusivities, computed with a variable mixing efficiency γ as described in Sec. 5.2.3 and shown in Fig. 5.7b, vary around $K_\rho = 10^{-6}$ m^2 s^{-1} in the stratified lower part of the water column after the wind event (Fig. 5.7d). Note, however, that the mixing parameters shown in Figs. 5.7a,d correspond to averages over many profiles. Mixing in the stratified interior occurs in banded structures that may exhibit mixing rates and diffusivities considerably above these average values.

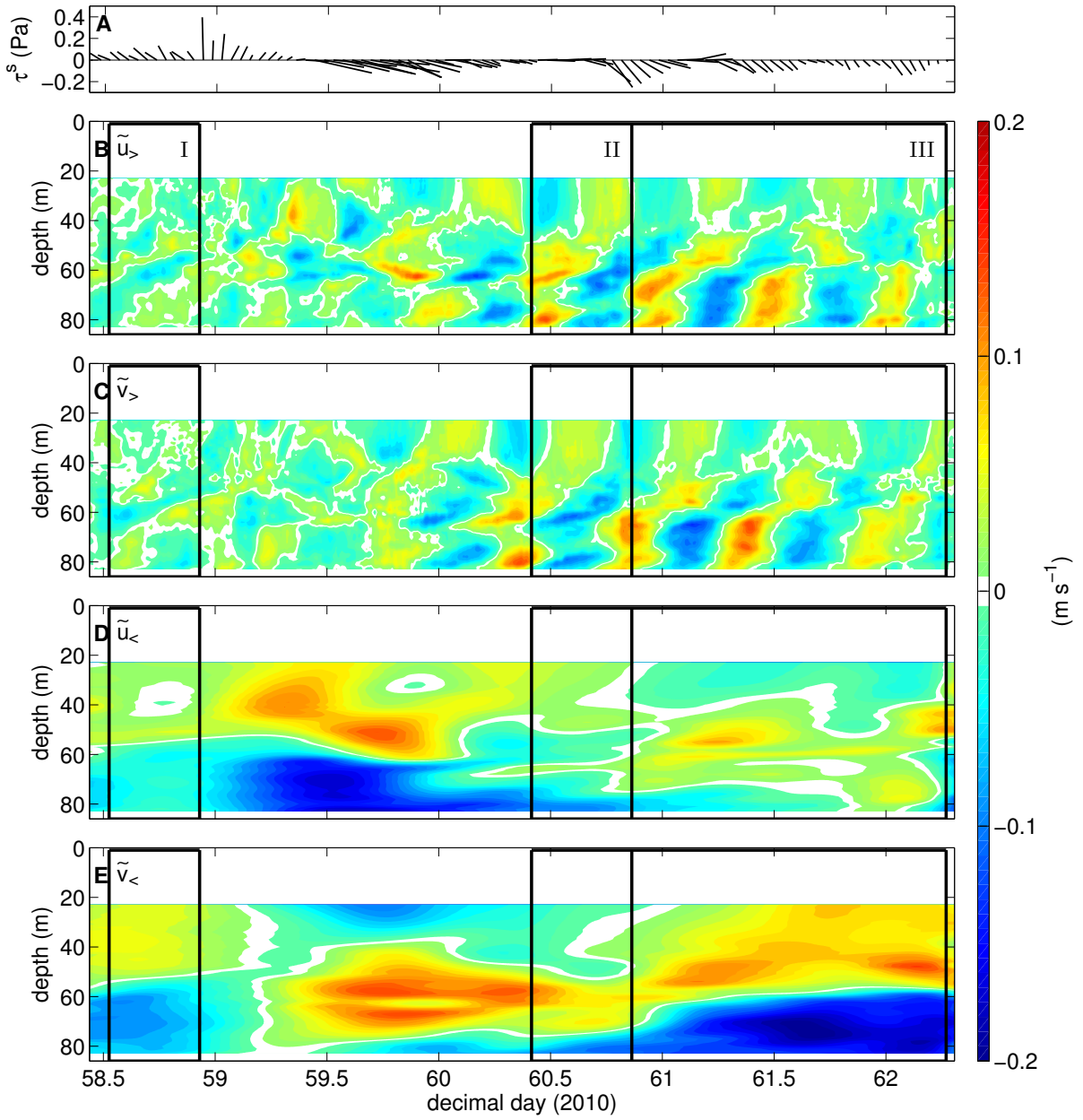

Figure 5.6: Time series for station S1 of (a) wind stress, (b) east and (c) north components of the super-inertial velocity $\tilde{\mathbf{u}}_>$, and (d) east and (e) north components of sub-inertial velocity $\tilde{\mathbf{u}}_<$. Black rectangles and Roman numbers indicate periods of microstructure measurements. Velocity data are composites with data below 54 m from a 600-kHz ADCP, and above from a 300-kHz ADCP.

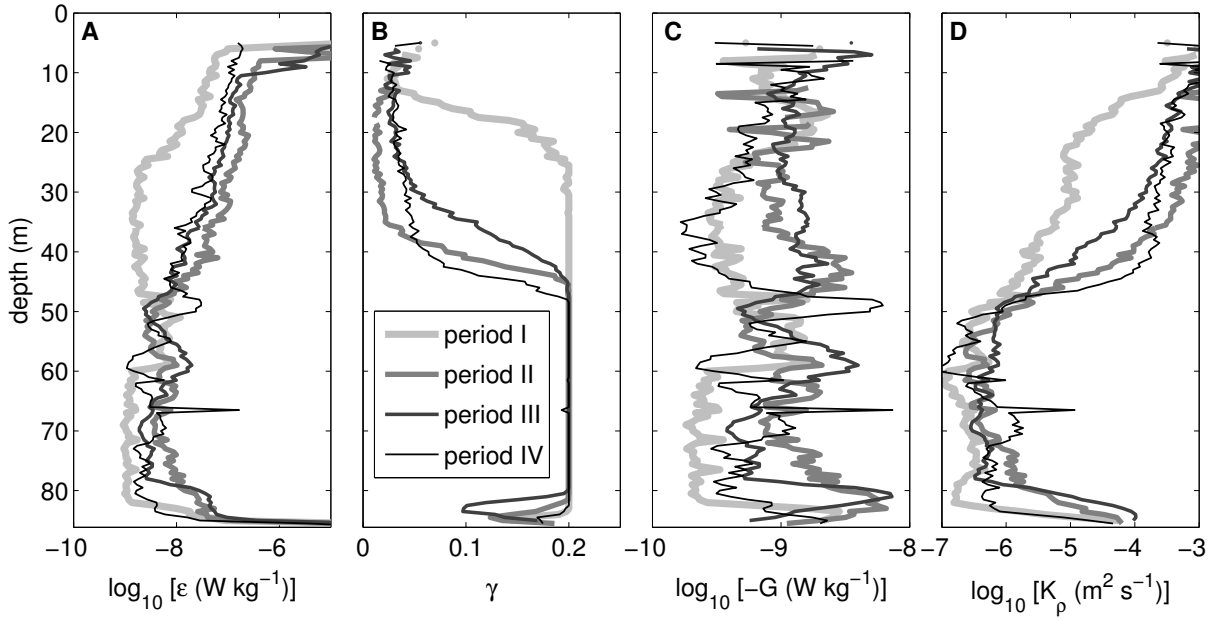

Figure 5.7: As in Fig. 5.3 but now for winter 2010. Different grey-shaded lines correspond to different microstructure periods (see text).

5.3.2 Near-inertial and sub-inertial variability

Analogous to Sec. 5.2.1, our analysis of the velocity structure observed at S1 is based on the decomposition of the velocity field into contributions from internal waves ($\tilde{\mathbf{u}}_>$), from sub-inertial motions ($\tilde{\mathbf{u}}_<$), and from vertical mean currents ($\bar{\mathbf{u}}$). As shown in Figs. 5.6a-c, near-inertial motions in the upper part of the water column set in immediately after the clockwise veering of the wind vector, when winds begin to strongly increase around day 59.3. Maximum velocities are comparable to those observed during summer conditions (see Fig. 5.1) but, as a consequence of the different vertical stratification, also the vertical structure of the velocity field is rather different. It is worth noting that near-inertial signals reach the deep layers below the halocline with a significant delay, which, similar to the summer situation, can be interpreted as a manifestation of the delayed arrival of internal wave modes generated at the lateral boundaries.

To investigate this point in more detail, the observed velocity field after the storm (periods II + III) has been projected onto normal modes as described in Sec. 5.2.2, and the temporal evolution of the kinetic energy and the shear variance associated with individual modes has been analysed. This procedure is completely analogous to that described for the summer data in the context of Fig. 5.2, and thus, for brevity, only the main results are summarised here. It was found that the relative contribution of individual modes to the total kinetic energy is not constant in time with most of the kinetic energy associated with the lowest modes, while higher modes contribute strongest to the shear variance. These results are qualitatively identical to

the situation in summer, as well as to the findings of *MacKinnon and Gregg* (2003a) on the shelf, providing further support for the idea that the internal wave dynamics in the Baltic Sea are more similar to those on the shelf than to those in the deep ocean, in spite of its confined character and the absence of tides. The main difference between summer and winter conditions is related to the dominance of mode-1 motions in winter, compared to mode-2 motions in summer. This may be explained by the observation that winter stratification corresponds, to first order, to a two-layer system centered around the halocline, whereas stratification in summer can be roughly represented by a three-layer system with the main pycnoclines formed by the thermocline and the halocline, respectively.

The temporal evolution of the sub-inertial velocity $\tilde{\mathbf{u}}_<$ is shown in Figs. 5.6d,e. The slowly varying signals that can be identified in these motions are difficult to interpret from single-point measurements; in view of previous investigations in this region (*Reißmann*, 2005) it is, however, not unlikely that they represent the signatures of mesoscale Baltic Sea eddies (so-called "Beddies"). Regardless of the physical nature of these motions, it is evident that they provide a sub-inertial contribution to the total shear that may be significant for small-scale internal wave motions and mixing.

5.3.3 Boundary-layer mixing and dynamics

A composite view of mixing, stratification, and near-inertial shear observed during periods II + III on 25 transects near position S1 is provided in Fig. 5.8. Similar to the summer situation, highest dissipation rates are seen to occur in the surface and bottom boundary layers (Fig. 5.8b). An interesting feature visible in this figure are pulsations in the near-bottom dissipation rates that occur with a period of approximately 12 hours, corresponding to the period of the near-inertial wave motions visible in Figs. 5.6b,c. As illustrated in Fig. 5.9a, the observed phenomenon can be explained as the simple superposition of near-inertial waves and the slowly varying (sub-inertial) currents, resulting in a net periodic modulation of the near-bottom speed (Fig. 5.9b), and thus in variable mixing rates.

To test the dynamical implications of this effect the bottom stress was computed from the law-of-the-wall relation as described in Sec. 3.3.2. Using the same method and identical instrumentation, *Umlauf and Arneborg* (2009) have recently shown good agreement between microstructure-based and direct bottom stress measurements from an Acoustic Doppler Velocimeter (ADV) in the bottom boundary layer of a neighbouring basin. Bottom stresses computed in this manner (Fig. 5.9c) show an almost perfect correlation with the near-bottom speeds (Fig. 5.9b) with a quadratic dependency between stress and speed, as indicated by the rather stable quadratic drag coefficient C_d shown in Fig. 5.9d. Values of the latter are seen to remain within a factor of 2 around the classical value $C_d \approx 2 \times 10^{-3}$, except for

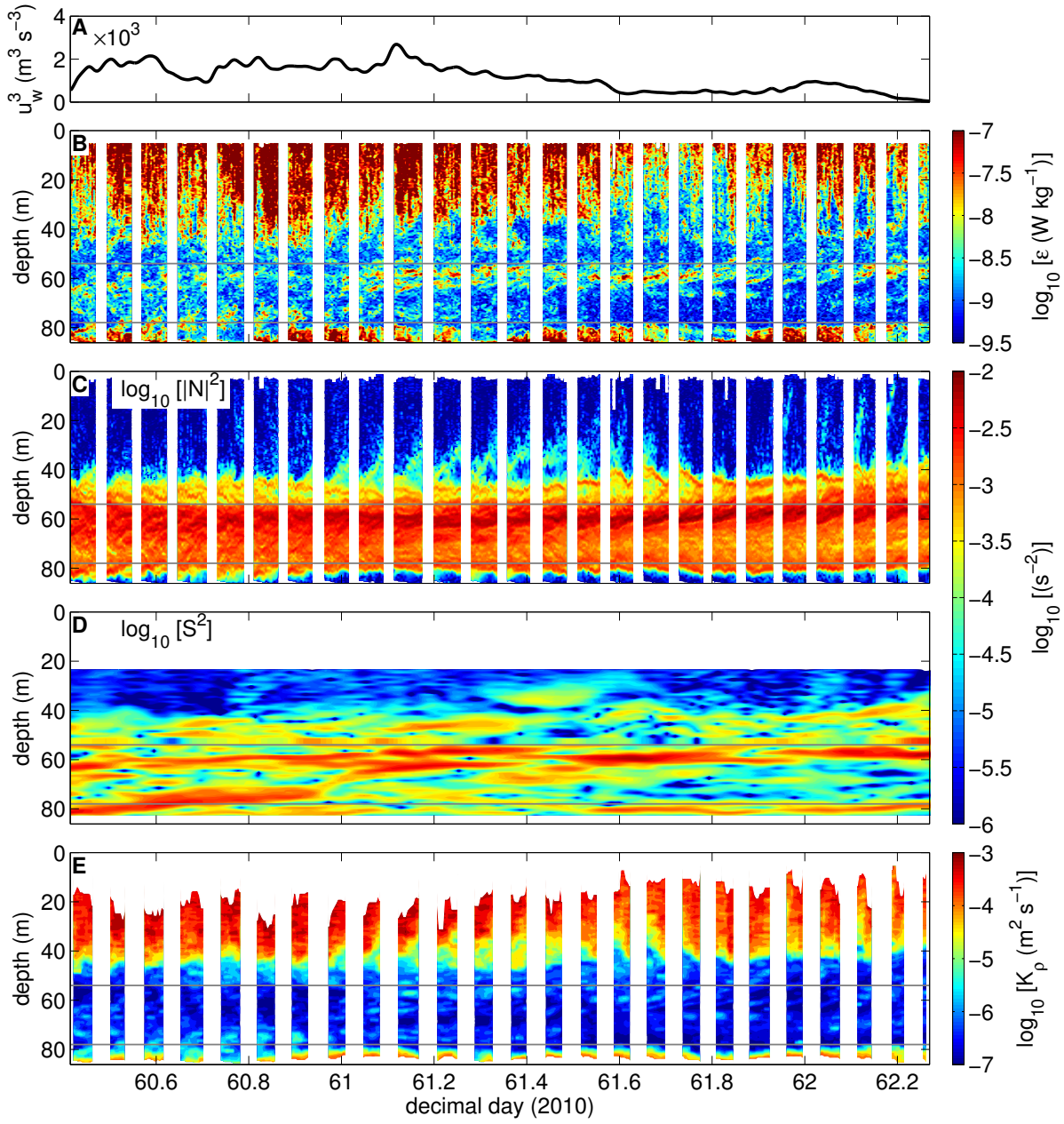

Figure 5.8: Time series, for the after-storm period (periods II + III, Fig. 5.6), of (a) wind speed cubed, (b) dissipation rate, (c) buoyancy frequency squared (based on vertically filtered quantities, see text), (d) shear squared, and (e) turbulent diffusivity, all for station S1 (winter). Horizontal grey lines define the upper and lower edges of the "interior" region. In panel (e), surface and bottom boundary layers with $L_0 > 0.4d$ are blanked.

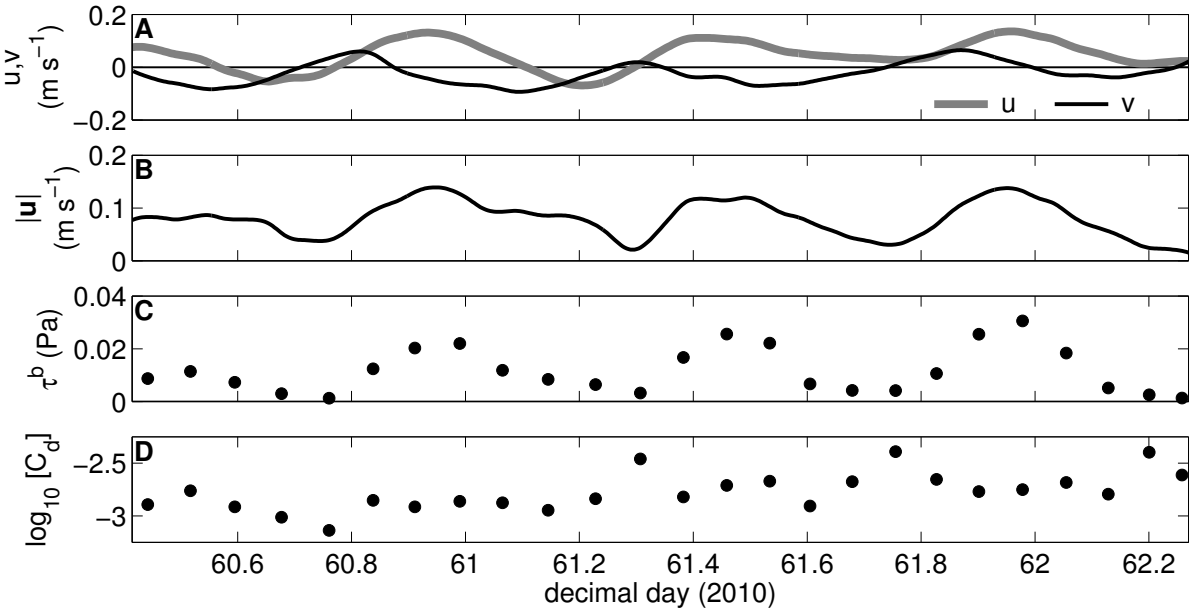

Figure 5.9: Time series of (a) near-bottom velocity components, (b) near-bottom speed, (c) bottom stress, and (d) quadratic drag coefficient. All quantities are based on 1-h low-pass filtered values obtained from the lowest bin of the 600 kHz ADCP (3 m above bottom). Bottom stresses are computed from near-bottom dissipation rates as described in the text.

times of very low current speeds when boundary-layer turbulence collapses and stratification effects become important. Maximum stresses do not exceed $\tau^b = 0.04$ Pa, which is about an order of magnitude smaller than the surface wind stress. Thus, although the bottom-stress is strong enough to create a nearly well-mixed bottom boundary layer of up to 4 m thickness (Fig. 5.8c), it will only have a relatively small impact on the near-inertial dynamics, at least for the relatively strong wind forcing at the time of our measurements.

5.3.4 Interior mixing

Mixing in the interior region above the bottom boundary layer (indicated by the grey lines in Fig. 5.8) is more energetic than in summer but exhibits a similar correlation between bands of elevated shear (Fig. 5.8d) and enhanced dissipation rates (Fig. 5.8b). Dissipation rates in the most energetic patches exceed $\varepsilon = 10^{-7}$ W kg^{-1}, which is also reflected in the turbulent diffusivities that may locally increase by almost an order of magnitude above the average value $K_\rho \approx 10^{-6}$ m^2 s^{-2} (Fig. 5.8e). Particularly interesting are the shear bands in the halocline slightly above 60 m depth that, in spite of decreasing wind speeds, lead to an intensification of mixing in this region after day 61 (Figs. 5.8b,d). As discussed above, part of this shear can be attributed to sub-inertial motions (Fig. 5.6e).

To investigate this aspect of mixing more closely, dissipation rates were averaged into logarithmically spaced bins of S^2 and N^2, exactly following the method described in Sec. 5.2.3.

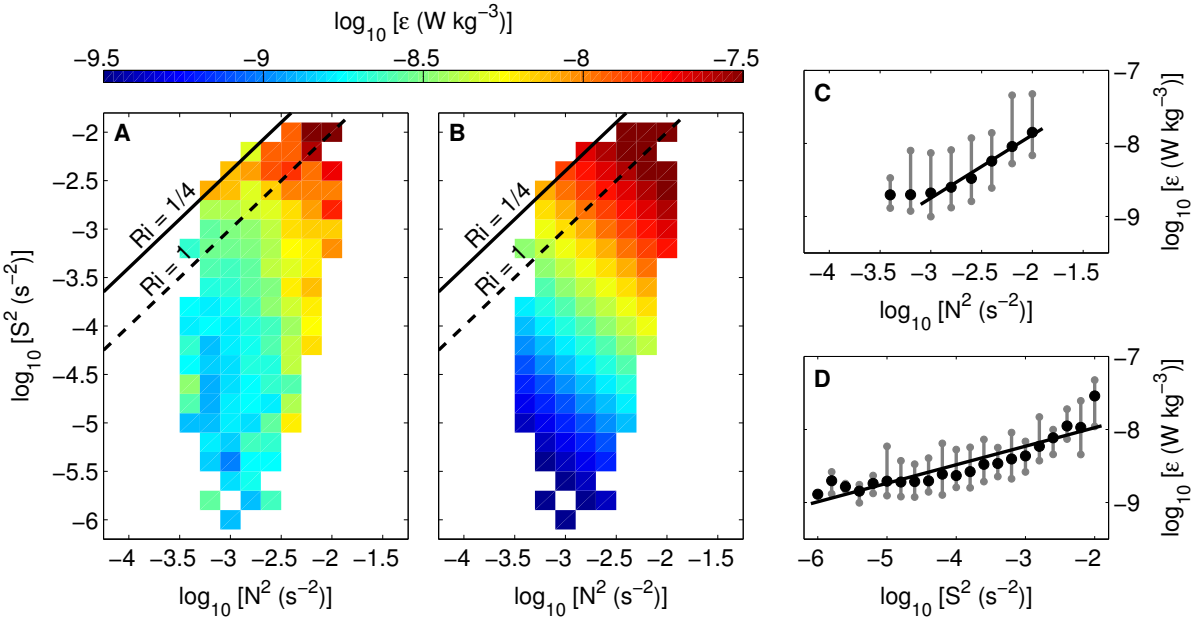

Figure 5.10: As Fig. 5.5 but now for the winter data set (interior region marked in Fig. 5.8). Panel (b) shows the parameterisation in (5.5) for $\varepsilon_0 = 1.7 \times 10^{-10}$ W kg^{-1}. Note that axes and color scales are identical to Fig. 5.5 for easy comparison.

Different here is only the smaller bin size of 1 m for the 600-kHz ADCP, and the associated reduction of the vertical filter width for stratification. Comparing the results for winter (Fig. 5.10a) and summer (Fig. 5.5a) reveals a similar parametric dependency on S^2 and N^2, however, with significantly enhanced energy dissipation levels during winter. The somewhat lower Richardson numbers found in winter may be partially due to the higher resolved shear associated with the small ADCP bin size. Good quantitative agreement with the parameterisation in (5.5) leads to $\varepsilon_0 = 1.7 \times 10^{-10}$ W kg^{-1}, only slightly larger than $\varepsilon_0 = 1.5 \times 10^{-10}$ W kg^{-1} found in summer. Averaging the observed two-dimensional dependency of the dissipation rate $\varepsilon(N^2, S^2)$ shown in (Fig. 5.10a) over S^2 and N^2, respectively, reveals clear trends in both quantities, as for the summer data (Fig. 5.10c,d).

The relative contributions of internal wave band and sub-inertial motions to the total shear are evaluated Fig. 5.11a, showing the average of S^2 over the complete period displayed in Fig. 5.8. The total shear is seen to be largely determined by the inertial shear for this long-term average, but it should be noted that, locally, the sub-inertial shear may occasionally become dominant (not shown). This is different from the long-term average of the kinetic energy shown in Fig. 5.11b, in which the total energy may be more than 6 times larger than the contribution from the internal wave band.

Comparing our model results from (5.5) with previous studies (Tab. 5.1) shows that the values for ε_0 found for the Baltic Sea are about one order of magnitude smaller than those previously reported for different sites on the continental shelves. In other words, for identical

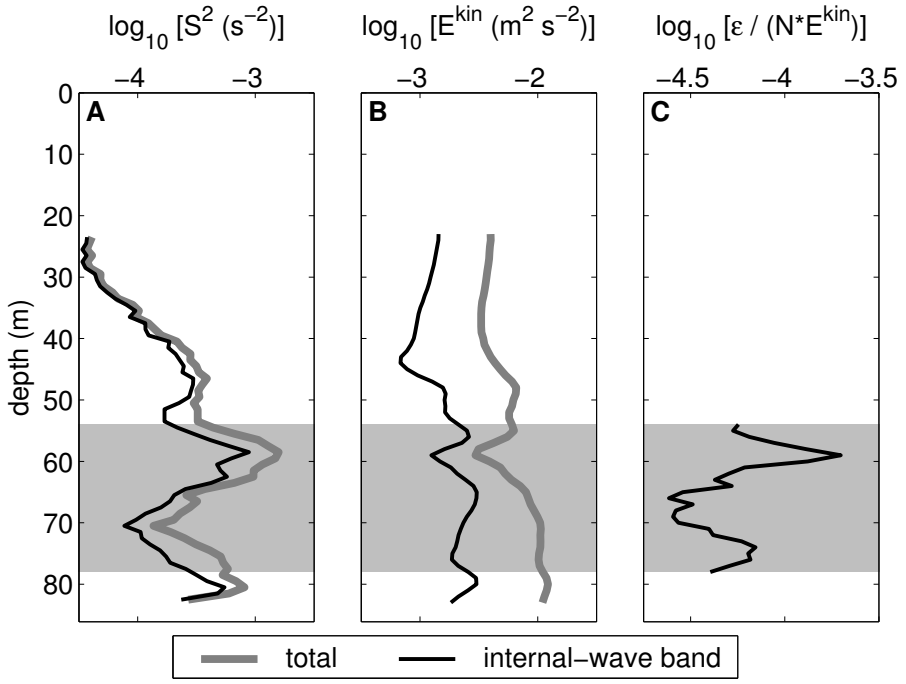

Figure 5.11: Profiles averaged over the period shown in Fig. 5.8 of (a) shear squared, (b) horizontal kinetic energy, and (c) dissipation rate normalised by NE^{kin}. Line coding as indicated in the legend. The grey areas represent the "interior" region marked in Fig. 5.8.

local shear and stratification parameters, dissipation rates at our measuring site are at least one order of magnitude smaller than those observed on the shelf. With this new data set, the total variability of ε_0 given in Tab. 5.1 increases to approximately two orders of magnitude. This clearly points towards a dependency of ε_0 (and, possibly, N_0 and S_0) on some properties of the small-scale internal wave field that do not directly depend on S^2 an N^2, and are not fully understood.

5.4 Conclusions

Internal-wave breaking has long been suspected to be one of the key mechanisms for mixing in the Baltic Sea below the depth levels directly affected by atmospheric forcing and coastal upwelling (*Stigebrandt*, 1987; *Axell*, 1998). In a recent review of mixing processes in the Baltic Sea, *Reißmann et al.* (2009) emphasised the ecological impact of deep-water mixing processes, but also pointed out that appropriate data for directly linking internal wave properties to observed mixing parameters are rare. The only exception we are aware of is the investigation of interior mixing in the central Baltic Sea by *Lass et al.* (2003), who suggested a scaling for the dissipation rate of the form $\varepsilon = \alpha_L NE$, where E is the total (potential plus kinetic) energy in the near-inertial wave field, and α_L a model constant. Assuming $E \approx E^{\mathrm{kin}}$, which is satistfied if near-inertial waves dominate the energy in the internal wave band (*Kundu and*

Cohen, 2008), this model was tested in Fig. 5.11c, showing $\alpha_L = \varepsilon/(NE)$. This ratio is seen to vary over an order of magnitude, and is moreover at least one order of magnitude smaller than $\alpha_L = 10^{-3}$ suggested by *Lass et al.* (2003). This failure of the model is little surprising, since our above analysis has clearly demonstrated that ε is correlated with the local shear, rather than with energy. A direct relationship between these two quantities does not exist because shear is associated with the higher modes that do not significantly contribute to the total energy (see Sec. 5.2.2), and probably also because sub-inertial motions, not taken into account in the internal wave model by *Lass et al.* (2003), may have a significant contribution.

From a modelling perspective, it is interesting to note that the shear and stratification parameters used to model the dissipation rate according to (5.5) are computed on vertical scales of the order of 1 m. Numerically, such resolution would require approximately 100 vertical layers for the given water depth, and probably less if vertically adaptive grids are used as recently suggested by *Hofmeister et al.* (2010). In the near future, this resolution will be computationally affordable, and the inclusion of finescale models like that in (5.5) will be the logical next step towards a more realistic representation of internal wave mixing that has so far been a weak point in numerical models.

In this chapter, focussing on the effect of near-inertial motions, the properties of the small-scale internal wave field have not been discussed, although it should be clear that they form an intrinsic part of the problem. This high-frequency part of the internal wave spectrum, and its relation to the low-frequency shear and mixing, is investigated in Chap. 6 with the help of data from additional fast-sampling moored instrumentation, deployed during the winter campaign at S1. Finally, it is important to note that this chapter has focussed on interior mixing, in spite of many indications for the importance of mixing processes near sloping topography. This aspect of the problem is currently investigated with the help of mixing data from the slope transect T1 shown in Fig. 2.1 that have been obtained simultaneously with the data discussed here.

Table 5.1: Observed variability of the model parameter ε_0 appearing in (5.5). ‡ *Johnston et al.* (2011) used 16-m shear instead of 4-m shear, ε_0 would be approx. halved if 4-m shear were used.

Paper	Area	Time	N_0 (cph)	S_0 (cph)	ε_0 (W kg^{-1})
MacKinnon and Gregg (2003b)	New England shelf	Aug/Sep 1996	3	3	6.9×10^{-10}
MacKinnon and Gregg (2005b)	New England shelf	Apr/May 1997	3	3	1.1×10^{-9}
Carter et al. (2005)	Monterey Bay shelf	Aug 1997	3	3	6.1×10^{-9}
Sundfjord et al. (2007)	Barents Sea	Jul/Aug 2004 + May/Jun 2005	3	3	4.5×10^{-8}
Palmer et al. (2008)	Celtic Sea	Aug 2003	6	6	1.75×10^{-8}
Schafstall et al. (2010)	Mauritanian shelf	Jul 2006 - Feb 2008	3	1.3	1.6×10^{-8}
Liu (2010)	Clyde Sea	Jul 2002	3	3	1.5×10^{-8}
Johnston et al. (2011)‡	Monterey Bay ridge	Aug 2006	3	3	7.5×10^{-8}
van der Lee and Umlauf (2011)	Baltic Sea	Sep 2008	3	3	1.5×10^{-10}
van der Lee and Umlauf (2011)	Baltic Sea	Feb/Mar 2010	3	3	1.7×10^{-10}

6 Waves near the buoyancy frequency

6.1 Introduction

After studying near-inertial waves in the previous chapter, this chapter will focus on the other natural frequency limit of internal waves: the buoyancy frequency N. As derived in Sec. 1.2 the level of stratification determines the upper frequency limit with stronger stratification (higher N) providing a stronger restoring force and thus faster oscillations. Therefore, opposed to near-inertial waves, the wave frequency is dependent upon depth and is maximal in pycnoclines. Frequencies higher than the buoyancy frequency do not represent freely propagating internal waves anymore, but are evanescent waves, instabilities or other turbulent phenomena. In this chapter the pathway of wave energy cascading from near-inertial waves to high-frequency waves and on to turbulent dissipation is followed. This decay process is especially easily observed in the wake of winterstorm Xynthia.

6.1.1 Near-N wave motions

The classical picture of internal wave dynamics in the open ocean describes the generation of energy at large wavenumbers and frequencies as a result of non-linear (triad) interactions, leading to a quick relaxation of spectral shapes towards the canoncial Garrett-Munk spectrum (*Thorpe*, 2005). Based on the idea that this spectral energy transport is ultimately dissipated by shear-instabilities of small-scale internal waves near the buoyancy frequency, a number of bulk parameterisations of internal wave mixing have been developed for the open ocean (*Gregg*, 1987; *Polzin et al.*, 1995; *Gregg et al.*, 2003), as well as for the continental shelves (*MacKinnon and Gregg*, 2003b). In the previous chapter, it has been shown that the latter model provides an excellent description of internal wave mixing also for the Baltic Sea.

However, other, more direct generation mechanisms for internal waves near the buoyancy frequency have also been suggested. Particularly relevant for the topographically constrained basins of the Baltic Sea are a number of studies in lakes, which have shown pronounced spectral peaks near the buoyancy frequency (*Antenucci and Imberger*, 2001a; *Boegman et al.*, 2003). As one possible explanation, linear stability analysis suggested that these motions are shear instabilties resulting from basin-scale internal shear. *Antenucci and Imberger* (2001b) also observed a correlation of the wind velocity, the surface layer shear and the phase of the basin-wide seiche. Internal waves with a frequency near N often have a low-modal structure and occur in packets or groups (e.g. *Antenucci and Imberger*, 2001a). Although from a completely

different context, these findings may be related to a recent study of mixing in the equatorial undercurrent by *Moum et al.* (2011) and *Smyth et al.* (2011), who explained the prominent spectral peak near N as a result of the random superposition of shear-instabilities.

In view of the fact that the Baltic Sea is rather shallow, it is also likely that motions in the upper part of the stratified interior are directly affected by processes in the surface layer. From some ideas previously suggested for the atmosphere (e.g., *Townsend*, 1965, 1966, 1968), *Bell* (1978) argued that high-frequency internal waves may also be generated directly by the interaction of inertial oscillations with the mixed layer base without the cascading of energy through intermediate frequencies. More recent laboratory studies have confirmed that different types of surface-layer turbulence effectively generate internal wave motions at the base of the mixed layer. This turbulence-wave interaction mechanism was shown to be strongly selective for waves near the buoyancy frequency (*Dohan and Sutherland*, 2003, 2005; *Ansong and Sutherland*, 2010). *Polton et al.* (2008) included Stokes drift and Langmuir circulation, and showed from their Large Eddy Simulations that, if these are also taken into account, the energy is radiated downward with the horizontal direction of the high-frequency waves matching that of the inertial motions in the surface layer minus a small lag.

Finally, the generation of short internal wave is known to be associated with the degeneration of large-scale motions near sloping topography in a stratified basin. Given the fact that even the largest basins of the Baltic Sea are strongly affected by lateral topography, it is likely that this is a relevant process at our observation site. While in the ocean internal wave generation near sloping topography if often dominated by internal tides, it has also been described in both observations (*Boegman et al.*, 2005; *Lorke*, 2007) and numerical simulations (*Vlasenko and Hutter*, 2002) of stratified basins without tides.

6.1.2 Baltic Sea investigations of high-frequency internal motions

Internal wave motions in the Baltic Sea have been studied since the early days of physical oceanography but the extent of available data focussing on the high-frequency part of the spectrum is suprisingly small. Most attention has been given to near-inertial waves discussed in the previous chapter (e.g. *Gustafson and Kullenberg*, 1933; *Kielmann et al.*, 1973; *Lass et al.*, 2003; *Nerheim*, 2004), although high-frequency waves have long been known to exist; Schumacher (in *Neumann*, 1946) found temperature fluctuations at 18 m depth in the Fehmarnbelt region with a period of 3.5 min. Geographically close, in the Kiel Bight, an energy peak was found at a period of 2 min in velocity and temperature records (*Hollan*, 1966a,b).

In more recent times, observational investigations about high-frequency motions in the Baltic Sea are extremely rare. One notable exception is the short paper by *Morozov et al.* (2007) describing measured internal wave spectra from the halocline region of the Gdansk

Deep. Towed isotherm displacement spectra were shown to have a slope similar to the Garrett-Munk spectrum (see Sec. 1.1 and below), but energy densities were approximately an order of magnitude lower. This finding is consistent with moored velocity and displacement spectra from the deep Gotland Basin discussed in *Holtermann and Umlauf* (2012), who also reported spectral slopes in accordance with GM but substantially lower energy levels.

Talipova et al. (1998) and *Kurkina et al.* (2011) calculated properties of the internal wave field in the Baltic Sea based on typical stratification profiles, using the extended Korteweg–de Vries equation. Theoretical phase velocities reached up to 1 m s^{-1} in the Eastern Gotland Basin, but were strongly dependent on depth so that for a 100 m deep water column $c \approx$ 0.4 m s^{-1} (*Talipova et al.*, 1998). However, in the absence of direct observations of internal wave motions, these results could not be verified.

6.2 Overview and background conditions

Before focussing on the high-frequency part of the spectrum, in the following a brief recapitulation of the background conditions during the cruise in February and March 2010 is given.

Over the course of the measurements at S1 the wind turned clockwise during the winter-storm Xynthia with wind speeds increasing to values above 15 m s^{-1} (Fig. 6.1a). Surface layer speeds exceeded 0.3 m s^{-1} immediately following the wind event, whereas maximum speeds in the halocline where reached with a delay of approximately half a day (Fig. 6.1b,c). After the maximum velocities died down, clockwise near-inertial motions became visible in the sub-pycnocline region. These motions were already set up during the storm in the surface layer, but were masked by the superimposed northeastward current. Their arrival in the deeper layer followed a delay of approximately 0.5 days, which, as argued in Chap. 5, is probably due to the later arrival of higher internal wave modes generated at the lateral boundaries of the basin. The vertical shear induced by these motions, in addition to the sub-inertial shear, was found to be highly correlated with enhanced dissipation rates in the halocline and sub-halocline regions (see Chap. 5). Apart from rare exceptions, Richardson numbers ($Ri = N^2/S^2$) were substantially larger than the critical value ($Ri < 0.25$) for shear instability, which is either an artefact attributable to the limited vertical resolution of our measurements, or due to additional shear provided by high-frequency internal wave motions that were filtered out before computing the low-frequency shear. These points will be discussed in more detail in the following.

The time periods of microstructure measurements are indicated in Figs. 6.1b,c with period `I` representing the "before storm" situation, and periods `II` & `III` the "after storm" situation. From the "during storm" period only mooring data are available; the section indicated by a grey box will be focussed on later.

As discussed in Chap. 4, the surface and bottom mixed layers were comparatively thin

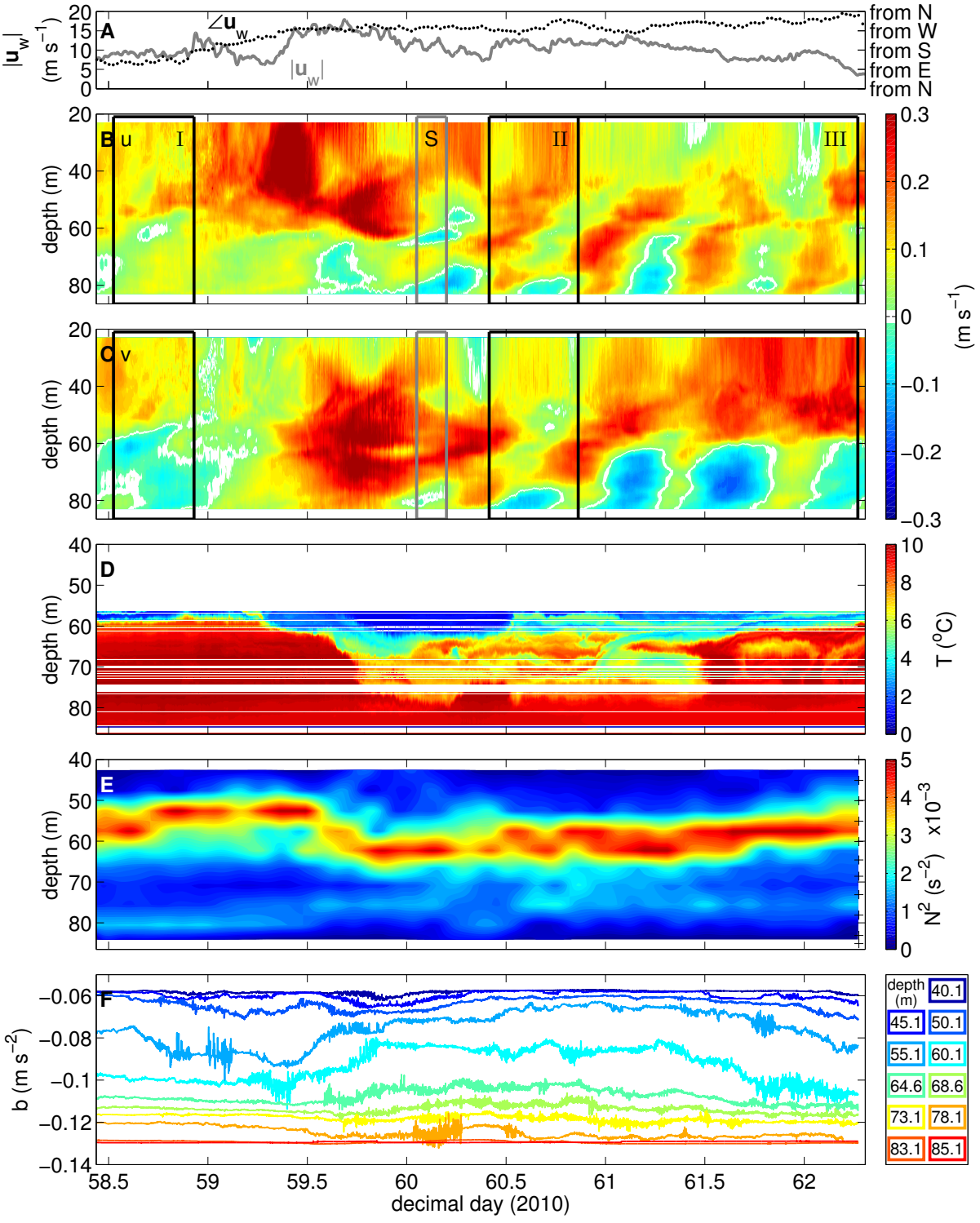

Figure 6.1: Time series of (a) wind speed $|\mathbf{u}_w|$ and direction $\angle\mathbf{u}_w$, (b) east velocity u, (c) north velocity v, (d) temperature T, (e) buoyancy frequency squared N^2, and (f) buoyancy b. The black boxes and roman numerals in (b,c) indicate the periods of MSS measurements while the grey box indicates the "during storm" period of Sec. 6.4. The black plusses in (e) are the depth levels of the microcats.

before the storm so that the water column between 17 and 84 m remained stratified ($N^2 > 5\times10^{-5}$ s^{-2}). Stratification consisted of a sharp inverse thermocline around 59 m, a much more gradual halocline at 50–70 m depth, and a weaker stratified deep layer (Fig. 4.8). Temperature data (Fig. 6.1d) from the densely spaced and highly accurate NIOZ thermistors (Sec. 2.3) clearly illustrate this sharp, inverse thermocline at the upper end of the thermistor chain. The storm brought on the quick descend and broadening of the thermocline between days 59.5 and 60. During and after the storm, small-scale intrusions appeared that were most pronounced in the layer between 60 and 70 m depth. High-frequency fluctuations are also captured by the high-resolution thermistor chain. These motions are barely visible on the scale of this plot but will be studied in great detail below. Around day 61.5 the temperature in 60–70 m depth jumped up from 4°C to 9°C, and the thermocline was restored roughly to pre-storm depth albeit with frequent temperature inversions.

Despite the chaotic temperature signal, density stratification remained stable throughout the observation period due to the dominant influence of salinity. This can be seen in Fig. 6.1e from a time series of the squared buoyancy frequency N^2 defined in (4.2) and calculated from low-pass filtered densities measured by the microcats on mooring TSC2. Although the depth of the main pycnocline varied, its strength remained relatively stable with values around $N^2 = 4-5\times10^{-3}$ s^{-2}. Fig. 6.1f shows the individual buoyancy time series for the 11 microcats, revealing the stochastic and intermittent nature of the high-frequency buoyancy fluctuations that exhibit on weak correlation in depth.

6.2.1 Spectral analysis of high-frequency motions

For the following spectral analysis, high-frequency buoyancy fluctuations b' were converted to isopycnal displacements according to the relationship:

$$\zeta_b = \frac{b'}{\frac{\partial b_{LP}}{\partial z}} = \frac{b'}{N^2} \quad , \tag{6.1}$$

where b_{LP} denotes the 4-hour low-pass filtered (8$^{\text{th}}$-order Butterworth) buoyancy such that $b' = b - b_{LP}$. The filter width was motivated by the time scale for the low frequency variations in N^2 evident, e.g. in Fig. 6.1e. Central differencing was used to calculate the buoyancy gradient for microcat number n:

$$\zeta_b(n) = b'(n) / \left[\left(b_{LP}(n+1) - b_{LP}(n-1) \right) / \left(z(n+1) - z(n-1) \right) \right] \quad , \tag{6.2}$$

except for the top and bottom microcats, for which one-sided differencing was used instead.

Fig. 6.2a shows the resulting time series of displacements, highlighting the depth-incoher-

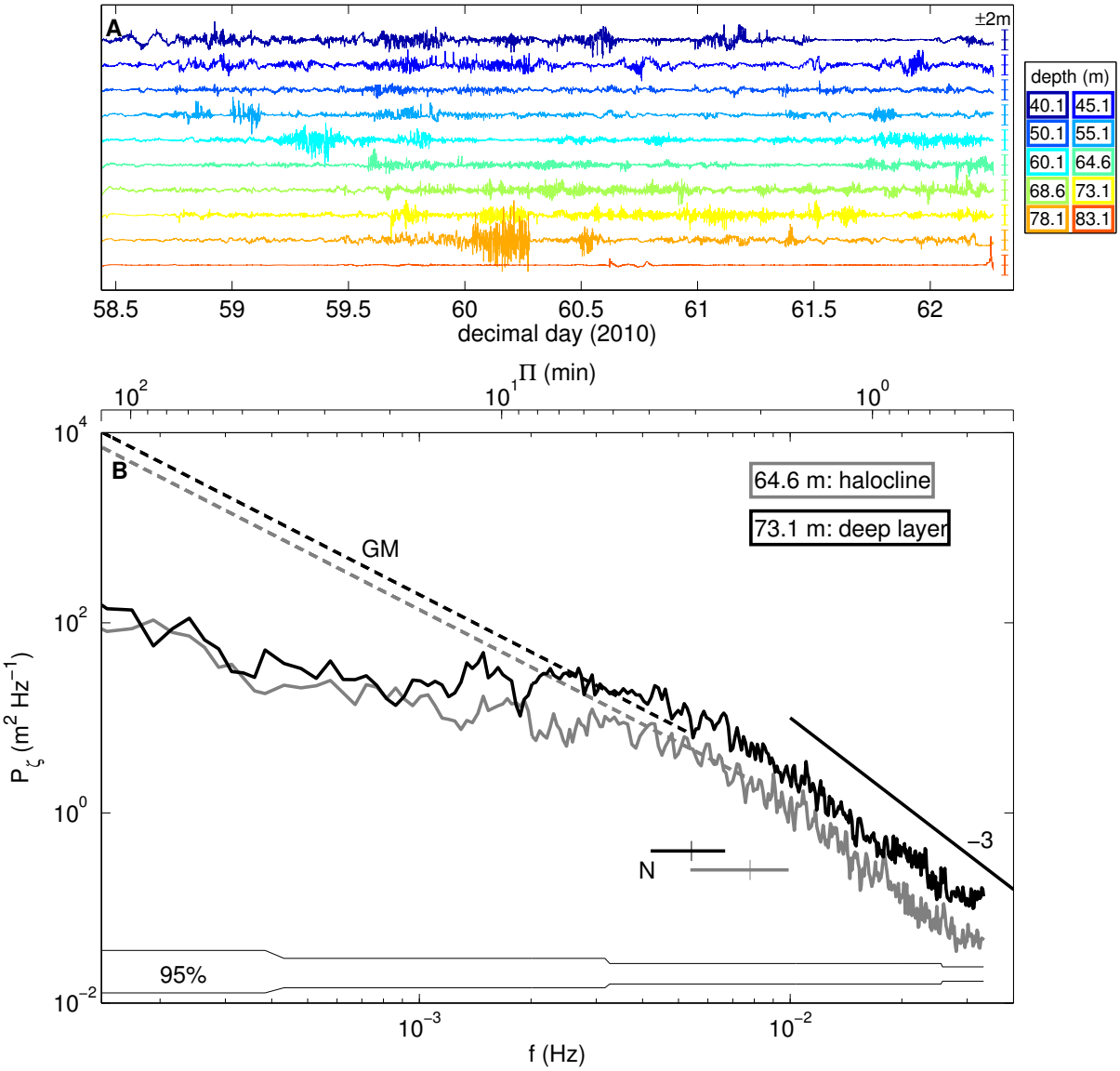

Figure 6.2: (a) Time series of isopycnal displacement (see individual ± 2 m axes on right-hand side) and (b) spectra of isopycnal displacement at 2 depths: 64.6 m (grey) and 73.1 m (black). For each depth a dashed line indicates the Garrett-Munk spectrum for the mean value of N, indicated by a vertical line in the horizontal bar showing the range of N-values encountered over the whole time series. Also shown for $f > N$ is a -3 slope.

ence and intermittency of the records. Displacements are typically less than 0.5 m in the deeper layers during the pre-storm period, increasing to values around 2 m in the intermittent patches observed during the windy period. Maximum displacements of 5.4 m at 60.1 m and of 7.9 m at 78.1 m depth were reached only in the deeper layers where stratification is comparatively weak (displacements for the deepest microcat, partly located in the bottom boundary layer, are not shown because the virtual absence of stratification leads to unrealistically large displacements.)

For the two depth levels representing the halocline region and the weakly stratified layer

underneath, displacement spectra are shown in Fig. 6.2b (only periods larger than the 4-h filter cutoff used for the computation of the displacement timeseries are displayed, see above). For comparison, Fig. 6.2b also includes the Garrett-Munk (GM79) spectrum based on *Garrett and Munk* (1979) as given by *Munk* (1981) and *Müller et al.* (1986), using local values for the Coriolis parameter f_i and the mean measured N:

$$E_{GM}(\omega) = \frac{2}{\pi}\, b_{GM}^2\, E0_{GM}\, N0_{GM}\, \frac{f_i}{N\omega^3}\, \sqrt{\omega^2 - f_i^2} \tag{6.3}$$

where b_{GM} is the scale depth of 1.3 km for the (assumed) exponentially stratified ocean: $N(z) = N0_{GM}e^{z/b_{GM}}$. $E0_{GM}$ represents the nondimensional energy parameter of 6.3×10^{-5} and $N0_{GM} = 3$ cph is the "*Brunt-Väisälä frequency at the top of the thermocline (extrapolated from abyssal depths)*" (*Garrett and Munk*, 1975).

Observed spectra are almost flat and substantially less energetic than GM79, except for a narrow frequency range in the vicinity of the buoyancy frequency, where the energy levels of the canonical spectrum are approximately reached (Fig. 6.2b). Internal wave energy levels substantially lower than the Garrett-Munk spectrum have been reported before for the Baltic Sea. However, those previous studies from the neighbouring Gotland Basin (*Lass et al.*, 2003; *Morozov et al.*, 2007; *Holtermann*, 2011) have observed spectral slopes to correspond to the -2 slope of the model spectrum. This suggests that the internal wave dynamics in the Bornholm Basin is somewhat different from the deeper Gotland Basin.

Above the buoyancy frequency, i.e. for frequencies that cannot represent internal wave motions any more, spectra drop off quickly with a slope of approximately -3 (Fig. 6.2b), consistent with the value for strongly stratified turbulence. Interpreting these results, it should be noted, however, that background conditions were extremely variable during the measurements, and the observed spectra are barely representative for any typical mean state. In fact, as shown below, spectral slopes from the periods before and during the storm exhibit rather different behaviour compared to the average spectrum for the whole time series shown in Fig. 6.2b.

In order to investigate the temporal evolution of spectral energy levels in more detail, the displacement time series were divided into 90 half-overlapping 2-hour windows for which individual spectra were computed. The results are presented in Figs. 6.3b,c for the two depth levels corresponding to the spectra shown in Fig. 6.2b. Clearly visible is the sudden increase of spectral energy associated with the rising wind speeds (Fig. 6.3a) after day 59.5, where the lower layer shows a small delay compared to the halocline. Spectral levels are seen to be highly intermittent but of the same order of magnitude in both layers. Intermittent events are, however, only weakly correlated in depth, which, given the close proximity of sensors, is rather surprising. An example for this are the low energy levels in the halocline around day 61.5 that are contrasted by high spectral energy in the deeper layer (Fig. 6.3b,c).

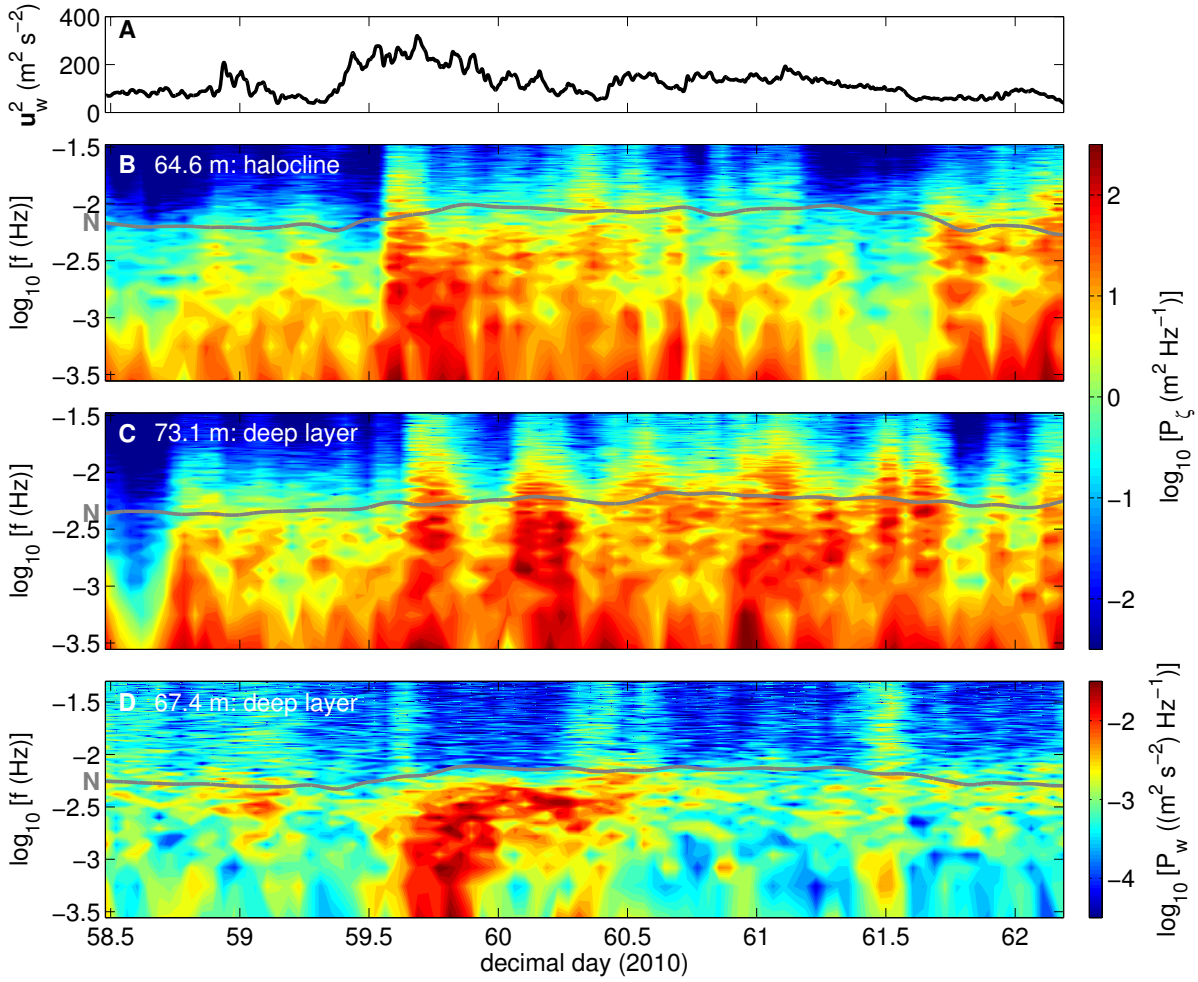

Figure 6.3: Time series of wind speed squared (a). Periodograms of isopycnal displacement at the 2 depths of Fig. 6.2b: (b) 64.6 m, and (c) 73.1 m. Periodogram of vertical velocity at 67.4 m depth (d).

A similar approach was used to visualise the temporal variablity of the high-frequency vertical velocity fluctuations inferred from the ADCP at S1. To this end, the unfiltered vertical velocity time series at the depth of 67.4 m was divided into half-overlapping 2-hour windows for the spectral analysis. The result shown in Fig. 6.3d illustrates the rapid increase of the spectral levels during the wind event that, analogously to behaviour of the displacement spectra shown in Figs. 6.3b,c. However, there are a number of remarkable differences that are difficult to explain from linear internal wave theory. While elevated displacement spectra are observed during the whole period following the storm event, for the vertical velocities this is the case only for the short period on days 59.5–60.5. Moreover, between days 60.0 and 60.5, vertical kinetic energy shows a narrow-band excitation of frequencies slightly below the buoyancy frequency, which is contrasted by the broad-band distribution of displacement spectra that exhibit no significant peak near N. For both types of spectra, however, energy rolls off quickly for frequencies higher than the buoyancy frequency. It should be noted that vertical velocity

spectra at high frequencies are occasionally affected by vertically migrating plankton species or fish (identified from backscatter data) such that the significance of velocity spectra for frequencies above N is somewhat unclear (this is not the case for displacement spectra).

In the following, the effect of the wind event, in particular the generation of high-frequency internal motions, will be investigated in more details by focussing on two different periods. Period `I` (see Fig. 6.1) is chosen to represent typical background conditions during moderate wind forcing, whereas the storm period (labelled S in Fig. 6.1) will be used to analyse the situation an extreme event.

6.3 High-frequency motions before the storm

In view of the weak correlation between density measurements at neighbouring microcat CTD loggers discussed above, the availability of data from the high-resolution thermistor chain (sensor spacing: 0.2 m) will be of great use for the following analysis. However, in spite of this obvious advantage, the interpretation of temperature data is somewhat complicated by the fact that the omnipresence of intrusions (see Fig. 6.1f) destroys any systematic relationship between temperature and density. These difficulties could only partly be overcome by carefully selecting periods and depth levels with smooth temperature gradients, where high-frequency temperature fluctuations could be converted to isotherm displacements following the method described in the context of (6.1). For this analysis, the filter cutoff used to separate the background gradient from the high-frequency fluctuations had to be reduced to 5.5×10^{-4} Hz (period: 30 minutes) because, for lower frequencies, temperature fluctuations due to internal wave motions and intrusions could no longer be separated.

Two examples where a straightforward interpretation of high-frequency temperature fluctuations was possible are shown in Fig. 6.4. This figure illustrates the first two hours of the temperature variability during period `I` at two depths: within the halocline and within the deep stratified layer (see Fig. 6.1e). Both the full temperature record, and the low-pass filtered temperature T_{LP} used to calculate the vertical background gradient are shown, where it should be noted that the temperature gradient changes sign between the two depth levels shown in Fig. 6.4. Already by visual inspection, it is evident that fluctuations are very coherent over the 1-m depth intervals shown in Fig. 6.4 with higher frequencies observed in the halocline layer (consistent with larger values of N).

Isopycnal and isotherm displacement spectra for the halocline and deep layers, respectively, for the whole duration of period `I` are displayed in Fig. 6.5. When interpreting these results it is important to note that temperature fluctuations can also be caused by lateral (isopycnal) advection of temperature variance, whereas buoyancy fluctuations are directly associated with isopcynal displacements (under the assumption that mixing does not have a dominant effect

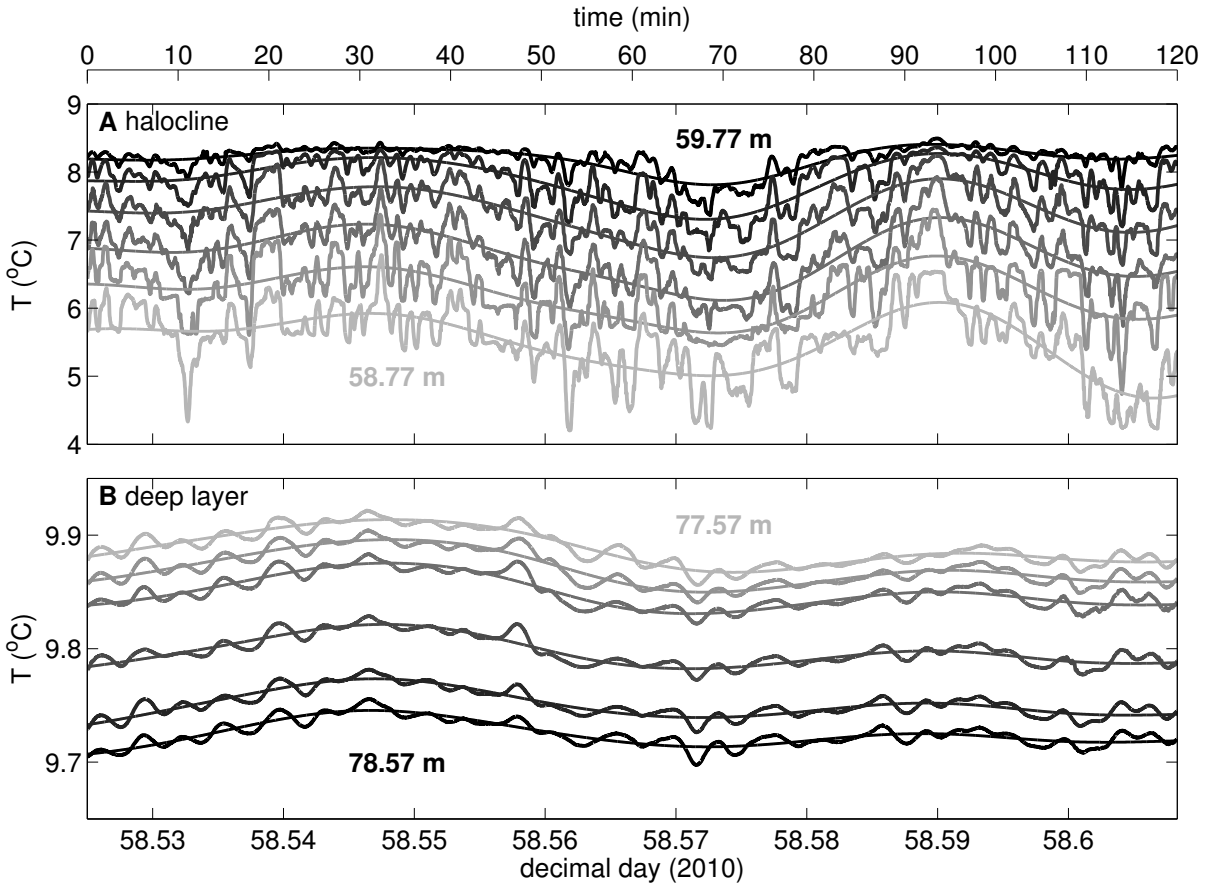

Figure 6.4: Time series of temperature fluctuations over the first two hours of MSS period I (a) within the halocline at $\sim$ 59 m and (b) within the deep stratified layer at $\sim$ 78 m. Shown are temperature records of 6 neighbouring thermistors (shallow/light to deep/dark) and their half-hour-filtered quantities (thin lines).

on such small time scales).

The close agreement of displacement spectra computed with both methods for frequencies below the buoyancy frequency suggests that temperature fluctuations inside the internal wave band are not strongly affected by lateral advection (Fig. 6.5). This will be useful for the further interpretation of the high-resolution temperature records below. Spectral slopes in this frequency range (2 h–2 min) are steeper than those shown in Fig. 6.2b but still less steep than the -2 slope of the Garrett-Munk spectrum.

For frequencies higher than the buoyancy frequency, isotherm and isopycnal displacement spectra drop off, and start to diverge, indicating that ζ_T spectra are increasingly affected by lateral advection. While the buoyancy spectra do not exhibit a universal behaviour in this high-frequency range (e.g. spectral slopes differ between both depth levels), temperature spectra converge to a slope of approx. -2. This slope provides a discernibly better fit to the high-frequency range than the classical $-5/3$ slope for turbulence spectra, which forms a somewhat puzzling result. One possible explanation was provided by *Phillips* (1971), who

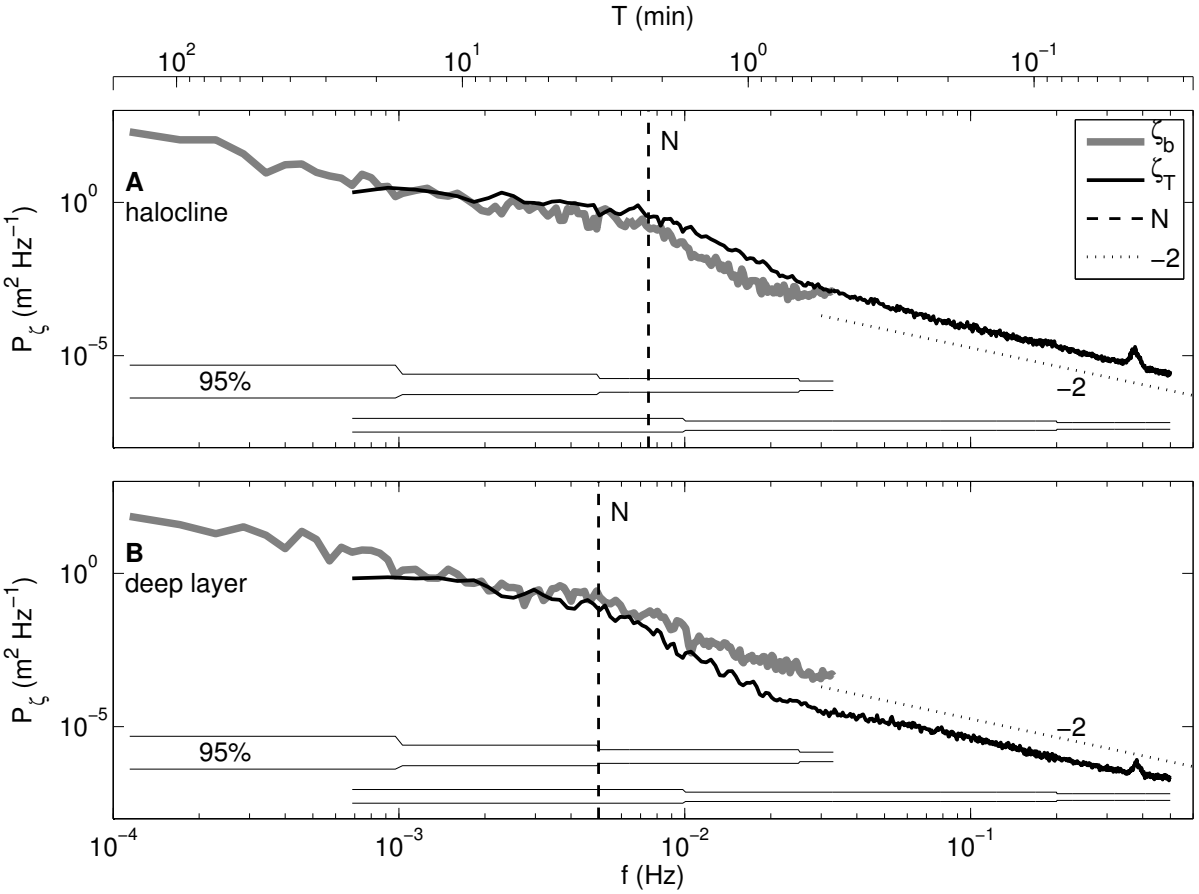

Figure 6.5: Displacement spectra of microcat isopycnals (thick, grey) and thermistor isotherms (thin, black) over MSS period `I` at (a) 60.1 m (ζ_b) and 59.2–59.6 m (ζ_T) depth and at (b) 78.1 m (ζ_b) and 78.0–78.4 m (ζ_T) depth (ζ_T spectra are averages over 3 spectra). Also indicated are mean N (from MSS at this depth level over period `I`), 95% confidence intervals and a slope of -2.

pointed out that the advection of randomly distributed steppy structures past a sensor is mirrored in a spectral slope of -2. This would indicate a streaky temperature distribution on isopycnals, consisting of small-scale patches with a homogeneous temperature separated by sharp boundaries.

Finally, it is worth noting that the spectral peak at 0.38 Hz ($\Pi = 2.6$ s) is most likely related to vertical oscillations of the mooring cable, probably induced by the action of surface waves on the floatation element at the top end of the thermistor chain. It does therefore not represent an internal physical process.

The extent to which these high-frequency motions are vertically coherent is investigated in Fig. 6.6a, showing the squared coherency γ_b^2 between buoyancy fluctuations at two neighbouring microcats in the region just below the halocline. In spite of the relatively small distance (4 m) between both instruments, values inside the internal wave band rarely exceed $\gamma_b^2 = 0.5$, pointing at a destructive interaction of modes. The coherency for frequencies above N drops

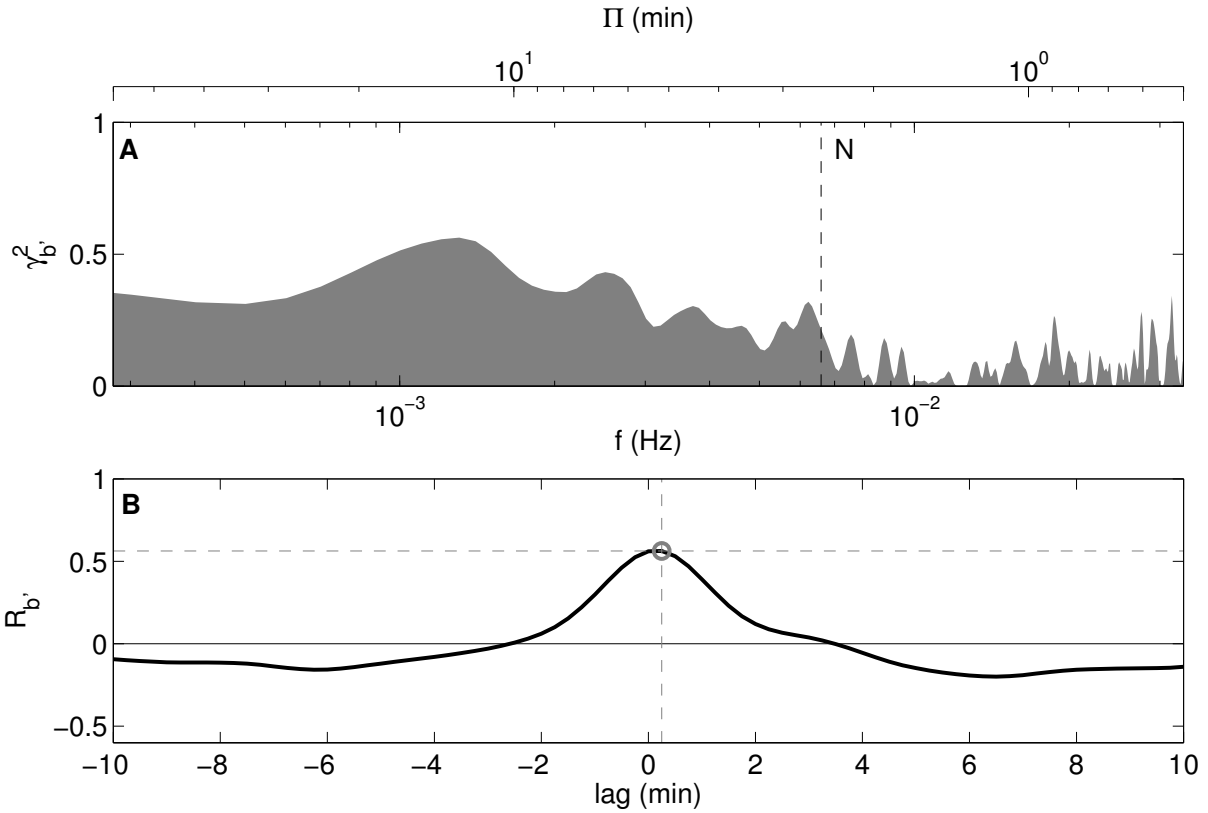

Figure 6.6: (a) Squared coherence, and (b) lagged cross-covariance of buoyancy fluctuations from two microcats at 64.6 m and 68.6 m depth during period I.

quickly to even lower values. The normalised lagged cross-covariance confirms a net correlation coefficient around 0.5, and does not reveal any signficiant phase lag (Fig. 6.6b).

A more refined view of the vertical correlations in the high-frequency band can be constructed with the help of data from the high-resolution thermistor chain. One important limitation of this approach that should be kept in mind is related to the fact that isopycnal displacements do not cause significant temperature fluctuations in the vicinity of local extrema of the background temperature. At these locations, the method spuriously underestimates the true coherency of isopcnal displacements.

Fig. 6.7a, focussing on vertical correlations with respect to a reference thermistor inside the halocline region, reveals that coherencies above 0.5 are confined to a narrow band of only a few meters thickness, consistent with the weak coherency inferred for the microcats (see above). For frequencies above the local buoyancy frequency, no significant correlation can be observed any more. For the deeper reference thermistor at 78.0 m depth (Fig. 6.7b), the depth-band of high-correlation ($\gamma^2_{T'} > 0.5$) is wider but asymmetrically distributed about the reference level. The rapid decay of coherency above the reference level can, however, be explained as a spurious result due to the vanishing temperature gradients (and thus vanishing temperature fluctuations) in this region (see above). Overall, it can be concluded that internal

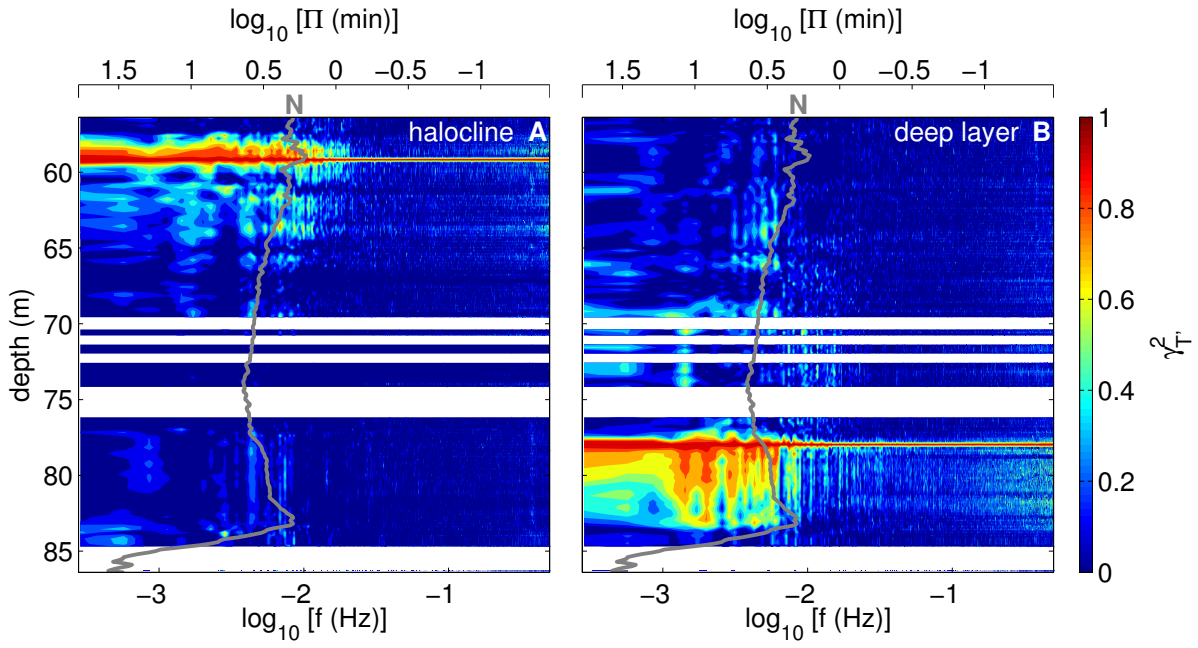

Figure 6.7: Coherency per frequency band over depth for period I, with reference levels at (a) 59.2 m and (b) 78.0 m. The grey line is the mean MSS N-profile over period I.

wave motions in the deep layer exhibit a substantially larger vertical correlation than in the halocline region.

6.4 High-frequency motions during the storm

During the time of strong wind forcing there was a period with highly vertically coherent (in velocity) motions near the buoyancy frequency that will be analysed in detail in the following. We will concentrate on days 60.05–60.2, where the velocity spectra shown in Fig. 6.3d exhibit a particularly strong peak near N. During this time, high-frequency waves are easily spotted in both the high-resolution temperature and vertical velocity fields (Figs. 6.8a,d), while background conditions in terms of stratification and shear (Figs. 6.8b,c) do not change qualitatively over this 3.6 hour time span. Note that since the temperature and velocity records have been derived from different moorings, separated by a distance of a few hundred meters, no direct correlation in the high-frequency band can be expected but in a statistical sense these neighbouring location may still be compared. To this end, sub-time series for temperature and velocity have been extracted as indicated by the black boxes in Figs. 6.8a,d.

The temperature sub-section is shown in Fig. 6.9a for the depth level of the halocline. As for the pre-storm timeseries, temperature fluctuations are highly coherent over the 1 m depth interval shown here, reaching up to 2.5°C with a period of $\sim$ 4 min. Corresponding

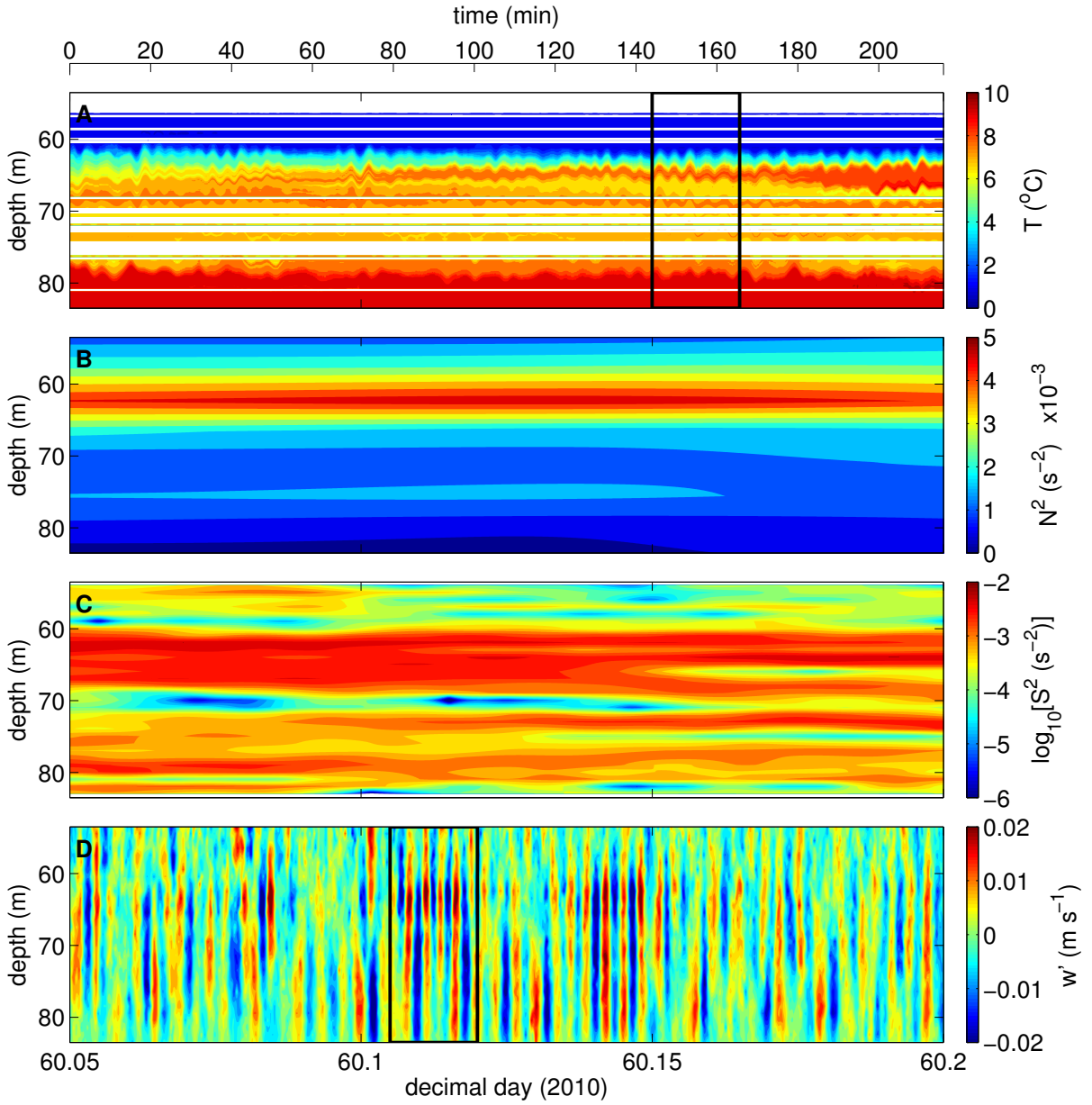

Figure 6.8: Close up of storm time series of (a) temperature, (b) buoyancy frequency squared, (c) shear squared, and (d) vertical velocity fluctuations. The black box in (a) denotes the time period shown in Fig. 6.9a, and the box in (d) the time period of Fig. 6.13.

displacements are of the order of 1 m. Calculated over the whole time period of Fig. 6.8 are the spectra of displacement in the halocline (Fig. 6.9b). The agreement between the buoyancy and isotherm displacement for their overlapping frequencies is even better than before the storm. Compared to the pre-storm period, spectral slopes in the internal wave-band are nearly flat which may be explained by excess energy near the buoyancy peak. Overall the energy levels are higher than before the storm, e.g. by a factor 3 at $\Pi = 0.1$ min. Particularly interesting is the fact that, as for the pre-storm period, temperature spectra in the high-frequency range

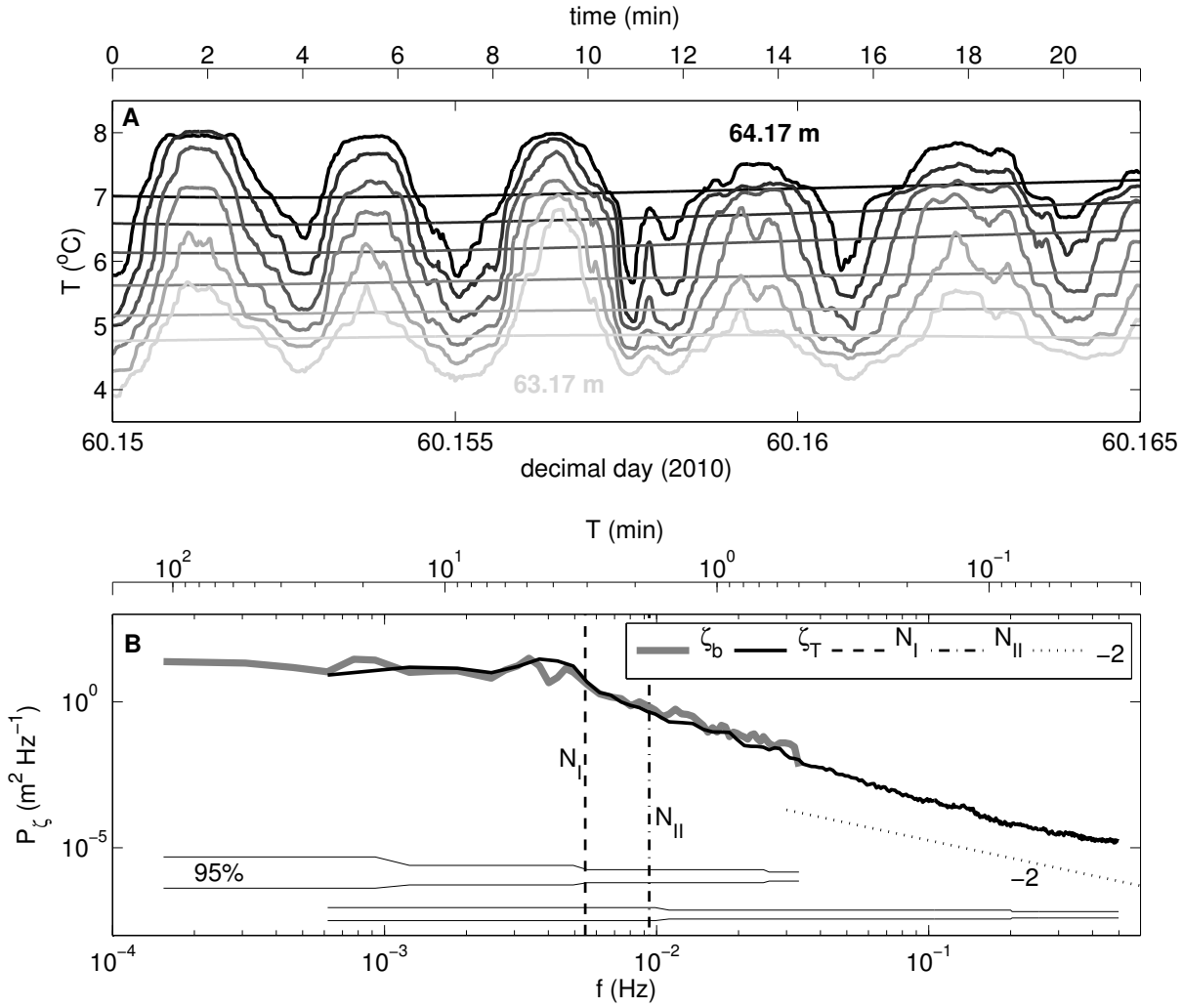

Figure 6.9: (a) Temperature fluctuations of 6 neighbouring thermistors (shallow/light to deep/dark) and their half-hour-filtered quantities (thin lines) at $\sim$ 63.7 m over the time period indicated by the black box in Fig. 6.8a. (b) Displacement spectra for the complete period shown in Fig. 6.8 at 64.6 m (ζ_b) and 63.6–64.0 m (ζ_T). N_{I} and N_{II} show mean N at 64.6 m depth over the last 15 MSS profiles before and the first 15 profiles after the storm respectively.

above N approach a slope of appoximately -2, for which the same explanation as above may apply.

Fig. 6.10 and Fig. 6.11, comparing the vertical correlation of buoyancy and velocity fluctations during the storm period, reveal a number of puzzling features. In spite of a very clear high-frequency signal in the vertical velocity (Fig. 6.9d) and substantially higher energy levels in the high-frequency band compared to the period with moderate wind forcing, the vertical coherency of buoyancy fluctuations in the halocline region exhibits a dramatic break-down (Fig. 6.10a). Also the maximum of the lagged correlation factors collapses to values near $R_{b'} = 0.3$, about a factor of 2 smaller compared to the pre-storm period (Fig. 6.10b). These values are, however, strongly contrasted by high coherencies and correlation factors (both close

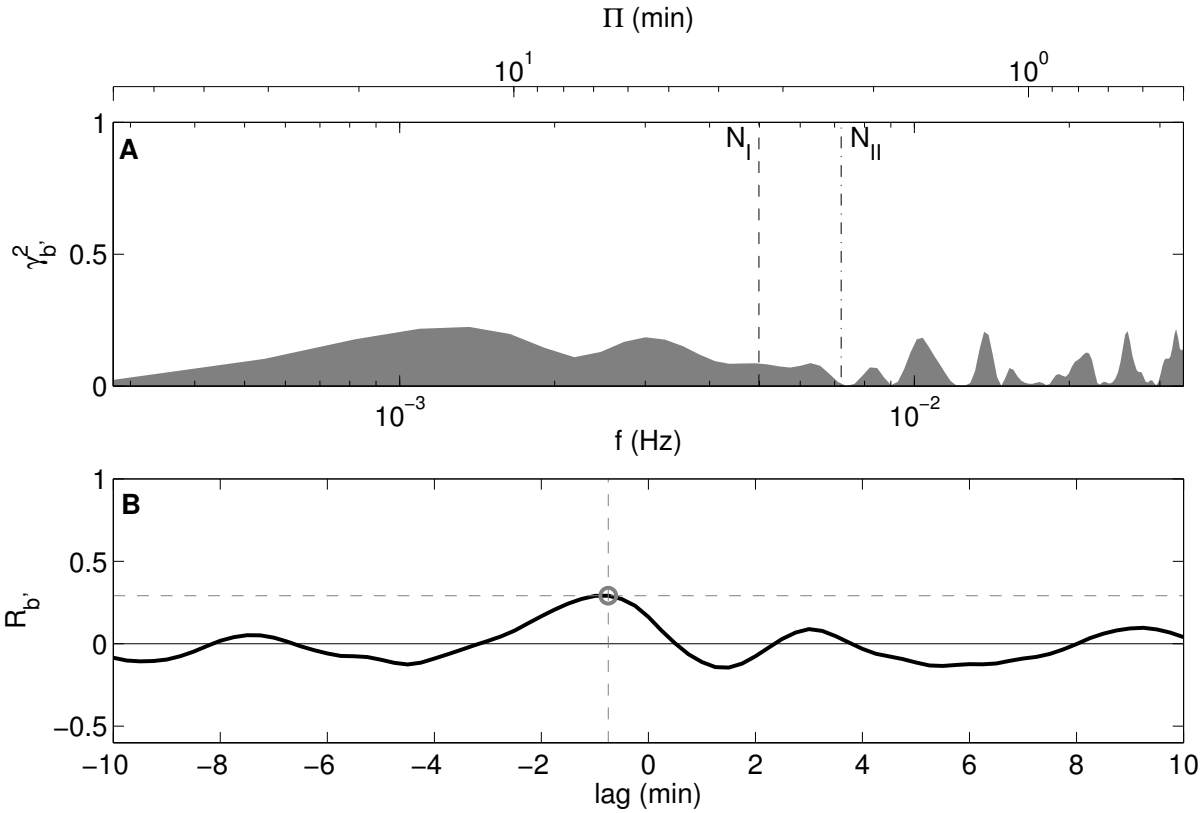

Figure 6.10: (a) Coherency per frequency band and (b) cross-covariance per lag time for buoyancy fluctuations at 64.6 m and 68.6 m depth during the storm period of Fig. 6.8.

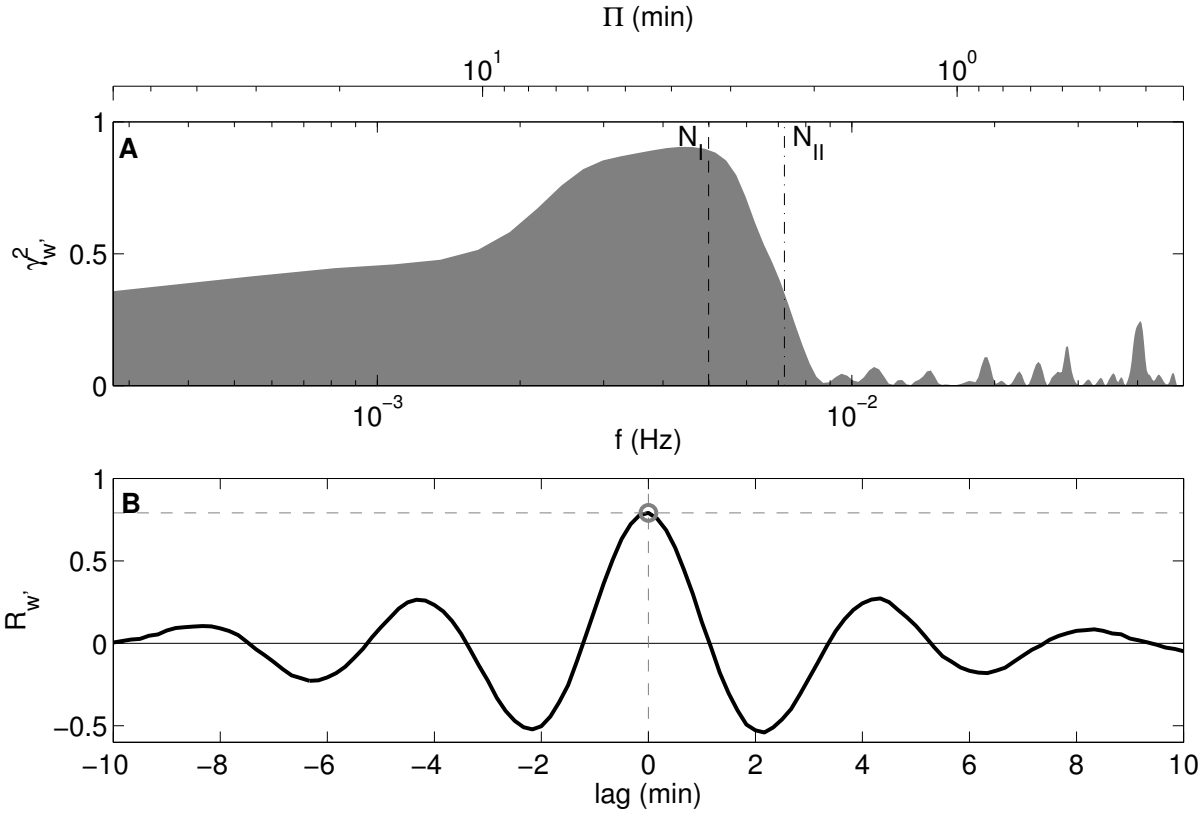

Figure 6.11: As for Fig.6.10, but for vertical velocity at 64.4 m and 68.4 m depth.

to the maximum value of 1) for the vertical velocities (Fig. 6.11). As illustrated in Fig. 6.11a, these high values are mainly stem from motions in a narrow frequency band slightly below the buoyancy frequency that are clearly evident already from Fig. 6.9d.

This surprising discrepency between buoyancy on velocity correlations is difficult to explain by any destructive interaction mechanism between different wave modes (which evidently should affect the correlation between both quantities in a similar way). One may speculate that this phenomenon is somehow connected to the strong shear bands in the halocline region (see Fig. 6.9c). Large-scale turbulent overturns in this region that could possibly have affected the buoyancy and velocity fluctuations in an asymmetric way could not be identified in the high-resolution temperature records, which is consistent with the very small Ozmidov-scales pointed out in Chap. 4. At the moment, the reason for the different correlation scales remains unclear, and clearly requires a more detailed investigation.

6.5 Direction and celerity

In order to estimate the direction of propagation of the high-frequency internal waves the major axis of the horizontal velocities was calculated by principal component analysis from the eigenvalues/vectors of the covariances. This method (described in detail in *Emery and Thomson*, 2001, Sec. 4.3.1) turns the axes until the variances (squared fluctuations) are maximal in the "along" (u'_R) and minimal in the "across" (v'_R) directions. Before calculation

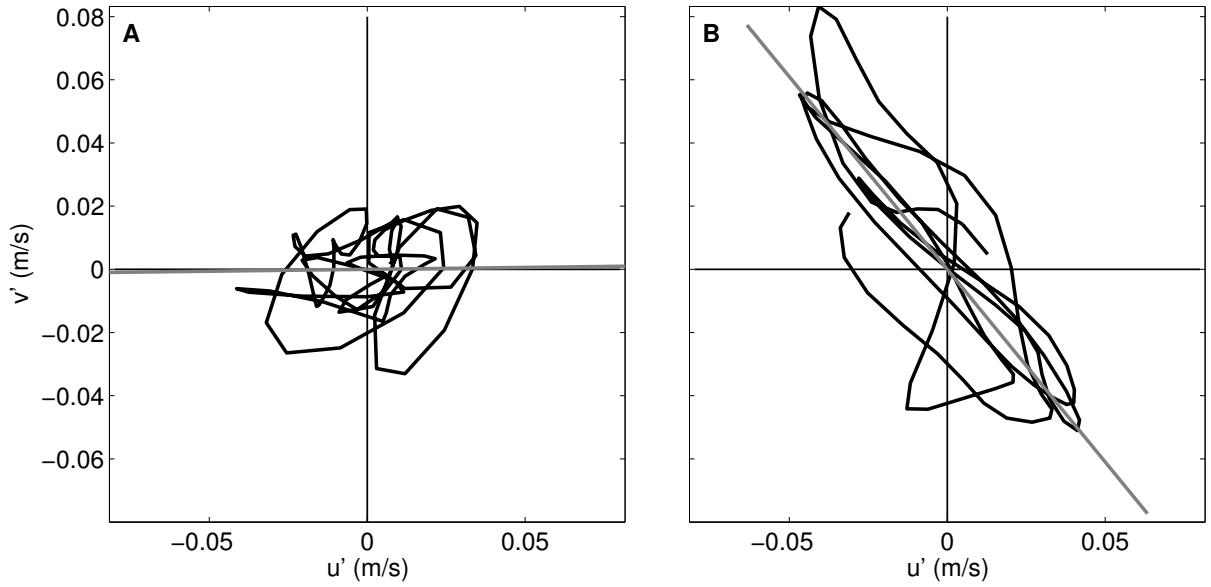

Figure 6.12: Two examples of finding the major current axis for 30-min windows: (a) before the storm and (b) just after the storm. The trace of the horizontal current is in black, the calculated major axis in grey.

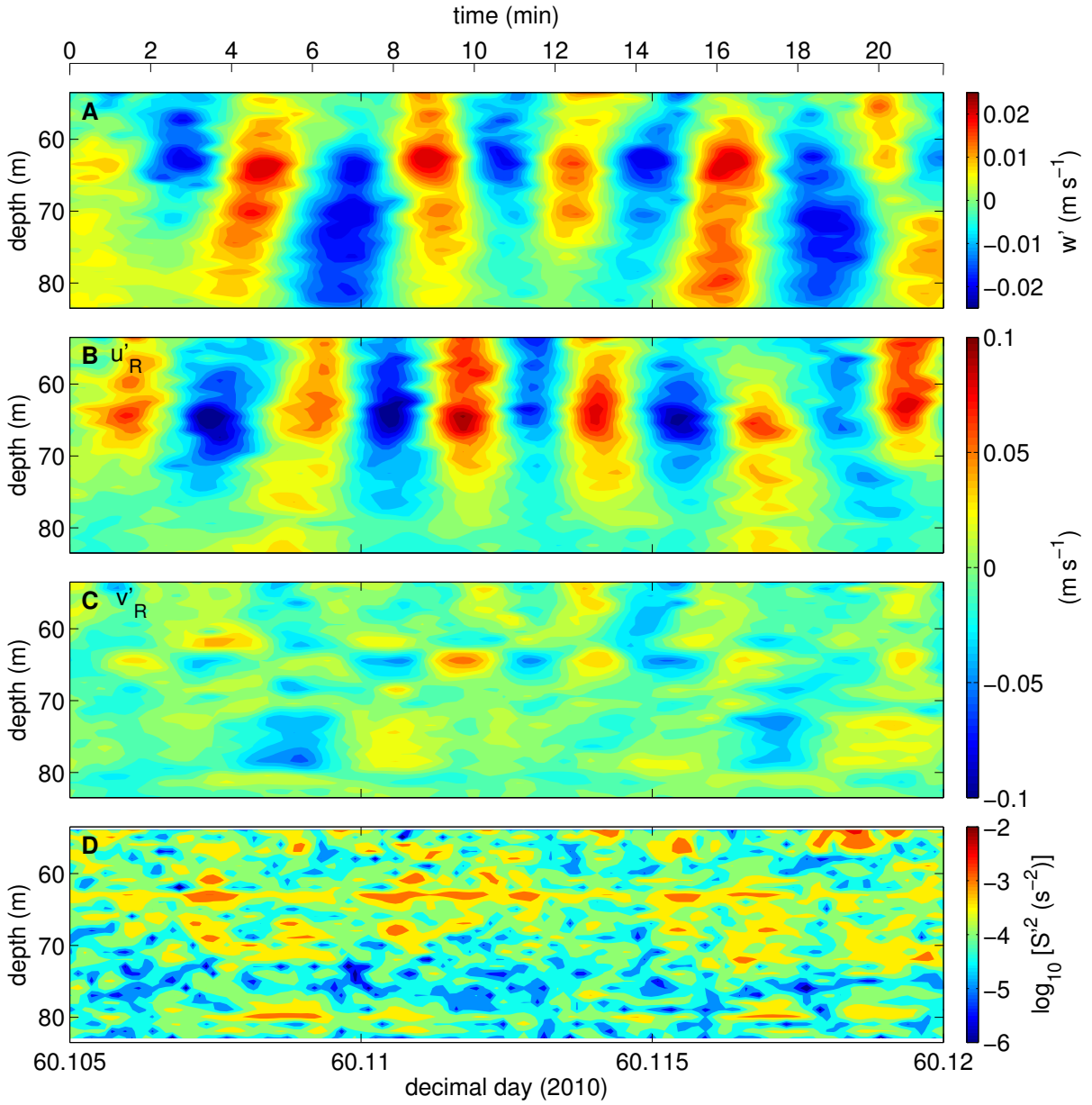

Figure 6.13: Velocity fluctuations in the (a) vertical, (b) along and (c) across directions and (d) the high-frequency shear generated.

of the major axis the horizontal velocities were high-pass filtered (8^{th}order, half-hour cutoff). The almost 4 days of measurements were subdivided into half-hour windows and for each of these windows the major axis was computed. As pointed out by *Holt and Thorpe* (1997), this approach leaves a factor of 180° undetermined in the propagation direction of waves.

Two examples of half-hour windows are shown in Fig. 6.12. Fig. 6.12a corresponds to a time period before the storm where high-frequency motions were weak and nearly isotropic, whereas Fig. 6.12b shows a period (indicated by the black box in Fig. 6.8d) of intense high-frequency activity with currents approximately rectilinearly from northeast to southwest and

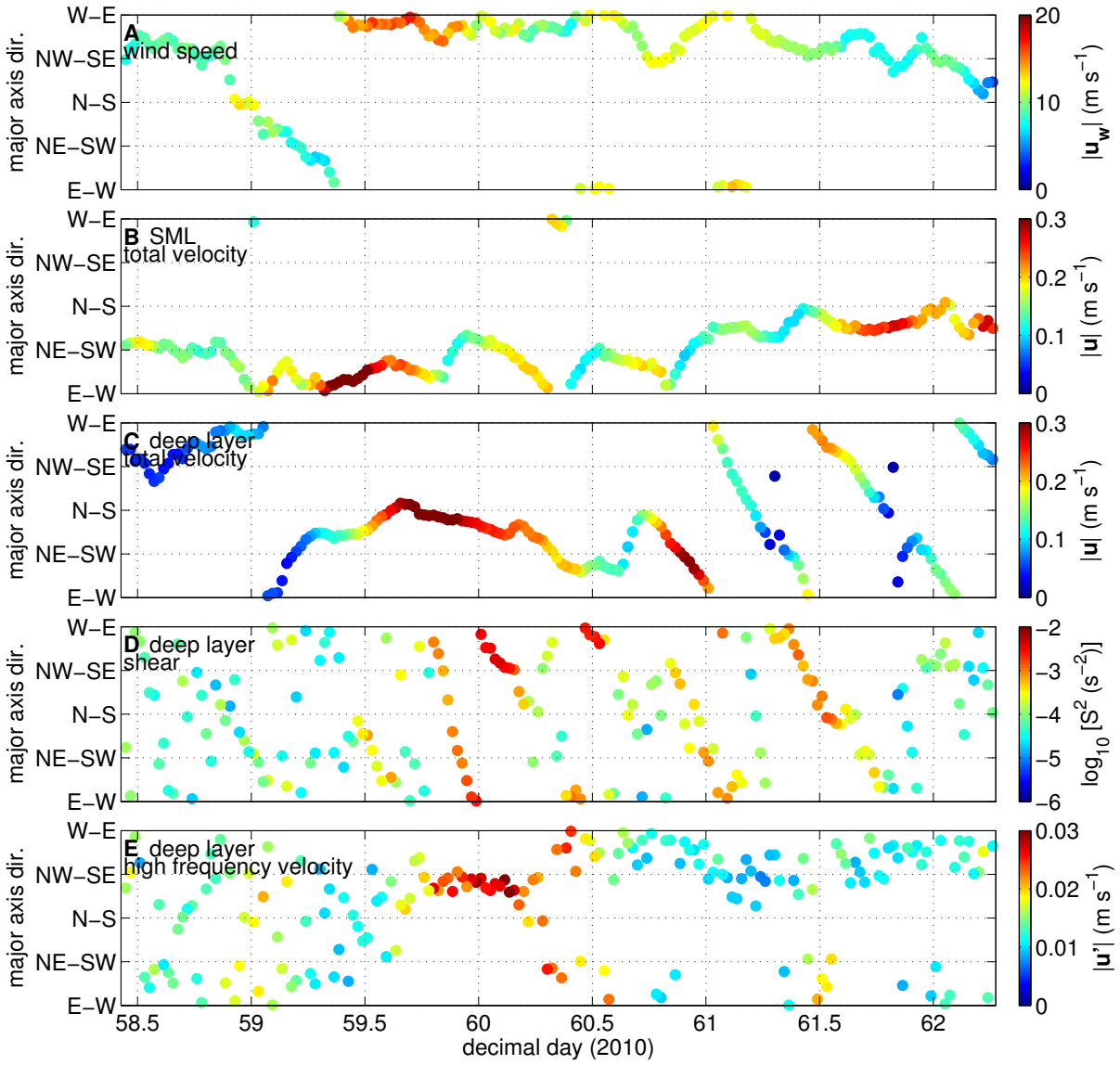

Figure 6.14: Time series of velocity and the direction of the major axis of (a) the wind, the background current in the surface mixed layer (b) and the deep layer (c), as well as the total shear (d) and the high-frequency motions (e) in half-hour windows. The deep layer is at 67.4 m (c–e).

vice versa. Fig. 6.13b,c illustrates that for this example the use of a rotated coordinate system removes most of the variance in the cross-current direction. Most importantly, comparing the shear from these high-frequency motions (Fig. 6.13d) with the low-frequency shear (Fig. 6.9), it becomes evident that the latter generally provides the dominant contribution inside the halocline region. A more detailed investigation including the whole storm period (not shown) reveals, however, that peaks in the high-frequency shear may occasionally exceed the low-frequency shear and thus contribute substanially to the destabilisation of the water column.

Since currents are nearly circular at times, especially when the overall current velocities

are small, the directional information has been plotted together with an indication of the current velocity in Figs. 6.14. This is used as an estimation of the significance of the major axis calculated because the stronger currents tend to be more unidirectional. Only half the directional possibilities are shown due to the directional ambiguity. In Figs. 6.14a,b the wind and surface current directions are shown; the wind turns before the storm and blows from west to east during and after the storm, while the current vector of the SML lies $\sim 45^\circ$ to the left of the wind, mainly east–west (E–W). In the deeper layer (at 67.4 m) during the storm velocities are aligned due north–south before the inertial oscillations kick in. The total shear at this depth has no favourite direction and rotates clockwise quickly at the time of the storm. A directional preference for the northwest–southeast is found in the high-frequency motions (Fig. 6.14e) ~ 6 hours after the strong north–south total currents, i.e. also $\sim 45^\circ$ to the left. As was seen in Fig. 6.3d high-frequency energy dissipates quickly after the storm, but a degree of directionality remains, with high-frequency waves favouring a westnorthwest–eastsoutheast direction. The direction of the high-frequency motions does not seem directly related to the background flow or shear as would be expected for shear instabilities.

6.6 Conclusions

At the end of winter in early 2010 high-frequency motions were observed in all high resolution mooring data collected in the central Bornholm Basin. This allowed a comparison between two situations typical for the Baltic Sea in winter; the moderate and strong wind periods. Spectra illustrate the drastic increase of motions at all frequencies during the wind event. Although the near-inertial waves outlasted our measurements, the medium frequency components, especially of the velocity, quickly dissipated their energy. Within a day of the passage of the storm power spectra were nearly back to pre-storm conditions. *Saggio and Imberger* (1998) observed the same quick energy decay after the passage of typhoons over lake Biwa (Japan). In contrast to lower frequencies, the high power of the motions near the buoyancy frequency created a long-lasting peak in the spectral level just below the local buoyancy frequency N. This peak was due to enhanced "vertical energy" (*Desaubies*, 1975) as the horizontal velocities of 10 cm s^{-1} were associated with vertical speeds exceeded 2 cm s^{-1}. This has often been observed, and (*Boegman et al.*, 2003) explain it as energy being trapped in the depth region where $f < N$, i.e. internal waves with frequency near the maximum N cannot leave the pycnocline region as stratification above and below is too weak to support them. Hence the energy stays contained within a narrow depth range (see also *Desaubies*, 1975; *Garrett and Munk*, 1975). The near-N region was also the only region where the spectra corresponded to the canonical Garrett-Munk spectrum, at lower frequencies energy levels were lower.

In accord with the vertical velocities, buoyancy fluctuations corresponded to typical isopy-

cnal displacements of 2 m. With their already intermittent pattern the effect of the storm was less discernible than for the vertical velocities. Deviating from linear internal wave theory, these isopycnal displacements show a much broader spectral distribution during the wind event than the vertical velocity and a much weaker vertical correlation. Whereas vertical velocities correlate over virtually the whole lower water column, buoyancy and temperature are only coherent over a few metres. This effect is partly caused by the weak, and also inverse, thermal stratification beneath the halocline. *Garrett and Munk* (1975) call this the "microstructure contamination" effect that "*spreads some of the spectral energy into the "forbidden frequencies" beyond the Väisälä frequency*" and causes a reduction of the coherence. It is also likely though that the low-frequency shear strongly impacts on the wave propagation.

High-frequency internal waves were found to be moving in any direction, but mainly in circles, before the storm. As the energy within these waves increased so did their directionality. Unfortunately the 180° ambiguity in high-frequency wave directions remains. Although high-frequency velocities are coherent over the depth range of the ADCP it could not be assumed this is the case over the entire water column. Therefore mode-1 waves could not be assumed and the method by *Holt and Thorpe* (1997) of determining direction via correlation with temperature fluctuations could not be tested. During the strong high-frequency activity just after the storm, near-N waves were rectilinear in the NW–SE direction over a period of almost 0.5 days. Over this time, the local shear was strongest but also variable in direction such that a relationship between shear and high-frequency motions, via shear-instabilities, is difficult to establish. This deserves a more careful investigation. Despite the strong wave activity the high-frequency motions did not contribute substantially to the shear within the strong background shear layer from near- and sub-inertial motions.

7 Summary and outlook

7.1 Summary

Shown in the previous chapters were detailed observations of internal waves at the centre of one of the tideless deep basins of the Baltic Sea. This extensive measurement programme included simultaneous measurements of temperature, salinity, current velocity and microstructure shear with the aim of characterising the internal wave field. Resolved frequencies spanned a wide range from the sub-inertial to the turbulent regime, encompassing the entire frequency range of internal waves. Also in (vertical) space the measurements were highly resolved, especially the NIOZ thermistor chain with its 20 cm resolution. The cruises in summer and winter allowed the comparison of different stratification and wind-forcing regimes. This was the first measurement programme of such scope in the Baltic Sea.

In summer the basin was strongly stratified with two pycnoclines; a thermocline at 30 m and a halocline at 50–65 m depth. Due to a previous inflow the deeper pycnocline corresponded to an inverse thermocline, making this region unusually warm. At near-inertial frequencies this three-layer system caused the dominance of vertical mode-2 motions, with slab-like clockwise-rotating near-inertial waves in the upper two layers and more vertically propagating near-inertial waves in the sub-halocline layer. This mode-2 dominance was also exemplified by the vertical modal energy. The total energy was lower than predicted by the Garrett-Munk model, which can be explained by the lack of tidal energy. However, this modal energy distribution, as well as the modal shear variance, fluctuated over time so that the assumptions for the Garrett-Munk and Gregg-Henyey models were invalidated. The continental-shelf model by MacKinnon and Gregg on the other hand proved to collapse the observed dissipation rates well. It was found that hotspots of turbulent dissipation occurred in long thin bands within the halocline where both the shear and the stratification were near their maximum, so that the dissipation rate was independent of the Richardson number.

In winter, due to the permanent halocline, the Bornholm Basin was still strongly stratified in the deeper layers. This stratification changed over the measurement period due to a strong storm; the pycnocline was deepened and temperature inversions and intrusions were formed. The near-inertial wave dynamics were more energetic than in summer, but followed the same correlation between shear, stratification and dissipation in thin bands in the halocline. Internal waves were probably the main mixing mechanism in the interior water column.

At the high-frequency end of the internal wave range a peak in energy just shy of the buoy-

ancy frequency was found. Although overall the energy levels were below the ones predicted by the Garrett-Munk model, near the buoyancy frequency they were equal. Even under moderate wind forcing high-frequency waves were omnipresent and coherent over at least several metres. Due to the passage of winterstorm Xynthia the energy in motions near the buoyancy frequency increased drastically and lingered for around a day. Horizontal and vertical velocities reached 10 cm s^{-1} and over 2 cm s^{-1}, respectively, the latter corresponding to vertical excursions of isopycnals of over 2 m. The shear from these motions, however, did not contribute significantly to the total shear within the thick shear band. During the 0.5 days of strong high-frequency waves their directions were nearly rectilinear, aligned in a northwest–southeast direction, in no obvious connection to the local shear as would be expected for shear instabilities.

7.2 Outlook

Although many features of internal waves have been observed here, some questions remain unanswered. A lot of those could still be addressed with the data set collected, as only a small part of the measurement programme was presented here.

One important aspect of internal wave mixing is missing in this thesis; the effect of boundary mixing mentioned in the introduction. Some preliminary results are available from transect T1 that show that near-inertial oscillations as well as high-frequency wave were measured here as well. The near-inertial oscillations were in phase with those at the central station. High-frequency wave components also showed a significant spectral bump near the buoyancy frequency. Comparing near-bottom velocities (measured with the vessel-mounted ADCP in combination with a towed "flying ADCP") with near-bed dissipation rates from the MSS transects showed that near-bottom currents oscillating with near-inertial frequency triggered a periodic near-bed dissipation rate signal and a growing and decaying bottom boundary layer thickness. These near-bottom buoyancy fluxes could dominate over interior mixing when the BBL was highly turbulent, especially since mixing was found to be rather efficient. The processes near the slopes deserve a more detailed analysis.

For better directional information, data from the specially-designed I-wave mooring could be analysed. This construction consists of three temperature-salinity chains (TSC) at the corners of an equilateral triangle. Each TSC held 4 microcats at equal heights above the bed. Comparing the signals received by the microcats, especially the lag times, would give an indication on how the internal wave propagated through the 3-dimensional space within the triangle.

Direct turbulence measurements were also taken close to the sea bed with an acoustic Doppler velocimeter (ADV). This instrument measures all three velocity components in a volume of a few cm^3. The set-up also included a fast termistor for the calculation of buoyancy

fluxes. Stationary, in situ measurements could give a much higher-resolved picture than MSS casts with 7 min intervals.

Away from the ILWAO data set, linear stability analysis could give an insight into the generation mechanism of the high-frequency waves observed. Possibilities include through basin-scale waves or intrusions or from shear instabilities. Also modelling of the Bornholm Basin could be used to narrow down internal wave generation mechanisms and sites. Modelling the internal wave field requires horizontal and vertical resolutions high enough to resolve at least the first few modes and also non-hydrostatic effects should be included. For the Bornholm Basin the parameterisation of internal wave mixing can be done by applying the MacKinnon and Gregg method presented here. If this yields feasable results the same scaling could be used for a model covering the whole Baltic Sea. If this parameterisation improves the results it would indicate that similar internal wave regimes as in the Bornholm Basin occur at other places too.

A Deriving the internal wave dispersion equation

Starting from the Boussinesq set of the equations of motion (see (1.9) in Sec. 1.2.2):

$$\frac{\partial u}{\partial x} + \frac{\partial v}{\partial y} + \frac{\partial w}{\partial z} = 0 \tag{A.1a}$$

$$\frac{\partial u}{\partial t} - f_i v = -\frac{1}{\rho_0}\frac{\partial p}{\partial x} \tag{A.1b}$$

$$\frac{\partial v}{\partial t} + f_i u = -\frac{1}{\rho_0}\frac{\partial p}{\partial y} \tag{A.1c}$$

$$\frac{\partial w}{\partial t} = -\frac{1}{\rho_0}\frac{\partial p}{\partial z} - \frac{\rho g}{\rho_0} \tag{A.1d}$$

$$\frac{\partial \rho}{\partial t} - \frac{\rho_0 N^2}{g} w = 0 \tag{A.1e}$$

the dispersion relation for waves in a rotating, continuously stratified fluid can be derived. Firstly u and v are eliminated by taking the time-derivative of (A.1a) and using (A.1b) and (A.1c):

$$\frac{\partial}{\partial t}\left(\frac{\partial u}{\partial x} + \frac{\partial v}{\partial y} + \frac{\partial w}{\partial z}\right) = 0$$

$$\frac{\partial}{\partial x}\left(\frac{\partial u}{\partial t}\right) + \frac{\partial}{\partial y}\left(\frac{\partial v}{\partial t}\right) + \frac{\partial}{\partial z}\left(\frac{\partial w}{\partial t}\right) = 0$$

$$\frac{\partial}{\partial x}\left(-\frac{1}{\rho_0}\frac{\partial p}{\partial x} + f_i v\right) + \frac{\partial}{\partial y}\left(-\frac{1}{\rho_0}\frac{\partial p}{\partial y} - f_i u\right) = -\frac{\partial^2 w}{\partial z \partial t}$$

$$-\frac{1}{\rho_0}\left(\frac{\partial^2 p}{\partial x^2} + \frac{\partial^2 p}{\partial y^2}\right) + f_i\left(\frac{\partial v}{\partial x} - \frac{\partial u}{\partial y}\right) = -\frac{\partial^2 w}{\partial z \partial t}$$

$$\frac{1}{\rho_0}\nabla_H^2(p) - f_i\left(\frac{\partial v}{\partial x} - \frac{\partial u}{\partial y}\right) = \frac{\partial^2 w}{\partial z \partial t} \tag{A.2}$$

where ∇^2 is the three-dimensional Laplacian operator and ∇_H^2 is the horizontal Laplacian operator:

$$\nabla^2 \equiv \nabla_H^2 + \frac{\partial^2}{\partial z^2} \equiv \frac{\partial^2}{\partial x^2} + \frac{\partial^2}{\partial y^2} + \frac{\partial^2}{\partial z^2}$$

The density ρ can be also be eliminated from (A.1) by first taking the time-derivative of (A.1d) and using (A.1e):

$$\begin{aligned}
\frac{\partial}{\partial t}\left(\frac{\partial w}{\partial t}\right) &= \frac{\partial}{\partial t}\left(-\frac{1}{\rho_0}\frac{\partial p}{\partial z} - \frac{\rho g}{\rho_0}\right) \\
\frac{\partial^2 w}{\partial t^2} &= -\frac{1}{\rho_0}\left(\frac{\partial^2 p}{\partial z \partial t} + g\frac{\partial \rho}{\partial t}\right) \\
&= -\frac{1}{\rho_0}\left(\frac{\partial^2 p}{\partial z \partial t} + g\frac{N^2 \rho_0}{g} w\right) \\
&= -\frac{1}{\rho_0}\frac{\partial^2 p}{\partial z \partial t} - N^2 w \\
\frac{1}{\rho_0}\frac{\partial^2 p}{\partial z \partial t} &= -\frac{\partial^2 w}{\partial t^2} - N^2 w \qquad \text{(A.3)}
\end{aligned}$$

Taking the horizontal Laplacian of (A.3) and using (A.2) gives us the w-equation ((A.4) = (1.10) in Sec. 1.2.2) that can be used to derive the dispersion relation:

$$\begin{aligned}
\nabla_H^2\left(\frac{1}{\rho_0}\frac{\partial^2 p}{\partial z \partial t}\right) &= \nabla_H^2\left(-\frac{\partial^2 w}{\partial t^2} - N^2 w\right) \\
\frac{\partial^2}{\partial z \partial t}\left(\frac{1}{\rho_0}\nabla_H^2(p)\right) &= -\nabla_H^2\left(\frac{\partial^2 w}{\partial t^2} + N^2 w\right) \\
\frac{\partial^2}{\partial z \partial t}\left(\frac{\partial^2 w}{\partial z \partial t} + f_i\left(\frac{\partial v}{\partial x} - \frac{\partial u}{\partial y}\right)\right) &= -\nabla_H^2\left(\frac{\partial^2 w}{\partial t^2} + N^2 w\right) \\
\frac{\partial^2}{\partial t^2}\left(\frac{\partial^2 w}{\partial z^2}\right) + f_i\frac{\partial^2}{\partial z \partial t}\left(\frac{\partial v}{\partial x} - \frac{\partial u}{\partial y}\right) &= -\frac{\partial^2}{\partial t^2}\left(\nabla_H^2(w)\right) - \nabla_H^2\left(N^2 w\right) \\
\frac{\partial^2}{\partial t^2}\left(\nabla^2(w)\right) + \nabla_H^2\left(N^2 w\right) + f_i^2\frac{\partial^2 w}{\partial z^2} &= 0 \qquad \text{(A.4)}
\end{aligned}$$

where in the last step this argument has been used:

$$\frac{\partial}{\partial y}\left(\frac{\partial u}{\partial t} - f_i v\right) = \frac{\partial}{\partial y}\left(-\frac{1}{\rho_0}\frac{\partial p}{\partial x}\right) \qquad \rightarrow \qquad -\frac{1}{\rho_0}\frac{\partial^2 p}{\partial x \partial y} = \frac{\partial^2 u}{\partial y \partial t} - f_i \frac{\partial v}{\partial y}$$

$$\frac{\partial}{\partial x}\left(\frac{\partial v}{\partial t} + f_i u\right) = \frac{\partial}{\partial x}\left(-\frac{1}{\rho_0}\frac{\partial p}{\partial y}\right) \qquad \rightarrow \qquad -\frac{1}{\rho_0}\frac{\partial^2 p}{\partial x \partial y} = \frac{\partial^2 v}{\partial x \partial t} + f_i \frac{\partial u}{\partial x}$$

$$\Rightarrow \qquad \frac{\partial^2 u}{\partial y \partial t} - f_i \frac{\partial v}{\partial y} = \frac{\partial^2 v}{\partial x \partial t} + f_i \frac{\partial u}{\partial x}$$

$$\frac{\partial^2 u}{\partial y \partial t} - f_i \frac{\partial v}{\partial y} = \frac{\partial^2 v}{\partial x \partial t} + f_i \frac{\partial u}{\partial x}$$

$$\frac{\partial}{\partial t}\left(\frac{\partial u}{\partial y} - \frac{\partial v}{\partial x}\right) = f_i \left(\frac{\partial v}{\partial y} + \frac{\partial u}{\partial x}\right)$$

$$-\frac{\partial}{\partial t}\left(\frac{\partial v}{\partial x} - \frac{\partial u}{\partial y}\right) = -f_i \frac{\partial w}{\partial z}$$

$$f_i \frac{\partial}{\partial z}\left(\frac{\partial}{\partial t}\left(\frac{\partial v}{\partial x} - \frac{\partial u}{\partial y}\right)\right) = f_i \frac{\partial}{\partial z}\left(f_i \frac{\partial w}{\partial z}\right)$$

$$= f_i^2 \frac{\partial^2 w}{\partial z^2}$$

B From microstructure shear to dissipation rates

An overview of many microstructure profilers developed over the years and in different countries is given in *Lueck et al.* (2002). Here the microstructure sonde MSS90L from ISW was used (a previous version is decribed in: *Prandke and Stips*, 1998). Its main frame is a 1.25 m long stainless steel tube, 90 mm in diameter, see Fig. B.1. As detailed in Sec. 2.2.1 the MSS was deployed from the stern of the ship where the profiler was connected to a winch via a thin cable (4.7 mm diameter) that was released with slack as the profiler descended so that it could free-fall. Going down, weights near the bottom and buoyancy elements at the top kept the profiler reasonably vertical, however, an accelerometer was also installed to record, and optionally correct for, tilting of the instrument. The sensors were mounted at the bottom of the instrument within a cone-shaped sensor protection cage (Fig. B.1) so that they measured the fluctuations in the undisturbed water below the profiler. The profiler was allowed to hit the bed, thus giving vertical profiles until $\sim$ 10 cm above the bed. The cable transmitted data in real-time so that the impact could be observed on the ship and the profiler winched up. When the profiler reached the surface a new cast was started immediately so that the instrument's path followed a "yo-yoing" pattern. The sonde carried multiple sensors, including CTD sensors, and occasionally oxygen and turbidity sensors. One of the main sensor types "on board" the MSS was the shear sensor from which the dissipation rate of turbulent kinetic energy ε was calculated, as detailed below.

B.1 The shear probe

The MSS carried two airfoil PNS06 shear sensors from ISW. These airfoil tips had a diameter of 6 mm and a length of 10 mm (*Prandke*, 2010) and consisted of a rubber tip around a cantilever that transmitted the lift force generated at the tip to a piezo-ceramic bimorph beam, see Fig. B.1. This cantilever construction, compared to direct transmission from tip to piezo-ceramic beam (see drawings in *Gregg*, 1999; *Lueck et al.*, 2002), is special to the ISW shear sensors and adds sensitivity, resolution and stability, but lowers the probe resonance frequency, which decreases the maximum profiling speed (*Prandke and Pfeiffer*, 1994; *Lueck et al.*, 2002).

As the MSS is vertically free-falling through the water the tips of the shear probes measure the fluctuations of one component of the horizontal velocity. The airfoil sensors need a

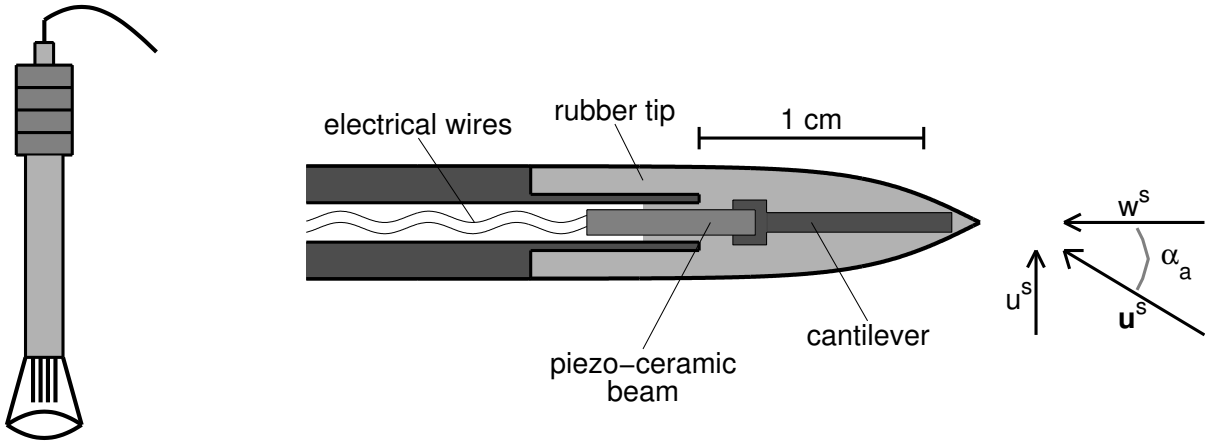

Figure B.1: Diagram of the MSS profiler and a shear probe, drawn after *Prandke and Stips* (1998).

minimum sinking speed of 0.5 m s^{-1} in order to accurately sense these fluctuations (*Fischer*, 2011). The sinking speed is sensed as an oncoming vertical velocity w^s so that fluctuations in the horizontal velocity u^s change the angle of attack α_a of the sensed total velocity $\mathbf{u}^s$ (*Fischer*, 2011), see Fig. B.1. The sensor tip is made of rubber and is bend a little in response to the flow, so that the piezo-ceramic beam in the middle of the probe is also bend, which, in turn, causes an electrical current to flow. The bursts of voltage produced by the probe E_p are proportional to the sinking speed w^s, the fluctuating horizontal velocities u^s and the probe's sensitivity $\hat{s}$ determined from calibration $E_p = \hat{s} w^s u^s$ (*Lueck et al.*, 2002). The voltage is differentiated and interpreted as vertical shear:

$$\frac{1}{\hat{s}\ w^{s2}} \frac{\mathrm{d}E_p}{\mathrm{d}t} = \frac{1}{w^s} \frac{\partial u^s}{\partial t} = \frac{\partial u^s}{\partial z} \tag{B.1}$$

B.2 Turbulence theory: isotropy and shear spectra

The justification for converting a time/space series to a space series, the cast duration from sea surface to sea bed was approx. 2–2.5 min, comes from Taylor's hypothesis of "frozen turbulence". (*Taylor*, 1938) proposed that one can assume "t*hat the sequence of changes in u at a fixed point are simply due to the passage of an unchanging pattern of turbulent motion over the point*" if the current velocity is much greater than the turbulent fluctuations. Hence, in order to call the measurements semi-synoptic and to apply Taylor's hypothesis, the MSS has to fall faster than a certain minimum speed (*Lueck et al.*, 2002), so that the flow field evolves slowly over the cast duration (*Stips*, 2005). This speed is given by the time scale of eddies $\sim (\nu/\varepsilon)^{1/2}$ in relation to their largest spatial scale $\sim 70(\nu^3/\varepsilon)^{1/4}$ (70 times the Kolmogorov

scale), so that the falling speed w^s must be faster than:

$$\frac{70(\nu^3/\varepsilon)^{1/4}}{(\nu/\varepsilon)^{1/2}} = 70(\nu\varepsilon)^{1/4} \quad . \tag{B.2}$$

This, for $\nu = 1 \times 10^{-6}$ m^2 s^{-1} and the observed range of ε (1×10^{-9}–1×10^{-5} W kg^{-1}), gives $w^s \gg 0.012$–0.12 m s^{-1}, which is always easily fullfilled.

From the vertical shear, and the kinematic viscosity ν, the symmetric part of the viscous stress tensor s_{ij} can be derived from which in turn the dissipation rate of turbulent kinetic energy ε can be calculated (*Stips*, 2005):

$$s_{ij} = \frac{1}{2}\left(\frac{\partial u_i^s}{\partial x_j} + \frac{\partial u_j^s}{\partial x_i}\right) \tag{B.3a}$$

$$\varepsilon = 2\nu \left\langle s_{ij} s_{ij} \right\rangle \tag{B.3b}$$

$$= \nu \left\langle \frac{\partial u_i^s}{\partial x_j} \frac{\partial u_j^s}{\partial x_i} \right\rangle \tag{B.3c}$$

$$= \begin{cases} 15\nu \left\langle \left(\dfrac{\partial u_i^s}{\partial x_j}\right)^2 \right\rangle & \text{for } i = j \\ 7.5\nu \left\langle \left(\dfrac{\partial u_i^s}{\partial x_j}\right)^2 \right\rangle & \text{for } i \neq j \quad . \end{cases} \tag{B.3d}$$

In (B.3) the Einstein convention of summation over repeated indices is used (*Einstein*, 1916). For the derivation of (B.3b) to (B.3d) see *Pope* (2000, Sec. 5.3).

In the step from (B.3c) to (B.3d) it is assumed that the turbulence is isotropic so that $\partial u_i^s/\partial x_j = \partial u_j^s/\partial x_i$ since only one component of s_{ij} is measured; the vertically profiling MSS measures fluctuations in one of the horizontal velocity components so that $i \neq j$ as $i = 1$ (u^s) and $j = 3$ (z). When isotropy is assumed where it might not be the case (e.g. in strongly stratified waters where the buoyancy Reynolds number Re_b is less than 100 (*Smyth and Moum*, 2000b), see Sec. 4.2.4) the dissipation rate can be overestimated by a factor of 3 (if horizontally homogeneous turbulence is still assumed, *Denman and Gargett*, 1988) or underestimated by a factor up to 7 (*Itsweire et al.*, 1993; *Hebert and de Bruyn Kops*, 2006). On the other hand, *Yamazaki and Osborn* (1990) state that, for $Re_b < 20$, the error can be in either direction, but is less than 35%. Hence consensus on this topic has not yet been reached. However, since direct measurements showed no enhancement of anisotropy at small scales in the pycnocline of the Baltic Sea (*Prandke and Stips*, 1992), and since no alternative method is available, all dissipation rates reported here have been calculated assuming isotropy.

In practise the total vertical shear $\partial u^s/\partial z$ is calculated, invoking Parseval's theorem of

equal power in integrals over the time and wavenumber domain (*Stips*, 2005), from the measured shear spectrum (*Moum et al.*, 1995):

$$\varepsilon = 7.5\nu \int_0^\infty S(m)\, \mathrm{d}m \tag{B.4a}$$

$$= 7.5\nu \int_2^{m_K} S(m)\, \mathrm{d}m + \varepsilon_c \tag{B.4b}$$

over the vertical wavenumber m, where the integration limits 0–∞ cannot be realised and are thus replaced by the limits 2–m_K. The term ε_c is introduced as a correction term to correct for shear in the missing part of the wavenumber spectrum, i.e. $m < 2$ and $m > m_K$. This correction term is calculated from a comparison of the data to the Nasmyth's universal spectrum, developed by Patrick Nasmyth in his PhD thesis from 1970 with values reported in the appendix of *Oakey* (1982). The minimum wavenumber 2 is given by the length of the profiler (*Fer et al.*, 2008) while the maximum wavenumber is given by the Kolmogorov wavenumber *Holtermann* (2011); *Prandke and Stips* (1998):

$$m_K = \frac{1}{2\pi} \left(\frac{\varepsilon}{\nu^3} \right)^{1/4} \quad . \tag{B.5}$$

Since the formulation of m_K includes the still-unknown ε the integration is done iteratively (for details see *Moum et al.*, 1995; *Stips*, 2005; *Fer*, 2006).

B.3 MSS validation routines

The raw data from the MSS sensors was despiked and averaged from 1024 to 256-Hz resolution for noise reduction. Dissipation rates were obtained with the method above by integrating vertical shear spectra over half-overlapping 256-point Hanning windows (corresponding to a data segment of 1 s in time, or 0.6–0.7 m in depth), assuming local isotropy in the dissipative subrange. This procedure was done for each shear probe individually and the resulting profiles compared for quality control. If there was an anomalously high value in one probe, e.g. due to the impact of plankton or a particle, the smaller value was taken. Casts showing a sudden and lasting increase in ε in both shear probes were endearingly called "jellyfish casts", as occasionally a jellyfish was spear-fished accidentally. These casts were completely discarded. If both shear probes agreed the dissipation rates were averaged into non-overlapping bins of 0.5-m thickness for further analysis. For example in summer 2008 at S1 52 casts were discarded compared to the 400 kept.

References

Aitsam, A., H. P. Hansen, J. Elken, M. Kahru, J. Laanemets, M. Pajuste, J. Pavelson, and L. Talpsepp (1984), Physical and chemical variability of the Baltic Sea: a joint experiment in the Gotland Basin, *Continental Shelf Research*, **3(3)**: 291–310, doi:10.1016/0278-4343(84)90013-X.

Aldridge, K. D., and L. I. Lumb (1987), Inertial waves identified in the earth's fluid outer core, *Nature*, **325(6103)**: 421–423, doi:10.1038/325421a0.

Alford, M. H., and M. Whitmont (2007), Seasonal and spatial variability of near-inertial kinetic energy from historical moored velocity records, *Journal of Physical Oceanography*, **37(8)**: 2022–2037, doi:10.1175/JPO3106.1.

Alford, M. H., M. C. Gregg, and M. A. Merrifield (2006), Structure, propagation, and mixing of energetic baroclinic tides in Mamala Bay, Oahu, Hawaii, *Journal of Physical Oceanography*, **36(6)**: 997–1018, doi:10.1175/JPO2877.1.

Andersen, B. G., and H. W. Borns, Jr. (1994), *The Ice Age World*, 208 pp., Scandinavian University Press, Oslo, N.

Andreas, E. L. (1989), Thermal and size evolution of sea spray droplets, *CRREL Report*, *89–11*, 47 pp., U.S. Army Cold Regions Research and Engineering Laboratory, Hanover, NH, USA, url: http://www.dtic.mil/cgi-bin/GetTRDoc?AD=ADA210484.

Ansong, J. K., and B. R. Sutherland (2010), Internal gravity waves generated by convective plumes, *Journal of Fluid Mechanics*, **648**: 405–434, doi:10.1017/S0022112009993193.

Antenucci, J. P., and J. Imberger (2001a), On internal waves near the high-frequency limit in an enclosed basin, *Journal of Geophysical Research – Oceans*, **106(C10)**: 22465–22474, doi: 10.1029/2000JC000465.

Antenucci, J. P., and J. Imberger (2001b), Energetics of long internal gravity waves in large lakes, *Limnology and Oceanography*, **46(7)**: 1760–1773, doi:10.4319/lo.2001.46.7.1760.

Avicola, G. S., J. N. Moum, A. Perlin, and M. D. Levine (2007), Enhanced turbulence due to the superposition of internal gravity waves and a coastal upwelling jet, *Journal of Geophysical Research – Oceans*, **112**: C06024, doi:10.1029/2006JC003831.

Axe, P. (2010), Hydrography and oxygen in the deep basins, *HELCOM Indicator Fact Sheets 2010*, url:http://www.helcom.fi/BSAP_assessment/ifs/ifs2010/en_GB/HydrographyOxygenDeepBasins.

Axell, L. B. (1998), On the variability of Baltic Sea deepwater mixing, *Journal of Geophysical Research – Oceans*, **103(C10)**: 21667–21682, doi:10.1029/98JC01714.

Bagge, O., F. Thurow, E. Steffensen, and J. Bray (1994), The Baltic cod, *Dana*, **10**: 1–28.

Becherer, J. K., and L. Umlauf (2011), Boundary mixing in lakes. Part I: Modeling the effect of shear-induced convection, *Journal of Geophysical Research – Oceans*, **116**: C10017, doi: 10.1029/2011JC007119.

Beckenbach, E., and E. Terrill (2008), Internal tides over abrupt topography in the Southern California Bight: Observations of diurnal waves poleward of the critical latitude, *Journal of Geophysical Research – Oceans*, **113**: C02001, doi:10.1029/2006JC003905.

Bell, T. H., Jr. (1974), Effects of shear on the properties of internal gravity wave modes, *Deutsche Hydrographische Zeitschrift*, **27(2)**: 57–62, doi:10.1007/BF02226477.

Bell, T. H., Jr. (1978), Radiation damping of inertial oscillations in the upper ocean, *Journal of Fluid Mechanics*, **88(2)**: 289–308, doi:10.1017/S0022112078002116.

Björck, S. (1995), A review of the history of the Baltic Sea, 13.0–8.0 ka BP, *Quaternary International*, **27**: 19–40, doi:10.1016/1040-6182(94)00057-C.

Björck, S. (2008), The late Quaternary development of the Baltic Sea, in *Assessment of climate change for the Baltic Sea Basin*, edited by The BACC Author Team, pp. 398–407, Springer-Verlag, Berlin, DE.

Björnsson, H., and S. A. Venegas (1997), A manual for EOF and SVD analyses of climate data, *Tech. Rep. 97–1*, 25 pp., Department of Atmospheric and Oceanic Sciences, McGill University, Montréal, Canada, url:http://andvari.vedur.is/ halldor/TEXT/eofsvd.html.

Boegman, L., J. Imberger, G. N. Ivey, and J. P. Antenucci (2003), High-frequency internal waves in large stratified lakes, *Limnology and Oceanography*, **48(2)**: 895–919, doi: 10.4319/lo.2003.48.2.0895.

Boegman, L., G. N. Ivey, and J. Imberger (2005), The degeneration of internal waves in lakes with sloping topography, *Limnology and Oceanography*, **50(5)**: 1620–1637, doi: 10.4319/lo.2005.50.5.1620.

Broszinski, A. (2002), Die subfossile Diatomeenflora der westlichen Ostsee, PhD thesis, 293 pp., Fachbereich Biologie, Johann Wolfgang Goethe-Universität, Frankfurt am Main, Germany.

Brown, E., A. Colling, D. Park, J. Phillips, D. Rothery, and J. Wright (2001), *Ocean Circulation*, 2nd ed., 286 pp., Open University, Milton Keynes, UK / Butterworth-Heinemann, Oxford, UK.

Brunt, D. (1927), The period of simple vertical oscillations in the atmosphere, *Quarterly Journal of the Royal Meteorological Society*, **53(221)**: 30–32, doi:10.1002/qj.49705322103.

Burchard, H., and R. Hofmeister (2008), A dynamic equation for the potential energy anomaly for analysing mixing and stratification in estuaries and coastal seas, *Estuarine, Coastal and Shelf Science*, **77(4)**: 679–687, doi:10.1016/j.ecss.2007.10.025.

Burchard, H., and T. P. Rippeth (2009), Generation of bulk shear spikes in shallow stratified tidal seas, *Journal of Physical Oceanography*, **39(4)**: 969–985, doi:10.1175/2008JPO4074.1.

Butman, B., P. S. Alexander, A. Scotti, R. C. Beardsley, and S. P. Anderson (2006), Large internal waves in Massachusetts Bay transport sediments offshore, *Continental Shelf Research*, **26(17–18)**: 2029–2049, doi:10.1016/j.csr.2006.07.022.

Butterworth, S. (1930), On the theory of filter amplifiers, *Experimental Wireless & the Wireless Engineer*, **7**: 536–541.

Bye, J. A. T., M. Ghantous, and J.-O. Wolff (2010), On the variability of the Charnock constant and the functional dependence of the drag coefficient on wind speed, *Ocean Dynamics*, **60(4)**: 851–860, doi:10.1007/s10236-010-0300-8.

Cacchione, D. A., L. F. Pratson, and A. S. Ogston (2002), The shaping of continental slopes by internal tides, *Science*, **296(5568)**: 724–727, doi:10.1126/science.1069803.

Carter, G. S., M. C. Gregg, and R.-C. Lien (2005), Internal waves, solitary-like waves, and mixing on the Monterey Bay shelf, *Continental Shelf Research*, **25(12–13)**: 1499–1520, doi:10.1016/j.csr.2005.04.011.

Charbonnel, C., and S. Talon (2005), Influence of gravity waves on the internal rotation and Li abundance of solar-type stars, *Science*, **309(5744)**: 2189–2191, doi:10.1126/science.1116849.

Charnock, H. (1955), Wind stress on a water surface, *Quarterly Journal of the Royal Meteorological Society*, **81(350)**: 639–640, doi:10.1002/qj.49708135027.

Charnock, H. (1958), A note on empirical wind-wave formulae, *Quarterly Journal of the Royal Meteorological Society*, **84(362)**: 443–447, doi:10.1002/qj.49708436212.

Cheney, R. E., and P. L. Richardson (1976), Observed decay of a cyclonic Gulf Stream ring, *Deep Sea Research and Oceanographic Abstracts*, **23(12)**: 143–155, doi:10.1016/S0011-7471(76)80023-X.

Christoffersen, P. L., C. Christiansen, J. B. Jensen, T. Leipe, and S. Hille (2007), Depositional conditions and organic matter distribution in the Bornholm Basin, Baltic Sea, *Geo-Marine Letters*, **27(5)**: 325–338, doi:10.1007/s00367-007-0054-6.

Craik, A. D. D. (2004), The origins of water wave theory, *Annual Review of Fluid Mechanics*, **36**: 1–28, doi:10.1146/annurev.fluid.36.050802.122118.

Craik, A. D. D. (2005), George Gabriel Stokes on water wave theory, *Annual Review of Fluid Mechanics*, **37**: 23–42, doi:10.1146/annurev.fluid.37.061903.175836.

Craik, A. D. D., and S. Leibovich (1976), A rational model for Langmuir circulations, *Journal of Fluid Mechanics*, **73(3)**: 401–426, doi:10.1017/S0022112076001420.

Cyr, F., D. Bourgault, and P. S. Galbraith (2011), Interior versus boundary mixing of a cold intermediate layer, *Journal of Geophysical Research – Oceans*, **116**: C12029, doi:10.1029/2011JC007359.

Darrigol, O. (2003), The spirited horse, the engineer, and the mathematician: water waves in nineteenth-century hydrodynamics, *Archive for History of Exact Sciences*, **58(1)**: 21–95, doi:10.1007/s00407-003-0070-5.

D'Asaro, E. A. (1985), The energy flux from the wind to near-inertial motions in the surface mixed layer, *Journal of Physical Oceanography*, **15(8)**: 1043–1059, doi:10.1175/1520-0485(1985)015<1043:TEFFTW>2.0.CO;2.

Dauxois, T., and W. R. Young (1999), Near-critical reflection of internal waves, *Journal of Fluid Mechanics*, **390**: 271–295.

Denman, K. L., and A. E. Gargett (1988), Multiple thermoclines are barriers to vertical exchange in the subarctic Pacific during SUPER, May 1984, *Journal of Marine Research*, **46(1)**: 77–103, doi:10.1357/002224088785113739.

Desaubies, Y. J. F. (1975), A linear theory of internal wave spectra and coherences near the Väisälä frequency, *Journal of Geophysical Research*, **80(6)**: 895–899, doi:10.1029/JC080i006p00895.

Deutscher Wetterdienst (2010), Severe storm Xynthia over southwestern and western Europe, *Tech. rep.*, url:http://www.dwd.de/bvbw/generator/DWDWWW/Content/Oeffentlichkeit/KU/KU2/KU23/rcc-cm/products/SWE/European/20100315__xynthia__en,templateId=raw,property=publicationFile.pdf /20100315_xynthia_en.pdf.

Dewar, W. K. (2009), A fishy mix, *Nature*, **460(7255)**: 581–582, doi:10.1038/460581a.

Dewar, W. K., R. J. Bingham, R. L. Iverson, D. P. Nowacek, L. C. St. Laurent, and P. H. Wiebe (2006), Does the marine biosphere mix the ocean?, *Journal of Marine Research*, **64(4)**: 541–561, doi:10.1357/002224006778715720.

Dewey, R. K., and W. R. Crawford (1988), Bottom stress estimates from vertical dissipation rate profiles on the continental shelf, *Journal of Physical Oceanography*, **18(8)**: 1167–1177, doi:10.1175/1520-0485(1988)018<1167:BSEFVD>2.0.CO;2.

Dillon, T. M. (1982), Vertical overturns: A comparison of Thorpe and Ozmidov length scales, *Journal of Geophysical Research – Oceans*, **87(C12)**: 9601–9613, doi:10.1029/JC087iC12p09601.

Dohan, K., and B. R. Sutherland (2003), Internal waves generated from a turbulent mixed region, *Physics of Fluids*, **15(2)**: 488–498, doi:10.1063/1.1530159.

Dohan, K., and B. R. Sutherland (2005), Numerical and laboratory generation of internal waves from turbulence, *Dynamics of Atmospheres and Oceans*, **40(1–2)**: 43–56, doi: 10.1016/j.dynatmoce.2004.10.004.

Döös, K., H. E. M. Meier, and R. Döscher (2004), The Baltic haline conveyor belt or the overturning circulation and mixing in the Baltic, *Ambio*, **33(4)**: 261–266, doi:10.1579/0044-7447-33.4.261.

Dutz, J., V. Mohrholz, J. Peters, J. Renz, and J. Alheit (2004), A strong impact of winter temperature on spring recruitment of a key copepod species in the Bornholm Basin: potential linkages to climate variability, *GLOBEC International Newsletter*, **10(1)**: 13–14.

Einstein, A. (1916), Die Grundlage der allgemeinen Relativitätstheorie, *Annalen der Physik*, **354(7)**: 769–822, doi:10.1002/andp.19163540702.

Ekman, V. W. (1905), On the influence of the earths rotation on ocean-currents, *Arkiv för Matematik, Astronomi och Fysik*, **2(11)**: 1–52.

Emeis, K.-C., R. Endler, U. Struck, and A. Kohly (2002), The post-glacial evolution of the Baltic Sea, in *Climate development and history of the North Atlantic realm*, edited by G. Wefer, W. H. Berger, K.-E. Behre, and E. Jansen, pp. 205–221, Springer-Verlag, Berlin, DE.

Emery, W. J., and R. E. Thomson (2001), *Data Analysis Methods in Physical Oceanography*, 2nd ed., 638 pp., Elsevier, Amsterdam, NL.

Feistel, R., and S. Weinreben (2008), Is Practical Salinity conservative in the Baltic Sea?, *Oceanologia*, **50(1)**: 73–82.

Feistel, R., G. Nausch, V. Morholz, E. Łysiak-Pastuszak, T. Seifert, W. Matthäus, S. Krüger, and I. S. Hansen (2003a), Warm waters of summer 2002 in the deep Baltic Proper, *Oceanologia*, **45(4)**: 571–592.

Feistel, R., G. Nausch, W. Matthäus, and E. Hagen (2003b), Temporal and spatial evolution of the Baltic deep water renewal in spring 2003, *Oceanologia*, **45(4)**: 623–642.

Feistel, R., S. Weinreben, H. Wolf, S. Seitz, P. Spitzer, B. Adel, G. Nausch, B. Schneider, and D. G. Wright (2010), Density and Absolute Salinity of the Baltic Sea 2006–2009, *Ocean Science*, **6(1)**: 3–24, doi:10.5194/os-6-3-2010.

Fennel, W. (1989), Inertial waves and inertial oscillations in channels, *Continental Shelf Research*, **9(5)**: 403–426, doi:10.1016/0278-4343(89)90007-1.

Fennel, W., and M. Schmidt (1993), Topographically forced inertial waves, *Journal of Marine Systems*, **4(1)**: 1–15, doi:10.1016/0924-7963(93)90016-F.

Fennel, W., and T. Seifert (1995), Kelvin wave controlled upwelling in the western Baltic, *Journal of Marine Systems*, **6(4)**: 289–300, doi:10.1016/0924-7963(94)00038-D.

Fer, I. (2006), Scaling turbulent dissipation in an Arctic fjord, *Deep-Sea Research II*, **53(1–2)**: 77–95, doi:10.1016/j.dsr2.2006.01.003.

Fer, I., and K. Widell (2007), Early spring turbulent mixing in an ice-covered Arctic fjord during transition to melting, *Continental Shelf Research*, **27(15)**: 1980–1999, doi:10.1016/j.csr.2007.04.003.

Fer, I., F. Geyer, and K. L. Daae (2008), Data report from the cruise HM2007 613 with R.V. Håkon Mosby 10 July–4 August 2007, *Reports in Meteorology and Oceanography, 2–2008*, Geophysical Institute, University of Bergen, Norway, url: http://folk.uib.no/ngfif/Reports/DataReport_HM2007613.pdf.

Fischer, T. (2011), Diapycnal diffusivity and transport of matter in the open ocean estimated from underway acoustic profiling and microstructure profiling, PhD thesis, 107 pp., Leibniz-Institut für Meereswissenschaften, Christian-Albrechts-Universität Kiel, Germany.

Flinkman, J., E. Aro, I. Vuorinen, and M. Viitasalo (1998), Changes in northern Baltic zooplankton and herring nutrition from 1980s to 1990s: top-down and bottom-up processes at work, *Marine Ecology Progress Series*, **165**: 127–136, doi:10.3354/meps165127.

Fonselius, S. H. (1969), Hydrography of the Baltic deep basins 3, *Fishery Board of Sweden: Series Hydrography*, **(23)**: 97.

Francis, S. H. (1975), Global propagation of atmospheric gravity waves: A review, *Journal of Atmospheric and Terrestrial Physics*, **37(6–7)**: 1011–1054, doi:10.1016/0021-9169(75)90012-4.

Garrett, C. (2001), What is the "near-inertial" band and why is it different from the rest of the internal wave spectrum?, *Journal of Physical Oceanography*, **31(4)**: 962–971, doi:10.1175/1520-0485(2001)031<0962:WITNIB>2.0.CO;2.

Garrett, C. (2009), Internal waves, in *Encyclopedia of Ocean Sciences*, edited by J. H. Steele, S. A. Thorpe, and K. K. Turekian, 2nd ed., pp. 266–273, Academic Press/Elsevier, Amsterdam, NL.

Garrett, C., and W. Munk (1972), Space-time scales of internal waves, *Geophysical & Astrophysical Fluid Dynamics*, **3(1)**: 225–264, doi:10.1080/03091927208236082.

Garrett, C., and W. Munk (1975), Space-time scales of internal waves: A progress report, *Journal of Geophysical Research*, **80(3)**: 291–297, doi:10.1029/JC080i003p00291.

Garrett, C., and W. Munk (1979), Internal waves in the ocean, *Annual Review of Fluid Mechanics*, **11**: 339–369, doi:10.1146/annurev.fl.11.010179.002011.

Gayen, B., and S. Sarkar (2011), Boundary mixing by density overturns in an internal tidal beam, *Geophysical Research Letters*, **38**: L14608, doi:10.1029/2011GL048135.

Gemmrich, J. R. (2010), Strong turbulence in the wave crest region, *Journal of Physical Oceanography*, **40(3)**: 583–595, doi:10.1175/2009JPO4179.1.

Gloor, M., A. Wüest, and D. M. Imboden (2000), Dynamics of mixed bottom boundary layers and its implications for diapycnal transport in a stratified, natural water basin, *Journal of Geophysical Research – Oceans*, **105(C4)**: 8629–8646, doi:10.1029/1999JC900303.

Görtler, H. (1943), Über eine Schwingungserscheinung in Flüssigkeiten mit stabiler Dichteschichtung, *Zeitschrift für Angewandte Mathematik und Mechanik*, **23(2)**: 65–71, doi:10.1002/zamm.19430230202.

Goudsmit, G.-H., F. Peeters, M. Gloor, and A. Wüest (1997), Boundary versus internal diapycnal mixing in stratified natural waters, *Journal of Geophysical Research – Oceans*, **102(C13)**: 27903–27914, doi:10.1029/97JC01861.

Graca, B., Z. Witek, D. Burska, I. Białkowska, K. Łukawska-Matuszewska, and J. Bolałek (2006), Pore water phosphate and ammonia below the permanent halocline in the south-eastern Baltic Sea and their benthic fluxes under anoxic conditions, *Journal of Marine Systems*, **63(3–4)**: 141–154, doi:10.1016/j.jmarsys.2006.06.003.

Grasshoff, K. (1975), The hydrochemistry of landlocked basins and fjords, in *Chemical Oceanography 2*, edited by J. P. Riley and G. Skirrow, 2nd ed., pp. 455–597, Academic Press, London, UK.

Gregg, M. C. (1987), Diapycnal mixing in the thermocline: A review, *Journal of Geophysical Research – Oceans*, **92(C5)**: 5249–5286, doi:10.1029/JC092iC05p05249.

Gregg, M. C. (1989), Scaling turbulent dissipation in the thermocline, *Journal of Geophysical Research – Oceans*, **94(C7)**: 9686–9698, doi:10.1029/JC094iC07p09686.

Gregg, M. C. (1999), Uncertainties and limitations in measuring ϵ and χ_t, *Journal of Atmospheric and Oceanic Technology*, **16(11)**: 1483–1490, doi:10.1175/1520-0426(1999)016<1483:UALIMA>2.0.CO;2.

Gregg, M. C., T. B. Sanford, and D. P. Winkel (2003), Reduced mixing from the breaking of internal waves in equatorial waters, *Nature*, **422(6931)**: 513–515, doi:10.1038/nature01507.

Grumm, R. H. (2010), The devastating Western European winter storm 27–28 February 2010, *Tech. rep.*, National Weather Service, Pennsylvania State University, USA, url: http://nws.met.psu.edu/severe/2010/28Feb2010.pdf.

Gustafson, T., and B. Kullenberg (1933), Inertia currents in the Baltic, *Nature*, **131(3312)**: 586–587, doi:10.1038/131586b0.

Gustafsson, B. G., and A. Stigebrandt (2007), Dynamics of nutrients and oxygen/hydrogen sulfide in the Baltic Sea deep water, *Journal of Geophysical Research – Biogeosciences*, **112**: G02023, doi:10.1029/2006JG000304.

Hällfors, G., A. Niemi, H. Ackefors, J. Lassig, and E. Leppäkoski (1981), Biological Oceanography, in *The Baltic Sea*, edited by A. Voipio, Elsevier Oceanography Series 30, pp. 219–274, Elsevier, Amsterdam, NL.

Hebert, D. A., and S. M. de Bruyn Kops (2006), Relationship between vertical shear rate and kinetic energy dissipation rate in stably stratified flows, *Geophysical Research Letters*, **33**: L06602, doi: 10.1029/2005GL025071.

HELCOM (1981), Assessment of the effects of pollution on the natural resources of the Baltic Sea, *Baltic Sea Environment Proceedings*, **5B**.

HELCOM (2007), Climate change in the Baltic Sea area, *Baltic Sea Environment Proceedings*, **111**.

HELCOM (2010), Hazardous substances in the Baltic Sea, *Baltic Sea Environment Proceedings*, **120B**.

Hinrichsen, H.-H., A. Lehmann, M. St. John, and B. Brügge (1997), Modeling the cod larvae drift in the Bornholm Basin in summer 1994, *Continental Shelf Research*, **17(14)**: 1765–1784, doi: 10.1016/S0278-4343(97)00045-9.

Hofmeister, R., H. Burchard, and J.-M. Beckers (2010), Non-uniform adaptive vertical grids for 3D numerical ocean models, *Ocean Modelling*, **33(1–2)**: 70–86, doi:10.1016/j.ocemod.2009.12.003.

Hollan, E. (1966a), Das Spektrum der internen Bewegungsvorgänge der westlichen Ostsee im Periodenbereich von 0,3 bis 60 Minuten. Teil 1: Interpretation der wellenförmigen Bewegungsanteile, *Deutsche Hydrographische Zeitschrift*, **19(5)**: 193–218, doi:10.1007/BF02226129.

Hollan, E. (1966b), Das Spektrum der internen Bewegungsvorgänge der westlichen Ostsee im Periodenbereich von 0,3 bis 60 Minuten. Teil 2: Beobachtungsergebnisse, *Deutsche Hydrographische Zeitschrift*, **19(6)**: 285–298, doi:10.1007/BF02225942.

Holt, J. T., and S. A. Thorpe (1997), The propagation of high frequency internal waves in the Celtic Sea, *Deep-Sea Research I*, **44(12)**: 2087–2116, doi:10.1016/S0967-0637(97)00091-5.

Holtermann, P. L. (2011), The Baltic Sea Tracer Release Experiment: Mixing processes in the Gotland Basin, PhD thesis, 122 pp., Leibniz-Institut für Ostseeforschung Warnemünde, Universität Rostock, Germany.

Holtermann, P. L., and L. Umlauf (2012), The Baltic Sea Tracer Release Experiment. Part II: Mixing processes, *Journal of Geophysical Research – Oceans*, **117**: C01022, doi:10.1029/2011JC007445.

Huntley, M. E., and M. Zhou (2004), Influence of animals on turbulence in the sea, *Marine Ecology Progress Series*, **273**: 65–79, doi:10.3354/meps273065.

Huppert, H. E. (1971), On the stability of a series of double-diffusive layers, *Deep-Sea Research and Oceanographic Abstracts*, **18(10)**: 1005–1021, doi:10.1016/0011-7471(71)90005-2.

Itsweire, E. C., J. R. Koseff, D. A. Briggs, and J. H. Ferziger (1993), Turbulence in stratified shear flows: Implications for interpreting shear-induced mixing in the ocean, *Journal of Physical Oceanography*, **23(7)**: 1508–1522, doi:10.1175/1520-0485(1993)023<1508:TISSFI>2.0.CO;2.

Jahn, A., I. Gamenick, and H. Theede (1996), Physiological adaptations of *Cyprideis torosa* (Crustacea, Ostracoda) to hydrogen sulphide, *Marine Ecology Progress Series*, **142**: 215–223, doi: 10.3354/meps142215.

Johnston, T. M. S., D. L. Rudnick, G. S. Carter, R. E. Todd, and S. T. Cole (2011), Internal tidal beams and mixing near Monterey Bay, *Journal of Geophysical Research – Oceans*, **116**: C03017, doi:10.1029/2010JC006592.

Kahru, M. (1983), Phytoplankton patchiness generated by long internal waves: A model, *Marine Ecology Progress Series*, **10**: 111–117, doi:10.3354/meps010111.

Kahru, M., J.-M. Leppänen, O. Rud, and O. P. Savchuk (2000), Cyanobacteria blooms in the Gulf of Finland triggered by saltwater inflow into the Baltic Sea, *Marine Ecology Progress Series*, **207**: 13–18, doi:10.3354/meps207013.

Kantha, L. H., and C. A. Clayson (2007), On leakage of energy from turbulence to internal waves in the oceanic mixed layer, *Ocean Dynamics*, **57(2)**: 151–156, doi:10.1007/s10236-006-0100-3.

Katija, K., and J. O. Dabiri (2009), A viscosity-enhanced mechanism for biogenic ocean mixing, *Nature*, **460(7255)**: 624–627, doi:10.1038/nature08207.

Katsman, C. A., P. C. F. Van der Vaart, H. A. Dijkstra, and W. P. M. de Ruijter (2003), Stability of multilayer ocean vortices: A parameter study including realistic Gulf Stream and Agulhas rings, *Journal of Physical Oceanography*, **33(6)**: 1197–1218, doi:10.1175/1520-0485(2003)033<1197:SOMOVA>2.0.CO;2.

Kielmann, J., W. Krauß, and K.-H. Keunecke (1973), Currents and stratification in the belt sea and the arkona basin during 1962–1968, *Kieler Meeresforschungen*, **29(2)**: 90–111.

Knox, J. A., J. D. Frye, J. D. Durkee, and C. M. Fuhrmann (2011), Non-convective high winds associated with extratropical cyclones, *Geography Compass*, **5(2)**: 63–89, doi:10.1111/j.1749-8198.2010.00395.x.

Knudsen, M. (1900), Erneuerung der unteren Wasserschichte in der Ostsee, *Annalen der Hydrographie und maritimen Meteorologie*, **28**: 586–590.

Kolmogorov, A. N. (1991a), The local structure of turbulence in incompressible viscous fluid for very large Reynolds Numbers, *Proceedings of the Royal Society A: Mathematical, Physical and Engineering Sciences*, **434(1890)**: 9–13, doi:10.1098/rspa.1991.0075.

Kolmogorov, A. N. (1991b), Dissipation of energy in the locally isotropic turbulence, *Proceedings of the Royal Society A: Mathematical, Physical and Engineering Sciences*, **434(1890)**: 15–17, doi:10.1098/rspa.1991.0076.

Konovalov, S. K., G. W. Luther III, G. E. Friederich, D. B. Nuzzio, B. M. Tebo, J. W. Murray, T. Oguz, B. Glazer, R. E. Trouwborst, B. Clement, K. J. Murray, and A. S. Romanov (2003), Lateral injection of oxygen with the Bosporus plume – Fingers of oxidizing potential in the Black Sea, *Limnology and Oceanography*, **48(6)**: 2369–2376, doi:10.4319/lo.2003.48.6.2369.

Kõuts, T., and A. Omstedt (1993), Deep water exchange in the Baltic Proper, *Tellus A*, **45(4)**: 311–324, doi:10.1034/j.1600-0870.1993.t01-1-00006.x.

Krauß, W. (1981), The erosion of a thermocline, *Journal of Physical Oceanography*, **11(4)**: 415–433, doi:10.1175/1520-0485(1981)011<0415:TEOAT>2.0.CO;2.

Kullenberg, G. (1981), Physical Oceanography, in *The Baltic Sea*, edited by A. Voipio, Elsevier Oceanography Series 30, pp. 135–181, Elsevier, Amsterdam, NL.

Kundu, P. K., and I. M. Cohen (2008), *Fluid Mechanics*, 4th ed., 872 pp., Academic Press, London, UK.

Kundu, P. K., S.-Y. Chao, and J. P. McCreary (1983), Transient coastal currents and inertio-gravity waves, *Deep-Sea Research A*, **30(10)**: 1059–1082, doi:10.1016/0198-0149(83)90061-4.

Kurkina, O., T. Talipova, E. Pelinovsky, and T. Soomere (2011), Mapping the internal wave field in the Baltic Sea in the context of sediment transport in shallow water, *Journal of Coastal Research (Proceedings of the 11th International Coastal Symposium)*, **SI 64**: 2042–2047.

Kuzmina, N., B. Rudels, T. Stipa, and V. Zhurbas (2005), The structure and driving mechanisms of the Baltic intrusions, *Journal of Physical Oceanography*, **35(6)**: 1120–1137, doi: 10.1175/JPO2749.1.

Langmuir, I. (1938), Surface motion of water induced by wind, *Science*, **87(2250)**: 119–123, doi: 10.1126/science.87.2250.119.

Lass, H.-U., and W. Matthäus (1996), On temporal wind variations forcing salt water inflows into the Baltic Sea, *Tellus A*, **48(5)**: 663–671, doi:10.1034/j.1600-0870.1996.t01-4-00005.x.

Lass, H.-U., and W. Matthäus (2008), General oceanography of the Baltic Sea, in *State and Evolution of the Baltic Sea, 1952-2005. A detailed 50-year survey of meteorology and climate, physics, chemistry, biology, and marine environment*, edited by R. Feistel, G. Nausch, and N. Wasmund, pp. 5–43, Wiley-Interscience, Hoboken, NJ, USA.

Lass, H.-U., and V. Mohrholz (2003), On dynamics and mixing of inflowing saltwater in the Arkona Sea, *Journal of Geophysical Research – Oceans*, **108(C2)**: 3042, doi:10.1029/2002JC001465.

Lass, H.-U., H. Prandke, and B. Liljebladh (2003), Dissipation in the Baltic Proper during winter stratification, *Journal of Geophysical Research – Oceans*, **108(C6)**: 3187, doi: 10.1029/2002JC001401.

Ledwell, J. R., A. J. Watson, and C. S. Law (1998), Mixing of a tracer in the pycnocline, *Journal of Geophysical Research – Oceans*, **103(C10)**: 21499–21529, doi:10.1029/98JC01738.

Ledwell, J. R., E. T. Montgomery, K. L. Polzin, L. C. St. Laurent, R. W. Schmitt, and J. M. Toole (2000), Evidence for enhanced mixing over rough topography in the abyssal ocean, *Nature*, **403(6766)**: 179–182, doi:10.1038/35003164.

Lehmann, A., and K. Myrberg (2008), Upwelling in the Baltic Sea – A review, *Journal of Marine Systems*, **74(Suppl.)**: S3–S12, doi:10.1016/j.jmarsys.2008.02.010.

Leshansky, A. M., and L. M. Pismen (2010), Do small swimmers mix the ocean?, *Physical Review E*, **82(2)**: 025301, doi:10.1103/PhysRevE.82.025301.

Levine, M. D. (2002), A modification of the Garrett–Munk internal wave spectrum, *Journal of Physical Oceanography*, **32(11)**: 3166–3181, doi:10.1175/1520-0485(2002)032<3166:AMOTGM>2.0.CO;2.

Liberato, M. L. R., J. G. Pinto, I. F. Trigo, and R. M. Trigo (2011), Klaus – an exceptional winter storm over northern Iberia and southern France, *Weather*, **66(12)**: 330–334, doi:10.1002/wea.755.

Liu, Z. (2010), Instability of baroclinic tidal flow in a stratified fjord, *Journal of Physical Oceanography*, **40(1)**: 139–154, doi:10.1175/2009JPO4154.1.

Lorke, A. (2007), Boundary mixing in the thermocline of a large lake, *Journal of Geophysical Research – Oceans*, **112**: C09019, doi:10.1029/2006JC004008.

Lorke, A., F. Peeters, and A. Wüest (2005), Shear-induced convective mixing in bottom boundary layers on slopes, *Limnology and Oceanography*, **50(5)**: 1612–1619, doi:10.4319/lo.2005.50.5.1612.

Lozovatsky, I., Z. Liu, H. Fernando, J. Armengol, and E. Roget (2012), Shallow water tidal currents in close proximity to the seafloor and boundary-induced turbulence, *Ocean Dynamics*, **62(2)**: 177–191, doi:10.1007/s10236-011-0495-3.

Lucas, A. J., P. J. S. Franks, and C. L. Dupont (2011), Horizontal internal-tide fluxes support elevated phytoplankton productivity over the inner continental shelf, *Limnology and Oceanography: Fluids & Environments*, **1(1)**: 56–74, doi:10.1215/21573698-1258185.

Lueck, R. G., F. Wolk, and H. Yamazaki (2002), Oceanic velocity microstructure measurements in the 20th century, *Journal of Oceanography*, **58(1)**: 153–174, doi:10.1023/A:1015837020019.

MacKinnon, J. A., and M. C. Gregg (2003a), Shear and baroclinic energy flux on the summer New England Shelf, *Journal of Physical Oceanography*, **33(7)**: 1462–1475, doi:10.1175/1520-0485(2003)033<1462:SABEFO>2.0.CO;2.

MacKinnon, J. A., and M. C. Gregg (2003b), Mixing on the late-summer New England Shelf – Solibores, shear, and stratification, *Journal of Physical Oceanography*, **33(7)**: 1476–1492, doi:10.1175/1520-0485(2003)033<1476:MOTLNE>2.0.CO;2.

MacKinnon, J. A., and M. C. Gregg (2005a), Near-inertial waves on the New England Shelf: The role of evolving stratification, turbulent dissipation, and bottom drag, *Journal of Physical Oceanography*, **35(12)**: 2408–2424, doi:10.1175/JPO2822.1.

MacKinnon, J. A., and M. C. Gregg (2005b), Spring mixing: Turbulence and internal waves during restratification on the New England Shelf, *Journal of Physical Oceanography*, **35(12)**: 2425–2443, doi:10.1175/JPO2821.1.

Matthäus, W. (1986), Charakteristische Eigenschaften von Stagnationsperioden im Tiefenwasser der Ostsee, *Beiträge zur Meereskunde*, **55**: 39–53.

Matthäus, W. (1990), Der Austausch durch die primäre Salzgehaltssprungschicht der Ostsee, *Beiträge zur Meereskunde*, **61**: 21–31.

Matthäus, W., and H. Franck (1992), Characteristics of major Baltic inflows – a statistical analysis, *Continental Shelf Research*, **12(12)**: 1375–1400, doi:10.1016/0278-4343(92)90060-W.

Matthäus, W., G. Nausch, H.-U. Lass, K. Nagel, and H. Siegel (1999), The Baltic Sea in 1998 – characteristic features of the current stagnation period, nutrient conditions in the surface layer and exceptionally high deep water temperatures, *Deutsche Hydrographische Zeitschrift*, **51(1)**: 67–84, doi:10.1007/BF02763957.

Matthäus, W., D. Nehring, R. Feistel, G. Nausch, V. Mohrholz, and H.-U. Lass (2008), The inflow of highly saline water into the Baltic Sea, in *State and Evolution of the Baltic Sea, 1952-2005. A detailed 50-year survey of meteorology and climate, physics, chemistry, biology, and marine environment*, edited by R. Feistel, G. Nausch, and N. Wasmund, pp. 265–309, Wiley-Interscience, Hoboken, NJ, USA.

Mattsson, J. (1996), Some comments on the barotropic flow through the Danish Straits and the division of the flow between the Belt Sea and the Öresund, *Tellus A*, **48(3)**: 456–464, doi:10.1034/j.1600-0870.1996.t01-2-00007.x.

McComas, C. H., and F. P. Bretherton (1977), Resonant interaction of oceanic internal waves, *Journal of Geophysical Research*, **82(9)**: 1397–1412, doi:10.1029/JC082i009p01397.

Meier, H. E. M. (2005), Modeling the age of Baltic Seawater masses: Quantification and steady state sensitivity experiments, *Journal of Geophysical Research – Oceans*, **110**: C02006, doi: 10.1029/2004JC002607.

Merryfield, W. J. (2005), Dependence of differential mixing on N and R_ρ, *Journal of Physical Oceanography*, **35(6)**: 991–1003, doi:10.1175/JPO2747.1.

Millero, F. J., R. Feistel, D. G. Wright, and T. J. McDougall (2008), The composition of Standard Seawater and the definition of the Reference-Composition Salinity Scale, *Deep-Sea Research Part I*, **55(1)**: 50–72, doi:10.1016/j.dsr.2007.10.001.

Missiaen, T., and L. Noppe (2010), Detailed seismic imaging of a chemical munition dumpsite in the Bornholm Basin, south-western Baltic, *Environmental Earth Sciences*, **60(1)**: 81–94, doi: 10.1007/s12665-009-0171-9.

Missiaen, T., I. P. M. Söderström, and P. Vanninen (2010), Evaluation of a chemical munition dumpsite in the Baltic Sea based on geophysical and chemical investigations, *Science of the Total Environment*, **408(17)**: 3536–3553, doi:10.1016/j.scitotenv.2010.04.056.

Mohrholz, V., J. Dutz, and G. Kraus (2006), The impact of exceptionally warm summer inflow events on the environmental conditions in the Bornholm Basin, *Journal of Marine Systems*, **60(3–4)**: 285–301, doi:10.1016/j.jmarsys.2005.10.002.

Möllmann, C., F. W. Köster, G. Kornilovs, and L. Sidrevics (2003), Interannual variability in population dynamics of calanoid copepods in the central Baltic Sea, *ICES Marine Science Symposia*, **219**: 220–230.

Morozov, E. G., S. A. Shchuka, and V. S. Zapotylko (2007), Towed spectra of internal waves in the pycnocline of the Baltic Sea, *Doklady Earth Sciences*, **412(1)**: 151–153, doi: 10.1134/S1028334X07010357.

Moum, J. N., M. C. Gregg, R.-C. Lien, and M. E. Carr (1995), Comparison of turbulence kinetic energy dissipation rate estimates from two ocean microstructure profilers, *Journal of Atmospheric and Oceanic Technology*, **12(2)**: 346–366, doi:10.1175/1520-0426(1995)012<0346:COTKED>2.0.CO;2.

Moum, J. N., A. Perlin, J. M. Klymak, M. D. Levine, T. Boyd, and P. M. Kosro (2004), Convectively-driven mixing in the bottom boundary layer, *Journal of Physical Oceanography*, **34(10)**: 2189–2202, doi:10.1175/1520-0485(2004)034<2189:CDMITB>2.0.CO;2.

Moum, J. N., J. D. Nash, and W. D. Smyth (2011), Narrowband oscillations in the upper equatorial ocean. Part I: Interpretation as shear instabilities, *Journal of Physical Oceanography*, **41(3)**: 397–411, doi:10.1175/2010JPO4450.1.

Mowbray, D. E., and B. S. H. Rarity (1967), A theoretical and experimental investigation of the phase configuration of internal waves of small amplitude in a density stratified liquid, *Journal of Fluid Mechanics*, **28(1)**: 1–16, doi:10.1017/S0022112067001867.

Mueller, R. D., W. D. Smyth, and B. Ruddick (2007), Shear and convective turbulence in a model of thermohaline intrusions, *Journal of Physical Oceanography*, **37(10)**: 2534–2549, doi: 10.1175/JPO3137.1.

Müller, P., G. Holloway, F. Henyey, and N. Pomphrey (1986), Nonlinear interactions among internal gravity waves, *Reviews of Geophysics*, **24(3)**: 493–536, doi:10.1029/RG024i003p00493.

Munk, W. H. (1966), Abyssal recipes, *Deep-Sea Research and Oceanographic Abstracts*, **13(4)**: 707–730, doi:10.1016/0011-7471(66)90602-4.

Munk, W. H. (1981), Internal waves and small-scale processes, in *Evolution of Physical Oceanography*, edited by B. A. Warren and C. Wunsch, pp. 264–291, MIT Press, Cambridge, MA, USA.

Nansen, F. (1897a), *Farthest North: Being the record of a voyage of exploration of the ship "Fram" 1893–96 and of a fifteen months' sleigh journey by Dr. Nansen and Lieut. Johansen – Vol. 1*, 587 pp., Harper & Brothers Publishers, New York, NY, USA.

Nansen, F. (1897b), *Farthest North: Being the record of a voyage of exploration of the ship "Fram" 1893–96 and of a fifteen months' sleigh journey by Dr. Nansen and Lieut. Johansen – Vol. 2*, 749 pp., Harper & Brothers Publishers, New York, NY, USA.

Nansen, F. (1902), The oceanography of the North Pole Basin, *Scientific Results of the Norwegian North Polar Expedition, 1893–1896*, **3(9)**: 427.

Nasmyth, P. W. (1970), Oceanic turbulence, PhD thesis, 106 pp., Department of Physics, University of British Columbia – Vancouver, Canada.

Nerheim, S. (2004), Shear-generating motions at various length scales and frequencies in the Baltic Sea – an attempt to narrow down the problem of horizontal dispersion, *Oceanologia*, **46(4)**: 477–503.

Neuenfeldt, S. (2002), The influence of oxygen saturation on the distributional overlap of predator (cod, *Gadus morhua*) and prey (herring, *Clupea harengus*) in the Bornholm Basin of the Baltic Sea, *Fisheries Oceanography*, **11(1)**: 11–17, doi:10.1046/j.1365-2419.2002.00183.x.

Neuenfeldt, S., K. H. Andersen, and H.-H. Hinrichsen (2009), Some Atlantic cod *Gadus morhua* in the Baltic Sea visit hypoxic water briefly but often, *Journal of Fish Biology*, **75(1)**: 290–294, doi:10.1111/j.1095-8649.2009.02281.x.

Neumann, G. (1946), Stehende zellulare Wellen im Meere, *Die Naturwissenschaften*, **33(9)**: 282–283, doi:10.1007/BF01197198.

Oakey, N. S. (1982), Determination of the rate of dissipation of turbulent energy from simultaneous temperature and velocity shear microstructure measurements, *Journal of Physical Oceanography*, **12(3)**: 256–271, doi:10.1175/1520-0485(1982)012<0256:DOTROD>2.0.CO;2.

Olson, P. (1977), Internal waves in the earth's core, *Geophysical Journal of the Royal Astronomical Society*, **51(1)**: 183–215, doi:10.1111/j.1365-246X.1977.tb04196.x.

Ozmidov, R. V. (1995), The role of boundary effects in the deepwater exchange in the Baltic Sea, *Oceanology*, **34(4)**: 440–444.

Palmer, M. R., T. P. Rippeth, and J. H. Simpson (2008), An investigation of internal mixing in a seasonally stratified shelf sea, *Journal of Geophysical Research – Oceans*, **113**: C12005, doi: 10.1029/2007JC004531.

Phillips, O. M. (1958), The equilibrium range in the spectrum of wind-generated waves, *Journal of Fluid Mechanics*, **4(4)**: 426–434, doi:10.1017/S0022112058000550.

Phillips, O. M. (1971), On spectra measured in an undulating layered medium, *Journal of Physical Oceanography*, **1(1)**: 1–6, doi:10.1175/1520-0485(1971)001<0001:OSMIAU>2.0.CO;2.

Phillips, O. M. (1991), The Kolmogorov spectrum and its oceanic cousins: A review, *Proceedings of the Royal Society A: Mathematical, Physical and Engineering Sciences*, **434(1890)**: 125–138, doi:10.1098/rspa.1991.0084.

Pohlmann, T. (1996), Simulating the heat storage in the North Sea with a three-dimensional circulation model, *Continental Shelf Research*, **16(2)**: 195–213, doi:10.1016/0278-4343(95)00032-V.

Polton, J. A., J. A. Smith, J. A. MacKinnon, and A. E. Tejada-Martínez (2008), Rapid generation of high-frequency internal waves beneath a wind and wave forced oceanic surface mixed layer, *Geophysical Research Letters*, **35**: L13602, doi:10.1029/2008GL033856.

Polzin, K. L., J. M. Toole, and R. W. Schmitt (1995), Finescale parameterizations of turbulent dissipation, *Journal of Physical Oceanography*, **25(3)**: 306–328, doi:10.1175/1520-0485(1995)025<0306:FPOTD>2.0.CO;2.

Polzin, K. L., J. M. Toole, J. R. Ledwell, and R. W. Schmitt (1997), Spatial variability of turbulent mixing in the abyssal ocean, *Science*, **276(5309)**: 93–96, doi:10.1126/science.276.5309.93.

Pope, S. B. (2000), *Turbulent Flows*, 749 pp., Cambridge Universtity Press, Cambridge, UK.

Prandke, H. (2010), PNS03/06 shear probes for microstructure measurements, *Tech. rep.*, 9 pp., ISW Wassermesstechnik, url:http://www.isw-wasser.com/prandke/images/pdf/shear_sensor.pdf.

Prandke, H., and K. Pfeiffer (1994), Shear probe for use in operational microstructure measuring systems, *OCEANS '94. 'Oceans Engineering for Today's Technology and Tomorrow's Preservation.' Proceedings*, **1**: 414–418, doi:10.1109/OCEANS.1994.363959.

Prandke, H., and A. Stips (1992), A model of Baltic thermocline turbulence patches, deduced from experimental investigations, *Continental Shelf Research*, **12(5–6)**: 643–659, doi:10.1016/0278-4343(92)90024-E.

Prandke, H., and A. Stips (1998), Test measurements with an operational microstructure-turbulence profiler: Detection limit of dissipation rates, *Aquatic Sciences*, **60(3)**: 191–209, doi:10.1007/s000270050036.

Press, W. H. (1981), Radiative and other effects from internal waves in solar and stellar interiors, *Astrophysical Journal*, **245**: 286–303, doi:10.1086/158809.

Puig, P., A. Palanques, J. Guillén, and M. El Khatab (2004), Role of internal waves in the generation of nepheloid layers on the northwestern Alboran slope: Implications for continental margin shaping, *Journal of Geophysical Research – Oceans*, **109**: C09011, doi:10.1029/2004JC002394.

Ray, R. D. (2009), Internal tides, in *Encyclopedia of Ocean Sciences*, edited by J. H. Steele, S. A. Thorpe, and K. K. Turekian, 2nd ed., pp. 258–265, Academic Press/Elsevier, Amsterdam, NL.

Ray, R. D., and G. T. Mitchum (1996), Surface manifestation of internal tides generated near Hawaii, *Geophysical Research Letters*, **23(16)**: 2101–2104, doi:0.1029/96GL02050.

Lord Rayleigh (1883), Investigation of the character of the equilibrium of an incompressible heavy fluid of variable density, *Proceedings of the London Mathematical Society*, **s1-14(1)**: 170–177, doi:10.1112/plms/s1-14.1.170.

Reißmann, J. H. (2005), An algorithm to detect isolated anomalies in three-dimensional stratified data fields with an application to density fields from four deep basins of the Baltic Sea, *Journal of Geophysical Research – Oceans*, **110**: C12018, doi:10.1029/2005JC002885.

Reißmann, J. H., H. Burchard, R. Feistel, E. Hagen, H.-U. Lass, V. Mohrholz, G. Nausch, L. Umlauf, and G. Wieczorek (2009), Vertical mixing in the Baltic Sea and consequences for eutrophication – A review, *Progress in Oceanography*, **82(1)**: 47–80, doi:10.1016/j.pocean.2007.10.004.

Roberts, J., and T. D. Roberts (1978), Use of the Butterworth low-pass filter for oceanographic data, *Journal of Geophysical Research – Oceans*, **83(C11)**: 5510–5514, doi:10.1029/JC083iC11p05510.

Rohde, K.-H. (1966), Untersuchungen über die Calcium- und Magnesiumanomalie in der Ostsee, *Beiträge zur Meereskunde*, **19**: 18–31.

Ruddick, B. (1983), A practical indicator of the stability of the water column to double-diffusive activity, *Deep-Sea Research A*, **30(10)**: 1105–1107, doi:10.1016/0198-0149(83)90063-8.

Saggio, A., and J. Imberger (1998), Internal wave weather in a stratified lake, *Limnology and Oceanography*, **43(8)**: 1780–1795.

Sauramo, M. R. (1958), *Die Geschichte der Ostsee*, Annales Academiæ Scientiarum Fennicæ Series A III 51, 522 pp., Suomalainen Tiedeakatemia, Helsinki, FI.

Schafstall, J., M. Dengler, P. Brandt, and H. Bange (2010), Tidal-induced mixing and diapycnal nutrient fluxes in the Mauritanian upwelling region, *Journal of Geophysical Research – Oceans*, **115**: C10014, doi:10.1029/2009JC005940.

Schmager, G., P. Fröhle, D. Schrader, R. Weisse, and S. Müller-Navarra (2008), Sea State, Tides, in *State and Evolution of the Baltic Sea, 1952-2005. A detailed 50-year survey of meteorology and climate, physics, chemistry, biology, and marine environment*, edited by R. Feistel, G. Nausch, and N. Wasmund, pp. 143–198, Wiley-Interscience, Hoboken, NJ, USA.

Schoning, K. (2001), The brackish Baltic Sea Yoldia Stage – palaeoenvironmental implications from marine benthic fauna and stable oxygen isotopes, *Boreas*, **30(4)**: 290–298, doi:10.1111/j.1502-3885.2001.tb01048.x.

Senf, F., and U. Achatz (2011), On the impact of middle-atmosphere thermal tides on the propagation and dissipation of gravity waves, *Journal of Geophysical Research – Atmospheres*, **116**: D24110, doi:10.1029/2011JD015794.

Shih, L. H., J. R. Koseff, G. N. Ivey, and J. H. Ferziger (2005), Parameterization of turbulent fluxes and scales using homogeneous sheared stably stratified turbulence simulations, *Journal of Fluid Mechanics*, **525**: 193–214, doi:10.1017/S0022112004002587.

Silverthorne, K. E., and J. M. Toole (2009), Seasonal kinetic energy variability of near-inertial motions, *Journal of Physical Oceanography*, **39(4)**: 1035–1049, doi:10.1175/2008JPO3920.1.

Simpson, J. H. (1981), The shelf-sea fronts: Implications of their existence and behaviour, *Philosophical Transactions of the Royal Society of London. Series A, Mathematical and Physical Sciences*, **302(1472)**: 531–546, doi:10.1098/rsta.1981.0181.

Simpson, J. H., and D. G. Bowers (1984), The role of tidal stirring in controlling the seasonal heat cycle in shelf seas, *Annales Geophysicae*, **2(4)**: 411–416.

Simpson, J. H., C. M. Allen, and N. C. G. Morris (1978), Fronts on the continental shelf, *Journal of Geophysical Research – Oceans*, **83(C9)**: 4607–4614, doi:10.1029/JC083iC09p04607.

Simpson, J. H., P. J. Wiles, and B. J. Lincoln (2011), Internal seiche modes and bottom boundary-layer dissipation in a temperate lake from acoustic measurements, *Limnology and Oceanography*, **56(5)**: 1893–1906, doi:10.4319/lo.2011.56.5.1893.

Smith, S. D. (1980), Wind stress and heat flux over the ocean in gale force winds, *Journal of Physical Oceanography*, **10(5)**: 709–726, doi:10.1175/1520-0485(1980)010<0709:WSAHFO>2.0.CO;2.

Smith, S. D. (1988), Coefficients for sea surface wind stress, heat flux, and wind profiles as a function of wind speed and temperature, *Journal of Geophysical Research – Oceans*, **93(C12)**: 15467–15472, doi:10.1029/JC093iC12p15467.

Smyth, W. D., and S. Kimura (2007), Instability and diapycnal momentum transport in a double-diffusive, stratified shear layer, *Journal of Physical Oceanography*, **37(6)**: 1551–1565, doi: 10.1175/JPO3070.1.

Smyth, W. D., and S. Kimura (2010), Turbulent mixing by Kelvin-Helmholtz billows in fingering-favorable stratification, *EOS Transactions AGU*, **91(26)**: Ocean Sciences Meeting Supplement, Abstract PO35K–07.

Smyth, W. D., and J. N. Moum (2000a), Length scales of turbulence in stably stratified mixing layers, *Physics of Fluids*, **12(6)**: 1327–1342, doi:10.1063/1.870385.

Smyth, W. D., and J. N. Moum (2000b), Anisotropy of turbulence in stably stratified mixing layers, *Physics of Fluids*, **12(6)**: 1343–1362, doi:10.1063/1.870386.

Smyth, W. D., J. N. Moum, and J. D. Nash (2011), Narrowband oscillations in the upper equatorial ocean. Part II: Properties of shear instabilities, *Journal of Physical Oceanography*, **41(3)**: 412–428, doi:10.1175/2010JPO4451.1.

Soulsby, R. L. (1983), The Bottom Boundary Layer of Shelf Seas, in *Physical Oceanography of Coastal and Shelf Seas*, edited by B. Johns, Elsevier Oceanography Series 35, pp. 189–266, Elsevier, Amsterdam, NL.

Stepputtis, D., H.-H. Hinrichsen, U. Böttcher, E. Götze, and V. Mohrholz (2011), An example of meso-scale hydrographic features in the central Baltic Sea and their influence on the distribution and vertical migration of sprat, *Sprattus sprattus balticus* (Schn.), *Fisheries Oceanography*, **20(1)**: 82–88, doi:10.1111/j.1365-2419.2010.00567.x.

Stigebrandt, A. (1987), A model for the vertical circulation of the Baltic deep water, *Journal of Physical Oceanograpy*, **17(10)**: 1772–1785, doi:10.1175/1520-0485(1987)017<1772:AMFTVC>2.0.CO;2.

Stigebrandt, A., H.-U. Lass, B. Liljebladh, P. Alenius, J. Piechura, R. Hietala, and A. Beszczyńska (2002), DIAMIX – An experimental study of diapycnal deep-water mixing in the virtually tideless Baltic Sea, *Boreal Environment Research*, **7(4)**: 363–369.

Stips, A. (2005), Dissipation measurement: theory, in *Marine Turbulence: Theories, Observations, and Models*, edited by H. Z. Baumert, J. Simpson, and J. Sündermann, pp. 115–126, Cambridge University Press, Cambridge, UK.

Stokes, G. G. (1847), On the theory of oscillatory waves, *Transactions of the Cambridge Philosophical Society*, **8(4)**: 441–455.

Sturm, M., R. Helm, and W. Fennel (1988), Mesoskale Wirbel in der westlichen Ostsee, *Beiträge zur Meereskunde*, **58**: 73–75.

Subramanian, G. (2010), Viscosity-enhanced bio-mixing of the oceans, *Current Science*, **98(8)**: 1103–1108.

Sundfjord, A., I. Fer, Y. Kasajima, and H. Svendsen (2007), Observations of turbulent mixing and hydrography in the marginal ice zone of the Barents Sea, *Journal of Geophysical Research – Oceans*, **112**: C05008, doi:10.1029/2006JC003524.

Talipova, T. G., E. N. Pelinovskii, and T. Kouts (1998), Kinematic characteristics of an internal wave field in the Gotland Deep in the Baltic Sea, *Oceanology*, **38(1)**: 33–42.

Taylor, G. I. (1938), The spectrum of turbulence, *Proceedings of the Royal Society of London A*, **164(919)**: 476–490, doi:10.1098/rspa.1938.0032.

Taylor, M. J., and M. A. Hapgood (1988), Identification of a thunderstorm as a source of short period gravity waves in the upper atmospheric nightglow emissions, *Planetary and Space Science*, **36(10)**: 975–985, doi:10.1016/0032-0633(88)90035-9.

Thorpe, S. A. (1977), Turbulence and mixing in a Scottish loch, *Philosophical Transactions of the Royal Society of London. Series A, Mathematical and Physical Sciences*, **286(1334)**: 125–181, doi:10.1098/rsta.1977.0112.

Thorpe, S. A. (1987), On the reflection of a train of finite-amplitude internal waves from a uniform slope, *Journal of Fluid Mechanics*, **178**: 279–302, doi:10.1017/S0022112087001228.

Thorpe, S. A. (1997), On the interactions of internal waves reflecting from slopes, *Journal of Physical Oceanography*, **27(9)**: 2072–2078, doi:10.1175/1520-0485(1997)027<2072:OTIOIW>2.0.CO;2.

Thorpe, S. A. (2005), *The Turbulent Ocean*, 439 pp., Cambridge University Press, Cambridge, UK.

Tikkanen, M., and J. Oksanen (2002), Late Weichselian and Holocene shore displacement history of the Baltic Sea in Finland, *Fennia*, **180(1–2)**: 9–20.

Toole, J. M., R. W. Schmitt, and K. L. Polzin (1994), Estimates of diapycnal mixing in the abyssal ocean, *Science*, **264(5162)**: 1120–1123, doi:10.1126/science.264.5162.1120.

Townsend, A. A. (1965), Excitation of internal waves by a turbulent boundary layer, *Journal of Fluid Mechanics*, **22(2)**: 241–252, doi:10.1017/S002211206500071X.

Townsend, A. A. (1966), Internal waves produced by a convective layer, *Journal of Fluid Mechanics*, **24(2)**: 307–319, doi:10.1017/S0022112066000661.

Townsend, A. A. (1968), Excitation of internal waves in a stably-stratified atmosphere with considerable wind-shear, *Journal of Fluid Mechanics*, **32(1)**: 145–171, doi:10.1017/S0022112068000637.

Tulkki, P. (1965), Disappearance of the benthic fauna from the Basin of Bornholm (Southern Baltic) due to oxygen deficiency, *Cahiers de Biologie Marine*, **VI**: 455–463.

Turner, J. S. (1965), The coupled turbulent transports of salt and and heat across a sharp density interface, *International Journal of Heat and Mass Transfer*, **8(5)**: 759–767 (759–760, IN3–IN4, 761–767), doi:10.1016/0017-9310(65)90022-0.

Turner, J. S. (1979), *Buoyancy effects in fluids*, 1st ed., 368 pp., Cambridge University Press, Cambridge, UK.

Umlauf, L., and L. Arneborg (2009), Dynamics of rotating shallow gravity currents passing through a channel. Part I: Observation of transverse structure, *Journal of Physical Oceanography*, **39(10)**: 2385–2401, doi:10.1175/2009JPO4159.1.

Umlauf, L., and E. M. van der Lee (2010), Notes on spectral analysis, version: August 19th 2010, Leibniz-Institut für Ostseeforschung Warnemünde, Germany, url:http://www.io-warnemuende.de/tl_files/staff/umlauf/pdf/spectra.pdf.

Väisälä, V. (1926), Über die Wirkung der Windschwankungen auf die Pilotbeobachtungen 1, *Societas scientiarum Fennica – Commentationes physico-mathematicae*, **2(19)**: 19–37.

van der Lee, E. M., and L. Umlauf (2011), Internal wave mixing in the Baltic Sea: Near-inertial waves in the absence of tides, *Journal of Geophysical Research – Oceans*, **116**: C10016, doi: 10.1029/2011JC007072.

van der Lee, E. M., and L. Umlauf (2012), Internal wave mixing in the Baltic Sea: Observation of high-frequency waves, *Continental Shelf Research*, in prep.

van Haren, H., and L. Gostiaux (2009), High-resolution open-ocean temperature spectra, *Journal of Geophysical Research – Oceans*, **114**: C05005, doi:10.1029/2008JC004967.

van Haren, H., M. Laan, D.-J. Buijsman, L. Gostiaux, M. G. Smit, and E. Keijzer (2009), NIOZ3: Independent temperature sensors sampling yearlong data at a rate of 1 Hz, *IEEE Journal of Oceanic Engineering*, **34(3)**: 315–322, doi:10.1109/JOE.2009.2021237.

Visser, A. W. (2007), Biomixing of the oceans?, *Science*, **316(5826)**: 838–839, doi: 10.1126/science.1141272.

Vlasenko, V., and K. Hutter (2002), Numerical experiments on the breaking of solitary internal waves over a slope–shelf topography, *Journal of Physical Oceanography*, **32(6)**: 1779–1793, doi: 10.1175/1520-0485(2002)032<1779:NEOTBO>2.0.CO;2.

Wain, D. J., and C. R. Rehmann (2010), Transport by an intrusion generated by boundary mixing in a lake, *Water Resources Research*, **46**: W08517, doi:10.1029/2009WR008391.

Wasmund, N., M. Voß, and H. Siegel (2011), Faktenblatt "Blaualgen" – Cyanobakterien, *Tech. rep.*, Leibniz-Institut für Ostseeforschung Warnemünde, Germany, url:http://www.io-warnemuende.de/blaualgen-cyanobakterien.html.

Watson, E. R. (1904), Movements of the waters of Loch Ness, as indicated by temperature observations, *The Geographical Journal*, **24(4)**: 430–437.

Wedderburn, E. M. (1907), The temperature of the fresh water lochs of Scotland, with special references to Loch Ness, *Transactions of the Royal Society of Edinburgh*, **45**: 407–489.

Wieczorek, G., E. Hagen, and L. Umlauf (2008), Eastern Gotland Basin case study of thermal variability in the wake of deep water intrusions, *Journal of Marine Systems*, **74(Supplement 1)**: S65–S79, doi:10.1016/j.jmarsys.2008.07.008.

Wieland, K., and F. Zuzarte (1991), Vertical distribution of cod and sprat eggs and larvae in the Bornholm Basin (Baltic Sea) 1987–1990, *ICES Council Meeting*, **J**: 37.

Winterhalter, B., T. Flodé, H. Ignatius, S. Axberg, and L. Niemistö (1981), Geology of the Baltic Sea, in *The Baltic Sea*, edited by A. Voipio, Elsevier Oceanography Series 30, pp. 1–121, Elsevier, Amsterdam, NL.

Wüest, A., G. Piepke, and D. C. Van Senden (2000), Turbulent kinetic energy balance as a tool for estimating vertical diffusivity in wind-forced stratified waters, *Limnology and Oceanography*, **45(6)**: 1388–1400, doi:10.4319/lo.2000.45.6.1388.

Xing, J., and A. M. Davies (2001), A three-dimensional baroclinic model of the Irish Sea: Formation of the thermal fronts and associated circulation, *Journal of Physical Oceanography*, **31(1)**: 94–114, doi:10.1175/1520-0485(2001)031<0094:ATDBMO>2.0.CO;2.

Yamazaki, H., and T. Osborn (1990), Dissipation estimates for stratified turbulence, *Journal of Geophysical Research – Oceans*, **95(C6)**: 9739–9744, doi:10.1029/JC095iC06p09739.

Zhang, H. P., B. King, and H. L. Swinney (2008), Resonant generation of internal waves on a model continental slope, *Physical Review Letters*, **100(24)**: 244504, doi:10.1103/PhysRevLett.100.244504.

Zhao, Z., M. H. Alford, J. Girton, T. M. S. Johnston, and G. Carter (2011), Internal tides around the Hawaiian Ridge estimated from multisatellite altimetry, *Journal of Geophysical Research – Oceans*, **116**: C12039, doi:10.1029/2011JC007045.

Zhurbas, V. M., and V. T. Paka (1997), Mesoscale thermohaline variability in the Eastern Gotland Basin following the 1993 major Baltic inflow, *Journal of Geophysical Research – Oceans*, **102(C9)**: 20917–20926, doi:10.1029/97JC00443.

Zhurbas, V. M., and V. T. Paka (1999), What drives thermohaline intrusions in the Baltic Sea?, *Journal of Marine Systems*, **21(1–4)**: 229–241, doi:10.1016/S0924-7963(99)00016-0.

List of Figures

List of Tables

Acknowledgements

I would like to thank the officers and crews of the R/V *Poseidon* and R/V *Alkor* as well as the scientists and students on board, especially those freezing outside during MSS night duty in February/March 2010. For mooring work and subsequent ADCP validation I would like to thank Volker Mohrholz and Toralf Heene. For providing additional data I thank Torsten Seifert (DWD model wind data), Ulf Gräwe (HELCOM BMPK02 station data) and Hans van Haren (his ADCP and thermistor chain data).

For guidance I thank the members of my thesis committee: Hans van Haren, Klaus Jürgens, Hans Burchard and Lars Umlauf. Hans van Haren joined the last cruise and will hopefully help improve Chap. 6 before submission. I especially thank my direct supervisor Lars Umlauf who forced me to learn physics, injected a lot of ideas as well as energy and enthusiasm into the project, and without whom this thesis would have been a whole different story.

For lots of discussions on hydrodynamics and oceanography, as well as help with crazy German Linux systems, Latex and Matlab I thank the whole COPPS working group, especially the (former) "inhabitants" of office 214.

Elisabeth Schulz I thank for corrected my German abstract so that native speakers do not have to cringe.

Peter Holtermann I thank for a million things, including programming Ubuntu tunnel / syncing / ssh "magic", lots of Matlab and Latex tips and tricks, theoretical discussion, proof-reading this whole thing, and for doing all the dishes over the last months of writing, thanks!

The PhD position was funded by the International Leibniz Graduate School for Gravity Waves and Turbulence in the Atmosphere and Ocean (ILWAO) project of the Leibniz-Gemeinschaft (WGL) and an extension by the Leibniz-Institut für Ostseeforschung Warnemünde.